VRIJE
UNIVERSITEIT
BRUSSEL

Thesis submitted in fulfilment of the requirements for the award of the degree of Doctor of Sciences

RESISTIVE ELECTRODES AND PARTICLE DETECTORS

Modeling and Measurements of Novel Detector Structures

Djunes Janssens

February 2024

Promotor: Prof. Dr. J. D'Hondth
Co-promotors: Dr. H. Schindler

Sciences and Bio-Engineering Sciences
Physics department

Abstract

Advancements in nuclear, particle, and astroparticle physics are intricately intertwined with technological progress in experimental instrumentation, particularly in the case of detectors used for precision measurements of the properties of particles. Furthermore, their use in radiation imaging fosters advancements in biomedical and material sciences. An emerging direction of development involves integrating resistive materials into detector architectures to enhance their performance and durability, thereby ensuring compliance with the stringent requirements for measurement precision and operation in more challenging conditions anticipated in future High Energy Physics (HEP) experiments. This movement is noticeable in detectors presently operational at the Large Hadron Collider experiments at CERN and those planned for the near future.

Continuous advancements in modeling and simulation tools, such as Garfield(++), have guided the widespread development and understanding of detector structures. Since new sensor technologies are proposed regularly, with resistive detectors becoming an ever-increasing fraction of these, it is prudent to reflect this progress in the capabilities of the modeling tools. Up to now, the effects of components with finite conductivity have not been modeled adequately in the software tools that are used for simulating the signal in particle detectors. As part of this thesis, a new framework was developed that is applicable to the wide range of detectors that are inaccessible through analytical means. Laboratory and test beam measurements are used to adjust and validate the simulation framework. Subsequently, the methodology is employed to test and optimize the response of various innovative particle detector readout structures.

Through simulation and measurement, we have explored novel solutions in the field of Multi-gap Resistive Plate Chambers, Micro Pattern Gaseous Detectors, and solid-state sensors, arising from the implementation of materials with finite conductivity. In addition to deepening the understanding of existing structures, these studies are necessary for designing and optimizing the next generation of particle detectors and their application to specific needs driven by HEP experiments and other applications.

Vooruitgang in de kern-, deeltjes- en astrodeeltjesfysica is nauw verbonden met de technologische vordering van experimentele instrumentatie, zoals detectoren die worden gebruikt voor het meten van de positie, tijd en energie van subatomaire deeltjes. Bovendien bevordert hun gebruik in radiologie verdere ontwikkelingen in de biomedische en materiaalwetenschappen. Gezien de striktere eisen voor meetnauwkeurigheid en de meer uitdagende meetomstandigheden die worden verwacht in toekomstige experimenten in de Hoge Energie Natuurkunde (HEP), worden er nieuwe oplossingen gezocht voor de volgende generatie van deeltjessensoren. Een veelbelovende innovatie is de integratie van materialen met een eindige elektrische weerstand die kunnen worden gebruikt om de nauwkeurigheid en robuustheid van het meetinstrument te verbeteren. Deze ontwikkeling kunnen we zien wanneer we kijken naar de detectoren die momenteel worden gebruikt in de experimenten van de Large Hadron Collider van CERN, of diegene die gepland zijn voor de nabije toekomst.

Voortdurende vooruitgang in simulatiesoftware, zoals Garfield(++), hebben bijgedragen aan de algemene ontwikkeling van detectiestructuren en de kennis over de achterliggende werking. Aangezien er regelmatig nieuwe sensortechnologieën worden voorgesteld waarbij detectoren met elektrische weerstandsmaterialen een steeds groter deel van zijn, is het nodig om deze vooruitgang te weerspiegelen in de berekeningscapaciteiten van de modelleringstools. Tot nu toe zijn de effecten van componenten met eindige elektrische geleidbaarheid ofwel niet, of niet nauwkeurig genoeg, gemodelleerd in de softwaretools die worden gebruikt voor het simuleren van het signaal in deeltjesdetectoren. Als onderdeel van dit proefschrift is er een nieuw raamwerk ontwikkeld dat van toepassing is op een breed scala van detectoren die niet toegankelijk zijn via analytische methoden. Laboratorium- en deeltjesbundelmetingen worden gebruikt om de simulatie aan te passen en te staven. Vervolgens wordt de methodologie gebruikt om de eigenschappen van verschillende innovatieve uitleesstructuren van de deeltjesdetector te testen en te optimaliseren.

Door middel van simulatie en metingen verkennen we nieuwe oplossingen op het gebied van Multi-gap Resistive Plate Chambers, Micro Pattern Gaseous Detectors en vaste-stof sensoren die voortkomen uit de implementatie van materialen met eindige elektrische geleidbaarheid. Naast het verdiepen van de kennis over bestaande structuren zijn deze studies essentieel voor het ontwerpen en optimaliseren van de volgende generatie deeltjesdetectoren en hun toepassing in HEP-experimenten en andere toepassingen met specifieke benodigdheden.

List of publications relevant to the project

- D. Janssens et al., "Induced signals in particle detectors with resistive elements: Numerically modeling novel structures (VCI 2022)", Nucl. Instrum. Meth. A 1040 (2022) 167227
- K.J. Flöthner, D. Janssens et al., "The XYU-GEM: Ambiguity-free coordinate readout of the Gas Electron Multiplier", Nucl. Instrum. Meth. A 1052 (2023) 168257
- M. Lisowska et al., "Towards robust PICOSEC Micromegas precise timing detectors", JINST **18** (2023) 07, C07018
- D. Janssens et al., "Studying signals in particle detectors with resistive elements such as the 2D resistive strip bulk MicroMegas", Journal of Instrumentation **18** (2023) 08, C08010
- D. Janssens and W. Riegler, "Noise in detectors containing distributed resistive elements", submitted to Nucl. Instrum. Meth. A, NIMA-D-23-01244.

Abbreviations

μ-RWELL	μ-Resistive WELL
AC	Alternating Current
ASIC	Application-Specific Integrated Circuit
ADC	Analogue-to-Digital Converter
ALICE	A Large Ion Collider Experiment
ATLAS	A Toroidal LHC Apparatus
CERN	European Organization for Nuclear Research
CFD	constant fraction discrimination
CMS	Compact Muon Solenoid
CoG	Centre-of-Gravity
COMPASS	Common Muon and Proton Apparatus for Structure and Spectroscopy
CVD	Chemical Vapor Deposited
DAQ	Data Acquisition
DC	Direct Current
DLC	Diamond-Like Carbon
DUT	Detector Under Test
ENC	Equivalent Noise Charge
FEM	Finite Element Method
FWHM	Full Width at Half Maximum
GEM	Gas Electron Multiplier
Heed	High Energy ElectroDynamics
HEP	High Energy Physics
HL-LHC	High-Luminosity Large Hadron Collider
HV	High Voltage
iRPC	Improved Resistive Plate Chamber
LGAD	Low Gain Avalanche Diode
LHC	Large Hadron Collider
LHCb	LHC Beauty
MCP	MicroChannel Plate
MCP-PMT	MicroChannel Plate PhotoMultiplier Tube
MicroCAT	Micro-Compteur à Trous
MicroMegas (MM)	micro-mesh Gaseous Structure

MIP	Minimum Ionizing Particle
MPGD	Micro-Pattern Gas Detector
MRPC	Multi-gap Resistive Plate Chamber
PH	Pulse Height
R&D	Research and Development
RICH	Ring-Imaging Cherenkov
RMS	Root Mean Square
RMSE	Root Mean Square Error
RPC	Resistive Plate Chamber
RSD	Resistive Silicon Detector
S/N	Signal-to-Noise Ratio
SAT	Signal Arival Time
SPS	Super Proton Synchrotron
T2K	Tokai to Kamioka
THL	Threshold Level
TIMESPOT	TIME and Space real-time Operating Tracker
TPC	Time Projection Chamber

Contents

Chapter 1

Introduction

Progress in experimental nuclear and particle physics hinges upon our ability to accurately measure the properties of particles coming from various sources, such as astrophysical events or particle colliders. For particle physics experiments, this progress is closely tied to the advancements in both particle accelerators and detector technologies. In such experiments – for example those found at the *Large Hadron Collider* (LHC) [1] at CERN – one strives to measure the kinematics of the particles, i.e., their energies, momenta, paths, and arrival times, and separate them based on their type. To this end, different kinds of detectors are designed to measure specific aspects of the particles: tracking detectors for the trajectories and momenta (given a magnetic field) of charged particles, hadronic and electromagnetic calorimeters for energy measurements, detectors using Cherenkov radiation for particle identification, etc. These detectors rely on the transfer of energy from incident particles to a sensitive detector medium, which is subsequently converted into a macroscopic observable. The nature of the interaction is subject to the type of the incident particle. For example, the strong interaction allows for detection of neutrons or energy measurements of hadrons, while the weak interaction enables the observation of neutrinos [2]. However, the most common interaction detector technologies rely on for their measurements is the electromagnetic interaction. Beyond the instrumentation of current or future collider experiments, particle detectors find application in, among other things, medical imaging [3], material science, nuclear reactor imaging [4], and archaeology through tomography of cosmic ray muons [5].

In this work we will primarily focus on so-called *ionization detectors*, the operational principle of which is based upon the creation of a *primary ionization pattern* in the sensitive medium by an incident particle. This pattern is comprised of clusters made up of either *electron-hole pairs* in the case of semiconductors, or *electron-ion pairs* in gases (or cryogenic liquids). The specific pattern – influenced by the detector medium, the particle's type, and energy – undergoes inherent fluctuations due to the stochastic nature of the underlying processes. These fluctuations can be characterized by the *mean interaction distance*, denoting the average distance between clusters, and the *cluster size distribution*, providing the number of pair productions in each cluster. Two examples are given in Fig. 1.1 (left) for the interaction of a photon and a relativistic muon with a gas medium. A detailed discussion of this topic can be found in most reference works, e.g., Ref. [2, 6]. Depending on their electric charge, electrons and ions (holes) undergo separation and travel through the detector when placed in an electric field. As they move, signals are induced on the readout electrodes, which can be subsequently processed and analyzed.

In gases, the amount of primary charge deposited by a single charged particle is typically below the observable limit. However, the application of strong electric fields triggers internal charge amplification through the generation of *Townsend avalanches*, enhancing the signal-to-noise ratio of the detector. A notable illustration is the Geiger-Müller counter, wherein a strong electric field near the central wire facilitates charge amplification by imparting enough energy to the electrons to ionize the atoms and molecules in the gas. This principle led to the seminal work of G. Charpak with the invention of the *Multi-Wire Proportional Chamber* (MWPC) in 1968 [7], which has been continuously refined since its introduction. MWPCs persist until today in High Energy Physics (HEP) experiments and can be found in the muon detector systems of experiments at the LHC. In 1988, a new category of gaseous detectors emerged, known as *Micro-pattern Gaseous Detectors* (MPGDs), driven by the need to surpass the limitations of wire-based detectors in terms of localization and rate capability. Two of the most well-known MPGDs are the *Gas Electron Multiplier* (GEM) devised by F. Sauli in 1997 [8] and the *micro-mesh gaseous structure* (MicroMegas) introduced by Y. Giomataris in 1996 [9]. Fig. 1.1 (left) illustrates the operating principle of a GEM detector, where high field regions are generated within conical holes inside a thin-foil made of copper-insulator-copper by applying a potential difference across the foil. A simulated Townsend avalanche inside a GEM hole is shown in Fig. 1.1 (right). While some will be collected on the surfaces of the insulator inside the hole or copper layer below, a significant fraction of electrons will be successfully extracted into the induction gap, where they continue to drift towards the anode plane where they will be collected. Multiple such GEM foils can be used in succession to increase the charge total amplification of the structure, while decreasing the risk of discharges [10]. Building on the extensive history of gaseous detectors, MPGDs have undergone continuous *Research and Development* (R&D) leading to their integration into the four large LHC experiments: ATLAS [11, 12], CMS [13, 14], ALICE [15, 16], and LHCb [17, 18]. An overview of these detectors and their applications can be found in Ref. [19, 20, 21].

While gaseous detectors are advantageous for instrumenting large areas, the need for precise tracking near the interaction vertices makes semiconductor sensors the preferred technology. In most large HEP experiments, the localization of primary interaction vertex and secondary vertices from decay particles is mostly performed by silicon pixel detectors positioned at the innermost layers close to the beam pipe. For reading on the underlying physics and operation of this detector family we refer to Ref. [23, 24]. As the High-Luminosity LHC (HL-LHC) [25] at CERN approaches, presenting unprecedented

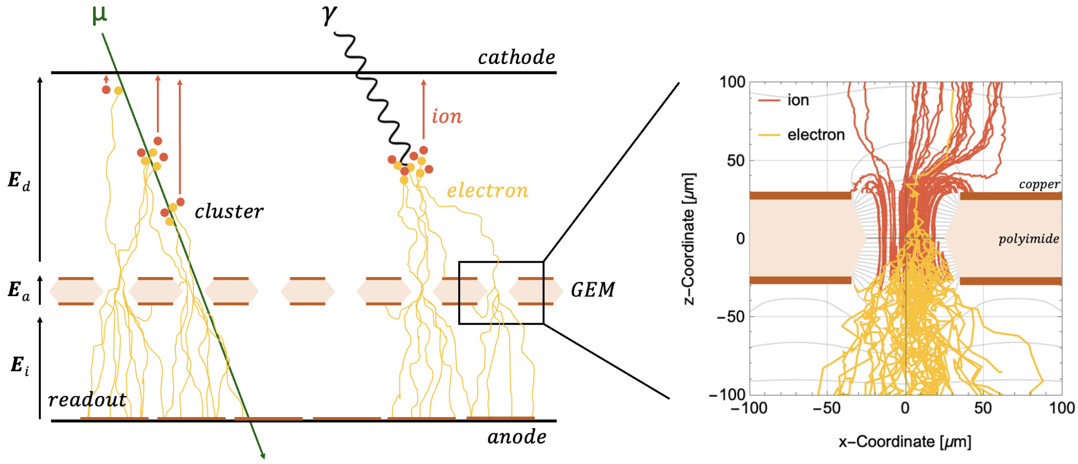

Figure 1.1: **Left:** Cross-sectional diagram of a GEM detector. By employing an electric field E_d, the primary electrons in the drift gap, resulting from the energy deposition by incident particles, are transported to the amplification region. Here, they undergo charge amplification and are subsequently extracted, along with the secondary electrons, to drift within the induction gap toward the readout plane. As they traverse the induction gap the movement of they a signal is induced on the electrodes that make up the readout. This diagram is based on Ref. [22]. **Right:** Simulated Townsend avalanche inside a GEM hole. The drift lines of the charge carries are overplayed with the equipotential lines resulting from the potential differences between the electrodes.

requirements for temporal, spatial performance, and radiation hardness, all while ensuring strong pileup mitigation, extensive R&D have been ongoing and continue to be pursued on different technologies to meet the stringent requirements [26]. One example is the advancements in tracking detectors to handle the increased number of primary vertices per bunch crossing. The availability of the time coordinate in addition to the spatial coordinates is advantageous for the next generation of tracking technologies, proving particularly beneficial for track and vertex reconstruction [27, 28]. This has spurred the development of so-called *4D-tracking sensors*, which combine a high granularity readout with precise timing capabilities; examples include the *Resistive Silicon Detector* (RSD) [29] and the *3D Diamond detector* [30] are prime examples. With the aim of performing precision measurements not achievable at the HL-LHC, colliders such as the Future Circular Collider (FCC) [31], the Compact Linear Collider (CLIC) [32] and the Muon Collider [33] are being proposed. These collider machines would tighten the requirements on the detector performances even further.

In the pursuit of more precise and robust detector designs for future experiments, there is a growing movement of incorporating materials with finite electrical conductivity, referred to as *resistive materials* or *resistive elements*, into the detector architectures [26]. This strategy offers a way to enhance operational stability, exemplified by the resistive strip MicroMegas of the ATLAS New Small Wheel (NSW) [34], and to optimize the performance of the detectors, as seen in the case of the RSD. The formation of the induced signal on the readout electrodes in the presence of these materials – which is the main topic of this thesis – can be said to be comprised of two constituents: (i) the direct induction from the movement of the free charge carriers in the detector medium (prompt response) and (ii) the induction from the time-dependent reaction of the resistive elements (delayed response). Consequently, the detector's response varies based on the specific implementation and characteristics of these resistive materials, expanding the range of possible configurations.

To further the capabilities of a detector design a good understanding of the underlying physics driving these devices is a prerequisite. Detailed simulation toolkits such as Geant4 [35, 36] and Garfield(++) [37, 38] have already played a key role in widespread development of particle detectors and detection methods. Therefore, extending the capability of these commonly used simulation software tools towards new technological solutions is vital. Theoretical estimates of the response of resistive detectors can, in part, be pursued analytically. While offering the benefit of insight through equations, solutions can only be obtained analytically for a small subset of the larger group of existing detectors. In this thesis, we present a novel numerical approach to characterise the response of various geometries of resistive materials by numerically applying an extended form of the Ramo-Shockley theorem with great flexibility. This was done in conjunction with work on the widely used program Garfield++ toolkit, which allows for the simulation of the physical processes underpinning the detectors. With this methodology we have explored novel solutions in the field of Multi-gap Resistive Plate Chambers (MRPCs), MPGDs, and semiconductor sensors. Measurements of the response of resistive detectors were performed to validate the accuracy of the macroscopic prediction derived from the Monte Carlo simulations. The application of this numerical approach to contemporary and future resistive technologies can inform the design of the next generation of particle detectors driven by the specific needs of future HEP experiments.

In Chapter 2, we delve into the fundamental principles of signal induction in resistive particle detectors. By treating Maxwell's equations in the quasi-static limit, we arrive at the extended form of the Ramo-Shockley theorem for conductive media, a central element in our work. This theorem is systematically applied to various toy model examples, elucidating the principles of signal response in both non-resistive and resistive devices. We discuss the merits of the extension to the Ramo-Shockley theorem compared to alternative methods, such as the transmission line equation, the two-dimensional Telegraph equation, and the RC-circuit element representations. With the framework for the computation of signal induction in resistive detectors established, we will explore the Johnson-Nyquist noise these resistive elements introduce into the system in Chapter 3. Here, a strategy is proposed to estimate the effect through both measurement and numerical simulation. The remainder of the work is the application, extension, and validation of the discussed numerical approaches to specific detector technologies. We have grouped these technologies based on the prominence the resistive elements have in their response, which is reflected in the division of the work into three remaining parts. In Part II, we consider the limit where the delayed response can be neglected. As an elementary case, we have the XYU-GEM detector of Chapter 4 for which resistive elements are absent. In this novel concept, we have developed a three-coordinate readout structure to resolve reconstruction ambiguities. In Chapter 5, the influence of a thin high resistivity layer on the timing performance will be discussed for the case of the precise timing PICOSEC MicroMegas detector, with the aim of developing a robust multi-pad that retains the below 25 ps resolution. Simulations were performed to inform the design of the prototype and to estimate the signal formation in the presence of a resistive layer and the rate capability of the device. The resulting prototype was characterized using *Minimally Ionising Particles* (MIPs). In Part III, detector technologies characterized by the predominant contribution of the resistive elements to their response will be discussed. A prime example of the leveraging the mechanism of signal formation in the presence of resistive elements is shown in Chapter 6, where the principles of resistive position-sensitive readout structures will be treated. Our numerical framework will be employed for the calculation of the characteristic correction map of the two-dimensional interpolation readout of the MICROCat detector in the absence and presence of non-uniformities in surface resistivity. As a radiation-tolerant 4D-tracking technology, the ongoing *R&D* for 3D diamond detectors uses two different simulation strategies. Both methods – the transmission line approach and the numerical application of the extended Ramo-Shockley theorem used through our collaboration with the TIMESPOT project – will be discussed in Chapter 7. In the final part, Part IV, the intermediate situation where both the prompt and delayed response are of significant importance will be discussed. Chapter 8 will be on the resistive strip MicroMegas. With this detector, a comparison of the measured and simulated induced current shape will be made to gauge the accuracy of the simulations. We will summarize the work contained in this thesis in chapter 9.

Part I

Resistive elements in particle detectors: fundamentals and applications

Chapter 2

Signal formation in resistive detectors

In this chapter, we provide a comprehensive survey of the essential theoretical foundations for the computation of induced signals in detectors containing resistive materials. We systematically examine fundamental principles, define key concepts, and present the numerical calculation techniques that have been implemented into Garfield++ [38, 39, 40]. While this will be a critical reference point for the subsequent chapters, it also introduces several benchmarking studies to validate our numerical approach.

2.1 Principles of current induction

Particles become detectable when they transfer (a portion of) their energy to the medium of the detector. Some of this energy leads to the creation of a primary ionization pattern through the ionization of nearby atoms and molecules. In the presence of an electric field, the resulting electron-hole or electron-ion pairs within semiconductor or gas-based media separate in accordance with their electrical charge polarity and traverse the detector medium. As we will explore further, this motion induces an electrical current on metal readout electrodes located inside the detector. This particular readout method is highly prevalent and commonly employed in both the MPGD and solid-state detector families. Notably, depending on the experimental application, there are other ways of particle detection, e.g., the detection of the emission spectrum coming from scintillation light inside the gas. This work will exclusively focus on the observation technique based on the induced signal formation on metal readout electrodes in ionisation detectors. The description of the motion of charges in the presence of electric and magnetic fields, as well as the resulting generation of current, fall within the domain of electrodynamics. In this field, the fundamental equations governing these phenomena are Maxwell's set of coupled partial differential equations. Together with the Lorentz force law, they are a cornerstone of classical electromagnetism and have played a pivotal role in our understanding of the fundamental forces, classical optics and electrical engineering.

Let us consider a linear material characterised by a non-uniform *volume resistivity* $\rho(\mathbf{x})$ which is the reciprocal of the *volume conductivity* of the material $\sigma = \rho^{-1}$, permittivity $\varepsilon(\mathbf{x})$, and permeability $\mu(\mathbf{x})$. The local current density resulting from the presence of an electric field $\mathbf{E}$ will be according to Ohm's microscopic law

$$\mathbf{j}(\mathbf{x}, t) = \sigma(\mathbf{x})\mathbf{E}(\mathbf{x}, t)\,, \tag{2.1.1}$$

with position $\mathbf{x} \in \mathbb{R}^3$ and time $t \in \mathbb{R}$. In this particular scenario, Maxwell's equations that govern the vector fields are expressed as follows

$$\nabla \cdot \mathbf{D}(\mathbf{x}, t) = \rho(\mathbf{x}, t) \qquad \text{(Gauss' law)} \tag{2.1.2a}$$

$$\nabla \cdot \mathbf{B}(\mathbf{x}, t) = 0 \qquad \text{(Gauss' law for magnetism)} \tag{2.1.2b}$$

$$\nabla \times \mathbf{E}(\mathbf{x}, t) = -\frac{\partial \mathbf{B}(\mathbf{x}, t)}{\partial t} \qquad \text{(Faraday's law)} \tag{2.1.2c}$$

$$\nabla \times \mathbf{H}(\mathbf{x}, t) = \frac{\partial \mathbf{D}(\mathbf{x}, t)}{\partial t} + \mathbf{j}_e(\mathbf{x}, t) + \sigma(\mathbf{x})\mathbf{E}(\mathbf{x}, t) \qquad \text{(Ampère's law)} \tag{2.1.2d}$$

for a *magnetic field* $\mathbf{B}(\mathbf{x}, t) = \mu(\mathbf{x})\mathbf{H}(\mathbf{x}, t)$ and *displacement field* $\mathbf{D}(\mathbf{x}, t) = \varepsilon(\mathbf{x})\mathbf{E}(\mathbf{x}, t)$. Contributing to the total current density is the externally impressed current density $\mathbf{j}_e$. It is related to the corresponding externally impressed charge density ρ_e through the continuity equation

$$\nabla \cdot \mathbf{j}_e(\mathbf{x}, t) = -\frac{\partial \rho_e(\mathbf{x}, t)}{\partial t}\,, \tag{2.1.3}$$

the empirical law expressing charge conservation.

When a perfectly conducting metal plate, i.e., $\sigma \to \infty$, is subjected to a static external electric field, the field induces a charge distribution on the metal's surface due to the redistribution of electrons within it. The resulting induced charge distribution creates an electric field within the plate that opposes the external field. Since the field lines are oriented perpendicular to the surface, we can employ the integral form of Gauss' law

$$\oint_{\partial V} \varepsilon(\mathbf{x})\mathbf{E}(\mathbf{x}) \cdot d\mathbf{A} = \int_V \rho(\mathbf{x}) d^3x \tag{2.1.4}$$

to establish a connection between the *surface charge density* $\sigma_s(x, y)$ [C/m^2] and the electric field at the metal surface. As depicted in the cross-section schematic in Fig. 2.1, we take a rectangular volume V that contains the plane S on the metal surface. For a uniform relative permittivity ε_r one can then obtain that

$$\hat{\mathbf{n}} \cdot \mathbf{E}(\mathbf{x})\big|_{\mathbf{x}\in S} = \frac{\sigma_s(x, y)}{\varepsilon_0 \varepsilon_r}\,, \tag{2.1.5}$$

with $\hat{\mathbf{n}}$ being the outward-pointing normal of S. More generally, taking the integral over the surface yields the *induced charge* on the metal plane

$$Q = \oint_{\partial V} \varepsilon(\mathbf{x})\mathbf{E}(\mathbf{x}) \cdot d\mathbf{A} = \int_S \sigma_s(x, y)\, dxdy\,. \tag{2.1.6}$$

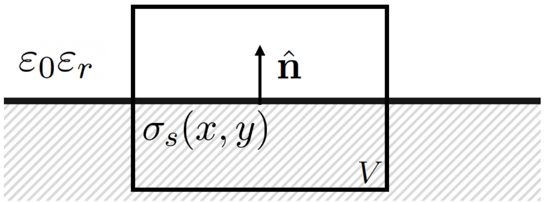

Figure 2.1: Induced surface charge density on the surface of a perfectly conducting metal.

This principle of charge density induction is at the foundation of how signals are formed in a particle detector. It is through this mechanism that both the movement of charge carriers in the medium and the reaction of the resistive elements induce an electrical current on the electrodes placed in the detector. To explore these concepts we present two practical textbook examples.

2.1.1 Charge moving in a half-space

To understand the mechanism behind the formation of signals on electrodes form the movement of charges, we will first focus on the idealized case where the system is only comprised of perfectly conducting and insulating materials. To review the basic principles, let us consider the example of a charge carrier q in a half-space $z > 0$ with a static homogeneous medium characterized by its permittivity ε and an infinitely extending, perfectly grounded metallic plate at $z = 0$ [41].

Working in the electrostatic regime, the field equation for the scalar potential ϕ is given by the Poisson equation

$$\nabla \cdot (\varepsilon(\mathbf{x})\nabla\phi(\mathbf{x})) = -\rho(\mathbf{x})\,, \tag{2.1.7}$$

where ρ is the charge density in the half-space. For a point-like particle at position $\mathbf{x}'$ this distribution can be written using a Dirac delta distribution

$$\rho(\mathbf{x}) = q\delta(\mathbf{x} - \mathbf{x}')\,. \tag{2.1.8}$$

If we impose the Dirichlet boundary condition

$$\phi(x, y, 0) = 0\,, \qquad \forall x, y \in \mathbb{R}\,, \tag{2.1.9}$$

the solution to Eq. (2.1.7) can be found through the method of images [42]

$$\begin{aligned}\phi(x,y,z) =& \frac{q}{4\pi\varepsilon}\frac{1}{\sqrt{(x-x')^2+(y-y')^2+(z-z')^2}} \\ &- \frac{q}{4\pi\varepsilon}\frac{1}{\sqrt{(x-x')^2+(y-y')^2+(z+z')^2}}\,.\end{aligned} \tag{2.1.10}$$

The two terms represent the combined free-space solutions for two charges located at heights z' and $-z'$, respectively. Because the right-hand side of Faraday's law (2.1.2c) vanishes, the electric field reads

$$\mathbf{E}(\mathbf{x}) = -\nabla\phi(\mathbf{x})\,. \tag{2.1.11}$$

Through induction the resulting electric field on the plate creates the charge distribution given by Eq. (2.1.5). Using Eq. (2.1.10) this distribution can be written as

$$\sigma_s(x,y) = -\,\varepsilon \frac{\partial\phi(x,y,z)}{\partial z}\bigg|_{z=0} = -\frac{q}{2\pi}\frac{z'}{\left((x-x')^2+(y-y')^2+z'^2\right)^{3/2}}\,. \tag{2.1.12}$$

Consequently, the overall charge induced on the metal surface is therefore

$$Q = \int_{-\infty}^{\infty}\int_{-\infty}^{\infty} \sigma_s(x,y,x',y')\,dxdy = -q\,, \tag{2.1.13}$$

which is independent of the position of charge q . So in this specific instance, the charges are merely redistributed on the surface when the charge carrier's position changes, and there is no flow of current between the plate and ground.

For most physics applications, position information of the incident particles is required, which is typically achieved through the segmentation of the readout plane into, for example, strip or pad electrodes. While the total amount of induced charge over the entire plane remains unchanging, the distribution of the surface charge density positioned on the surface S_k of electrode $k \in \mathbb{Z}$ is depending on the position of charge q. As an example we partition the grounded metal plate into strip electrodes running in the y-direction and individually ground them. Assuming that the width w_x of the strip is considerably greater than the spacing between neighboring strips, we can approximate them as being perfectly adjacent. The total induced charge on strip with index k is then given by

$$Q_k\left(x',z'\right) = \int_{-\infty}^{\infty}\int_{kw_x-w_x/2}^{kw_x+w_x/2} \sigma(x,y)\,dxdy \tag{2.1.14}$$

$$= -\frac{q}{\pi}\left[\arctan\left(\frac{w_x-2(x'-kw_x)}{2z'}\right) - \arctan\left(\frac{w_x+2(x'-kw_x)}{2z'}\right)\right]. \tag{2.1.15}$$

This induced charge on the grounded readout strip now depends on the point charge's position above the readout plane. If it were to move along a trajectory $\mathbf{x}(t)$ this becomes time-dependent and result in a current

$$I_k(t) = -\frac{dQ_k(\mathbf{x}'(t))}{dt}\,, \tag{2.1.16}$$

flowing between the electrode and ground. Here, we adhere to the 'conventional current direction', in which the current arrow is oriented away from the electrode. A positive current, therefore, signifies a decrease of positive charge on the electrode. If q traverses the path given by $\mathbf{x}'(t) = (x', y', -vt)$ for $v > 0$ and $t < 0$, the induced current has the form

$$I_k(t) = \frac{4qvw_x\left[4t^2v^2 + w_x^2 - 4(x' - kw_x)^2\right]}{\pi\left[4t^2v^2 + (w_x + 2x' - 2kw_x)^2\right)\left(4t^2v^2 + (w_x - 2x' + 2kw_x)^2\right]}\,, \qquad (2.1.17)$$

until q reaches the metal surface. For this reason we conclude it is the motion of the charge that is responsible for generating the signal being picked up by the electrode. As shown in Fig. 2.2 (left), the signal on the strip located below the charge's trajectory increases sharply when approaching its surface. The degree of sharpness intensifies as the strip narrows, and in the limit $w_x \to 0$, the induced current approaches a Dirac delta distribution:

$$\lim_{w_x \to 0} I_k(t) = q\delta(t)\,, \qquad \mathbf{x}'(0) \in S_k\,. \qquad (2.1.18)$$

This 'small pixel effect' resembles charge collection, where a current spike occurs as the charge reaches the electrode. This aspect should be taken into consideration when designing components like small silicon pixels, for instance. However, this is not the typical operating regime for most particle detectors, which usually feature electrodes with a substantial surface area, leading to more complex induced signal shapes. In general, the notion of 'pulsed' signals through charge collection is not applicable and we have to work with the induced currents. Henceforth, in the ongoing course of this work, the term "signal" will be used interchangeably with "induced signal" or "induced current", with the process of induction implied.

The amount of charge collected on each readout strip can be determined through integration of the signal over its duration, i.e., when $(x', y') \in S_k$ we have

$$\int_{-\infty}^{0} I_l(t)dt = q\delta_{kl}\,, \qquad l \in \mathbb{Z}\,, \qquad (2.1.19)$$

where we used the Kronecker delta function δ_{kl}. While smaller in amplitude, the neighboring electrodes do see a signal, referred to as *signal sharing*, as plotted in Fig. 2.2 (center and right) despite no charge being collected there. The time-dependent induced charge distribution in Eq. 2.1.12 stretches until these strips, causing in a current that has both a positive and negative component, resulting in a vanishing induced charge contribution when integrated.

2.1.2 Maxwell's equations in the quasi-static limit

Up to this point, we have exclusively addressed the subject of signal formation in the presence of dielectric media. In order to transition towards materials with finite conductivity, often referred to as *resistive materials* or *resistive elements*, we will now proceed with an example involving the diffusion of charge at the interface between two such media. To accomplish this, we will handle Maxwell's equations within the quasi-static regime

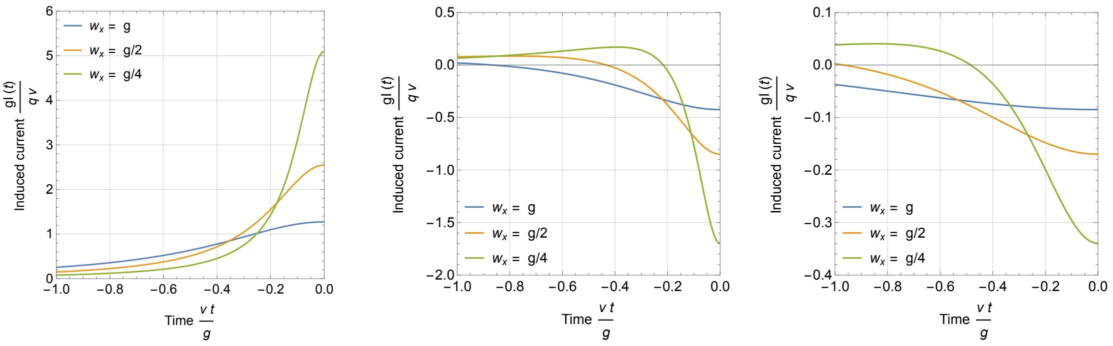

Figure 2.2: Current induced by the movement of a charge carrier in a half space, starting from $x' = 0$ and $z' = g$, on three neighboring strips, as described by Eq. 2.1.17. The strips are centered at $x = 0$ (left), $x = w_x$ (center), $x = 2w_x$ (right).

[43, 44, 45], an essential element in formulating the theorems detailed in the following section.

Quasi-statics refers to a regime in which the dimensions of the system are considerably smaller than the electromagnetic wavelength associated with the primary timescale of the problem. This results in the nearly instantaneous propagation of electromagnetic fields, essentially approaching the limit where the speed of light, denoted as c, tends toward $c \to \infty$. Within this derivation, our focus is on electroquasistatics, which incorporates capacitive effects while excluding inductive influences. This applies to conventional particle detectors in cases where the velocity of the moving charges is significantly slower than the speed of light and the conductivity σ is small. As a result the right hand side of Faraday's law is neglected, i.e.

$$\nabla \times \mathbf{E}(\mathbf{x}, t) \approx 0 \quad \Rightarrow \quad \mathbf{E}(\mathbf{x}, t) = -\nabla\phi(\mathbf{x}, t)\,, \tag{2.1.20}$$

where the electric field can be expressed as the gradient of the potential. Using this result in Ampère's law (2.1.2d), and taking the divergence in the Laplace domain yields

$$\nabla[\sigma(\mathbf{x}, s) \cdot \nabla]\phi(\mathbf{x}, s) + \nabla[\varepsilon(\mathbf{x}, s) \cdot \nabla]s\phi(\mathbf{x}, s) = -s\rho_e(\mathbf{x}, s)\,, \tag{2.1.21}$$

for an arbitrary linear isotropic medium dependent on the Laplace parameter s. This can be written more concisely by defining an *effective permittivity*

$$\varepsilon_f(\mathbf{x}, s) := \varepsilon_r(\mathbf{x}, s)\varepsilon_0 + \frac{\sigma(\mathbf{x}, s)}{s}\,. \tag{2.1.22}$$

Using this, Eq. (2.1.21) updates to

$$\nabla \cdot (\varepsilon_f(\mathbf{x}, s)\nabla)\,\phi(\mathbf{x}, s) = -\rho_{\mathrm{e}}(\mathbf{x}, s)\,. \tag{2.1.23}$$

Written in this way, the above equation has the form of the Poisson equation (2.1.7) in the Laplace domain found for electrostatic systems. As a result, we can determine the time-dependent solutions for a medium with a specified conductivity by first solving the related

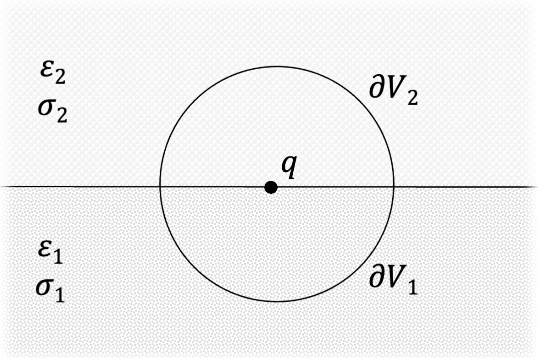

Figure 2.3: Schematic representation of a charge deposited at the interface between two resistive half-space materials.

electrostatic system and then replacing $\varepsilon_r \to \varepsilon_f$ in the Laplace domain. Subsequently, the inverse Laplace transform must be applied to return to the time domain. It is important to note that the same conclusion applies to Green's functions, as they represent the potential for a source of the form $\delta^3(\mathbf{x})\delta(t)$ in an electrodynamics problem.

This brings us to the example treated in Ref. [46], where a charge q is placed at the boundary surface between two half-space resistive materials, as shown in Fig. 2.3. In the electrostatic system the solution to the Poisson equation is given by

$$\phi(\mathbf{x}) = \frac{q}{2\pi\left(\varepsilon_1 + \varepsilon_2\right)} \frac{1}{|\mathbf{x}|}\,, \tag{2.1.24}$$

with ε_1 and ε_2 being the permittivity of the bottom and top material, respectively. With the introduction of a point charge q at $t = 0$ positioned along the interfacing surface that separates two distinct half-spaces, the charge density can be expressed in terms of the Heaviside distribution $\Theta(t)$ with the definition

$$\Theta(t) := \begin{cases} 0 & \text{if } t < 0 \\ 1 & \text{if } t \geq 0 \end{cases}. \tag{2.1.25}$$

At this point we note that its Laplace transform is given by

$$\mathscr{L}[\Theta(t)] = \frac{1}{s}\,. \tag{2.1.26}$$

As we aim for our solution to commence at $t = 0$, we must not only substitute the permittivities with their corresponding effective quantity as given in Eq. (2.1.22), but we also introduce the factor $q\Theta(t)$, which implies dividing the charge by the Laplace parameter, i.e., $q \to q/s$. The solution in the Laplace domain then reads

$$\phi(\mathbf{x}, s) = \frac{q}{2\pi\left(\varepsilon_1 + \varepsilon_2\right)\left(s + 1/\tau\right)} \frac{1}{|\mathbf{x}|}\,. \tag{2.1.27}$$

where $\tau := (\varepsilon_1 + \varepsilon_2)/(\sigma_1 + \sigma_2)$. Moving back to the time domain then reveals that

$$\phi(\mathbf{x}, t) = \mathscr{L}^{-1}[\phi(\mathbf{x}, s)] = \frac{q}{2\pi\,(\varepsilon_1 + \varepsilon_2)} \frac{1}{|\mathbf{x}|} e^{-t/\tau}\,, \qquad t \geq 0\,, \tag{2.1.28}$$

and we have a seemingly exponentially decaying point charge characterized by the time constant τ. This can be interpreted as the resistive medium responding to the sudden introduction of a point charge within it, resulting in the generation of currents aimed at mitigating its presence. This we can see by calculating the current on two half-spheres enveloping the charge q and centered at its position. Let ∂V_1 and ∂V_2 denote the surfaces of the top and bottom half-sphere. Then for $l \in \{1, 2\}$ the current going through them can be determined using the flux

$$\begin{aligned} I_l(t) &= \oint_{\partial V_l} \mathbf{j}(\mathbf{x}, s) \cdot d\mathbf{A} \\ &= -q \frac{\sigma_l e^{-t/\tau}}{2\pi\,(\varepsilon_1 + \varepsilon_2)} \int_{V_l} \nabla^2 \frac{1}{4\pi|\mathbf{x}|} dV \\ &= q \frac{\sigma_l}{(\varepsilon_1 + \varepsilon_2)} e^{-t/\tau}\,, \qquad t \geq 0\,. \end{aligned} \tag{2.1.29}$$

This can be related to the total charge that flows through each surface by integrating the currents

$$Q_l = \int_0^\infty I_l(t) dt = \frac{\sigma_l}{\sigma_1 + \sigma_2} q\,, \tag{2.1.30}$$

and all of the charge initially positioned at $t = 0$ is compensated by charges flowing into the volume, since $Q_1 + Q_2 = q$.

2.2 Weighting potentials and Ramo-Shockley theorem

In the preceding section, we explored the fundamental principles governing induced currents on a grounded electrode, which are generated by the electric field of a mobile charge carrier and the subsequent response of the resistive medium. While the principles remain the same for more intricate detector designs, the calculations can swiftly become quite challenging and computationally-intensive. Since most particle detectors can, by approximation, be considered to be made of perfect insulators and ideal electrodes, the Ramo-Shockley theorem applies. This late 1930's seminal work from Shockley [47] and Ramo [48] provides us with the capability to compute the current induced by an externally applied charge density on any grounded electrode. This is achieved through the use of a static weighting potential, a scalar field that encapsulates the electrode's reaction to an external source. The primary benefit of this potential is that it is purely dependent on the arrangement of the geometry, and therefore decoupled from the motion of the charge carriers that induces the signal. Hence, the weighting potential method provides computational efficiency when performing Monte Carlo simulations. After calculating the weighting potential using a finite element solver, subsequent steps such as charge deposition, charge transport, and the computation of the induced signal can be executed using software tools like Garfield++ [38, 39, 49]. In addition, this strategy avoids the need to solve the Poisson equation of the system for all moving electrons, ions and holes in the detector medium to obtain the generated signal in all readout electrodes, making the overall computation less involved. Continued efforts have been made to extend the applicability of the result of Shockley and Ramo. These endeavors aim to encompass a broader range of scenarios, including signal formation in the presence of a static space-charge distribution [50], incorporation of external impedance elements connected to the electrodes [51], the connection with the equivalent electrical circuit description [6], and induced currents in the presence of dielectric and nonlinear media [52, 53].

For detectors containing weakly conducting materials, the time dependence of the signals is given by both the movement of the free charge carriers in the detector medium and the dynamic reaction of the resistive materials. In this case an extension to the basic form of the Ramo-Shockley theorem needs to be employed which utilizes a dynamic weighting potential that encompasses the behavior of the resistive medium [46, 54, 49]. This can be derived by treating Maxwell's equations in the quasi-static regime as discussed in Sec. 2.1.2 and employing Green's reciprocity theorem to link charge distributions with their corresponding electrostatic potentials. The resulting theorem is the same as the one found for the case of the presence of an external impedance network [51], highlighting its close tie with the lumped element representation of detector geometries as a (continuum limit of) linear network of interconnected discrete complex impedances. In these works the weighting potentials are obtained through the use of a Dirac delta function which can be numerically difficult to deal with. Therefore another approach can be used following Ref. [55, 56]. While we will only give the proof for weakly conducting media, a more general proof that the result of this extension to the Ramo-Shockley theorem satisfies the full Maxwell's equations can be found in the work of W. Riegler and P. Windischhofer [57] based on the Lorentz-reciprocity [58].

2.2.1 Extended form of the Ramo-Shockley theorem for conductive media

Let us examine an arbitrary configuration consisting of K perfectly grounded metal electrodes positioned within a linear medium. This medium is characterized by its position and frequency-dependent permittivity $\varepsilon(\mathbf{x}, s)$ and conductivity $\sigma(\mathbf{x}, s)$. We place within this system an externally impressed time varying charge density $\rho_e(\mathbf{x}, s)$ that will induce currents flowing from the electrodes to ground. This setup is depicted in Fig. 2.4 (left). When treating Maxwell's equations in the quasi-static limit, the resulting scalar field $\phi(\mathbf{x}, s)$ is a solution to the Poisson equation (2.1.23) with the effective permittivity given by Eq. (2.1.22).

Through the use of the reciprocity theorem we can relate this solution to the solution of a closely related system where $\rho_e(\mathbf{x}, s)$ is absent and all but one electrode are grounded. The electrode under study, denoted by index $k \in \{0, 1, \dots, K\}$, is put under a potential

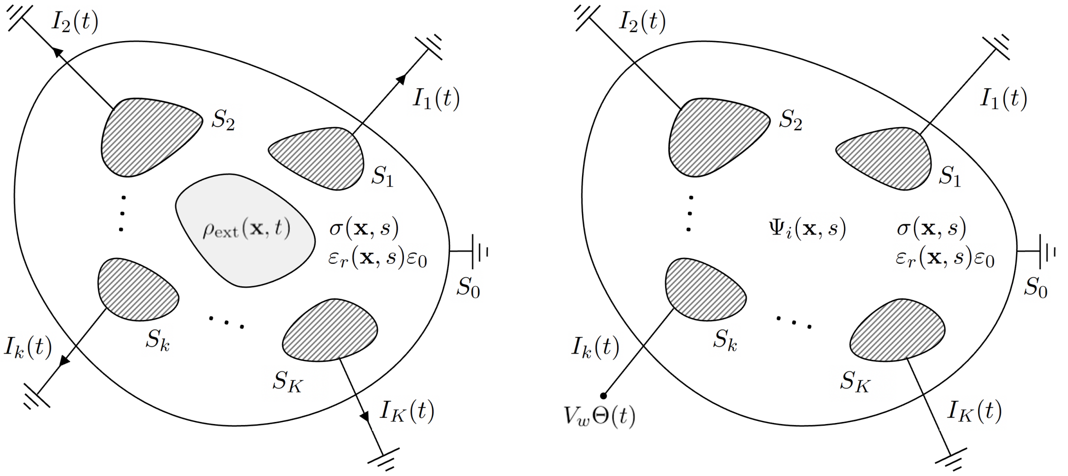

Figure 2.4: **Left:** The generation of currents, denoted as I_k, on electrodes S_k, is the result of an externally impressed charge density $\rho_e(\mathbf{x}, s)$. **Right:** Setup to calculate the dynamic weighting potential $\Psi_k(\mathbf{x}, t)$ of electrode k.

step of height V_w at time $t = 0$ resulting in a potential $\Psi_k(\mathbf{x}, s)$ permeating through the system. In Fig. 2.4 the system is depicted. The field equation in the Laplace domain then reads

$$\nabla \cdot (\varepsilon_f(\mathbf{x}, s)\nabla)\, \Psi_k(\mathbf{x}, s) = 0\,, \tag{2.2.1}$$

which is subject to the Dirichlet boundary conditions

$$\Psi_k(\mathbf{x}, s)|_{\mathbf{x}\in S_l} = \frac{V_w}{s}\delta_{kl}\,, \tag{2.2.2}$$

on surfaces S_l of electrode l. Using Green's second theorem and suppressing the arguments of the functions we have the following relation

$$\oint_{\partial V} (\Psi_k \varepsilon_f \nabla\phi - \phi\varepsilon_f \nabla\Psi_k) \cdot d\mathbf{S} = \int_V (\Psi_k \nabla \cdot [\varepsilon_f \nabla]\phi - \phi\nabla \cdot [\varepsilon_f \nabla]\Psi_k)\; d^3x\,, \tag{2.2.3}$$

with V being the volume encapsulated by the electrodes. Considering the Laplace equation (2.2.1) and the imposed condition in Eq. (2.2.2) the above equation reduces to

$$\frac{V_w}{s} \oint_{S_k} \varepsilon_f(\mathbf{x}, s)\nabla\phi(\mathbf{x}, s) \cdot d\mathbf{S} = -\int_V \Psi_k(\mathbf{x}, s)\rho_{\mathrm{e}}(\mathbf{x}, s)\, d^3x\,. \tag{2.2.4}$$

Following Eq.(2.1.6), the right hand side of the above expression represents the charge induced on electrode k

$$Q_k(s) = -\frac{s}{V_w}\int_V \Psi_k(\mathbf{x}, s)\rho_{\mathrm{e}}(\mathbf{x}, s)\, d^3x\,. \tag{2.2.5}$$

Now that we have established this relationship, we can turn to the time domain. We will make use of the continuity equation (2.1.3) and leverage the Laplace convolution property

$$\mathcal{L}^{-1}\left(F(s)G(s)\right) = \int_0^t f(t-t')g(t')\,dt'\,, \tag{2.2.6}$$

to obtain

$$Q_k(t) = -\frac{1}{V_w}\int_0^t \int_V \Psi_k(\mathbf{x}, t-t')\frac{\partial \rho_e(\mathbf{x}, t')}{\partial t'}\,d^3x dt' \tag{2.2.7}$$

$$= -\frac{1}{V_w}\int_0^t \int_V \nabla\Psi_k(\mathbf{x}, t-t')\cdot \mathbf{j}_e(\mathbf{x}, t')\,d^3x dt'\,, \tag{2.2.8}$$

where the gradient of Ψ_k expresses the electric field, i.e.,

$$Q_k(t) = \frac{1}{V_w}\int_0^t \int_V \mathbf{E}_k(\mathbf{x}, t-t')\cdot \mathbf{j}_e(\mathbf{x}, t')\,d^3x dt'\,. \tag{2.2.9}$$

At this point, the utility of this approach begins to become apparent. The time-dependent potential $\Psi_k(x,t)$ signifies the response of the detector given a source. Here $\Psi_k(x,t)$ is called the *weighting potential* of the k'th electrode of the system, which can be computed independently from $\mathbf{j}_e$. The associated vector field $\mathbf{E}_k(\mathbf{x},t)$ is referred to as the *weighting field.* When taking $\sigma \to 0$ in the above expression the weighting potentials become static and instantaneous, i.e. $\Psi_k(t,\mathbf{x}) \to \psi_k(\mathbf{x})\Theta(t)$. In this limit, the induced charge reduces to

$$Q_k(t) = -\frac{1}{V_w}\int_V \Psi_k(\mathbf{x})\rho_e(t,\mathbf{x})\,d^3x\,, \tag{2.2.10}$$

which represents the case where the detector is comprised of perfectly insulating and ideally conducting materials.

The time-dependent external charge density is a sum of all charges propagating through the detector's medium, coming from the primary ionization pattern sourced by an incident particle and possible Townsend avalanches in the presence of a high electric field. Given the linearity of Maxwell's equations, we can treat the contribution from individual charges separately and sum up all the solutions at the end. Compared to the overall scale of the detector, the ions can be approximated as being point-like alongside the electrons and holes. For a point-like charge carrier following the trajectory $\mathbf{x}_q(t)$ shown in Fig. 2.5 (left) starting at $t = 0$, the charge density takes the form

$$\rho_e(\mathbf{x}, t) = q\delta^3(\mathbf{x} - \mathbf{x}_q(t))\Theta(t)\,, \tag{2.2.11}$$

given an electrical charge q. The current density then reads

$$\mathbf{j}_e(\mathbf{x}, t) = \rho_e(\mathbf{x}, t)\dot{\mathbf{x}}_q\left(t\right)\,, \tag{2.2.12}$$

with the dot notation denoting the derivative with respect to time: $\dot{\mathbf{x}}\left(t\right) := d\mathbf{x}\left(t\right)/dt$. Performing the volume integral of equation (2.2.9) yields an induced charge of

$$Q_k(t) = \frac{q}{V_w}\int_0^t \mathbf{E}_k(\mathbf{x}_q(t'), t-t')\cdot \dot{\mathbf{x}}_{\mathrm{q}}(t')\,dt'\,. \tag{2.2.13}$$

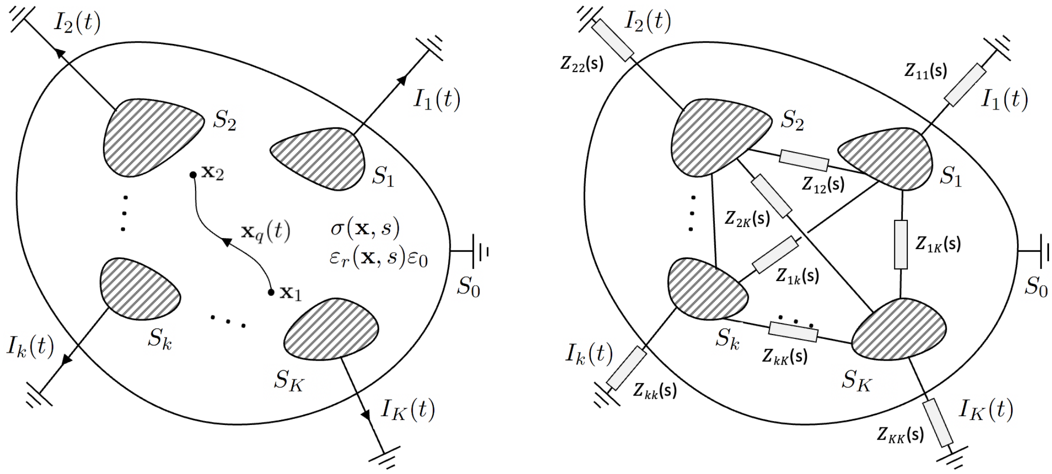

Figure 2.5: **Left:** Induction of currents I_k on electrodes S_k though the movement of a charge carrier along its $\mathbf{x}_q(t)$ trajectory. **Right:** An equivalent circuit diagram can depict the impact of the medium, where, if the medium is insulating, the impedance components $Z_{kl}(s)$ are represented by the mutual capacitance between the electrodes.

For $\mathbf{x}_1$ and $\mathbf{x}_2$ being the start and end point, respectively, of $\mathbf{x}_q(t)$, it follows that the total induced charge on the electrode is given by

$$Q_k = \frac{q}{V_w} \lim_{t\to\infty} \Big(\Psi_k(\mathbf{x}_1, t) - \Psi_k(\mathbf{x}_2, t) \Big) . \tag{2.2.14}$$

This suggests that the eventual quantity of induced charge is independent of the path taken by charge q. As one takes the k'th weighting potential to be static, i.e., the detector materials other than the electrodes are perfectly insulating, the time integral reduces to

$$Q_k(t) = \frac{q}{V_w} \left[\Psi_k(\mathbf{x}_q(0)) - \Psi_k(\mathbf{x}_q(t)) \right] . \tag{2.2.15}$$

To obtain the induced current on the electrode as given by Eq. (2.1.16), we take the time derivative of Eq. (2.2.9). For this we note that

$$\begin{aligned}
&\frac{d}{dt} \int_0^t \mathbf{E}_k \left(\mathbf{x}_q\left(t'\right), t - t'\right) \cdot \dot{\mathbf{x}}\left(t'\right) \, dt' \\
&= \int_0^\infty \frac{d}{dt} \left(\mathbf{E}_k \left(\mathbf{x}_q\left(t'\right), t - t'\right) \Theta\left(t - t'\right)\right) \cdot \dot{\mathbf{x}}\left(t'\right) \, dt' \\
&= \int_0^t \mathbf{H}_k \left(\mathbf{x}_q\left(t'\right), t - t'\right) \cdot \dot{\mathbf{x}}\left(t'\right) \, dt' ,
\end{aligned} \tag{2.2.16}$$

where we have defined the vector field vector field given by

$$\mathbf{H}_k(\mathbf{x}, t) := -\nabla \frac{\partial \Psi_k(\mathbf{x}, t)\Theta(t)}{\partial t} . \tag{2.2.17}$$

Using this result, we find the induced current is given by

$$I_k(t) = -\frac{q}{V_w}\int_0^t \mathbf{H}_k\left[\mathbf{x}_q\left(t'\right), t-t'\right]\cdot\dot{\mathbf{x}}_q\left(t'\right)\,dt'\,. \tag{2.2.18}$$

Noting that $\mathbf{H}_k(\mathbf{x},t)$ has the dimension [V m^{-1} s^{-1}], it cannot be interpreted as an electric field. In the quasi-static regime, when we neglect the propagation times of electric fields, the introduction of a step voltage $V_w\theta(t)$ leads to an immediate potential $\Psi_k(x,0)$ permeating the detector volume, from which point it is a smooth function of time. Furthermore, at $t=0$ all conducting components exhibit insulating characteristics as they do not have sufficient time to react. Conversely, for $t\to\infty$, all resistive elements behave like perfect conductors. We can therefore say that $\Psi_k(x,t)$ is comprised of two components: the static *prompt* component $\psi_k^p(\mathbf{x}) := \Psi_k(x,0)$, and the dynamic *delayed* component $\psi_k^d(\mathbf{x},t)$, i.e.,

$$\Psi_k(\mathbf{x},t) := \psi_k^p(\mathbf{x}) + \psi_k^d(\mathbf{x},t)\,, \tag{2.2.19}$$

where $\psi_k^d(\mathbf{x},0)=0$ by definition. The first term gives the immediate generation of current on the electrode due to the motion of a charge carrier within the medium, whereas the second term encompasses the reaction of the resistive materials. Using the definition in Eq. (2.2.19) the weighting vector can be expressed as

$$\begin{aligned}\mathbf{H}_k(\mathbf{x},t) &= -\nabla\psi_k^p(\mathbf{x})\delta(t) - \nabla\frac{\partial\psi_k^d(\mathbf{x},t)\Theta(t)}{\partial t}\\ &=: \mathbf{E}_k^p(\mathbf{x})\delta(t) + \mathbf{H}_k^d(\mathbf{x},t)\,,\end{aligned} \tag{2.2.20}$$

where $\mathbf{E}_k^p(\mathbf{x})$ will be the *prompt weighting field* and $\mathbf{H}_k^d(\mathbf{x},t)$ the *delayed weighting vector*. Expressed in this way we can write the induced current as

$$I_k(t) = -\frac{q}{V_w}\mathbf{E}_k^p(\mathbf{x}_q(t))\cdot\dot{\mathbf{x}}_p(t) - \frac{q}{V_w}\int_0^t \mathbf{H}_k^d\left[\mathbf{x}_q\left(t'\right), t-t'\right]\cdot\dot{\mathbf{x}}_q\left(t'\right)\,dt'\,, \tag{2.2.21}$$

where the first term is the relation found for the basic form of the Ramo-Shockley theorem, while the second term is the time-dependent contribution of the resistive media that this extension adds. It is now straightforward to show that in the limit where the materials are either perfectly insulating or ideal conductors, the induced current is given by

$$I_k(t) = -\int_V \mathbf{E}_k^p(\mathbf{x})\cdot\mathbf{j}_e(\mathbf{x},t)\,\mathrm{d}^3x\,, \tag{2.2.22}$$

which is the original Ramo-Shockley theorem.

The medium between the electrodes can be represented by a linear equivalent circuit comprised of 'lumped' impedance elements $Z_{kl}(s)$, $k,l\in\{0,1,\ldots,K\}$ as shown in Fig. 2.5 (right), The current flowing between node k and l is related to the respective node voltages v_k and v_l by $i_{kl} = (v_k - v_l)/Z_{kl}$ [46]. The entries in the related admittance matrix $\hat{Y} = \hat{Z}^{-1}$ is then defined as

$$Y_{mn}(s) = \frac{s}{V_w}\oint_{\mathbf{S}_n}\varepsilon_{eff}(\mathbf{x},s)\nabla\Psi_m(\mathbf{x},s)\cdot d\mathbf{S}\,, \tag{2.2.23}$$

in terms of which the entries in the impedance matrix can be expressed as

$$Z_{kl}(s) = -\frac{1}{Y_{kl}(s)} \qquad k \neq l \tag{2.2.24a}$$

$$Z_{kk}(s) = \frac{1}{\sum_{l=1}^{N} Y_{kl}(s)} \,. \tag{2.2.24b}$$

If there exists a static charge distribution $\rho(\mathbf{x})$ in addition to the externally applied time-dependent charge distribution, such as the accumulation of charge on dielectric surfaces in MPGD structures, the induced current of the basic form of the Ramo-Shockley theorem can be expressed as

$$\begin{aligned} I_k(t) &= \frac{1}{V_w}\int_V \Psi_k(\mathbf{x})\frac{d}{dt}\left(\rho(\mathbf{x}) + \rho_e(\mathbf{x},t)\right)\, d^3x \\ &= \frac{1}{V_w}\int_V \Psi_k(\mathbf{x})\frac{d\rho_e(\mathbf{x},t)}{dt}\, d^3x \,, \end{aligned} \tag{2.2.25}$$

using Eq. (2.2.10). While space charge does influence the motion of drifting charges, it is not necessary to consider it when calculating the weighting potential.

2.2.2 Weighting potential for a N-layer parallel plate type geometry

In this section we discuss the potential for a point charge in the system depicted in Fig. 2.6. It consists of N parallel layers with varying permittivity and conductivity, confined from above and below by two grounded planes. In situations where one of the grounded planes is divided into strips and pads, the obtained solution is employed to calculate the time-dependent weighting potential associated with these electrodes. This layout is the basis for a multitude of detector designs, such as the (Multi-gap) Resistive Plate Chamber (MRPC) [59, 60], the amplification gap of a MicroMegas (MM) detector [9], the induction gap of a Gas Electron Multiplier (GEM) [8], and the silicon bulk of the RSDs. The techniques that will be presented here have been taken from Ref. [54, 45, 61], which will provide us with necessary equations for the examples that will follow.

Working in the quasi-static limit, the solution to the problem has can be expressed in terms of a the Green's function $G(\mathbf{x}, \mathbf{x}', s)$:

$$\phi(\mathbf{x}, s) = \frac{1}{\varepsilon_0}\int_V G(\mathbf{x}, \mathbf{x}', s)\rho(\mathbf{x}', s)\, d^3x' \,, \tag{2.2.26}$$

which satisfies the relation

$$\nabla \cdot (\varepsilon_f(\mathbf{x}, s)\nabla)\, G(\mathbf{x}, \mathbf{x}', s) = -\delta^3(\mathbf{x} - \mathbf{x}') \,. \tag{2.2.27}$$

Since in this regime there is a close connection between the static and time-dependent solution, it suffices to find the solution for the electrostatic system

$$\nabla \cdot (\varepsilon(\mathbf{x})\nabla)\, G(\mathbf{x}, \mathbf{x}') = -\delta^3(\mathbf{x} - \mathbf{x}') \,, \tag{2.2.28}$$

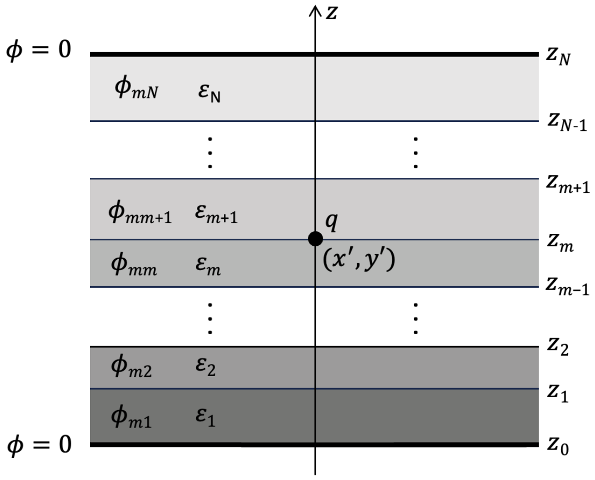

Figure 2.6: A configuration comprising N insulating layers with relative dielectric permittivities (denoted by n) and grounded plates positioned at $z = z_0$ and $z = z_N$. A point charge q is located at the interface between layer m and $m + 1$ at $z = z_m$.

from which the dynamic solution follows. In addition to two grounded metal plates between which the layered geometry resides, we impose that the geometry of Fig. 2.6 is also grounded on the edges positioned $x = 0, a$ and $y = 0, b$. We place a point charge on the interface of layer m and $m + 1$ at $\mathbf{x}_m = (x_0, y_0, z_m)$. After a Fourier expansion in x and y we can write the most general solution of the Green's function in layer n as

$$G_{mn}(\mathbf{x}, \mathbf{x}_m) = \frac{4}{ab} \sum_{\alpha,\beta=1}^{\infty} \sin\left(\alpha\pi\frac{x}{a}\right) \sin\left(\alpha\pi\frac{x_0}{a}\right) \sin\left(\beta\pi\frac{y}{b}\right) \sin\left(\beta\pi\frac{y_0}{b}\right) \frac{f_{mn}(k_{\alpha\beta}, z)}{k_{\alpha\beta}}, \tag{2.2.29}$$

where $k_{\alpha\beta} := \pi\sqrt{\frac{\alpha^2}{a^2} + \frac{\beta^2}{b^2}}$ and the geometry dependent function $f_{mn}(k, z)$ containing the height dependence that is of the form

$$f_{mn}(k, z) = A_n(k)e^{kz} + B_n(k)e^{-kz}, \quad n \in \{1, 2, \ldots, N\}. \tag{2.2.30}$$

The coefficients $A_n(k)$ and $B_n(k)$ must be determined by the boundary condition

$$f_{m1}(k, z_0) = 0 \qquad f_{mN}(k, z_N) = 0 \tag{2.2.31}$$

and the continuity condition on the interfaces between the different materials

$$\begin{aligned} &f_{mn}(k, z_n) = f_{m(n+1)}(k, z_n) \\ &\varepsilon_n \frac{\partial f_{mn}(k, z)}{\partial z}\bigg|_{z=z_n} = \varepsilon_{n+1} \frac{\partial f_{m(n+1)}(k, z)}{\partial z}\bigg|_{z=z_n} + k\delta_{mn}. \end{aligned} \tag{2.2.32}$$

The potential on layer n from a point-charge q with corresponding charge density $\rho_e(\mathbf{x}) = q\delta^3(\mathbf{x} - \mathbf{x}_m)$ can then be determined through

$$\phi_{mn}(x, y, z) = \frac{q}{\varepsilon_0} G_{mn}(x, y, z), \qquad z_{n-1} < z < z_n, \tag{2.2.33}$$

which induces a charge density distribution on the metal plates.

If we segment the bottom metal plane into electrodes with surfaces S_l, integrating the charge distribution over this surface yields the induced charge on it

$$Q^{ind}\left(x', y', z_m\right) = -\,\varepsilon_0 \varepsilon_1 \int_{S_l} \left.\frac{\partial \phi_{m1}\left(x, x', y, y', z, z_m\right)}{\partial z}\right|_{z=z_0} dS\,. \tag{2.2.34}$$

This induced charge is related to the weighting potential through $\rho_e(\mathbf{x})$ using Eq. 2.2.10. Performing the surface integral over a rectangular pad electrode of width $w_x \times w_y$ positioned at $\mathbf{x} = (x_p, y_p, z_0)$ on the anode, gives an expression of the weighting potential of the form

$$\Psi\left(x', y', z_m\right) = \varepsilon_1 V_w \int_{x_p - w_x/2}^{x_p + w_x/2} \int_{y_p - w_y/2}^{y_p + w_y/2} \left.\frac{\partial G_{m1}\left(x, x', y, y', z, z_m\right)}{\partial z}\right|_{z=z_0} dx dy\,. \tag{2.2.35}$$

Going back to our Green's function (2.2.29), we obtain the solution

$$\begin{aligned}\Psi\left(x', y', z_m\right) =& \frac{16 V_w}{\pi^2} \sum_{\alpha,\beta=1}^{\infty} \frac{\sin\left(\alpha\pi \frac{w_x}{2a}\right) \sin\left(\alpha\pi \frac{x_p}{a}\right) \sin\left(\alpha\pi \frac{x'}{a}\right)}{\alpha} \\ &\times \frac{\sin\left(\beta\pi \frac{w_y}{2b}\right) \sin\left(\beta\pi \frac{y_p}{b}\right) \sin\left(\beta\pi \frac{y'}{b}\right)}{\beta} h_m\left(k_{\alpha\beta}, z_m\right)\,,\end{aligned} \tag{2.2.36}$$

where we defined

$$h_m\left(k, z_m\right) := \frac{\varepsilon_1}{k} \left.\frac{\partial f_{m1}(k, z)}{\partial z}\right|_{(z=z_0)}\,. \tag{2.2.37}$$

This result gives the weighting potential solution for heights corresponding to the interface of the stacked dielectric layers. To obtain the solution at a point within a dielectric layer we can simply segment it into two at the height of the charge and assign the same permittivity to both layer m and layer $m+1$. Now that we have the static solution, we note that all information about the permittivity of each layer is contained in the function $h_m(k, z)$, such that the time-dependent solution can be obtained by replacing $h_m(k, z) \to h_m(k, z, s)$ following Eq. (2.1.22), $V_w \to V_w/s$ and performing the inverse Laplace transformation.

To determine the solution for a geometry that extends infinitely, we can perform the coordinate transformation $\tilde{x} := x - a/2$ and $\tilde{y} := y - b/2$ such that the origin of the coordinate system coincides with the center of the layout. Afterward, one can proceed by taking the limit $a, b \to \infty$. We take $k_x := \alpha\pi/a$ and $k_y := \beta\pi/b$ such that the solution reads

$$G_{mn}\left(\tilde{x}, \tilde{x}', \tilde{y}, \tilde{y}', z, z_m\right) = \frac{1}{\pi^2} \int_0^{\infty} \int_0^{\infty} \cos\left[k_x\left(\tilde{x} - \tilde{x}'\right)\right] \cos\left[k_y\left(\tilde{y} - \tilde{y}'\right)\right] \frac{f_{mn}(k, z)}{k}\, dk_x dk_y\,, \tag{2.2.38}$$

since $\sum_{\alpha,\beta=1} \to \int\int d\alpha d\beta = ab/\pi^2 \int\int dk_x dk_y$ [61]. The weighting potential for an pad located in an infinitely extending system then reads

$$\begin{aligned}\Psi\left(\tilde{x}', \tilde{y}', z_m\right) =& \frac{4V_w}{\pi^2} \int_0^\infty \int_0^\infty \cos\left(k_x\left(\tilde{x}-\tilde{x}'\right)\right) \sin\left(\frac{k_x w_x}{2}\right) \\ & \times \cos\left(k_y\left(\tilde{y}-\tilde{y}'\right)\right) \sin\left(\frac{k_y w_y}{2}\right) \frac{h_m\left(k, z_m\right)}{k_x k_y} dk_x dk_y\,. \end{aligned} \tag{2.2.39}$$

Similarly we can derive the solution for a strip of width w_x extending to infinity in the y-direction, which reads

$$\Psi\left(\tilde{x}', z_m\right) = \frac{2V_w}{\pi} \int_0^\infty \cos\left(k\left(\tilde{x}-\tilde{x}'\right)\right) \sin\left(\frac{k w_x}{2}\right) \frac{h_m\left(k, z_m\right)}{k} dk\,. \tag{2.2.40}$$

The presented expressions can be used to derive electric fields and weighting fields for a wide range of detectors. For more examples and a discussion on the speed of convergence of the above relations we refer to Ref. [61], where it is demonstrated that they are well-suited for numerical evaluation.

2.3 Toy model examples for parallel plate geometries

Having established the general framework of the extended form of the Ramo-Shockley theorem for conductive media, we can now continue our discussion on the characteristics of the signals formed in resistive and non-resistive toy model detector structures. This analysis will help us pinpoint crucial factors that will be significant in numerical computations of more intricate detector configurations, which will be the focus of the following chapters. For simplicity, we will restrict our examples to geometries involving parallel plates. This limitation will allow us to utilize the results obtained in Sec. 2.2.2. Commencing with two examples where the basic form of the Ramo-Shockley theorem is applicable, we will then proceed to two examples involving resistive elements. These examples are based on the ones presented in Ref. [41]. Additional instances of signal formation in resistive detectors are explored in Ref. [61].

2.3.1 Electron-ion pair in a parallel plate chamber

Let us consider a gas volume bounded from above and below by two parallel metal plates separated by a distance g. The weighting potential is given by

$$\Psi(z) = \frac{V_w}{g}(g-z)\,. \tag{2.3.1}$$

For an electron-ion pair placed at a height z_0 in an electric field along the positive z-axis, the differently charged particles $\pm q$ drift in opposite direction to the cathode and anode with a constant velocity v_{ion} and $-v_e$ for the ion and electron, respectively. The induced

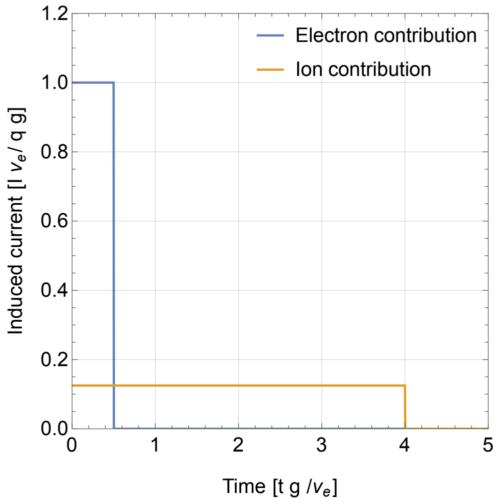

Figure 2.7: The induced current on the anode resulting from the creation of an electron-ion pair within a parallel plate chamber for $z_0 = g/2$ and $v_e = 8v_{\text{ion}}$.

current flowing from the anode is given by

$$\begin{aligned} I_e(t) &= \frac{q}{g} v_e\,, \qquad 0 \leq t \leq \frac{g}{v_e}\,, \\ I_{\text{ion}}(t) &= \frac{q}{g} v_{\text{ion}}\,, \qquad 0 \leq t \leq \frac{g}{v_{\text{ion}}}\,, \end{aligned} \tag{2.3.2}$$

taking the form of a square with the same polarity. An example is given in Fig. 2.7. Both signals have an area of

$$Q_e = \frac{q z_0}{g}\,, \qquad Q_{\text{ion}} = \frac{q(g - z_0)}{g}\,, \tag{2.3.3}$$

As already indicated by Eq. (2.2.15), the total amount of charge on the anode equals the amount of collected charge once both charges have reached their endpoints of their paths, regardless of the initial position of the pair: $Q_e + Q_{\text{ion}} = q$. Nonetheless, the fraction contributed by each depends on z_0 because of their varying path lengths.

As a next step we segment the anode into infinitely long strips $l \in \mathbb{Z}$ running in the y-direction and centered at $x = lw_x$. Through conformal mapping to an upper half-plane a closed formed solution for the weighting potentials can be found [62]:

$$\Psi_l(\mathbf{x}) = \frac{V_w}{\pi} \arctan\left(\frac{\sin\left(\pi \frac{x - lw_x}{d}\right) \sinh\left(\pi \frac{w_x}{2d}\right)}{\cosh\left(\pi \frac{x - lw_x}{d}\right) - \cos\left(\pi \frac{z}{d}\right) \cosh\left(\pi \frac{w_x}{2d}\right)} \right)\,. \tag{2.3.4}$$

In Fig. 2.8 (left), the weighting field strength is plotted. Due to the imposed boundary conditions, the solution for the weighting potential has a discontinuity at the edges of the

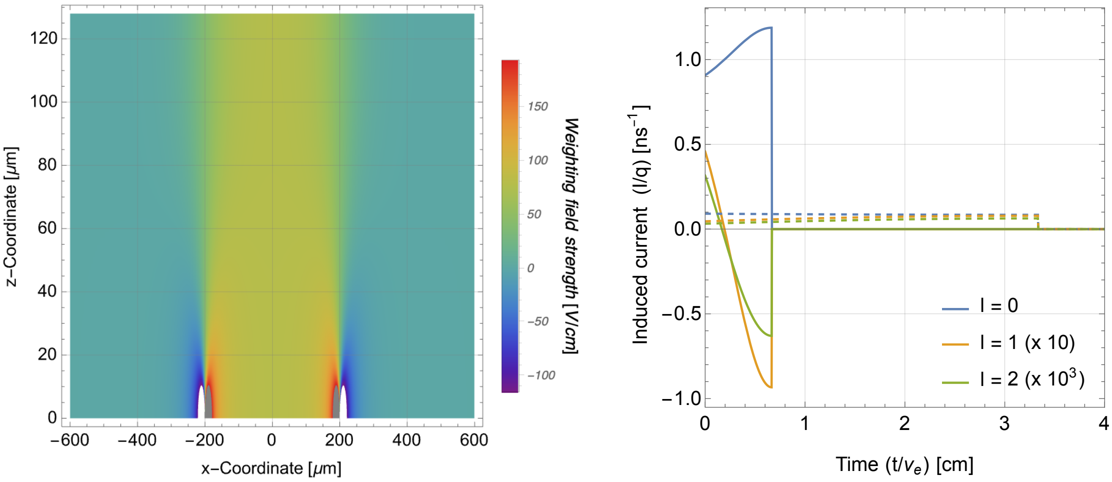

Figure 2.8: **Left:** Weighting field strength of a 400 μm wide readout strip within a 128 μm high parallel plate geometry. Here a divergent solution is found at the corners of the electrode due to its perfect adjacency with its neighboring electrode. **Right:** An example of the electron component (represented by the solid line) and the ion component (represented by the dashed line) of the induced signal on three adjacent strips located on the anode.

strip, resulting in diverging weighting field there. In reality, neighboring strips or pads are not perfectly adjacent in the manufactured readout structure, and this divergence is an unwelcome feature of the simplification used here. Regardless, the edges of the strips, while not yielding infinitely big weighting fields, do result in noticeably higher field strengths from their sharp metal corners, resulting in an increased sensitivity for any charge carrier passing through this area. The signal from the above electron-ion pair induced on three neighboring strips is shown in Fig. 2.8 (right). Integration of these gives the induced charge contributed by the electron

$$
\begin{aligned}
Q_l^e = & \frac{q}{\pi}\tan^{-1}\left[\tan\left(\frac{\pi z_0}{2g}\right)\coth\left(\frac{\pi((2l+1)w_x-2x_0)}{4g}\right)\right] \\
& + \frac{q}{\pi}\tan^{-1}\left[\tan\left(\frac{\pi z_0}{2g}\right)\coth\left(\frac{\pi(2x_0-(2l-1)w_x)}{4g}\right)\right].
\end{aligned}
\tag{2.3.5}
$$

The result for both components is shown in Fig. 2.9 for different values of z_0. As established before, the total charge flowing from the electrode to ground through induction will equal the collected charge once all electrons and ions have reached the end of their trajectories. However, if the electron is collected on the adjacent strip, its contribution is negative due to the negative weighting field strength in that region. When combined with the positive contribution of the ion, the total sum equals zero.

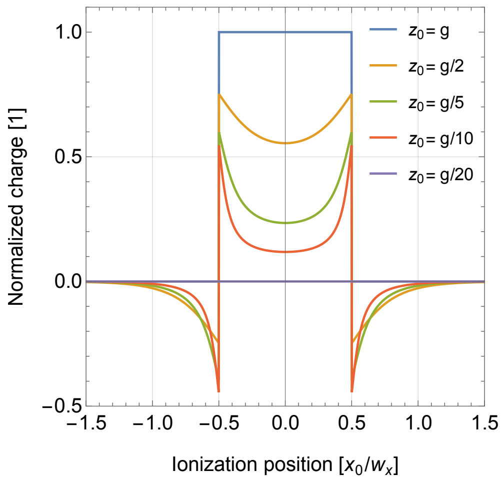

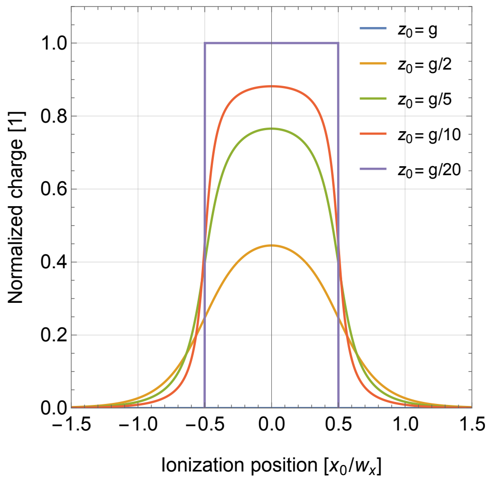

Figure 2.9: Contributions to the total amount of charge flowing from the readout strip to ground. **Left:** The electron contribution as a function of the ionization position. **Right:** The ion contribution plotted as a function of the ionization position.

2.3.2 Current induction from a Townsend avalanche

The amount of charge due to primary ionization that is being deposited in a gaseous detector medium is typically too small for direct detection. To improve the *signal-to-noise ratio* (S/N), internal charge amplification is required, which involves electron multiplication within a strong electric field. In the case of the MicroMegas device, these Townsend avalanches are generated between the mesh electrode and anode structure, called the *amplification gap*, where the rapidly growing number of electrons and ions will result in a current on each readout channel. This example will consider the signal induced on an infinitely extending grounded metal anode plane by such an avalanche.

To simplify our calculations for the signal induction in the amplification gap with size g, we will approximate the mesh as a metal plane, creating a uniform electric field in the induction gap where the electrons and ions will be drifting at constant velocities v_e and v_{ion}, respectively, along the z-axis. Furthermore, the avalanche growth at high electric field strengths will be treated as exponential, i.e.,

$$N_{\text{e}}(z) := e^{\bar{\alpha} z}\,, \qquad N_{\text{e}}(t) = e^{\bar{\alpha} v_e t}\Theta\left(\frac{g}{v_e} - t\right)\,, \qquad 0 \leq t \leq \frac{g}{v_e}\,, \tag{2.3.6}$$

where $\bar{\alpha}$ denotes the *effective Townsend coefficient*, given by the difference between the *Townsend* α and *attachment coefficient* η. This is the *gain factor*, indicating on average the number of electrons that will be generated in the avalanche per primary electron. Splitting the externally impressed current density in the electron and ion current contributions – indicated by the subscript e and *ion*, respectively – the former comes in the form

$$\mathbf{j}_e(\mathbf{x},t) = \rho_e(\mathbf{x},t)\mathbf{v}_e(t)\,, \tag{2.3.7}$$

where the charge density is given by

$$\rho_e(\mathbf{x},t) = qN_e(z_e(t))\delta^3(\mathbf{x}-\mathbf{x}_e(t))\Theta(t)\,. \tag{2.3.8}$$

Evaluating the volume integral in Eq. (2.2.22) the electron component of the signal reduces to

$$I^{\mathrm{e}}(t) = -e_0 N_e(t)\mathbf{E}_w(\mathbf{x}_e(t))\cdot\mathbf{v}_e(t)\,, \tag{2.3.9}$$

with e_0 being the elementary charge. For this parallel plate geometry the velocity vector can be taken as $\mathbf{v}_e(t) = -v_e\hat{\mathbf{z}}$ and the weighting field as $\mathbf{E}_w(\mathbf{x}) = -\hat{\mathbf{z}}/g$.

During the evolution of the avalanche, the electrons are created alongside the secondary ions that drift in the opposite direction toward the cathode. To obtain the charge density of these ions, $\rho_{\mathrm{ion}}(\mathbf{x},t)$, we use the continuity equation (2.1.3) where the externally impressed charge density in the MM amplification gap is given by $\rho(\mathbf{x},t) = \rho_e(\mathbf{x},t)+\rho_{\mathrm{ion}}(\mathbf{x},t)$ and the total current density can be expressed as $\mathbf{j}(\mathbf{x},t) = \mathbf{v}_e\rho_e(\mathbf{x},t)+\mathbf{v}_{\mathrm{ion}}\rho_{\mathrm{ion}}(\mathbf{x},t)$. To simplify the calculation, let us go to the one-dimensional case and take $\rho_e(z,t) = \exp(\bar{\alpha}\,(g-z))\delta(z-g+v_et)$ and add the condition that $\rho_e(z,t) = 0$ for $t \notin (0, g/v_e)$ later. The continuity conservation equation (2.1.3) becomes

$$\frac{\partial\rho_{\mathrm{ion}}(z,t)}{\partial t} + v_{\mathrm{ion}}\frac{\partial\rho_{\mathrm{ion}}(z,t)}{\partial z} = qv_e\bar{\alpha}\delta\left(z-g+v_et\right)\,, \tag{2.3.10}$$

the solution of which is given by

$$\begin{aligned}\rho_{\mathrm{ion}}(z,t) =& f_1(z-v_{\mathrm{ion}}t) - \frac{qv_e\bar{\alpha}}{v_e+v_{\mathrm{ion}}}\int_1^t \exp\left[\bar{\alpha}\left(g-z+v_{\mathrm{ion}}t-v_{\mathrm{ion}}t'\right)\right] \\ &\times\delta\left(t'-\frac{g+v_{\mathrm{ion}}t-z}{v_e+v_{\mathrm{ion}}}\right)dt'\,,\end{aligned} \tag{2.3.11}$$

where the function $f_1(z)$ can be fixed by requiring that $\rho_{\mathrm{ion}}(z,t) = 0$ as long as the electron avalanche did not yet pass through z, i.e., $z > g - v_et$. Thus the function is given by

$$f_1(z) = \frac{q\bar{\alpha}v_e}{v_e+v_{\mathrm{ion}}}e^{\frac{\bar{\alpha}v_e(g-z)}{v_e+v_{\mathrm{ion}}}}\,. \tag{2.3.12}$$

When the electron avalanche comes to a halt at the anode, we need to ensure that the ion density becomes zero for $z < v_{\mathrm{ion}}(t-g/v_e)$. This condition leads to the final solution

$$\rho_{\mathrm{ion}}(\mathbf{x},t) = \frac{q\bar{\alpha}v_e}{v_e+v_{\mathrm{ion}}}e^{\frac{\bar{\alpha}v_e(g+v_{\mathrm{ion}}t-z)}{v_e+v_{\mathrm{ion}}}}\delta(x)\delta(y)\left[\Theta\left(t-\frac{g-z}{v_e}\right)-\Theta\left(t-\frac{v_{\mathrm{ion}}g+v_ez}{v_ev_{\mathrm{ion}}}\right)\right]\,, \tag{2.3.13}$$

after going back to three spatial dimensions. Integrating equation (2.2.22) over the length of the gap $z \in [0, g]$ we obtain the contribution of the ions

$$I_{\mathrm{ion}}(t) = -e_0N_{\mathrm{ion}}(t)\frac{v_{\mathrm{ion}}}{g}\,. \tag{2.3.14}$$

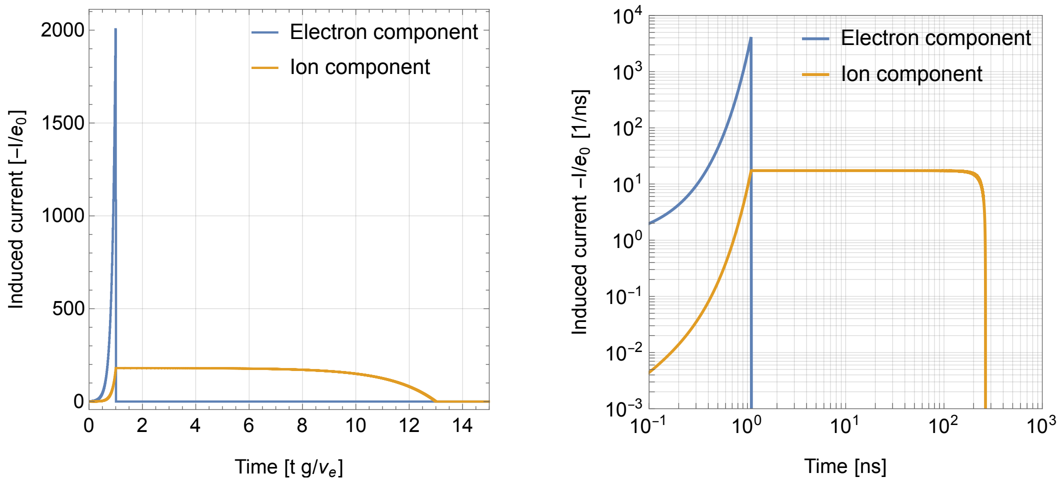

Figure 2.10: **Left:** General MM induced signal shape for a anode plane. **Right:** Toy model induced current on MM plane anode for Ar/ CO_2 93%/7% at a potential difference between anode and mesh of 510 V.

Here, $N_{\text{ion}}(t)$ represents the number of ions present in the amplification gap at time t and can be expressed as:

$$N_{\text{ion}}(t) := \left(e^{\bar{\alpha}g} - e^{\bar{\alpha}v_e v_{\text{ion}} t/(v_e+v_{\text{ion}})}\right)\Theta\left(\frac{g}{v_e} + \frac{g}{v_{\text{ion}}} - t\right) - \left(e^{\bar{\alpha}g} - e^{\bar{\alpha}v_e t}\right)\Theta\left(\frac{g}{v_e} - t\right). \tag{2.3.15}$$

To illustrate the typical shape of the signal in a parallel plate geometry the left panel of Fig. 2.10 shows the fast electron peak and slow ion tail. To provide a more realistic example, we will examine a MicroMegas with a gas mixture consisting of 93% Argon and 7% CO_2. The relevant electron transport data for this gas mixture were calculated using MAGBOLTZ [63, 64], considering atmospheric pressure and an absolute temperature of 293.15 K. These electron transport properties are illustrated in Fig. 2.11, in conjunction with the ion transport properties for Ar^+ in Ar [65, 66, 67]. For an induction gap measuring 128 µm and a potential difference of 510 V between the cathode and anode, the Townsend and attachment coefficients are $\alpha = 659.47$ cm^{-1} and $\eta = 1.25717$ cm^{-1} respectively, which includes the Penning transfer rate of $r = 4.0477 \cdot 10^{-1}$. This configuration yields a total gain of $\exp(\bar{\alpha}g) = 4560.21$. The velocities of the charge carriers become $v_e = 1.17276 \cdot 10^{-2}$ cm/ns and $v_{\text{ion}} = 4.86209 \cdot 10^{-5}$ cm/ns while their transversal diffusion coefficients are $D_T = 1.84373 \cdot 10^{-2}\ \sqrt{\text{cm}}$ and $1.12607 \cdot 10^{-3}\ \sqrt{\text{cm}}$, for the electrons and ions respectively.

The total contributions of both the electron peak and the ion tail to the total amount

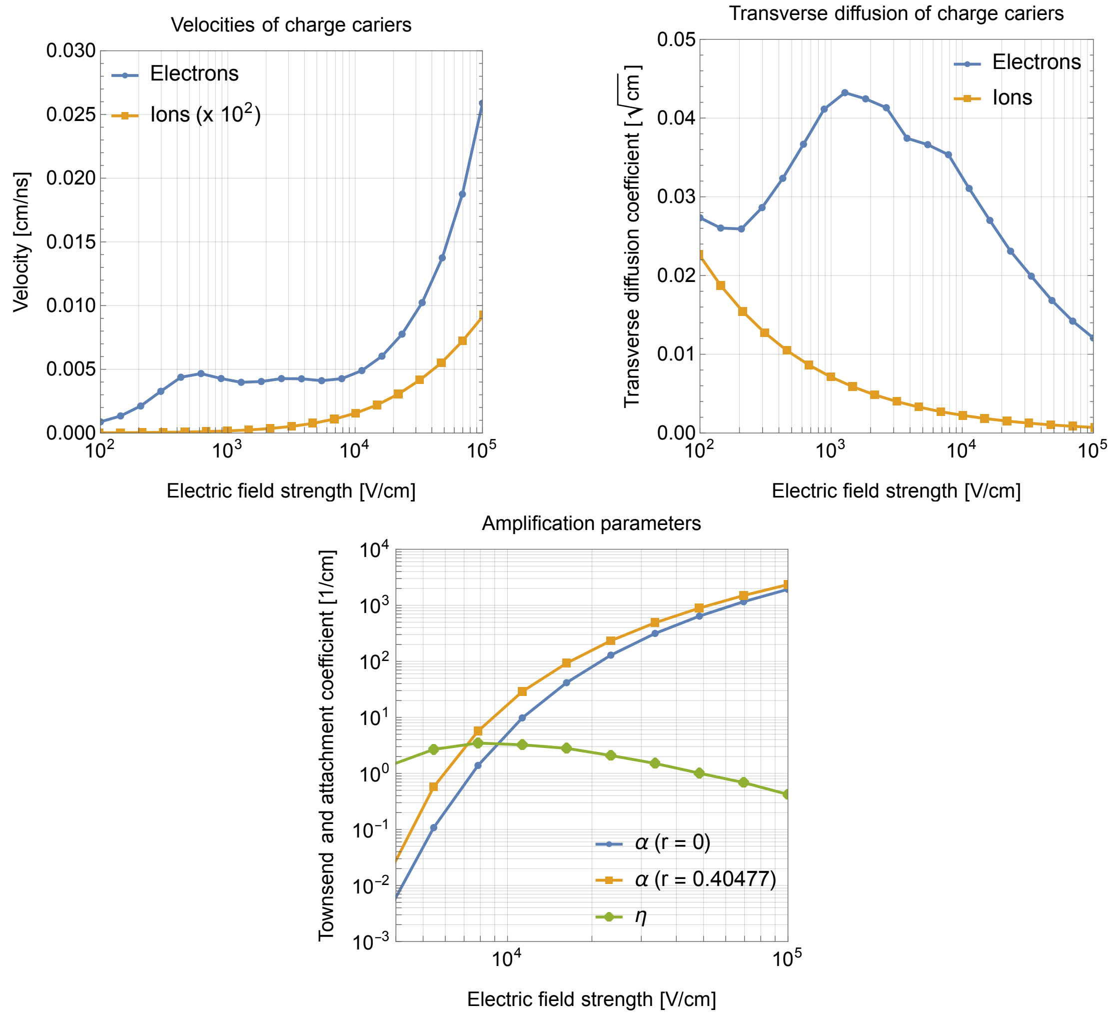

Figure 2.11: Gas properties plots for in Ar/CO_2 93%/7%. **Top left:** Electric field strength dependence on the velocities of the electrons and ions. **Top Right:** Transverse diffusion coefficient D_T of the electrons and ions. **Bottom:** An electric field strength scan of the attachment coefficient η and Townsend coefficient α with and without appropriate penning transfer r.

of charge flowing between the anode and ground is

$$
\begin{aligned}
Q_e &= \int_0^\infty I_e(t)\,\mathrm{d}t = -e_0 \frac{e^{\bar{\alpha}g} - 1}{\bar{\alpha}g}\,, \\
Q_{\text{ion}} &= \int_0^\infty I_{\text{ion}}(t)\,\mathrm{d}t = -e_0 \frac{e^{\bar{\alpha}g}(\bar{\alpha}g - 1) + 1}{\bar{\alpha}g}\,.
\end{aligned}
\tag{2.3.16}
$$

The total amount of induced charge Q equals the total collected charge, i.e.,

$$
Q := Q_e + Q_{\text{ion}} = -e_0 e^{\bar{\alpha}g}\,. \tag{2.3.17}
$$

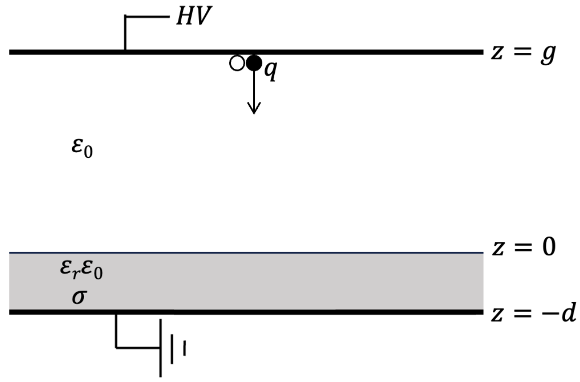

Figure 2.12: A schematic illustration depicting a bulk resistive layer that separates the anode from the gas gap. A charge q moves through the gap at a consistent velocity before reaching the resistive plate.

Following straight from the arguments of Sec. 2.3.1 the fraction of Q contained in the electron and ion current is dependant on $\bar{\alpha}g$, giving for higher values an increased contribution of the ion signal. This phenomenon arises from the exponential growth in the number of ions generated near the anode. These ions must traverse a substantial portion of the gas gap, which is significantly longer compared to the relatively shorter path of most electrons. Following from Eq. 2.3.16, the ratio of the two contributions can be calculated

$$\frac{Q_e}{Q_{\text{ion}}} = \frac{e^{\bar{\alpha}g} - 1}{(\bar{\alpha}g - 1)e^{\bar{\alpha}g} + 1} \approx \frac{1}{\bar{\alpha}g - 1}, \qquad \text{for } e^{\bar{\alpha}g} \gg 1, \tag{2.3.18}$$

where for our reference settings we get a ratio of 0.134644. Equivalently, the fraction of the total charge contained in the electron peak is

$$\frac{Q_e}{Q} = \frac{1 - e^{-\bar{\alpha}g}}{\bar{\alpha}g} \approx \frac{1}{\bar{\alpha}g}, \qquad \text{for } e^{\bar{\alpha}g} \gg 1. \tag{2.3.19}$$

Under our reference settings, it is observed that only 12% of the total charge is concentrated within the electron peak. The above equations show that the division of Q in Q_e and Q_{ion} is solely dependent on the gain in the volume below the mesh where for higher gains, Q_{ion} dominates.

2.3.3 Resistive Plate Chamber (RPC)

We start by applying the extended formalism introduced in the preceding sections to examine a specific case containing a resistive element, namely, the single-gap RPC-type geometry illustrated in Fig. 2.12. This configuration consists of a two-layer parallel plate structure comprising a resistive plate with a thickness denoted as d and a gas gap with a thickness of g. Within this setup, a point charge q undergoes motion from a position $z = g$ to $z = 0$ at a velocity of $v = g/T$. The resistive layer is characterized by a relative permittivity ε_r and a conductivity denoted as σ. The prompt solution to the static version of this system is

$$\psi^p(z) = V_w \varepsilon_r \frac{g-z}{d+\varepsilon_r g}\,, \qquad 0 < z < g\,. \tag{2.3.20}$$

Making the transformation to the effective permittivity (2.1.22) yields a time-dependent weighting potential of the form

$$\begin{aligned} \Psi(z,t) &= \psi^p(z) + \psi^d(z,t) && t \geq 0 \\ &= V_w \left(1 - \frac{d}{d+\varepsilon_r g} e^{-t/\tau}\right)\left(1 - \frac{z}{g}\right), && 0 < z < g\,, \end{aligned} \tag{2.3.21}$$

where we have defined the characteristic time constant $\tau := \frac{\varepsilon_0}{\sigma}\frac{d+\varepsilon_r g}{g}$. The contribution to the signal coming from the bulk resistive material is then given by the delayed weighting potential

$$\psi^d(z,t) = V_w \left(1 - e^{-t/\tau}\right) \frac{d}{g} \frac{g-z}{d+\varepsilon_r g}\,. \tag{2.3.22}$$

The weighting vector $\mathbf{H}(z,t)$ is given by

$$\mathbf{H}(z,t) = \hat{\mathbf{z}} \frac{V_w \varepsilon_r}{d+\varepsilon_r g}\delta(t) + \hat{\mathbf{z}} \frac{V_w}{g\tau}\frac{d}{d+\varepsilon_r g} e^{-t/\tau}\Theta(t)\,. \tag{2.3.23}$$

The resulting prompt signal is then given by

$$I^p(t) = \begin{cases} \dfrac{q\varepsilon_r v}{d+\varepsilon_r g} & t \leq T \\ 0 & t > T \end{cases}\,, \tag{2.3.24}$$

which is independent of the conductivity of the resistive plate. An additional contribution coming from the delayed part of the signal

$$I^d(t) = \begin{cases} \dfrac{qv}{d+\varepsilon_r g}\dfrac{d}{g}\left(1 - e^{-t/\tau}\right) & t \leq T \\ \dfrac{qv}{d+\varepsilon_r g}\dfrac{d}{g}\left(e^{T/\tau} - 1\right)e^{-t/\tau} & t > T \end{cases}\,, \tag{2.3.25}$$

which, in general, does not immediately vanish after the charge q has terminated its motion since the resistive plate continues in its effort to compensate the newly arrived charge. However, when, we consider the limit $\tau \to \infty$, it becomes evident that the current $I^d(t)$ tends to approach zero $\forall t \geq 0$. In this scenario, the bottom layer essentially functions as an insulating layer, leading to a reduction in the pure prompt signal amplitude as the distance d between layers increases. On the other hand, in the opposite extreme where $\tau \to 0$, the bottom layer behaves like a perfectly conducting medium and effectively extends the anode. In this regime the total signal then takes the form

$$I(t) = \frac{qv}{g}\Theta(T-t)\,, \tag{2.3.26}$$

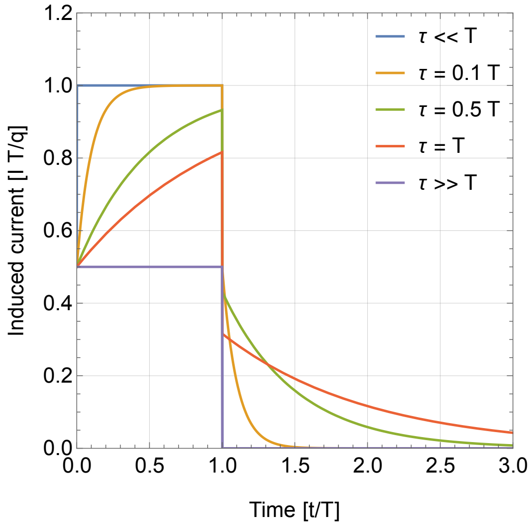

Figure 2.13: The signal induced at the anode, resulting from the motion of a charge q as it moves through the gas gap towards the resistive plate with changing conductivity, occurs over a time period T. Here we have taken $\varepsilon_r = 1$.

where the distance between anode and cathode is effectively reduced to a distance g.

The total induced signal for different characteristic time constant are shown in Fig. 2.13. The induced charge is given by

$$\begin{aligned} Q^p &= -\int_0^\infty I^p(t)\,dt = \frac{q}{V_w}\left[\psi^p(g) - \psi^p(0)\right] = -\frac{qg\varepsilon_r}{d+\varepsilon_r g}\,, \\ Q^d &= -\int_0^\infty I^d(t)\,dt = \lim_{t\to\infty}\frac{q}{V_w}\left[\psi^d(g,t) - \psi^d(0,t)\right] = -\frac{qd}{d+\varepsilon_r g}\,, \end{aligned} \tag{2.3.27}$$

where the total induced signal is then given by

$$Q = Q^p + Q^d = \frac{q}{V_w}\lim_{t\to\infty}\left[\Psi(g,t) - \Psi(0,t)\right] = -q\,. \tag{2.3.28}$$

Here, the contribution from Q^d can be interpreted as the result of currents that are drawn from the anode to compensate for the arrived charge on the resistive plate.

Most RPC designs employ a phenolic-paper laminate (bakelite) or high-resistivity glass material for the resistive plate. For these materials, the typical volume conductivity falls in the range of $\mathcal{O}(10^9 - 10^{12})$ Ω/cm. Consequently, this results in a characteristic time constant of $\tau \propto \varepsilon_0/\sigma \approx \mathcal{O}(10^{-3} - 1)$ s, which is notably longer than the typical signal duration of $T \approx \mathcal{O}(1-10)$ ns. This corresponds to the case of $\tau \gg T$ in Fig. 2.13, such that for RPCs, the induced signal is predominantly given by the prompt component

[68]. It directly follows that this observation also holds for MRPCs, for which the prompt weighting potentials are given in Sec. 2.2.2[1].

2.3.4 Signal spreading in a resistive layer

As will be discussed at the outset of Chapter 4, the size and spacing of the readout electrodes compared to the width of the collected charge cloud poses a strict lower bound on the spatial resolution that can be obtained. In the case of a MicroMegas where the transversal diffusion of the Townsend avalanche can be negligible compared to the pad size, the position reconstruction is made more difficult due to the limited sampling of the collected charge distribution. A substantial increase in the number of electronic channels would be needed to improve the position resolution significantly through charge sharing between pads. Nevertheless, implementing a high-granularity readout in specific detector applications, such as for a Time Projection Chamber (TPC), can become impractical. Instead, the signal can be shared over adjacent channels through the use of a thin layer with finite conductivity, an advancement that has been developed with a TPC application in mind [69]. This technique is employed in, for example, the RSD and resistive plane MicroMegas for the Tokai to Kamioka (T2K) Near Detector upgrade [70].

When examining the conduction within a thin sheet of finite surface area in Fig. 2.14 (left) with a height denoted by d_R and conductivity σ, we can use the second Ohm's law to define the quantity

$$R = \frac{\rho}{d_R}\frac{b}{a} =: R_1\frac{b}{a}\,, \tag{2.3.29}$$

called the *surface resistivity* $[\Omega/\Box]^2$. Here R_1 is the equivalent resistance across the foil when measured from sides b that is, characteristically, unchanged for all square sizes. To relate the current density and electric field in this thin layer, the microscopic Ohm's law can then be written as

$$\mathbf{j}(x,y,t) = \frac{1}{R}\mathbf{E}(x,y,t)\,. \tag{2.3.30}$$

This layer can act as a resistive anode separated from the grounded readout plane by an insulating layer, such as Kapton® (Apical®). A schematic representation of the geometry is given in Fig. 2.14 (right), where the thin rectangular resistive layer is grounded on the edges of the geometry $x = 0, a$ and $y = 0, b$. Structures such as these are becoming more prevalent in particle detectors for various reasons: (i) discharge protection by offering an increased impedance to ground [71, 34], (ii) separating the high voltage circuit from the readout circuit, and (iii) the charge spreading in the layer resulting in an increased number of channels participating in the event which can be beneficial during reconstruction

[1] We have integrated the evaluation of these weighting potential equations into Garfield++ for plane, strip, and rectangular pad electrodes. This implementation is available as part of the *ComponentParallelPlate* class, which can be used for simulating MRPCs. An illustrative calculation of an MRPC signal can be found on the Garfield++ webpage [38].

[2] The unit $\Omega/\Box$ is pronounced 'ohm per square'.

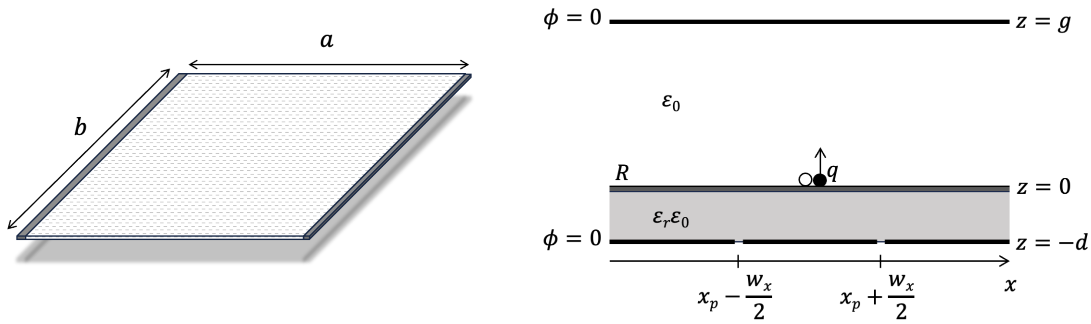

Figure 2.14: **Left:** A thin sheet of material with surface resistivity R. **Right:** Schematically depicted parallel plate geometry with a gas gap of size g and a thin resistive surface separated from the bottom grounded plane by an insulator of thickness d. A charge pair $\pm q$ is placed at the height of the resistive layer, after which the charge q traverses the gas gap at a constant velocity.

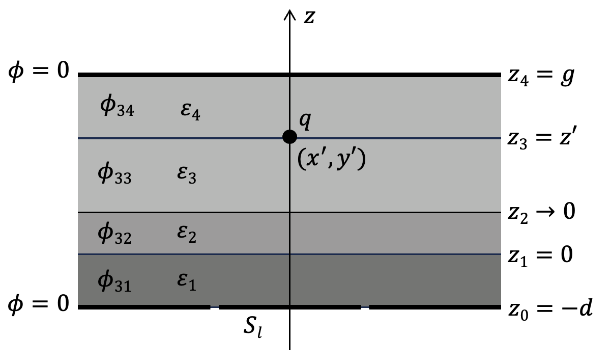

Figure 2.15: A diagram illustrating a four-layer configuration with an electrode featuring surface S_l positioned on the lower grounded plate is shown. This configuration is a limit case of the structure depicted in Fig. 2.14 (right). In this setup, a charge q resides at the interface between layers 3 and 4 situated at coordinates $(x, y) = (x', y')$.

as mentioned earlier[3]. The surface resistivity value R is subject to the desired application, with higher values generally preferred for robustness reasons. In this example, we will examine the case of a MicroMegas containing an insulating layer covered by a thin resistive coating, such as Diamond Like Carbon (DLC).

To find the solution of the weighting potential for an electrode in the geometry under consideration we note that it is the limit case of the four-layered arrangement shown in Fig. 2.15, the general solution to which is outlined is Sec. 2.2.2. If we want layer m to represent a thin resistive layer with surface resistivity R, we define the effective

[3] As we will explore in Chapter 5, the introduction of resistive elements into the readout structure generally decreases the device's rate-capability. Various novel strategies for enhancing charge evacuation are being developed for different resistive gaseous technologies to counteract this impact [72, 73, 74].

permitivity

$$\varepsilon_m \quad \to \quad \varepsilon_m + \frac{1}{(z_m - z_{m-1})\,\varepsilon_0 R s}\,, \tag{2.3.31}$$

with ε_m the relative permittivity of the layer. To obtain the dynamic weighting potential solution in the Laplace domain for the infinitesimally thin layer we take the limit $\lim_{z_m \to z_{m-1}} f_{nm}(k,z,s)$. In the case of the four layer geometry the function $f_{13}(k,z,s)$ reads

$$f_{13}(k,z,s) = \frac{\varepsilon_0 R \sinh(k(d+z))\sinh(k(g-z_0))}{Rs\varepsilon_0\varepsilon_3 \sinh(dk)\cosh(gk) + \sinh(gk)(Rs\varepsilon_0\varepsilon_1\cosh(dk) + k\sinh(dk))}\,, \tag{2.3.32}$$

where we have set $\varepsilon_4 = \varepsilon_3$, to reflect the charge position inside the gas gap. Its representation in the time domain is then

$$f_{13}(k,z,t) = \frac{\sinh(k(d+z))\sinh(k(g-z_0))e^{\frac{-t}{\tau(k)}}}{\varepsilon_3\sinh(dk)\cosh(gk) + \varepsilon_1\cosh(dk)\sinh(gk)}\,. \tag{2.3.33}$$

Here, we define the k-dependent time constants given by

$$\tau(k) := \frac{\varepsilon_0 R}{k}\left[\varepsilon_1 \coth(kd) + \varepsilon_3 \coth(kg)\right]\,. \tag{2.3.34}$$

As a first step we want to know the induced charge on a pad located on the grounded anode plane below the resistive layer for a charge deposited on the resistive layer at position $\mathbf{x}'$ and time $t = 0$. Since for a bounded geometry this weighting potential is given by Eq. (2.2.36), then

$$\begin{aligned} Q^{ind}\left(\mathbf{x}',t\right) =& \Theta(t)\frac{16q}{\pi^2}\sum_{\alpha,\beta=1}^{\infty}\frac{\sin\left(\alpha\pi\frac{w_x}{2a}\right)\sin\left(\alpha\pi\frac{x_p}{a}\right)\sin\left(\alpha\pi\frac{x'}{a}\right)}{\alpha} \\ &\times\frac{\sin\left(\beta\pi\frac{w_y}{2b}\right)\sin\left(\beta\pi\frac{y_p}{b}\right)\sin\left(\beta\pi\frac{y'}{b}\right)}{\beta}h_3\left(k_{\alpha\beta},z',t\right)\,, \end{aligned} \tag{2.3.35}$$

for $k_{\alpha\beta} := \pi\sqrt{(\alpha/a)^2 + (\beta/b)^2}$ and we use definition (2.2.37) to write

$$h_3(k,z,t) = \frac{\varepsilon_1 \sinh(k(g-z_0))e^{\frac{-t}{\tau(k)}}}{\varepsilon_3\sinh(dk)\cosh(gk) + \varepsilon_1\cosh(dk)\sinh(gk)}\,. \tag{2.3.36}$$

This outcome sharply contrasts against the previous example, where instead of having one time constant that governs the time development of the weighting potential, we now have a continuous distribution of them, all of which contribute. Since $k_{\alpha\beta}$ is dependent on a and b, these time constants are dependent on the size of the grounded resistive layer, where the diffusion of the charge in the layer is slower for larger sizes. For a resistive layer grounded on the edge of a finite square of length $a = b$, the induced charge on the segmented anode's 1×1 mm^2 pads has been calculated following Eq. (2.3.35). Using a surface resistivity of $R = 1\ \mathrm{M\Omega}/\square$ these solutions are shown in Figure 2.16 for three adjacent pads for different values of a. They suggest that in the central region of the detector, the early-time behavior is minimally affected when varying a. Nevertheless, at late times, the difference in the size of the resistive layer becomes apparent, where the smaller area detectors drain the diffusing charge distribution in the layer more efficiently. This is when the largest time constant $\tau_{11} := \tau(k_{\alpha\beta})|_{\alpha,\beta=1}$ starts dominating. In the case of $a = b$ it can be written in terms of the total capacitance of the resistive layer to ground as if it was a metal plane, i.e., for small values of k we have

$$\tau_{11} \approx \frac{1}{2\pi^2} R \left(\varepsilon_1 \frac{a^2}{d} + \varepsilon_3 \frac{a^2}{g} \right) = \frac{1}{2\pi^2} R \left(C_1 + C_3 \right) , \tag{2.3.37}$$

where C_1 and C_2 denote the capacitance to the anode and cathode, respectively.

The solution given in Eq. (2.3.35) is not in closed form and has to be evaluated numerically. This double sum can be shown to converge more slowly as the area of the detector increases; for large values of k the summand is suppressed by $(\alpha\beta)^{-1}$ and

$$h(k,t) \approx \frac{2\varepsilon_1}{\varepsilon_1 + \varepsilon_3} \exp\left[-k \left(d + \frac{t}{R\left(\varepsilon_1 + \varepsilon_3\right)} \right) \right] . \tag{2.3.38}$$

While the convergence speed is independent of the distance between the resistive layer and the cathode, we do find that it slows significantly for high ratios of ab/d^2. The number of terms that need to be summed for an accurate evaluation quickly rises as soon as one steps into the area of applications in HEP experiments. To illustrate this, we can take the T2K ND280 upgrade detector prototype where $a = 36$ cm, $b = 38$ cm and $d = 50$ µm. Here, we require a total number of terms of $\mathcal{O}(10^8)$ to evaluate the solution at $t = 0$ alone [75]. The convergence speed can possibly be improved by using series acceleration methods. However, for geometries lacking an analytical solution, ways to manage larger area structures numerically ought to be devised.

The scenario in which a charge q appears seemingly out of nowhere at time $t = 0$ is not in line with physical principles. A more natural scenario for charge deposition within the active area occurs through pair production resulting from the primary ionization pattern caused by an incident particle or through the multiplication process during an electron avalanche. When a Townsend avalanche is generated inside the gas gap, the ions also contribute to constructing the delayed part of the signal. Since the dominant fraction of the total number of electron-ion pairs is formed at the bottom of the amplification gap, we can, as a first approximation, consider the case of Fig. 2.14 (right) where a charge pair q and $-q$ is generated at $t = 0$. Let the charge q subsequently traverse the gas gap from $z = 0$ to $z = g$ at a constant speed v within a time interval $0 \leq t \leq T := g/v$, then the prompt induced current for a strip centered at $x = 0$ is given by

$$I^p(t) = \frac{2g\varepsilon_1}{\pi T} \int_0^\infty \frac{\sin\left(\frac{kw_x}{2}\right) \cos(kx) \cosh\left(k\left(g - \frac{gt}{T}\right)\right)}{D(k)} dk , \qquad t < T , \tag{2.3.39}$$

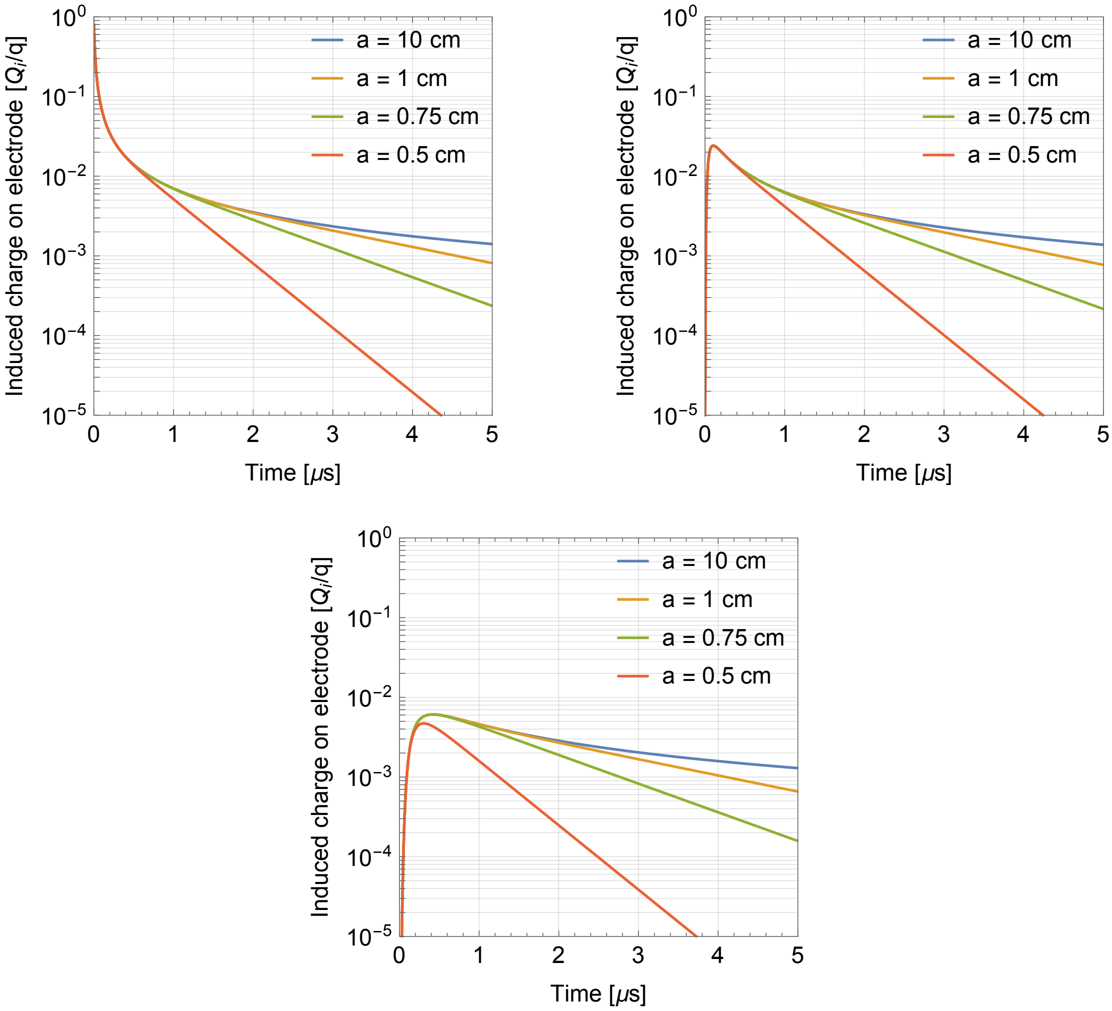

Figure 2.16: Induced charge on three 1×1 mm^2 neighboring pads positioned at $\mathbf{x} = (x_p, 0, -d)$ from a charge q deposited at the center ($\mathbf{x} = (a/2, a/2, 0)$)) of a square resistive layer with various widths a. Here, $g = 128$ µm, $d = 100$ µm, and $R = 1$ M$\Omega/\Box$ and the result is given for $x_p = a/2$ (top left), $x_p = a/2 + 1$ mm (top right) and $x_p = a/2 + 2$ mm (bottom).

where the denominator is

$$D(k) := \varepsilon_1 \cosh(dk) \sinh(gk) + \varepsilon_3 \sinh(dk) \cosh(gk) \,. \tag{2.3.40}$$

The reaction of the resistive layer is captured by the delayed current flowing from the electrode to ground, reading

$$\begin{aligned} I^d(t) &= \frac{g\varepsilon_1 q}{\pi}\int_0^\infty \frac{\sin\left(\frac{kw_x}{2}\right)\cos(kx)\left(F_1(k,t)+F_2(k,t)\right)\exp\left\{-gk-\frac{t}{\tau(k)}\right\}}{D(k)}\,dk \qquad t<T \\ &= \frac{g\varepsilon_1 q}{\pi}\int_0^\infty \frac{\sin\left(\frac{kw_x}{2}\right)\cos(kx)\left(F_3(k)+F_4(k)\right)\exp\left\{-gk-\frac{t}{\tau(k)}\right\}}{D(k)\left(gk\tau(k)+T\right)\left(gk\tau(k)-T\right)}\,dk \qquad t\geq T\,, \end{aligned} \tag{2.3.41}$$

where we have defined the functions

$$\begin{aligned} F_1(k,t) &:= \frac{e^{2gk}}{T-gk\tau(k)}\left(1-e^{t\left(\frac{1}{\tau(k)}-\frac{gk}{T}\right)}\right) \\ F_2(k,t) &:= \frac{1-\exp\left\{t\left(\frac{gk}{T}+\frac{1}{\tau(k)}\right)\right\}}{gk\tau(k)+T} \\ F_3(k) &:= T\left(2e^{gk+\frac{T}{\tau(k)}}-e^{2gk}-1\right) \\ F_4(k) &:= gk\left(1-e^{2gk}\right)\tau(k)\,. \end{aligned} \tag{2.3.42}$$

The sum of both components results in a bipolar signal. From Eq.(2.3.36) we deduce that $\int_0^\infty h_3(k,z,t)\,dt = 0$, which directly shows that $\int_0^\infty I^p(t)+I^d(t)\,dt = 0$ for all electrodes on the bottom plane, corresponding to the net zero amount of charge collected on the electrodes. This is because the current compensating the point charge $-q$ exclusively flows to ground through the infinitesimally thin resistive layer. Since most track reconstruction algorithms in HEP experiments rely on the center-of-gravity (CoG) of the quantity of charge in adjacent readout channels, the total amount of induced charge cannot be used. Instead the peak value of the signal from each channel is used for the purpose of reconstruction.

As we will see, this method uses a more ambiguously defined quantity that is subject to the nature of the shaping performed by external front-end electronics. This signal shaping is typically done to increase the signal-to-noise ratio via frequency filtering. We consider an unipolar shaper with an impulse response function of the form

$$f(t) = g\exp(n)\left(\frac{t}{t_p}\right)^n\exp(-t/\tau), \quad t_p = n\tau \tag{2.3.43}$$

where n the order of the shaper, τ is the RC time constant, g is the gain factor. When we assume that the multiplicative growth of Townsend avalanche is exponential, following Eq. (2.3.6), in addition to imposing that the transversal diffusion is negligible compared to the electrode's size, we can estimate the current formation along the lines of Sec. 2.3.2. The resulting current induced on three 1 mm wide neighboring strips is presented in Fig. 2.17 for different surface resistivities. Since the ions' electric field also permeates through the resistive layer, it spurs the flow of current in it. Consequently, both the electrons and ions contribute to the 'spreading' of the signal to neighboring channels. Fig 2.17

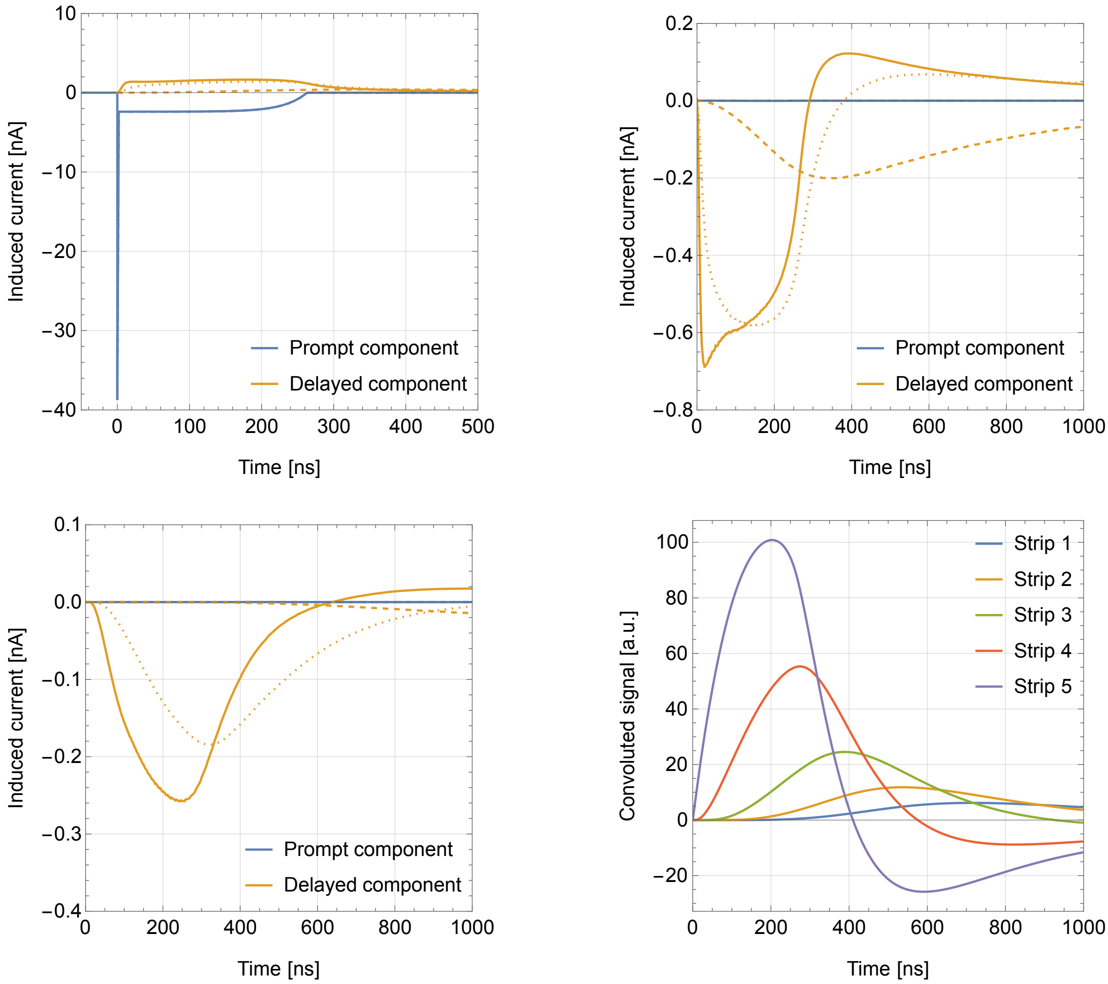

Figure 2.17: Induced current of a Townsend avalanche in the gap on adjacent neighboring 1 mm wide strip channels for a surface resistivity R of 500 k$\Omega/\square$ (full line), 1 M$\Omega/\square$ (dotted line), 10 M$\Omega/\square$ (dashed line). **Top left:** Prompt and delayed component of strip 1 centered below the avalanche. **Top right:** Strip 2 as nearest neighbor to strip 1. **Bottom left:** Strip 3 as next nearest neighbor to strip 1. **Bottom right:** Convoluted signal in five neighboring strips for a shaper with $t_p = 50$ ns, $n = 1$ and $R = 500$ k$\Omega/\square$.

shows the resulting currents at the output stage of a first-order shaper. As a result, the maximum amplitude, also called the *Pulse Height* (PH), and peaking time of the signal in each channel is given in Fig. 2.18 for different peaking times. Here a clear dependence of the PH distribution over the channels on the shaping time can be observed. Most notably, for large peaking times the PH value goes down again due to the bipolar nature of the induced current.

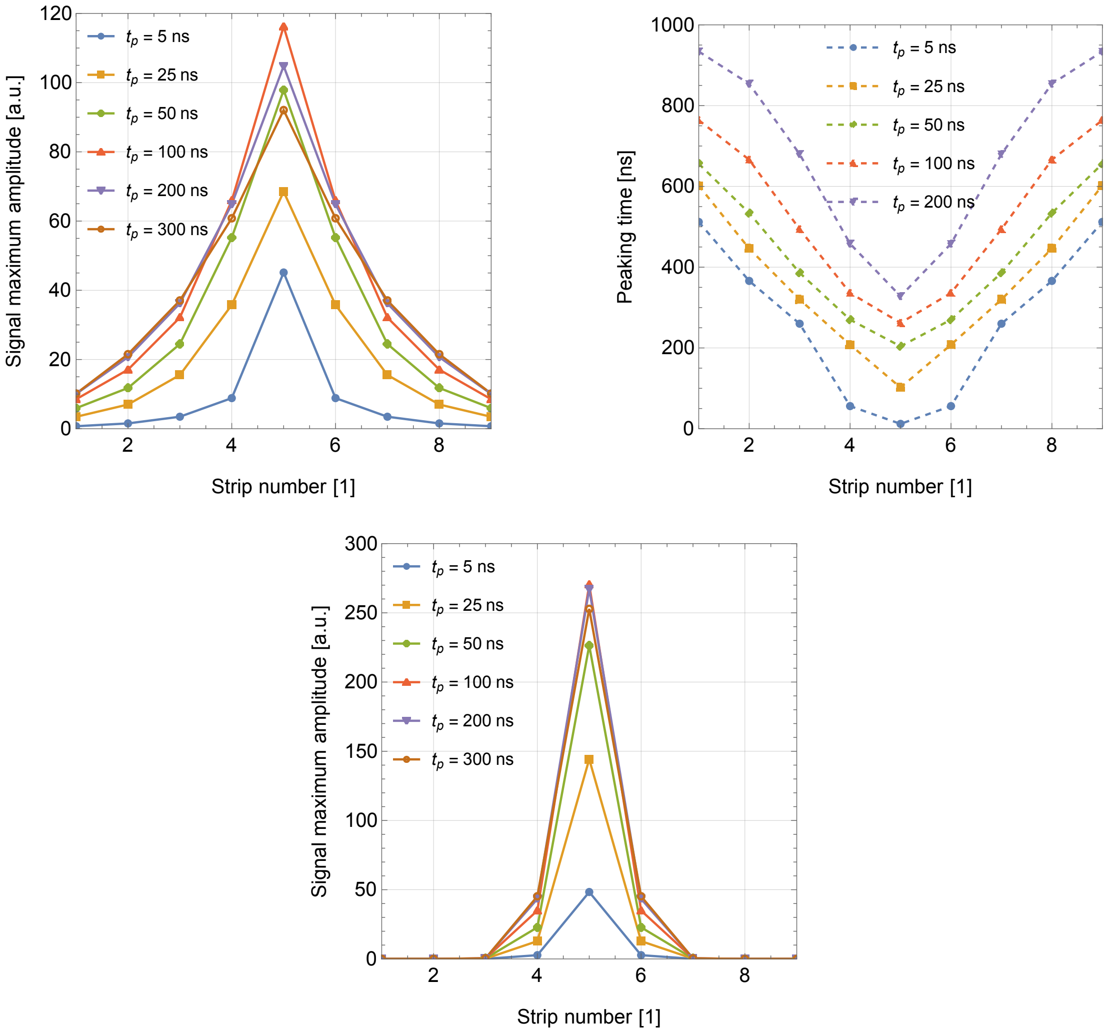

Figure 2.18: Characteristics of the resulting signal following shaping. The connecting lines are for guiding the eye. **Top left:** The PH as a function of the strip number, with $R = 500$ k$\Omega/\square$, and strip 5 corresponds to the location where the electron avalanche was centered. **Top right:** The peaking time of the signal in adjacent strips with $R = 500$ k$\Omega/\square$. **Bottom:** The PH as a function of the strip number, with a surface resistivity of 10 M$\Omega/\square$, again with strip 5 corresponding to the location where the electron avalanche was centered.

When two events that virtually coincide occur in close spatial proximity, a phenomenon known as *pileup* occurs, wherein local electrodes register an overlapping signal. Since the reduction in surface resistivity leads to the spreading of the signal across a greater number of channels, this causes an increase in the minimum distance required between two events to prevent pileup. Consequently, the adoption of signal spreading using a resistive sheet may result in a diminished overall rate capability of the detector.

2.4 On the use of the Telegraph equation

Regarding the MPGD family, the role of a thin layer of resistive material in diffusing the charge was noted in the seminal work of M. S. Dixit [69]. Here, using the *lumped element approximation* an infinitesimally thin resistive anode separated from a segmented readout plane with an insulating layer is often considered as the continuum limit of a two-dimensional RC network. In this case, we can define an equivalent capacitance between the resistive layer and ground. The surface charge density $\sigma_s(x, y, t)$ [C/cm^2] due to the diffusion of the charge deposited on the conductive layer is then governed by the *two-dimensional Telegraph equation*

$$\frac{\partial \sigma_s(x,y,t)}{\partial t} = \frac{1}{Rc}\left(\frac{\partial^2 \sigma_s(x,y,t)}{\partial x^2} + \frac{\partial^2 \sigma_s(x,y,t)}{\partial y^2}\right), \tag{2.4.1}$$

with R being the surface resistivity and c the distributed capacitance per unit area. The solution for an infinitely extending layer is a Gaussian distribution centered at the deposition position that widens over time [69]. Within this section, we will discuss using the Telegraph equation as a limit case of the solution found using the quasi-static limit of the Maxwell equations of the previous section. Furthermore, we will describe the scenarios in which this approximation is satisfactory.

2.4.1 Charge diffusion in a resistive layer

We reconsider the parallel plate system depicted in Fig. 2.14 (right) where a charge q is deposited on an infinitesimally thin resistive layer that this time is grounded at infinity. Discussion of the scenario involving a finite rectangular plane will be reserved for the conclusion. For q placed at $(x, y, z) = (x', y', 0)$ we can write the time evolution of the surface charge density on the resistive anode using Gauss' law as

$$\sigma_s(x,y,t) = \varepsilon_0\varepsilon_1 \left.\frac{\partial \phi_{13}}{\partial z}\right|_{z=0} - \varepsilon_0\varepsilon_3 \left.\frac{\partial \phi_{43}}{\partial z}\right|_{z=0}, \tag{2.4.2}$$

where ϕ_{mn} is given by Eq. (2.2.33) and (2.2.38) [61]. For the charge located at surface of the conductive layer, ϕ_{33} vanishes and ϕ_{43} can be written in terms of

$$f_{43}(k,z,t) = \frac{\sinh(k(g-z))e^{\frac{-t}{\tau(k)}}}{\varepsilon_1 \coth(dk)\sinh(gk) + \varepsilon_3 \cosh(gk)}. \tag{2.4.3}$$

With this, the surface charge density can be expressed as

$$\sigma_s(x,y,t) = \frac{q}{\pi^2}\int_0^\infty \int_0^\infty \cos\left[k_x\left(x-x'\right)\right]\cos\left[k_y\left(y-y'\right)\right] e^{\frac{-t}{\tau(k)}}\, dk_x dk_y\,, \tag{2.4.4}$$

where once more we have an infinite number of time constants (2.3.34) governing the time evolution of the solution. For late times, the slower suppression of the integrand is primarily influenced by the longer time constants, which take precedence. These are given by small values of k, and in this regime can be approximated as

$$\tau(k) \approx \frac{\varepsilon_0 R}{k^2}\left(\frac{\varepsilon_1}{d}+\frac{\varepsilon_3}{g}\right) = \frac{R}{k^2}\left(c_1+c_3\right) = \frac{R}{k^2}c\,, \tag{2.4.5}$$

in terms of the capacitance c per unit area of the resistive layer (treating it as though it were a metallic plane) to the top and bottom grounded plane, denoted by c_1 and c_2, respectively. In this limit Eq. (2.4.4) reduces to

$$\sigma_s(x,y,t) \approx \frac{Q}{4\pi Rct}\exp\left(-\frac{\left(x-x'\right)^2+\left(y-y'\right)^2}{4Rct}\right)\,, \tag{2.4.6}$$

which is the Gaussian function that solves the Telegraph equation (2.4.1). This can be understood when noting that the current density flowing over the resistive layer is related to the potential on it using Eq. (2.3.30) and $\mathbf{E} = -\nabla\phi$. Utilizing this relation in the continuity equation yields

$$\frac{\partial\sigma_s(x,y,t)}{\partial t} = \frac{1}{R}\left(\frac{\partial^2\phi(x,y,t)}{\partial x^2}+\frac{\partial^2\phi(x,y,t)}{\partial y^2}\right)\,, \tag{2.4.7}$$

of which Eq. (2.4.4) is a solution. Through approximation, we establish a connection between the voltage and surface charge density on the conducting surface, expressed as $\sigma_s(x,y,t) = c\phi(x,y,t)$, transforming the above relation into the Telegraph equation (2.4.1). Nevertheless, this approximation holds true only when the charge distribution exhibits a negligible gradient over distances of the order of d [61]. During early times, i.e., $t < Rc$, when the charge distribution is highly localized around its placement location, this simplification becomes inadequate.

2.4.2 Signal induction at late times

The induced charge on a strip of width w_x located on the bottom plane that stretches to infinity in the y-direction can be obtained through the weighting potential in Eq. (2.2.40). For small values of k, the denominator of the integrand takes the form

$$\varepsilon_1\cosh(dk)\sinh(gk)+\varepsilon_3\coth(gk) \approx \varepsilon_1+\varepsilon_3\frac{d}{g}\,. \tag{2.4.8}$$

After integration, the charge induced on the readout strip is given by

$$Q_{\mathrm{Tel}}(x',y',t) = \frac{\varepsilon_1 qg}{2\left(\varepsilon_1 g+\varepsilon_3 d\right)}\left(\mathrm{erf}\left(\frac{w_x-2(x-x')}{4\sqrt{\frac{t}{Rc}}}\right)+\mathrm{erf}\left(\frac{w_x+2(x-x')}{4\sqrt{\frac{t}{Rc}}}\right)\right)\,, \tag{2.4.9}$$

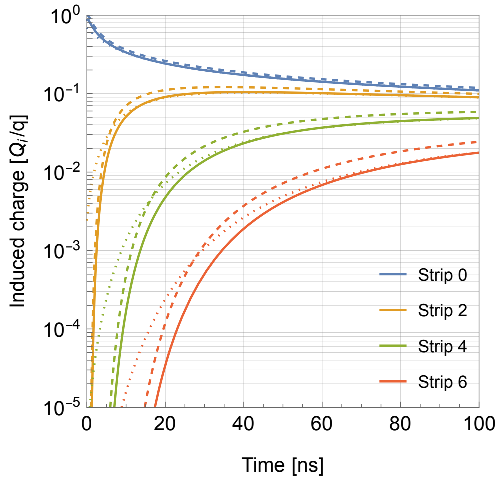

Figure 2.19: The induced charge on neighboring strips k, each measuring $w_x = 200$ µm in width, and positioned at $x_p = kw_x$, in response to a charge deposition at $x' = 0$ on the thin resistive layer. The solution is presented for three cases: the complete solution of Eq. (2.4.4) (represented by the dotted line), Q_{Tel} (depicted by the solid line), and Q_{Tel}^{∞} (shown as a dashed line), all as functions of time. The parameters used in this context are $g = 128$ µm, $d = 80$ µm, and $R = 1$ MΩ/□.

of which the factor $\varepsilon_1 g/(\varepsilon_1 g + \varepsilon_3 d)$ signifies that part of the signal is also coupled out through the top grounded plane. When neglecting the capacitance to the cathode plane, we can write

$$
\begin{aligned}
Q_{\text{Tel}}^{\infty}(x', y', t) &:= \lim_{g \to \infty} Q_{\text{Tel}}(x', y', t) \\
&= \frac{q}{2}\left(\operatorname{erf}\left(\frac{w_x - 2(x - x')}{4\sqrt{\frac{t}{Rc_1}}}\right) + \operatorname{erf}\left(\frac{w_x + 2(x - x')}{4\sqrt{\frac{t}{Rc_1}}}\right)\right) .
\end{aligned}
\tag{2.4.10}
$$

The same result is found when the ground bottom plane should perfectly reflect the charge density on the resistive layer $-\sigma_s(x, y, t)$. Integrating it over the surface of the electrode then yields the above relation [61]. For the case of a resistive plane MicroMegas, the results for Q_{Tel} and Q_{Tel}^{∞} are compared to the complete solution of Eq. (2.4.4) in Fig. 2.19. We find that the early time behavior is not accurately captured by the Gaussian shaped Q_{Tel} predicted by the Telegraph equation, yet it becomes a viable description when the charge distribution becomes broad for time $t > Rc$ where the curves approach the exact solution. Exclusively taking into account the capacitive coupling between the resistive anode and the grounded readout plane, the induced charge is consistently overestimated at all times. The same observations can be made for the induced current shown in Fig. 2.20, where the induced currents is zero at $t = 0$ for the Gaussian approximation.

For charges drifting in the gas gap following a path $\mathbf{x}_q(t)$, the induced charge density is given by Eq. (2.2.13) where the z dependence of the weighting field is given by the factor $\cosh\left[k(g-z)\right] \approx 1$ for small values of k. In this limit we can write

$$\begin{aligned} Q(t) &\approx -\frac{q}{V_w}\int_0^t T\left[x_q(t'), y_q(t'), t-t'\right] \mathbf{E}_{\text{plane}}\left[\mathbf{x}_q(t')\right] \cdot \dot{\mathbf{x}}_q(t')\, dt' \\ &= \int_0^t T\left[(x_q(t'), y_q(t'), t-t'\right] I_0(t')\, dt' , \end{aligned} \tag{2.4.11}$$

where we define the impulse response function $T(x', y', t) := Q_{\text{Tel}}(x', y', t)/q$ using Eq. (2.4.9) and the static weighting field $\mathbf{E}_{\text{plane}}(x) = -\hat{\mathbf{z}}/g$. Following the basic form of the Ramo-Shockley theorem, the current $I_0(t)$ can be interpreted as the one being induced on the resistive layer, if it were considered to be a perfectly conducting surface, by the motion of the charge carrier q inside the gas gap. The dynamics of the resistive layer is then captured by $T(x', y', t)$ that one has to convolve with $I_0(t)$ to get the complete solution. This is precisely the methodology under which the RC-circuit representations of this geometry operate.

2.4.3 Conclusion

The Telegraph equation approach is widely adopted for the description of the diffusion of a charge on an infinitesimally thin resistive layer by defining a capacitance of the resistive layer to ground. The solution for a grounded resistive anode at infinity is a Gaussian shaped surface charge density that 'spreads' inside the resistive anode with an Rc time constant. We have found that this description is a late-time limit of the full solution that satisfies Maxwell's field equations in the quasi-static regime. When considering both approaches, it can be deduced that the Telegraph equation produces satisfactory outcomes for time intervals beyond $t > Rc$, but it falls short in capturing the initial segment of the signal. When only taking the capacitive coupling to the bottom grounded readout plane, the total induced signal resulting from the charge diffusion is overestimated. In addition, the Rc time constant is derived for an infinitely extending geometry, while the edges of a $a \times b$ finite active area do affect the time evolution of the full solution:

$$\tau\left(k_{\alpha\beta}\right) = \frac{\varepsilon_0 R}{\pi\sqrt{\frac{\alpha^2}{a^2} + \frac{\beta^2}{b^2}}}\left[\varepsilon_1 \coth\left(\pi\sqrt{\frac{\alpha^2}{a^2} + \frac{\beta^2}{b^2}}d\right) + \varepsilon_3 \coth\left(\pi\sqrt{\frac{\alpha^2}{a^2} + \frac{\beta^2}{b^2}}g\right)\right] , \tag{2.4.12}$$

where the dominant time constant is then given by Eq. (2.3.37). Since we have assumed that the propagation speed within the field is negligible in comparison to the overall size of the system, we can assert the charge initiating diffusion at $t = 0$ is immediately 'aware' of the finite distance to the grounded edge of the resistive layer. Consequently, when considering the application of the Telegraph equation approach to scenarios in which the distance to ground cannot be simplified as infinite, caution must be exercised. Nevertheless, this challenge can be effectively addressed by using the dominant time constant

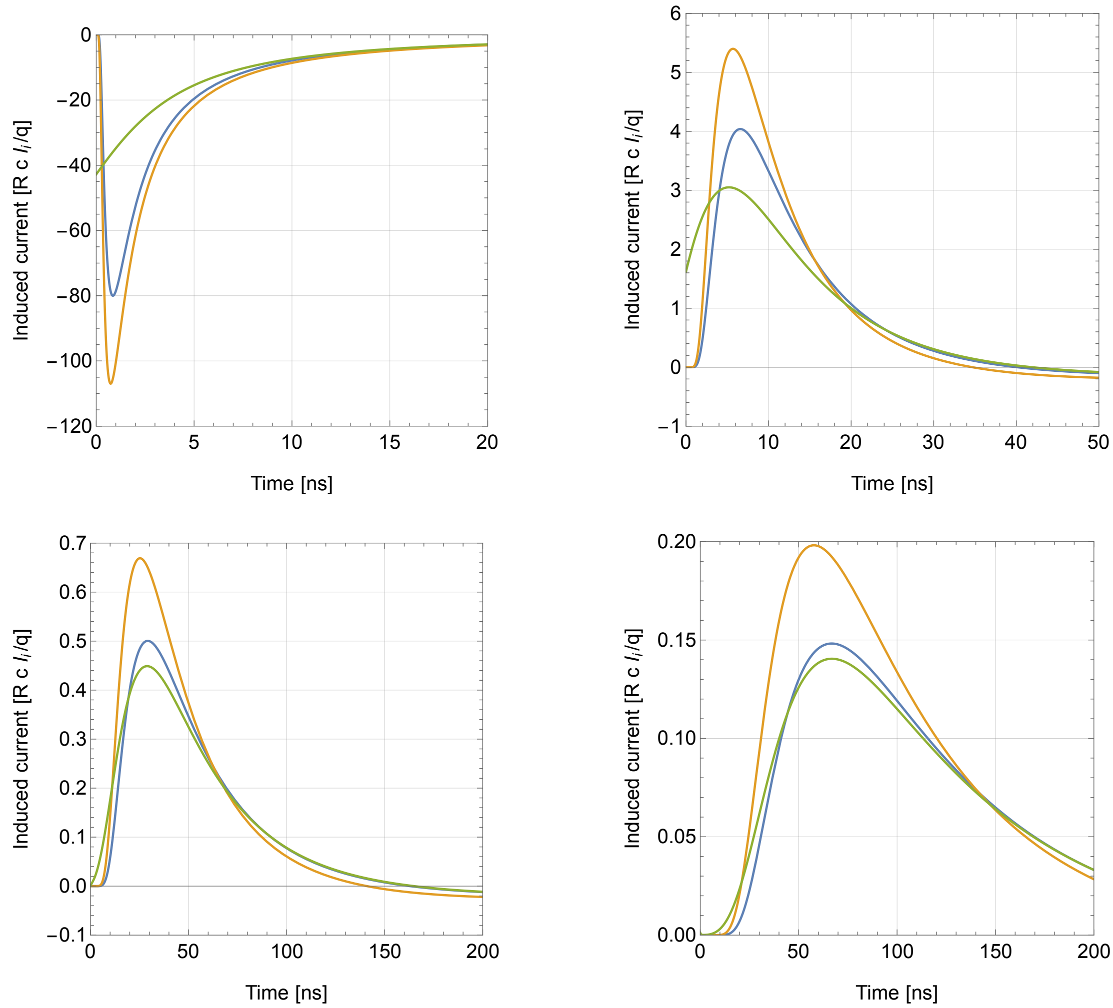

Figure 2.20: The graph displays the induced current on four neighboring readout strips resulting from the induced charge, as shown in Fig. 2.19, at different positions: $x_p = 0$ (top left), $x_p = 200$ µm (top right), $x_p = 400$ µm (bottom left), and $x_p = 600$ µm (bottom right). The data is presented for three solutions: the full solution according to Eq. (2.4.4) (depicted by the green line), Q_{Tel} (represented by the blue line), and $Q^{\infty}_{\mathrm{Tel}}$ (shown as the yellow line).

(2.3.37) within the infinite sum (2.3.35), or employing a discrete approach to solve the Telegraph equation such as through the use of an RC-circuit representation, allowing for the incorporation of the finite dimensions of the system. This lumped element approach does imply that the surface charge density σ_s and potential voltage ϕ directly related through the capacitance: $\sigma_s = c\phi$. Here it is critical to note that this approximation holds true only when the gradient σ_s remains small across the surface of the resistive

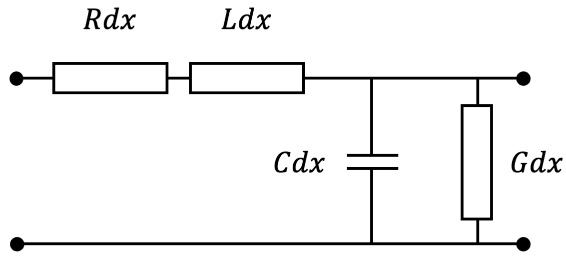

Figure 2.21: Schematic depiction of the circuit representation of an infinitesimally short repeating segment of the transmission line.

layer [61]. When the primary goal of the calculation is to provide an estimate of the number of channels over which the signal will be shared, the so-called *cluster size*[4], in a resistive readout, these descriptions will yield a satisfactory result, particularly for electrodes that are located further away from the CoG of the event. Moreover, when dealing with resistive readouts, like the two-dimensional resistive readout structure utilized in the MicroCAT detector [76] (see Chapter 6), it becomes feasible to obtain a good approximation of the total charge that flows to ground from each electrode on the resistive layer. Nevertheless, for accurately resolving of the signal's leading-edge, it becomes necessary to depend on the complete extended version of the Ramo-Shockley theorem.

Eq. (2.4.1) is frequently expressed analogously to the one-dimensional *transmission line equation*. When the distributed transconductance G is negligible, this equation can be written as

$$\frac{\partial^2 V(x,t)}{\partial x^2} = LC\frac{\partial^2 V(x,t)}{\partial t^2} + RC\frac{\partial V(x,t)}{\partial t}\,, \tag{2.4.13}$$

with R, L and C being – in units per length – the distributed resistance, inductance and capacitance, respectively. This equation is found as the continuum limit of an infinite series of the repeating lumped element circuit unit cell shown in Fig. 2.21. Therefore, the arguments made for the RC-circuit representation also apply here [61].

2.5 Numerical signal calculations

In detectors that contain resistive components, the process of signal generation on an electrode can be ascertained by utilizing its time-dependent weighting potential. In the preceding two sections, we have computed the induced signals when dealing with either a bulk resistive layer or an extremely thin layer with finite conductivity in a parallel plate configuration. For most intricate resistive detector architectures these potentials can not be obtained through analytical methods, rather, a numerical method is needed. As will

[4]This should not be mistaken for the quantity of electron-ion or electron-hole pairs generated within a singular cluster through the ionization of the medium, even though the same term denotes it.

be presented here, the time-dependent weighting potential can be obtained using Finite Element Method calculations. The conjunction with the Garfield++ toolkit enables for the modeling of the response of complex detector geometries containing resistive media. This approach, which will be the focus of this section, has in part been discussed in our publications [56, 77].

2.5.1 Signal induction from a segmented path

The Monte Carlo algorithm employed in Garfield++ for the microscopic electron transport within the drift medium relies on the energy-dependent collision rate of an electron with the medium's composites. Thus, due to the influence of the electric field, the electron experiences variations in both energy and collision rate during its free flight phase. This variability can be accounted for using the null-collision technique, as described in Ref. [78, 39]. Using this algorithm, a *free time* Δt can be obtained, resulting in one segment of the overall path composed of numerous such segments. To then numerically calculate the resulting induced signal from this particle's partitioned trajectory, a discretized version of the framework described in Sec. 2.2 is needed.

Let us partition the path $\mathbf{x}_q(t)$ of a point-like charge q into L segments, each defined by its begin $\mathbf{x}_n$ and end point $\mathbf{x}_{n+1}$ corresponding to respective times t_n and t_{n+1}, with index $n \in \{1, 2, \ldots, L\}$. For each small segment the charge induced on electrode k at time t can be approximated by

$$\begin{aligned} \Delta Q_{k,n}(t) \simeq \frac{q}{V_w} \big[& \psi_k^p(\mathbf{x}_n) - \psi_k^p(\mathbf{x}_{n+1}) \\ & + \psi_k^d(\mathbf{x}_n, t - t_n) - \psi_k^d(\mathbf{x}_{n+1}, t - t_n) \big] \\ & \times \Theta(t - t_n) \, , \end{aligned} \tag{2.5.1}$$

for small step sizes [56]. Here, we favor utilizing the scalar weighting potential field over the vector weighting field due to its singular value at every point in space, which improves numerical efficiency. Summing over all L segments of the total path yields the induced charge $Q_k(t)$ sourced by the particle track

$$Q_k(t) \simeq \sum_{n=1}^{L} \Delta Q_{k,n}(t) = Q_{k,p}(t) + Q_{k,d}(t) \; . \tag{2.5.2}$$

The induced current is then the time derivative of this signal

$$I_k(t_{n+1}) \simeq -\frac{Q_k(t_{n+1}) - Q_k(t_n)}{t_{n+1} - t_n} \, . \tag{2.5.3}$$

Considering that the objective is to compute the induced signals arising from the motion of charges in gases or semiconductors, the induced charge for each single particle track is determined separately using Eq. (2.5.1), and these individual contributions are then summed to obtain the total result. This algorithm has been implemented into the Sensor class of Garfield++, where we need the weighting potential for each electrode under study in the detector architecture.

2.5.2 Time-dependent weighting potential

With the inherent complexity of contemporary detectors, characterized by intricate electrode, dielectric, and resistive element shapes, we can not rely on analytical methods alone to provide the dynamic weighting potential. Instead, we must use tools such as the commercially available COMSOL® Multiphysics software package [79] to provide these solutions numerically. As a Finite Element Method (FEM)-based solver capable of solving the field equations governing electrodynamics systems using the Backward Differentiation Formula (BDF) method [80, 81], this toolkit permits the modeling of geometries with nearly arbitrary shapes. A pivotal aspect of FEM computations involves segmenting, or meshing, the physical surfaces and domain into discrete two or three-dimensional elements that locally make polynomial approximations, often of second-order, of the potential. The primary disadvantage of this method is for geometries containing features with dimensions considerably smaller than the overall scale of the model, e.g., the MicroMegas' woven wires of 18 μm thickness in a 50×50 cm^2 chamber. Such instances result in demanding computation time since a high accuracy for the potential necessitates a dense mesh, resulting in a large field map and, accordingly, slower interpolation [39]. Calculating the time-dependent weighting potential accurately for resistive elements terminated at a boundary situated at a considerable distance from the region of interest then becomes challenging due to the impact on the time evolution of the solution, as indicated in Eq. (2.4.12) for a resistive layer. Consequently, it is necessary to represent the boundary conditions accurately. Further constraints inherent in finite element field calculations involve the non-differentiability of the electric potential across neighboring elements and the approximate representation of the field through low-order polynomials [82].

The FEM approach offers significant flexibility in applying the extended form of the Ramo-Shockley theorem for conductive media to a wide range of detector designs. In this approach, the dynamic weighting potential solution is entirely determined by the configuration and characteristics of the materials within the structure. Given the detector layout we want to study, the dynamic weighting potential can then be calculated for each electrode separately using the following recipe:

- Disregard any externally impressed or static charge densities.
- Perfectly ground all electrodes except the one under study to which we will apply a potential step $V_w\Theta(t)$. To avoid the discontinuity of the Heaviside step function described in Eq. (2.2.18), we can apply a voltage ramp of $V_w = 1$ V instead. The ramping time of the function needs to be smaller then the reaction time of the resistive material such that at time $t = 0$ the contribution coming from $\psi_k^d(\mathbf{x}, t)$ is negligible. An example of such a ramping function is given in Fig. 2.22.
- Evaluate the solution at logarithmic spaced time points to accurately capture the early-time dynamics of the solution. From examples 2.3.3 and 2.3.4 we found that the dynamic weighting potential has the strongest change in time during its

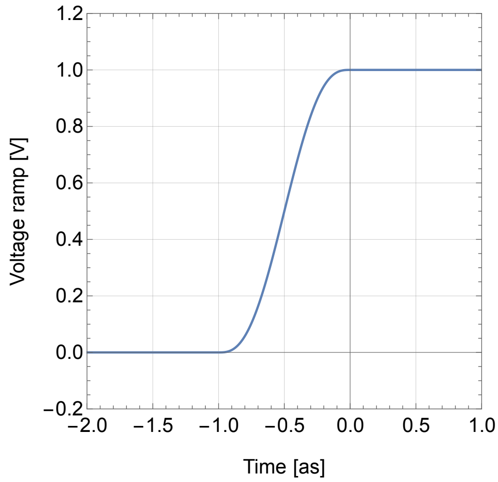

Figure 2.22: Example of a voltage ramp to numerically represent the step function needed to determine the time-dependent weighting potential.

early-stage, requiring finer sampling of the solution in that time domain that can gradually coarsen as time progresses.

The outcome is a finite set of N time-sliced weighting potential maps $\Psi_k(\mathbf{x}, t_n)$, $n \in \{1, 2, \ldots, N\}$, that can be provided to Garfield++ for the signal induction calculations. We identify the slice at $t_1 = 0$ as the prompt weighting potential $\psi_k^p(\mathbf{x})$ such that $\psi_k^d(\mathbf{x}, t_n) = \Psi_k(\mathbf{x}, t_n) - \psi_k^p(\mathbf{x})$. To evaluate the delayed potential for other times, the value is linearly interpolated from the two closest time-slices

$$\psi_k^d(\mathbf{x}, t) \approx \frac{\psi_k^d(\mathbf{x}, t_n)\,(t_{n+1} - t) + \psi_k^d(\mathbf{x}, t_{n+1})\,(t - t_n)}{t_{n+1} - t_n}\,, \qquad t_n < t < t_{n+1}\,. \tag{2.5.4}$$

When the time intervals $t_{n+1} - t_n$ are sufficiently small, much less than the average free time Δt of the electron, ion, or hole, this interpolation will yield a reliable estimation of the induced current throughout the free path. However, for larger time intervals, the time derivative results in a constant current.

As mentioned above, implementing this approach in the context of large-area detector configurations that incorporate resistive components terminated at the edge of the geometry requires further consideration. We can imagine representing an infinitesimally thin resistive layer accurately by a finely meshed thin layer with corresponding finite bulk resistivity $\rho = Rd_R$ for a thickness d_R negligible compared to the overall size of the geometry. Yet, when grounded on the edge such a representation of an expansive resistive layer can become cumbersome given the number of finite elements involved. To this end, we used two techniques applicable to any detector size to simplify the computations. The first was to avoid the need to mesh the thin resistive layer using the

Electric Shielding surface condition, available in the COMSOL® Multiphysics toolkit, to the interfacing surface between two domains between which the thin resistive layer resides. This condition relates the potential above and below the resistive sheet using the junction condition

$$\hat{\mathbf{n}} \cdot (\mathbf{j}_1 - \mathbf{j}_2) = -\nabla_T \cdot d_R \left(\left(\sigma + \varepsilon_0 \varepsilon_r \frac{\partial}{\partial t} \right) \nabla_T \Psi_k \right) , \tag{2.5.5}$$

for a conductivity $\sigma = (Rd_R)^{-1}$, relative permittivity ε_r, $\hat{\mathbf{n}}$ being the normal vector of the resistive surface, and $\mathbf{j}_i$ the current densities of the region above and below the layer. The operator ∇_T represents the tangential derivative along the layer. The second technique was to stretch the model using coordinate mapping rather than directly implementing the total active area. In order to faithfully depict the boundary conditions within the finite element model, we utilized coordinate scaling outside a specific region of interest. This mathematical stretching of the outer regions of the detector also apply on the finite elements that segment it, given reason to use cell element shapes for which the solution is resilient to the elongation (such as pentahedrals). For a finite linear scaling the function *Scaling System* was used, while for pushing the boundary to infinity the *Infinite Element Domain* condition was applied. This approach enabled us to create a more numerically manageable representation of the geometry, which is smaller than the complete active area of the detector, yet equivalent to it. An example can be found on the Garfield++ webpage [38].

Referring to the example discussed in Sec. 2.3.4, which concerns the induced charge arising from a charge diffusion within a confined $a \times b$ resistive layer, the time-dependent weighting potential of the pads has been calculated using a FEM-based model, where the above two techniques were applied to describe the entire 10×10 cm^2 grounded resistive anode. Detailed instructions for constructing and solving this system in COMSOL® are provided in Appendix A. The comparison between this computed solution and the analytical one of Eq. (2.3.35) is illustrated in Fig. 2.23, demonstrating a within 3.15% agreement between the two approaches. With this, we successfully circumvent the slow convergence of the series in the analytical solution. Compared to the equivalent FEM model with similar mesh quality but lacking the thin resistive layer junction condition and coordinate scaling, these techniques reduce the model's degrees of freedom from $8.8 \cdot 10^6$ to $3.5 \cdot 10^6$, resulting in a 21-fold decrease in computation time[5]. In Fig. 2.24, the weighting potential of different time slices is given for an infinitely extending resistive layer where $a, b \to \infty$. The solution at $t = 0$ corresponds to the prompt solution, which commences 'spreading' over the resistive layer at $z = 0$ as time progresses. This layer will act as a metal plane for $t \to \infty$, fully canceling out all field lines permeating it and subsequently shielding the readout electrode from any charges that drift within the gas gap.

[5] The computation was carried out using a four-core Apple M1 chip with 8GB of memory. Meshing the one µm thick resistive layer was accomplished using shell (pentahedral) elements since the same precision could not be reached using tetrahedral elements.

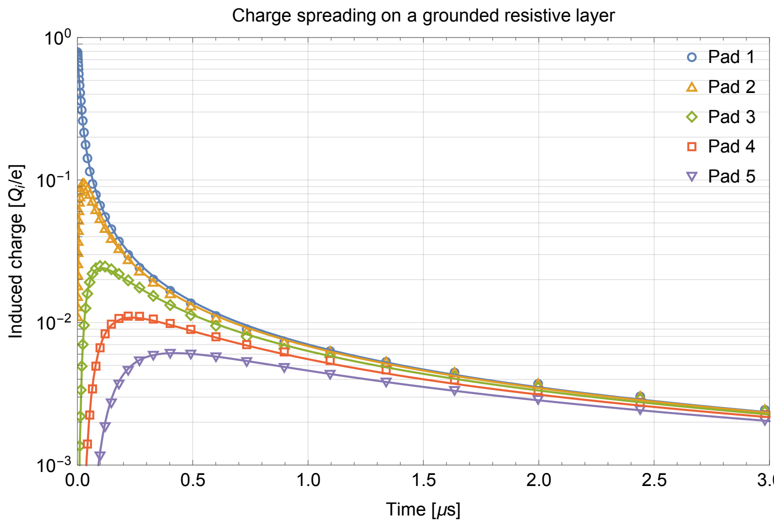

Figure 2.23: Comparison between the induced charge on neighboring pads determined analytically and the corresponding COMSOL® solution. The former is given by the full lines, while the latter is given by the markers of the same colour for several time points. The charge is deposited in the centre of a 10×10 cm^2 resistive layer with R $= 1$ M$\Omega/\square$. The five 0.5×0.5 mm^2 pads with index k are centered at $x_p = 4.5 + 0.5k$ mm and $y_p = 0$.

The outlined method is appropriate for geometries composed of linear materials, meaning materials whose resistivity remains constant irrespective of the applied voltage. Nevertheless, when working with non-linear silicon sensors, it is important to recognize that the volume resistivity changes with varying applied voltage. Using a TCAD simulation toolkit, we can set up the geometry of the sensor that includes a specific doping profile and biasing potential across the sensor [55]. This allows us to determine the static electric field as well as the electron density $n_e(\mathbf{x})$ and hole density $n_h(\mathbf{x})$ within the semiconductor bulk. Using the Drude model, the conductivity $\sigma(\mathbf{x})$ can then be expressed as

$$\sigma(\mathbf{x}) = q\left[\mu_e n_e(\mathbf{x}) + \mu_h n_h(\mathbf{x})\right] , \tag{2.5.6}$$

where μ_e and μ_h denote the mobilities of the electrons and holes [55]. When the sensor is fully depleted $n_e(\mathbf{x}) = n_h(\mathbf{x}) = 0$, the signal can be calculated by using the static weighting potential from the basic form of the Ramo-Shockley theorem. For only a partially depleted sensor, however, the finite value of σ contributes to the formation of the induced signals, and the time-dependent weighting potential needs to be obtained. Following the steps outlined in Sec. 2.2, the conductivity parameter σ is influenced by the voltage applied to the electrode in the case of a completely unbiased sensor, leading to an inaccurate representation of the conductivity distribution. To address this, we introduce a small voltage increment to the relevant electrode while the sensor is biased. Subsequently, we calculate the difference between the resulting time-dependent and static electric fields, as described in [55]. We have implemented the importing of the solution into Garfield++ through the *ComponentTcad2d* or *ComponentTcad3d* class. While we will discuss the signal formation inside solid-state detectors, taking the doping profile into account using the TCAD approach falls outside the scope of this work.

2.5.3 Implementation in Garfield++

Until now, we have discussed the implementation of the extended Ramo-Shockley theorem for numerically obtaining the required time-dependent weighting potential using a FEM-based solver. We have also examined how to derive the signal from a moving charge carrier when dealing with a segmented trajectory. In this section, we bring together these two elements and outline the necessary steps for configuring these calculations within Garfield++ using the dynamic weighting potential maps obtained using COMSOL®.

To import the set of time-sliced weighting potential maps $\Psi_i(\mathbf{x}, t_n)$, $n \in \{1, 2, \ldots, N\}$, from the FEM calculation, the following files are needed: (i) *mesh.mphtxt* containing the node positions and cell types that constitute the mesh, (ii) *Potential.txt* that holds the static potential value on each mesh node for the biasing of the cathode and anode giving the applied field that drifts the charges, (iii) *dielectrics.dat* assigning the dielectric constants to each material, and (iv) *WPotential.txt* giving the electrode's weighting potential on the nodes for each time slice. Using the *ComponentCOMSOL* class, we can import this information into our simulation:

```
// Import COMSOL's potential, mesh and dielectric constant map
ComponentCOMSOL fm;
fm.Initialise("mesh.mphtxt", "dielectrics.dat", "Potential.txt", "m");
fm.EnableMirrorPeriodicityX();
fm.EnableMirrorPeriodicityY();
fm.PrintRange();

// Import weighting potential maps of two neighboring electrodes
const std::string label[2] = {"electrode1","electrode2"};
fm.SetDynamicWeightingPotential("WPotential.txt",label[0]);
```

When the readout structure exhibits symmetry such that the weighting potential of a second electrode can be mapped through rotation or translation of the solution of a first electrode, we can duplicate the weighting potential of the initial electrode.

```
const double pitch = 0.1; // Pitch between electrodes [cm]
fm.CopyWeightingPotential(label[1], label[0], pitch, 0, 0, 0, 0, 0);
```

where we have performed a translation of 1 mm along the x-axis to represent a neighboring electrode. To determine which domain(s) constitute the drift-able medium, we should designate a gas medium to the domain characterized by a unit relative permittivity:

```
// Setup of the gas
MediumMagboltz gas;
gas.SetComposition("ar", 70., "co2", 30.); // [%]
gas.SetTemperature(293.15); // [K]
gas.Initialise(true);
```

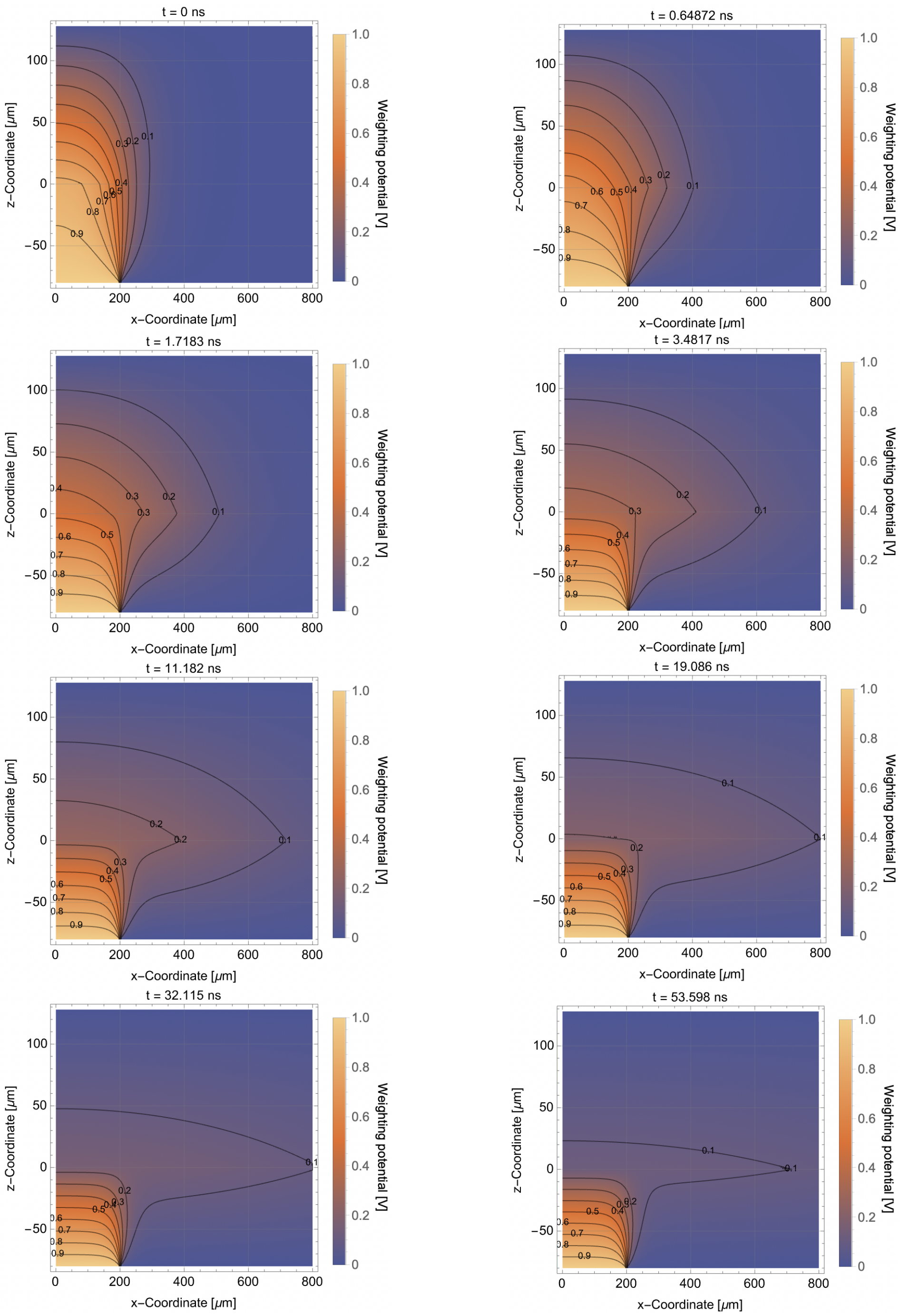

Figure 2.24: Cross-section view of the weighting potential solution of a 400 μm wide strip located at $\mathbf{x} = (0, 0, -80)$ μm evaluated at different times of a parallel plate geometry with an infinitely extending resistive layer.

```
// Assign relative permittivity to geometry domains
const unsigned int nMaterials = fm.GetNumberOfMaterials();
for (unsigned int i = 0; i < nMaterials; ++i){
    const double eps = fm.GetPermittivity(i);
    if(eps==1) fm.SetMedium(i, &gas);
}

// Print all materials
fm.PrintMaterials();
```

Within the *Sensor* class, an assembly of components can be made, which is used to calculate the induction of current on an electrode due to drifting charges given the applied field and weighting potentials. Here we can assign which potential map will be used to propagate the charges, and for which electrodes the signal needs to be calculated:

```
// Setup of the sensor
Sensor sensor;
sensor.AddComponent(&fm); // Assign potential map
sensor.AddElectrode(&fm, label[0]); // Assign weighting potential map
sensor.AddElectrode(&fm, label[1]);
sensor.EnableDelayedSignal();  // Enable delayed signal calculation
```

The resulting signal will be coarse-grained into a number of time bins of predetermined length. The bounds of the time window in which the signal needs to be computed, and how finely it is resolved, can be set:

```
// Set time interval
const double tmin =  0.; // [ns]
const double tmax = 1e3.; // [ns]
const int nTimeBins = 100;
const double tstep = (tmax - tmin) / nTimeBins;
sensor.SetTimeWindow(tmin, tstep, nTimeBins);
```

The time convolution of the velocity vector with the weighting field in Eq. (2.5.1) needs to be evaluated over the set time range at a number of predetermined time points. This can be performed for each time bin:

```
// Time points at where the delayed signal is calculated
std::vector<double> times;
for(int i=0;i<nTimeBins;i++) times.push_back(tmin+tstep/2+i*tstep); // [ns]
sensor.SetDelayedSignalTimes(times);
```

Alternatively, a more coarse approach can be employed where the evaluation is done for fewer number of points. The final step involves enabling signal calculation within the class used for charge propagation:

```
// Setup of electron transport
AvalancheMicroscopic aval;
aval.SetSensor(&sensor);
aval.EnableSignalCalculation();
```

The signal will then be calculated for each segment of the charge carrier during its drift calculation.

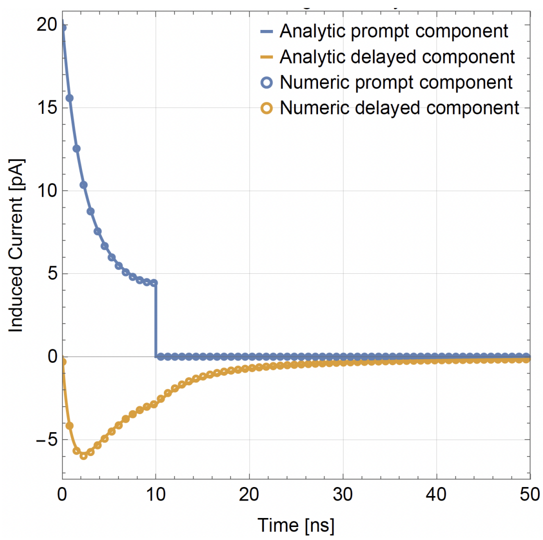

Figure 2.25: Toy model calculations for the induced current sourced by uniform charge movement on a readout strip positioned at $x_p = 0$ obtained though the numerical and analytical method. Here, the positively charged point charge moves from $z = 0$ to $z = g = 1$ mm, with $\varepsilon_r = 8$, $w_x = g/2$, $d = 0.4$ mm, $T = 10$ ns, $x = 0$ mm and $R = 100$ k$\Omega/\square$.

The complete simulation chain has been validated against various analytical toy-model examples. The one illustrated in Fig. 2.25 involves an electron-ion pair generated above an infinitely extended resistive layer, with the ion moving upward at a constant velocity. This particular example showcases the capacity to faithfully reproduce the analytical solutions presented in Eq. (2.3.39) and (2.3.41) for the prompt and delayed current, respectively.

2.5.4 External impedance elements

When a particle traverses an electrode, we observe two mechanisms that cause neighboring electrodes to detect a signal: (i) direct induction, which occurs when a particle crosses between two neighboring electrodes or near the electrode's edge, and (ii) so-called *capacitive coupling* between the electrodes, where the signal is coupled to nearby electrodes due to their finite mutual impedance. The former was already covered using the framework outlined in Sec. 2.2 where all electrodes are considered to be perfectly grounded. Hence, the resulting current flows unimpeded to ground once induced. The cross-coupling between the metal electrodes that are found in detector readout structures is due to the presence of a non-zero impedance to ground coming from the front-end electronics, electrical protection circuit, and high-voltage supply. When the electrodes are connected with discrete linear impedance components, we can treat them as integral to the medium, and thus, we need to incorporate these into the time-dependent weighting potential.

As an example we can take the single gap RPC geometry given in Fig. 2.12 of Sec. 2.3.3, that contains a bulk resistive layer with conductivity σ. As demonstrated in Ref. [54], the detector system can be precisely depicted using an equivalent circuit. We will index the top and bottom metal plane using $i = 1$ and $i = 2$, respectively. Using Eq. (2.2.23) and (2.3.21) we find that impedance between the two is given by

$$Z_{12}(s) = \frac{1}{sC_1} + \frac{R/sC_2}{R + 1/sC_2} \tag{2.5.7}$$

where A is the surface area of the detector and the two capacitances and the resistance are given by

$$C_1 = \frac{\varepsilon_r \varepsilon_0 A}{d}, \qquad R = \frac{d}{\sigma A}, \qquad C_2 = \frac{\varepsilon_0 A}{g}. \tag{2.5.8}$$

Here, $Z_{12}(s)$ takes the form of a capacitor in series with a parallel coupled resistor and capacitor. Consequently, to derive the induced signal after connecting external electrical components, we can first calculate the currents induced on the grounded electrodes. Then, we can impress these currents as ideal current sources in the equivalent circuit of of the detector, to which we attach the external impedance elements [55]. Typically, this step is executed using an analog circuit simulation software program such as LTSpice [83]. In Fig. 2.26 the equivalent circuit of the system is shown where the two electrodes are terminated using impedance elements Z_c and Z_a for the cathode and anode, respectively.

Alternatively, we have integrated the external impedance at the level of the weighting potential $\Psi_2(\mathbf{x}, t)$ by including it in the FEM calculations. In COMSOL®, this can be achieved by using the *Terminal* condition on the electrodes, which allows us to interface with the *Electrical Circuit* module, where we can define a linear network comprising interconnected discrete electrical components. The connection between the terminal and the linear circuit is established using the *External I vs. U* coupling. Subsequently, we apply the voltage (ramp) pulse $V_w\Theta(t)$ at the specific location where we wish to determine the induced signal, for example, after the lumped impedance Z_a connected to electrode 2. Taking Z_c and Z_a as two 50 Ω resistors we calculate the signal after Z_a from an Townsend avalanche inside the gas gap using both approaches. The comparison can be found in Fig. 2.27, where the calculation for the equivalent circuit was performed using LTSpice. With an average absolute difference of 5.32% between the two solutions, the methods are demonstrated to be compatible. However, the complete weighting potential description performed better in capturing the electron peak compared to the general circuit approach. This improvement can be attributed to the LTSpice model's limited sampling of the electron peak of the injected currents.

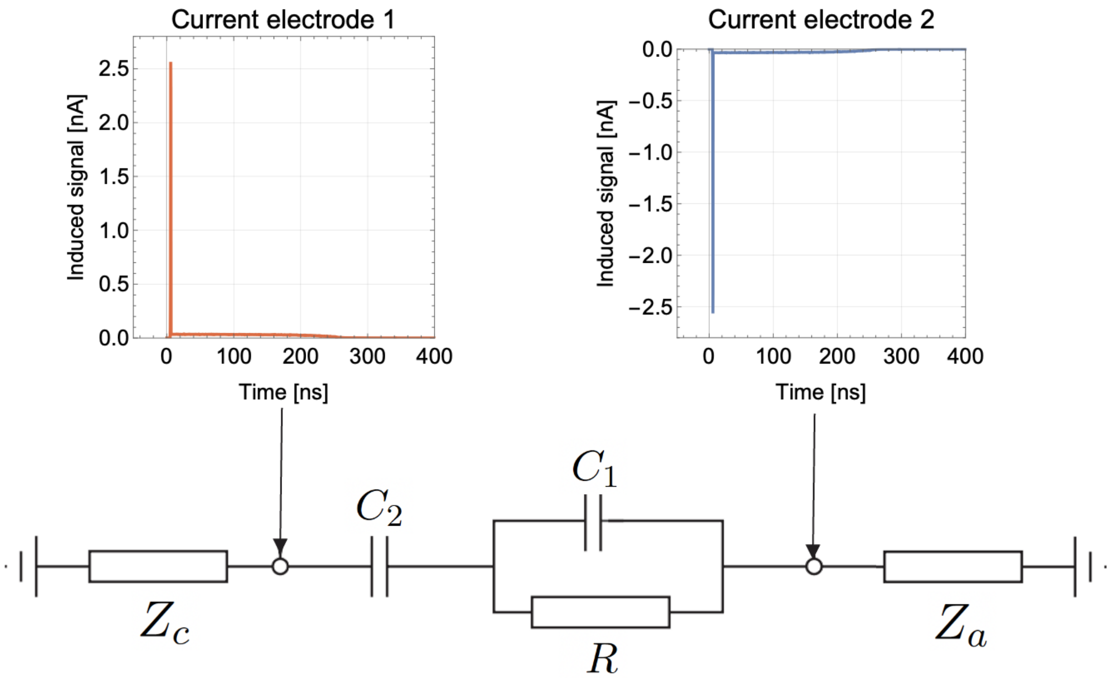

Figure 2.26: The equivalence circuit of the geometry shown in Fig. 2.12, with two added impedance elements. The induced signal on both electrodes obtained through the weighting potential formalism can be injected as ideal currents into the circuit to obtain the effect of the external elements and the cross-coupling between the two electrodes.

2.6 Summary

Materials with a finite conductivity are increasingly being incorporated in particle detectors for various purposes, including enhancing their robustness and optimizing their performance. When these materials are introduced into the detector design – or are inherent to the detector's medium, as is the case with undepleted silicon sensors – the total induced signal in the readout electrodes is a superposition of two contributions:

- **Prompt component:** the direct induction of current on the electrode from the movement of charged particles within the drift medium. In this contribution, the conductivity of the resistive elements is inconsequential, as they function as if they were perfect insulators.

- **Delayed component:** the current that comes from the time-dependent reaction of the resistive materials due to their finite conductivity.

The contribution from the former component is captured by the Ramo-Shockley theorem, which allows us to calculate the current induced by an externally impressed charge density on any grounded electrode by using a so-called weighting potential. Given detector architectures containing resistive elements, the weighting potential becomes dynamic

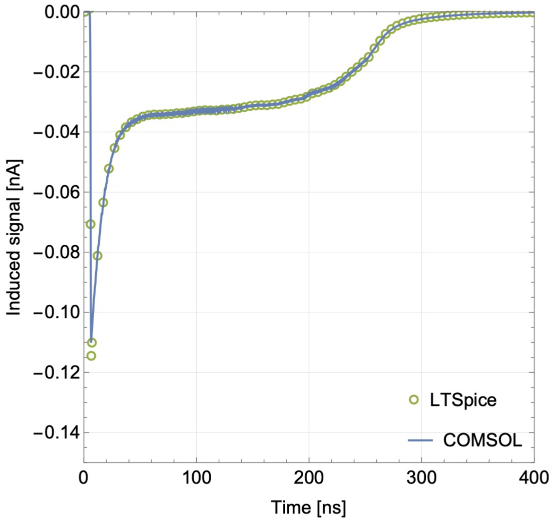

Figure 2.27: Comparison of the equivalent circuit description with the formulation using the time-dependent weighting potential, which includes the impact of the external impedance elements. The graph displays the induced current after passing through the 50 Ω resistor connected to the anode for both methods.

owing to the medium's finite conductivity. Since solutions are obtainable for only a limited group of primarily parallel plate detector geometries using analytical techniques, a numerical approach is needed to describe the broader range of resistive readout structures.

The finite element method approach facilitates the computation of time-dependent weighting potentials for virtually arbitrarily shaped resistive readout structures. This is achieved by removing all externally imposed charge densities, applying a rapid voltage ramp to the electrode under examination, and grounding all other electrodes. The integration of this method with microscopic modeling tools, such as Garfield++, enables the calculation of the response of complex detector geometries that include resistive media. Different techniques can be employed to expand the applicability of this approach to encompass a wider range of cases:

- Coordinate mapping allows for the accurate representation of the boundary conditions related to the resistive elements in large area systems.

- The application of junction conditions instead of the meshing of thin resistive layers reduces the number of elements needed during the solving of the electrodynamics system.

- The inclusion of the impact of an external linear impedance network on the signal formation within the weighting potential can be achieved either by directly incorporating the impedance elements within the model geometry or by interfacing the electrodynamics solver with a general-purpose circuit simulation program during the weighting potential solving step.

For a toy model representation of a 10×10 cm^2 resistive plane MicroMegas, it was shown that the first two points allowed for a reduction of the computation time by more than one order of magnitude. The overall numerical methodology shows good agreement when benchmarked against analytically derivable toy models.

An alternative approach for characterizing a readout structure that is AC-coupled with a thin resistive layer is presented by the two-dimensional Telegraph equation (or the Transmission line equation in the one-dimensional case). The solution to this equation approximates the diffusion of charge inside the resistive sheet by using a capacitance of the layer to the ground frame. While the Telegraph equation accurately captures the late-time behavior of the signal shape ($t > Rc$), it does not faithfully represent the initial part when compared to the discussed extended form of the Ramo-Shockley theorem.

Chapter 3

Noise in detectors containing resistive elements

The preceding chapter covered the principles of signal induction in detectors containing materials with finite conductivities. Besides playing a part in signal formation, rate-capability, and discharge protection, these materials contribute to the background noise generated by the system. Particle detectors are susceptible to various sources of noise coming from statistical fluctuation in the devices themselves and from the external circuits connected to them. These unavoidable fluctuations are superimposed on the induced signals and, therefore, pose a practical limit on the signal-to-noise ratio, which can reduce the measurement accuracy of the device. Given the growing complexity found in modern detector designs that incorporate resistive elements, there is a need for a comprehensive numerical technique to evaluate the impact of noise originating from resistive materials. This chapter introduces an approach based on the finite element method for computing the thermal noise power spectral density, relying on the self-impedances of the readout electrodes. The accuracy of this methodology is validated through comparison with analytically solvable systems, and its application to a resistive plane MicroMegas geometry will be discussed. The contents of this chapter are presented, for the most part, in our publication [84].

3.1 Noise Characterization

3.1.1 Noise power spectrum

Stochastic processes inside the material of the system – the random movement of the atoms and molecules of which the matter is comprised – generate a background of current or voltage fluctuations around a baseline value n_0. Given the situation depicted in Fig. 3.1 where a noise signal $n(t)$ is observed over a time interval $0 \leq t \leq T$, a useful quantity to quantify the noise is the variance of the fluctuations [6]

$$\sigma_n^2 = \overline{n^2} - \bar{n}^2 = \frac{1}{T}\int_0^T (n(t) - n_0)^2 \, dt \,, \tag{3.1.1}$$

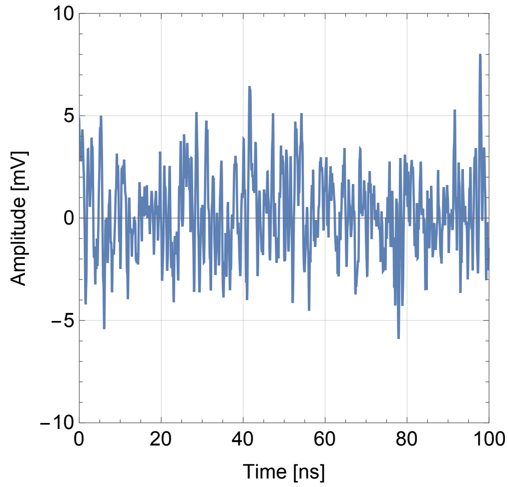

Figure 3.1: Noise sampled at a rate of 20 GHz at the output of the front-end circuit connected to a detector readout electrode.

where commonly the mean value n_0 is taken as zero. For most application it is beneficial to characterize the frequency content of the noise by going to the Fourier domain. In the case of a finite value of T, the signal can be characterized using a finite set of discrete frequencies $f_l = l/2\pi T$ for $l \in \mathbb{N}_0$. However, in the limit $T \to \infty$ the distribution of f_l becomes continues, allowing us to define a *noise power spectrum* $w(f)$. This quantity signifies the contribution to the variance of the noise given a frequency interval Δf. As a result, the variance of the noise is given by

$$\sigma_n^2 = \int_0^\infty w(f)\, df = \frac{1}{2\pi} \int_0^\infty w(\omega)\, d\omega\,, \tag{3.1.2}$$

with frequency $f = \omega/2\pi$ [6]. From the above equation we note that since $n(t)$ has the dimensions of a current or voltage such that $w(f)$ has the dimension A^2/Hz or V^2/Hz, respectively, which denotes a power density.

3.1.2 Johnson-Nyquist noise

In a resistive material free charge carriers exhibit random motion driven by their thermal kinetic energy. This effect was already contemplated by A. Einstein in 1906 where for a resistor in thermal equilibrium there would be a noise voltage signals between the resistors ends due to the Brownian movement of the free charges [85]. This phenomena was initially observed in 1928 by J. B. Johnson in [86], briefly after which the thermal noise power spectrum was derived by H. Nyquist [87]. In principle, external noise sources, such as those originating from the readout electronics, can be reduced to arbitrary levels. However, the *thermal noise* (or *Johnson-Nyquist noise*) associated with resistive elements in the detector is inherent to the device itself and therefore irreducible.

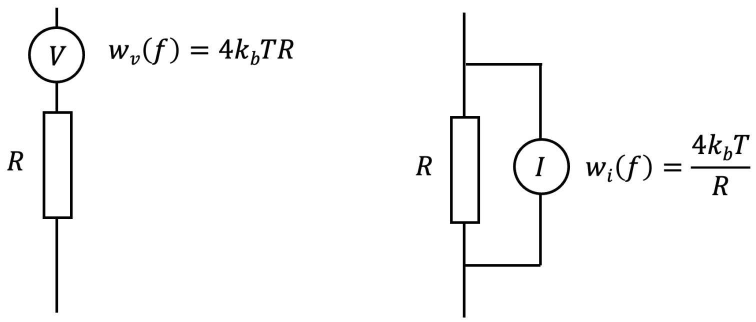

Figure 3.2: Noise generator produces a power spectrum $w_v(f)$ (left panel) or $w_i(f)$ (right pannel).

The original derivation of H. Nyquist of the resulting noise power spectrum is performed by considering two resistors connected to the endpoints of a lossless transmission line and assumes them to be in thermal equilibrium. The result follows from counting the vibrational modes of the electromagnetic waves after suddenly shorting both ends of the line and noting that each mode carries an average energy of

$$\epsilon(\omega) = \frac{\hbar\omega}{e^{\hbar\omega/k_bT} - 1}\,, \tag{3.1.3}$$

with $\hbar$ being the reduced Planck constant, T the absolute temperature and k_b the Boltzmann constant. In the classical limit, i.e., $\hbar\omega \ll k_bT$, the energy per mode can be taken as k_bT. As a result from the counting the derived noise power spectrum w_v (w_i) for the voltage (current) fluctuation is given by [87]

$$w_v(f) = 4k_bTR \tag{3.1.4a}$$

$$w_i(f) = \frac{4k_bT}{R}\,, \tag{3.1.4b}$$

which is known to generate *white noise*, i.e., the spectrum is frequency independent. As shown in see Fig. 3.2, the outcome can be represented as a voltage (current) source in series (parallel) with the an 'ideal' resistor R. If we have a general network with discrete resistive elements rather than a single resistor, and the total impedance seen by the terminals is $Z(f)$, then the noise power spectrum can be written as

$$w_v(f) = 4k_bT\,\mathrm{Re}[Z(f)] \tag{3.1.5a}$$

$$w_i(f) = 4k_bT\,\mathrm{Re}\left[\frac{1}{Z(f)}\right]\,, \tag{3.1.5b}$$

which again is formulated in term of a noise source connected in series or in parallel with the impedance network, as depicted in Fig. 3.3.

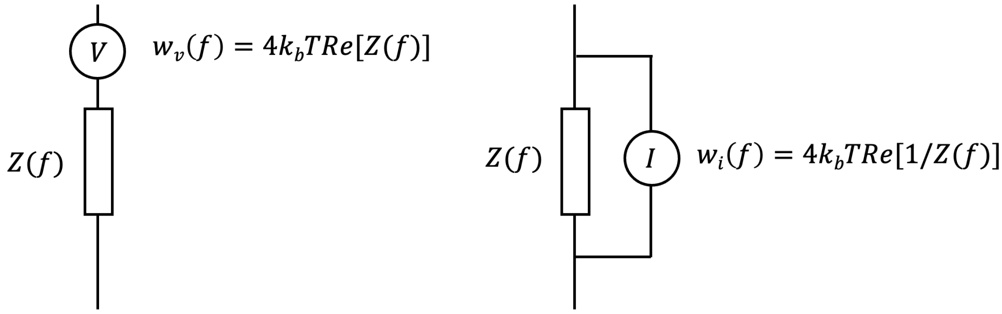

Figure 3.3: Noise characterised by the power spectrum of Eq. 3.1.5 is generated by the general passive network.

The above relations can be proven as follows: we consider the passive linear network, such as the one shown in Fig. 3.4, where N nodes are connected by $N(N+1)/2$ impedance elements $Z_{mn}(f)$ for $m, n \in \{1, 2, \ldots, N\}$. Without loss of generality, the $Z_{mn}(f)$ can be decomposed into a real resistance $R_{mn}(f)$ and a general inductive element $iF_{mn}(f)$, with $F_{mn}(f)$ being the so-called *reactance*. The power spectra of the noise currents i_{mn} from the resistors are

$$w_{mn}(f) = \frac{4k_bT}{R_{mn}(f)} = 4k_bT\,\mathrm{Re}\left[\frac{1}{Z_{mn}(f)}\right] . \tag{3.1.6}$$

For simplicity we will mostly truncate the frequency dependence for what follows. Following Sec. 2.2, the externally impressed currents i_n are related to the voltages u_n on node n by the impedance matrix $\hat{Z}$ following

$$u_n = \sum_{m=1}^{N} Z_{nm} i_m , \tag{3.1.7}$$

or the inverse

$$i_n = \sum_{m=1}^{N} Y_{nm} u_m , \tag{3.1.8}$$

where we have used the admittance matrix $\hat{Z} = \hat{Y}^{-1}$, the entries of which are related to the impedance elements by Eq. 2.2.24. Let node $n = 1$ be the point where we intend to measure the voltage noise fluctuations. When we introduce a current I_0 at this node, we find the related voltage $v_1 = Z_{11}I_0$ at this point, where we have the network impedance $Z = Z_{11} = R_{11} + iF_{11}$. Therefore we find a noise power spectrum of

$$w_v(f) = 4k_bTR_{11}(f) = 4k_bT\,\mathrm{Re}\left[Z_{11}(f)\right] . \tag{3.1.9}$$

If instead we place currents i_{mn} and $-i_{mn}$ on nodes m and n respectively, the voltage on node 1 would read $v_1 = (Z_{1m} - Z_{1n})i_{mn}$. Repeating this process by placing current

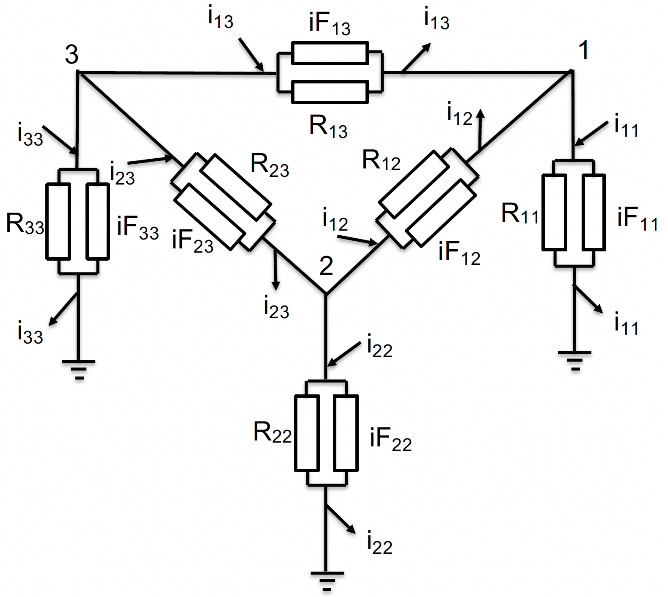

Figure 3.4: Schematic representation of a general passive network where with interconnected nodes using resistors R_{mn} and reactance elements F_{mn}.

sources on all the nodes, the outcome becomes

$$v_1 = \sum_{n=1}^{N} Z_{1n} i_{nn} + \sum_{n=1}^{N} \sum_{m \neq n=1}^{N} \left(Z_{1n} - Z_{1m}\right) i_{mn} \, . \tag{3.1.10}$$

As a next step, we can write the variance of voltage v_1 in terms of the variances w_{mn} of the currents

$$w_v = \sum_{n=1}^{N} |Z_{1n}|^2 w_{nn} + \sum_{n=1}^{N} \sum_{m \neq n=1}^{N} |Z_{1n} - Z_{1m}|^2 w_{mn} \tag{3.1.11}$$

$$= 4k_bT \sum_{n=1}^{N} \mathrm{Re}\left[\frac{1}{Z_{nn}}\right] |Z_{1n}|^2 + 4k_bT \sum_{n=1}^{N} \sum_{m \neq n=1}^{N} \mathrm{Re}\left[\frac{1}{Z_{mn}}\right] |Z_{1n} - Z_{1m}|^2 \, , \tag{3.1.12}$$

which is the power spectrum as seen from node 1. Inserting the definition for Y_{mn} we can write the expression as

$$\sum_{n=1}^{N} \frac{1}{Z_{nn}} |Z_{n1}|^2 + \sum_{n=1}^{N} \sum_{m \neq n=1}^{N} \frac{1}{Z_{mn}} \left(|Z_{n1}|^2 - Z_{m1} Z_{n1}^*\right) = Z_{11}^* \, , \tag{3.1.13}$$

in which we employ the notation * to denote complex conjugation. Here we have used the identity

$$\sum_{m=1}^{N} Y_{nm} Z_{mk} = \delta_{nk} \, . \tag{3.1.14}$$

After additional expansion, Eq. (3.1.9) reduces to Eq. (3.1.11). Once more Nyquist offers an elegant derivation of this result by considering a resistor connected to one end of a lossless transmission line while a complex impedance $Z(f) = R(f) + iF(f)$ is connected to the other end and assuming thermal equilibrium. From this Eq. 3.1.5 directly follows.

These results identify the complex impedance $Z(f)$ as seen from the input terminal of the readout electronics as the key quantity defining the noise power spectrum in structures with distributed passive materials. If our detector shows a linear response to a signal applied at a terminal, it indicates that a complex impedance can fully capture its behavior. Hence, to find the thermal noise from a general detector, we have to know its complex impedance. We will see below that this quantity can be determined either through theoretical analysis or measurement. While analytical calculations suffice for some simplified geometries, numerical simulation programs are essential for general detector geometries.

3.2 Numerical determination of noise power spectra

This section presents a methodology for computing the noise power spectrum for arbitrary detector structures. The numerical approach is subsequently validated by comparing it against example resistive structures with closed-form analytical solutions.

3.2.1 Description of numerical methodology

Let us consider the system depicted in Fig. 3.5, where N ideally conducting electrodes are embedded in a linear anisotropic medium characterised by its 3×3 frequency dependent permittivity matrix $\hat{\varepsilon}$ and conductivity matrix $\hat{\sigma}$. In analogy to the arguments presented in Sec. 2.2, the impedance matrix $\hat{Z}$ relates the applied voltages and corresponding currents between electrodes m, $n \in \{0, 1, \ldots, N\}$. To obtain the self-impedance $Z_{nn}(\omega)$ as seen from the terminal of electrode n, we impose the following Dirichlet boundary conditions to the system:

$$V_m := \phi_n(\mathbf{x}, \omega)|_{\mathbf{x} \in S_m} = V \delta_{mn} \, , \tag{3.2.1}$$

where all electrodes other than the one under study are grounded. If we work under the premise that inductive effects are negligible, Maxwell's equations (2.1.2) in the Fourier domain reduce to

$$\nabla \cdot \mathbf{j}_n(\mathbf{x}, \omega) = -i\omega\rho_n(\mathbf{x}, \omega) \tag{3.2.2a}$$

$$\mathbf{j}_n(\mathbf{x}, \omega) = (\hat{\sigma}(\mathbf{x}, \omega) + i\omega\hat{\varepsilon}(\mathbf{x}, \omega)) \cdot \mathbf{E}_n(\mathbf{x}, \omega) + \mathbf{j}_e(\mathbf{x}, \omega) \tag{3.2.2b}$$

$$\mathbf{E}_n(\mathbf{x}, \omega) = -\nabla\phi_n(\mathbf{x}, \omega) \tag{3.2.2c}$$

where the subscript n denotes the solving of the system for electrode n. This set of equations can be solved in the frequency domain using FEM toolkits. Consequently, we obtain the solution for the current density $\mathbf{j}_n(\mathbf{x}, \omega)$ of the problem, allowing us to

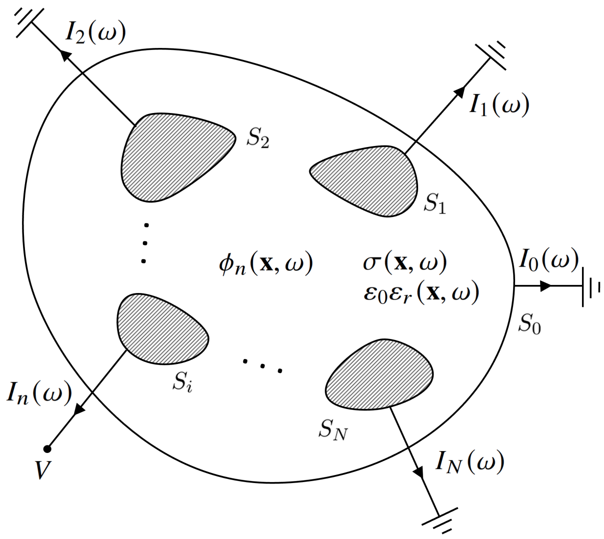

Figure 3.5: Illustration of the experimental and numerical strategies for obtaining the self-impedance Z_{nn} of electrode n. The frequency-dependent currents $I_m(\omega)$ flow through the surfaces S_m of the electrodes as a potential V is applied to terminal n.

subsequently calculate the current $I_n(\omega)$ flowing through the surface S_n of electrode n out of the system. Given that $I(\omega) = V(\omega)/Z(\omega)$ we have

$$Z_{nn}(\omega) = \frac{V_n}{\int_{S_n} \hat{\mathbf{n}} \cdot \mathbf{j}_n(\mathbf{x},\omega)\, dS}\,, \tag{3.2.3}$$

where the unit vector $\hat{\mathbf{n}}$ is normal to the surface of electrode n. Note that the same techniques discussed in Sec. 2.5.2 can be applied to perform computations for large area structures. Alternatively, given that the content of the admittance matrix is captured by the dynamic weighting potential, the self-impedance can calculated following Eq. 2.2.23, where in general we would determine the weighting potential numerically.

In practice, we can experimentally obtain $Z_{nn}(f)$ by placing a wire between electrode n and the voltage source with which we apply a potential V, as shown in Fig. 3.5. With this experimental setup we can perform a frequency-sweep analysis of the current $I_n(f)$ flowing through the wire. This strategy can be reflected in the numerical simulations by the representation of the connecting wire. This can take two forms:

- The wire can be represented as a physical entity within the system's geometry.
- By interfacing the EM solver with a discrete circuit solver module the wire can be treated as a virtual component. Using the DC voltage source of the module, the potential V can be applied to terminal n resulting in the computation of $I_n(\omega)$ along the connection. As described in Sec. 2.5.4, this approach allows a the integration of a general external circuit into the calculation, in a straight forward manner.

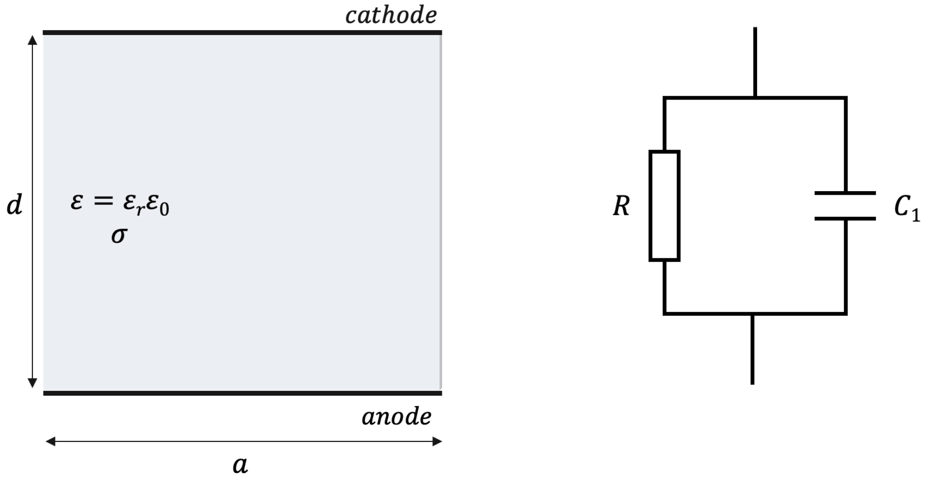

Figure 3.6: **Left:** Diagrammatic depictions of the example comprised of a capacitor containing a homogeneous material with finite conductivity. **Right:** Equivalent circuit diagrams of the system.

For both cases, the current $I_n(\omega)$ is calculated through the integral of $\mathbf{j}_n(\mathbf{x}, \omega)$ over S_n. This makes it sufficient to directly apply the potential to the electrode without loss of generality. Dedicated FEM tools, such as the electric currents module in the COMSOL® streamline this process by providing the self-impedance value for the specific electrode directly after solving the system.

3.2.2 Toy model examples

To assess the accuracy of our numerical approach, we evaluate its ability to determine the impedance for the electrodes of two example geometries with exact lumped circuit representations. For these we compare the numerical results with the closed-form analytical representation of the self-impedance of the anode. Taken from Sec. 2.5.4 the two systems we will study are:

- An $a \times a$ wide capacitor geometry with a gap size b containing a resistive material between the capacitor plates that is characterised by its volume conductivity σ and relative permittivity ε_r (see Fig. 3.6).
- The single-gap RPC structure of Sec. 2.3.3, where the gas gap of size g is separated from the anode by an $a \times a$ wide resistive plate of thickness b, volume conductivity σ and relative permittivity ε_r (see Fig. 3.7).

Following Eq. (2.2.23), one can show that both can be expressed in terms of a circuit of resistors and capacitors [54].

Since the system in Fig. 3.6 can be treated as the limit case of the RPC geometry, we will start with the solution of the circuit shown in Fig. 3.7 (right). Here we find that

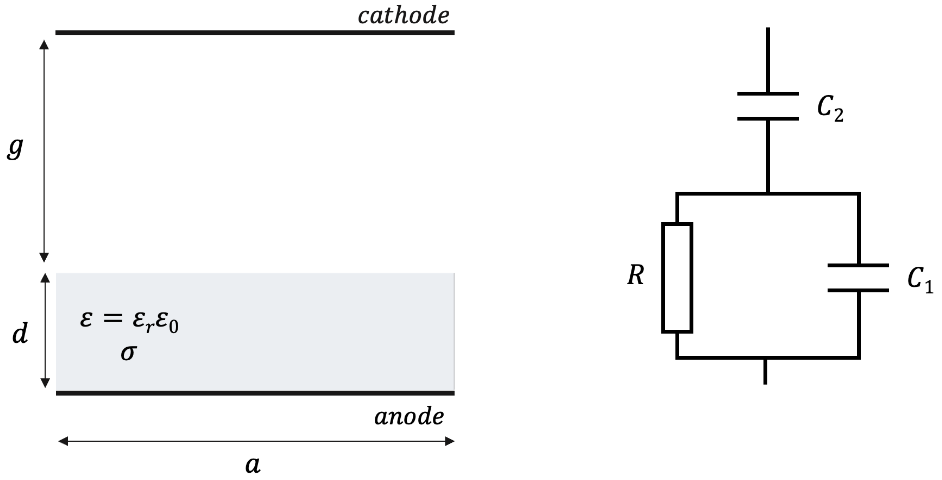

Figure 3.7: **Left:** Schematic representation of of the example system where a resistive material is situated beneath a gas gap between two metal plates that run parallel to each other. **Right:** The equivalent circuit representation of the detector geometry.

the configuration for the RPC corresponds to a series coupling of a capacitor C_2 with a parallel circuit composed of another capacitor C_1 and a resistor R. Denoting the anode as electrode 1, its self-impedance reads

$$Z_{11}(f) = \frac{1}{2\pi i C_2 f} + \frac{R}{2\pi i R C_1 f + 1}\,, \tag{3.2.4}$$

where the relation of the lumped parameters with the dimensions and properties of the medium are given in Eq. (2.5.8). In Fig. 3.8 (left) the self-impedance of the anode in the capacitor structure, i.e., $\lim_{g\to 0} Z_{11}(f)$, is shown superimposed on the corresponding numerically acquired values using the methodology outlined in the preceding subsection. For this, maximum absolute difference between the numerical and analytical result is $7\cdot 10^{-4}\%$. The results for the RPC ($g > 0$) is depicted in Fig. 3.8 (right), where both the analytical and FEM solutions are shown. For this system we find that the FEM solutions are within 1.40% agreement with the analytical results.

3.2.3 Self-admittance of a pad electrode

Following the discussion in Sec. 2.4, it becomes evident that the parallel plate readout architecture shown in Fig. 2.14 (right) − which is composed of a resistive layer AC-coupled to the embedded readout electrodes − lacks an exact lumped element circuit representation. If we consider the cathode plane as an approximation of a micro-mesh, this geometry can be viewed as a toy model for the amplification and readout region of a resistive plane MicroMegas. The readout plane can be segmented into perfectly adjacent square pads of size $w \times w$, positioned at a distance d below the infinitesimally thin resistive layer located in the xy-plane. To reflect the finite size of the active area,

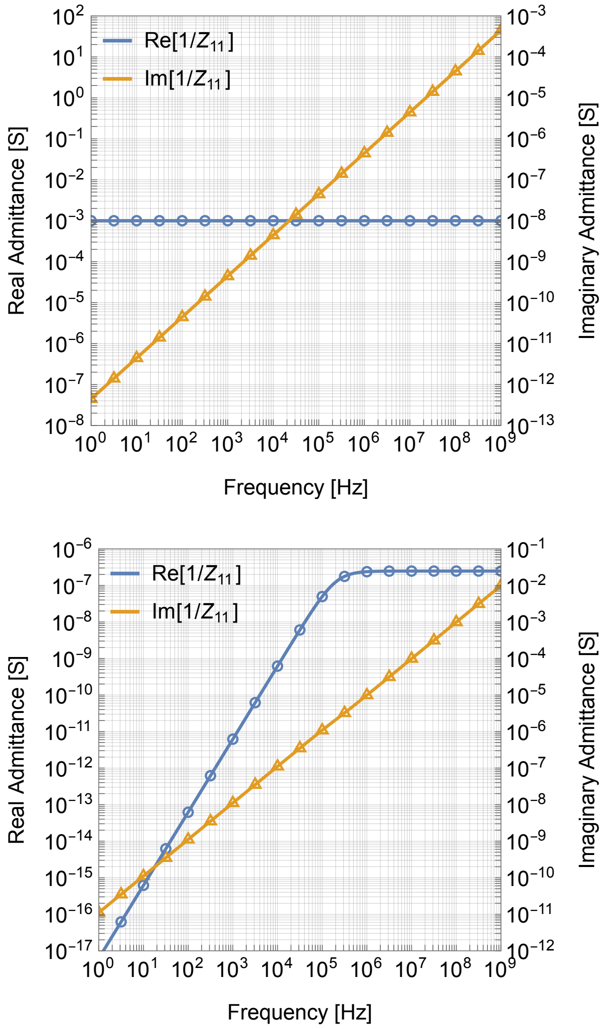

Figure 3.8: A comparison between the numerical results (solid line) and analytical solutions of Eq. (3.2.4) (markers). **Top:** Real and imaginary parts of the inverse impedance Z_{11}^{-1} for the anode of a bulk resistive material placed between two metal electrodes with dimensions $a = d = 1$ mm, conductivity $\sigma = 1$ S, and relative permittivity $\varepsilon_r = 8$. **Bottom:** Admittance of the anode for the RPC geometry with parameters $g = d = a = 1$ mm, conductivity $\sigma = 1$ S, and relative permittivity $\varepsilon_r = 8$.

we impose the boundary conditions that ϕ_n vanishes at the edges of the resistive layer, i.e., at $(x, y) = (\pm a/2, y)$ and $(x, y) = (x, \pm b/2)$, grounding all electrodes other than the pad under study, and placing insulating boundary conditions at the remaining edges. To cope with the large size of $a = b = 10$ cm, we used both the coordinate mapping and junction condition techniques of Sec. 2.5.2. In Fig 3.9 the self-impedance on the pad positioned at the center of the active area is shown for different values for the surface

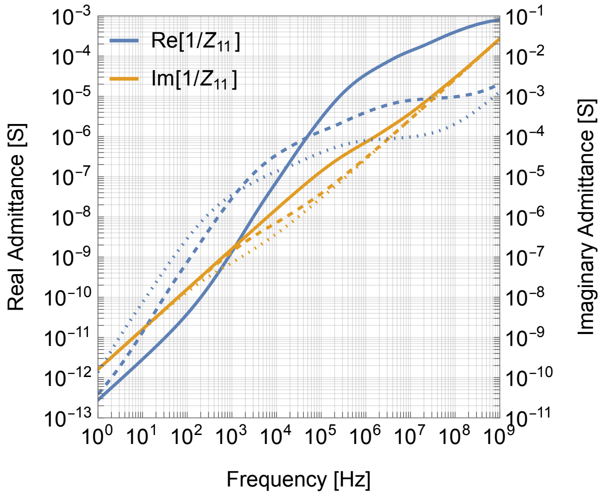

Figure 3.9: Real and imaginary part of the admittance of the central pad electrode for $w = 8$ mm, $a = b = 10$ cm, $g = 128$ µm, and $d = 80$ µm evaluated for the different surface resistivities: 100 kΩ/□ (full line), 10 MΩ/□ (dashed line), and 100 MΩ/□ (dotted line).

resistivities R. Here, we find that the real part of the inverse self-impedance is sensitive to the value of R and that this dependence goes in the opposite direction for high and low frequencies.

3.2.4 Noise after the amplifier

A useful quantity to characterise the noise behaviour of different amplifiers is the *Equivalent Noise Charge* (ENC). This number corresponds to the amount of electrical charge that, when introduced into the detector, produces a signal equal in amplitude than the *Root Mean Square* (RMS) of the amplifier output noise [6]. By using the numerically obtained noise power spectrum at the input terminal of an amplifier connected to the pad electrode, we can establish the contribution of ENC originating from thermal noise. Let the response of the amplifier be by given the transfer function $gf(i\omega)$ with gain g, then the current noise power spectrum transforms

$$w_i(\omega) \to w_i(\omega) g^2 |f(i\omega)|^2 \,, \tag{3.2.5}$$

at the output terminal of the front-end. The resulting ENC can then be calculated through the variance of this distribution

$$\mathrm{ENC}^2 = \left(\frac{\sigma_v}{g}\right)^2 = \frac{2k_b T}{\pi} \int_0^\infty Re\left[\frac{1}{Z_{11}(\omega)}\right] |f(i\omega)|^2 d\omega \,. \tag{3.2.6}$$

As we are now in a position to calculate the amplifier output noise, we just need an expression for $f(i\omega)$. As an example, let us take the Fourier transform of the n'th order

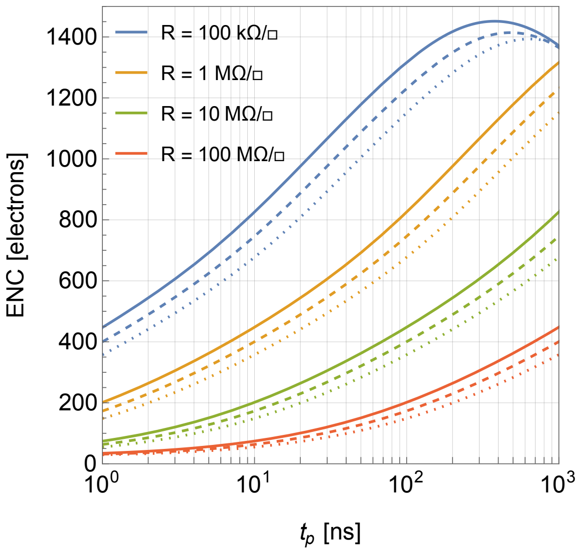

Figure 3.10: Thermal noise contribution to the Equivalent noise charge (ENC) at the output of an n'th order unipolar shaper connected to the central pad electrode as a function of the peaking time. Here $w = 8$ mm, $a = b = 10$ cm, $g = 128$ µm, and $d = 80$ µm for various shaper orders: $n = 1$ (solid lines), $n = 2$ (dashed lines), and $n = 4$ (dotted lines).

unipolar shaper of Eq. 2.3.43, which reads

$$|f(i\omega)|^2 = \frac{(n!e^n t_p)^2}{\left[n^2 + (\omega t_p)^2\right]^{n+1}}, \qquad n \in \mathbb{N}_0 . \tag{3.2.7}$$

Plugging this into Eq. (3.2.6) and performing the integration numerically we can evaluate the ENC for different shaping orders and peaking times. Fig. 3.10 shows the thermal noise impact on the ENC at the output stage of the amplifier. As expected, the corresponding ENC rapidly decreases as the surface resistivity increases. Indeed, the limit case of $R \to 0$ would correspond to a purely insulating medium and therefore free from any thermal noise.

3.3 Summary

Materials with a finite conductivity contribute to the current and voltage fluctuations that form the background on which the induced signals are superimposed. Coming from the random thermal motion of the free charges in these materials, it represents an irreducible noise source inherent to the detector design. To quantify the magnitude of this contribution the self-impedance needs to be obtained as the quantity describing the thermal noise. We proposed a FEM approach to obtain the thermal noise power spectrum for arbitrary detector geometries by performing a frequency-sweep of the electrode under study. After validating the approach against toy model examples, it was subsequently employed to compute the ENC at the output of an amplifier coming from the thermal noise of a resistive layer in a resistive plane MicroMegas design.

Part II

Detectors dominated by prompt signal induction

Chapter 4

Ambiguity-free coordinate readout

As an elementary case of a detector structure where the prompt component of the induced signal is predominant, we will consider a non-resistive readout structure in a Gas Electron Multiplier device (GEM) [8]. In this detector sub-mm position determination is achieved by collecting the amplified electron charge on sets of narrow-pitch anode strips and performing a CoG calculation on the recorded charge distributions. Since this geometry is effectively composed of perfectly insulating and ideally conducting materials, the basic form of the Ramo-Shockley theorem applies, as given by Eq. (2.2.22). Starting from a brief discussion on the spatial resolution using a Q^r weighted CoG method for a one-dimensional strip readout, we will continue with the description of the development of a three-coordinate projective strip readout aimed at resolving ambiguities in high event rate applications. The static weighting potential of the strip electrodes was computed and, in conjunction with Garfield++, used to estimate the charge sharing between the three coordinate planes, informing the design of the first prototype. After production, the device was used to verify these results experimentally. This shall serve as an illustrative instance of the utility of this firmly established framework, a tool that we aspire to broaden in scope with the inclusion of resistive structures.

4.1 Position resolution of a one-dimensional readout

Structured electrodes can be found in particle detectors for the purpose of position determination of the signal in the readout plane of the detector. The most elementary hit reconstruction only requires a signal above a certain threshold on one electrode channel, resulting in a binary outcome of either a hit or a miss. As will become apparent below, it can be more beneficial to sample the collected charge distribution using multiple electrodes. In this section, we will delve into the spatial resolution of a one-dimensional anode, examining how it varies with factors such as the strip's width, the spatial distribution of the charge cloud collected on the anode, and the signal-to-noise ratio (S/N). The ideas presented here are based of the work performed by P. Fischer [88, 2], which will be extended with a discussion on the Q^r weighting used in the Centre-of-Gravity method.

4.1.1 Best possible spatial resolution using a strip readout

The preceding chapter detailed that the signal observed in the electrode channels results from the induction of current due to an externally impressed charge density, such as an electron cloud, propagating through the drift medium within the detector. Once the signal is integrated over its entire duration, it yields a measurement of the total charge accumulated on that electrode, which by extension provides a sampling of the charge cloud distribution collected on the anode. The spatial extent of this distribution arises from a combination of factors, including the primary ionization pattern, field configuration, and Gaussian broadening of the charge cloud caused by lateral diffusion. The latter is a consequence of the random nature of the scattering process and has a standard deviation of $\sigma = D_T\sqrt{d}$ over a distance d with a gas-dependent transversal diffusion constant D_T [39]. Electrodes that intercept a portion of this distribution will generate a discernible 'signal' when integrated if it is bigger then a predefined *Threshold Level* (THL). First we will examine the ideal scenario of a noiseless and perfectly neighboring electrode structure, the outcome of which can be extended to pad electrodes.

Let $\sigma_s(x, y)$ denote the net surface charge distribution on the anode resulting from an externally impressed charge distribution, then the total charge induced on the surface S_k of electrode $k \in \mathbb{Z}$ is given by

$$Q_k = \int_{S_k} \sigma_s(x, y)\, dS\,. \tag{4.1.1}$$

For now we will limit ourselves to the case of perfectly adjacent readout strips with width and pitch w_x. To estimate the hit position x_0 of the incident particle a multitude of algebraic methods can be used [89]. A popular choice is the charge CoG method

$$x_r = \frac{\sum_k k w_x Q_k^r}{\sum_k Q_k^r}\,, \tag{4.1.2}$$

using weighting of the induced charge by an exponent $r \in \mathbb{R}_0^+$. Towards the conclusion of this section, we will revisit the general case for r, but for the subsequent discussions, we will consider $r = 1$, which corresponds to the more conventional CoG form. By employing a Fourier series the equation above can be reformulated as follows

$$\begin{aligned} x_r &= \frac{w_x}{2} - \frac{w_x}{2} \sum_{m=-\infty}^{\infty} \mathcal{Q}\left(\frac{m}{w_x}\right) \frac{\sin\left(m\pi - \frac{2\pi m x_0}{w_x}\right)}{m\pi} \\ &= x_0 - \frac{w_x}{\pi} \sum_{m=1}^{\infty} \mathcal{Q}\left(\frac{m}{w_x}\right) \frac{\sin\left(m\pi - \frac{2\pi m x_0}{w_x}\right)}{m} \end{aligned} \tag{4.1.3}$$

where $\mathcal{Q}$ is the charge distribution in Fourier space and we normalize such that $\sum_k Q_k = 1$ [88]. The residual is thus given by

$$x_\varepsilon := x_r - x_0 = \frac{w_x}{\pi} \sum_{m=1}^{\infty} \frac{(-1)^m}{m} \mathcal{Q}\left(\frac{m}{w_x}\right) \sin\left(\frac{2\pi m x_0}{w_x}\right)\,. \tag{4.1.4}$$

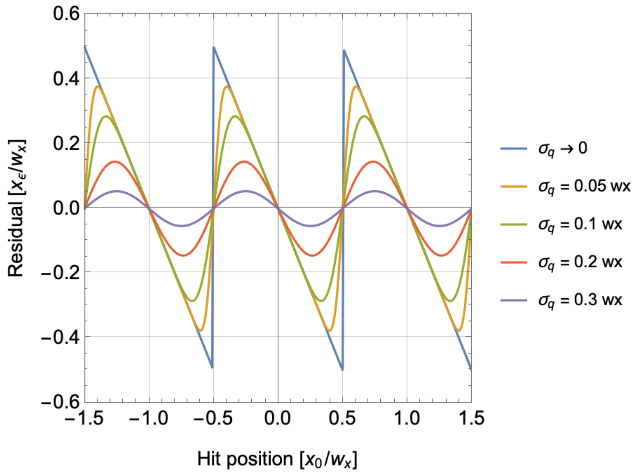

Figure 4.1: Comparison of residual distribution as a function of the hit position for different charge distribution widths.

Taking the variance of this error gives us the relation for the spatial resolution σ_{res} of the strip readout [88]

$$\begin{aligned} \sigma_{\text{res}}^2 &= \frac{1}{w_x} \int_{-w_x/2}^{w_x/2} x_\varepsilon^2 (x)\ dx \\ &= \frac{w_x^2}{2\pi^2} \sum_{m=1}^{\infty} \frac{1}{m^2} \mathcal{Q}^2 \left(\frac{m}{w_x}\right) . \end{aligned} \tag{4.1.5}$$

In case where the width of the total induced charge distribution is negligible compared to the pitch of the strip electrodes, i.e., a binary readout, we can take the limit $\sigma_s(x,y) \to \delta(x)\delta(y)$. As a result the spatial resolution updates to

$$\left(\frac{\sigma_{\text{res}}}{w_x}\right)^2 = \frac{1}{2\pi^2} \sum_{m=1}^{\infty} \frac{1}{m^2} = \frac{1}{12} . \tag{4.1.6}$$

This limit case applies to detectors with low-granularity readouts where the charge collection is confined to a single electrode. One such example is the CMS GEMs [90] where a strip pitch of 455 μrad is used resulting in $\sigma_{\text{res}} = 131$ μrad, close to the measured resolution of 137 ± 1 μrad [91].

Given that the transversal diffusion of the charge cloud in the gas volume is given by a Gaussian distribution with a standard deviation σ_q, the Fourier transform of the charge distribution can be written as

$$\mathcal{Q}_{\text{g}}(k) = \exp\left(-2\pi^2 k^2 \sigma_q^2\right) . \tag{4.1.7}$$

Substituting this into Eq. (4.1.4) yields the residuals depicted in Fig. 4.1, which vary with the standard deviation of the distribution. This method possesses inherent limitations stemming from structured electrodes and threshold-based effects, resulting in a periodic pattern in the reconstructed position – an observation first made with MWPC [92]. As the distribution widens, information regarding the deposited distribution becomes increasingly shared with neighboring channels, leading to enhanced reconstruction capabilities. This trend continues until, for $\sigma_q \to \infty$, we observe $x_\varepsilon \to 0$. However, in practice, we must contend with a noise background originating from various sources and limited sensitivities of the readout system, preventing us from reaching this ideal state. Plugging Eq. (4.1.7) into Eq. (4.1.5) provides us with the expression for the spatial resolution of a strip-segmented readout

$$\left(\frac{\sigma_{\text{res}}}{w_x}\right)^2 = \frac{1}{2\pi^2}\sum_{m=1}^{\infty}\frac{\exp\left(-\frac{4m^2\pi^2\sigma_q^2}{w_x^2}\right)}{m^2}\,, \tag{4.1.8}$$

As a result, the spatial resolution is dependent on the width of the charge distribution on the anode relative to the width of the strips. In the context of this noiseless example, it can be regarded as the lower limit of achievable resolution using the CoG method. Fig. 4.2 illustrates the behavior of this relationship, showing that we achieve nearly perfect reconstruction when σ_q exceeds half of the strip width.

If we instead consider the electron-ion pairs clusters in a drift gap of size g,formed along the trajectory of a relativistic charge moving perpendicular to the readout plane, each electron will cover variable distances $0 \le d \le g$ to reach the anode, undergoing diffusion along the way. Without loss of generality, we can take a uniform distribution for the initial heights in the gap. If we impose a constant D_T over the electron's trajectories the distribution on the anode is then given by

$$\sigma_s(x) = \frac{\sqrt{\pi}|x|\left[\operatorname{erf}\left(\frac{|x|}{2\sigma_q}\right)-1\right]+2\sigma_q e^{-\frac{x^2}{4\sigma_q^2}}}{2\sqrt{\pi}\sigma_q^2}\,, \tag{4.1.9}$$

which in Fourier space reads

$$\mathcal{Q}_{\text{track}}(k) = \frac{1-e^{-4\pi^2k^2\sigma_q^2}}{4\pi^2k^2\sigma_q^2}\,. \tag{4.1.10}$$

Here, the variance is given by $\sigma_q^2 := D_T^2 g/2$, which is related to the maximal diffusion from the electrons created at the top of the drift gap. In Fig. 4.2, the resulting spatial resolution is shown as a function of the pitch of the readout strips. Since the distribution in Eq. (4.1.9) is more peaked at the center compared to the Gaussian distribution, an equivalent improvement to the spatial resolution would require a denser readout structure.

4.1.2 Spatial resolution and noise

Achieving the optimal resolution with a strip readout necessitates a careful alignment of the readout pitch with the width of the charge distribution, especially in the presence

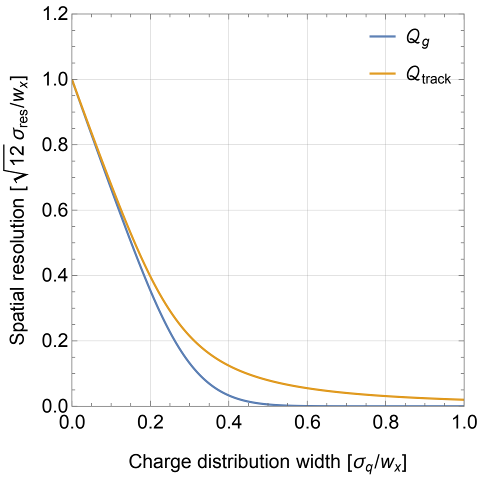

Figure 4.2: Comparison of residual distribution as a function of the hit position for different charge distribution widths.

of noise on the readout channels. The S/N establishes a lower limit on the achievable resolution, which becomes dominant when $\sigma_q \gg w_x/2$. In such cases, the division of the total charge over numerous channels results in small fractions per electrode, ultimately impacting the reconstruction capability due to the dominating noise contributions. We employ a simple Monte Carlo simulation to estimate the spatial resolution for different S/Ns.

Consider a noise impulse, denoted as n_k, occurring on electrode k so that the measured charge is given by $Q_k + n_k$. The noise distribution is characterized by its variance of the common mode fluctuations $< n_k^2 >= \sigma_n^2$, with a vanishing average value $< n_k >= 0$. We will disregard correlated noise sources, commonly referred to as *common mode noise*, such as those produced by electromagnetic interference, and assume that the noise hits in each channel are statistically uncorrelated, i.e., $< n_k n_l >= \delta_{kl}\sigma_q^2$. We will express S/N as the ratio between the total charge $\sum_k Q_k = 1$, and the standard deviation of the noise fluctuations σ_n. In our specific example, we assume that the noise distribution in each channel follows a normal distribution with the same standard deviation, σ_n. Furthermore, this distribution is normalized with respect to the total amount of collected charge, i.e., $\sum_k Q_k$. A uniform THL is employed across all readout channels, usually determined based on the noise level. This threshold is designed such that a channel is only read out when the charge fraction exceeds its predefined value, thereby filtering the noise hits. Sampling the initial cluster position from a uniform distribution over w_x the spatial resolution as a function of the strip pitch, charge distribution width, and S/N is depicted in Fig. 4.3 for three different acceptance thresholds for the signals. As expected, the best resolutions tend to be achieved with lower values of S/N. When facing elevated noise levels, however, raising the THL can be beneficial up to a certain value, beyond which it severely limits the cluster size of the event, i.e., the number of neighboring channels that cross over THL.

The experimental constraints on the gas choice and electric field configurations can limit the freedom of tuning the width of the collected charge distribution. In addition, sampling the signal in a densely packed readout structure requires many readout channels to be read out. As previously discussed in Sec. 2.3.4, another approach involves incorporating an extremely thin layer of material with finite conductivity, allowing for signal sharing among neighboring channels even with relatively large pitches of $\mathcal{O}(1-10)$ mm. This approach offers increased degrees of freedom for achieving optimal spatial resolution. However, the bipolar signal results in a net charge of zero after integration, requiring the use of peak signal amplitudes instead. This, in turn, leads to a non-Gaussian distribution of charge information among adjacent channels, necessitating additional care in determining the optimal spatial resolution in such cases.

4.1.3 Weighted Centre-of-Gravity method

We revisit the charge-weighted version of the CoG method as presented in Eq. (4.1.2). In this approach, the value of $r = 2$ is utilized to enhance the precision of position reconstruction in strip-based readouts, as outlined in Ref. [93, 94]. The previously explained Monte Carlo simulation can be iterated for varying values of $r > 1$. This is done to determine the optimal value of r as a function of the charge cloud width with respect to the strip pitch.

In Fig. 4.4 (left) a map of the spatial resolution is displayed for various charge weighting orders. Although there appears to be an improvement in position reconstruction for values of $r > 1$, this improvement is constrained to values of $r < 3$, beyond which the resolution begins to deteriorate again. Furthermore, when the spatial extent of the charge cloud is relatively small compared to w_x, a higher weighting order will bias the position reconstruction towards the center of the strip containing the bulk of the collected charge. In such cases, the more conventional CoG method would be preferable since it more accurately takes into account the small corrections made by the charge input of the neighboring channels. The position resolution for the optimal σ_q/w_x ratio is presented in Fig. 4.4 (right) as a function of r. In this plot, we can observe that the most significant improvements are achieved for higher S/N values as long as the THL does not excessively limit the cluster size.

4.2 Induced signal on a two-dimensional strip readout

In the preceding section, we discussed the position resolution of a strip readout. In cases where a sub-mm two-dimensional localization is needed, there are several approaches available. One option is to employ a second detector that is rotated and positioned behind the first one. Alternatively, a two-dimensional patterned readout electrode, such as

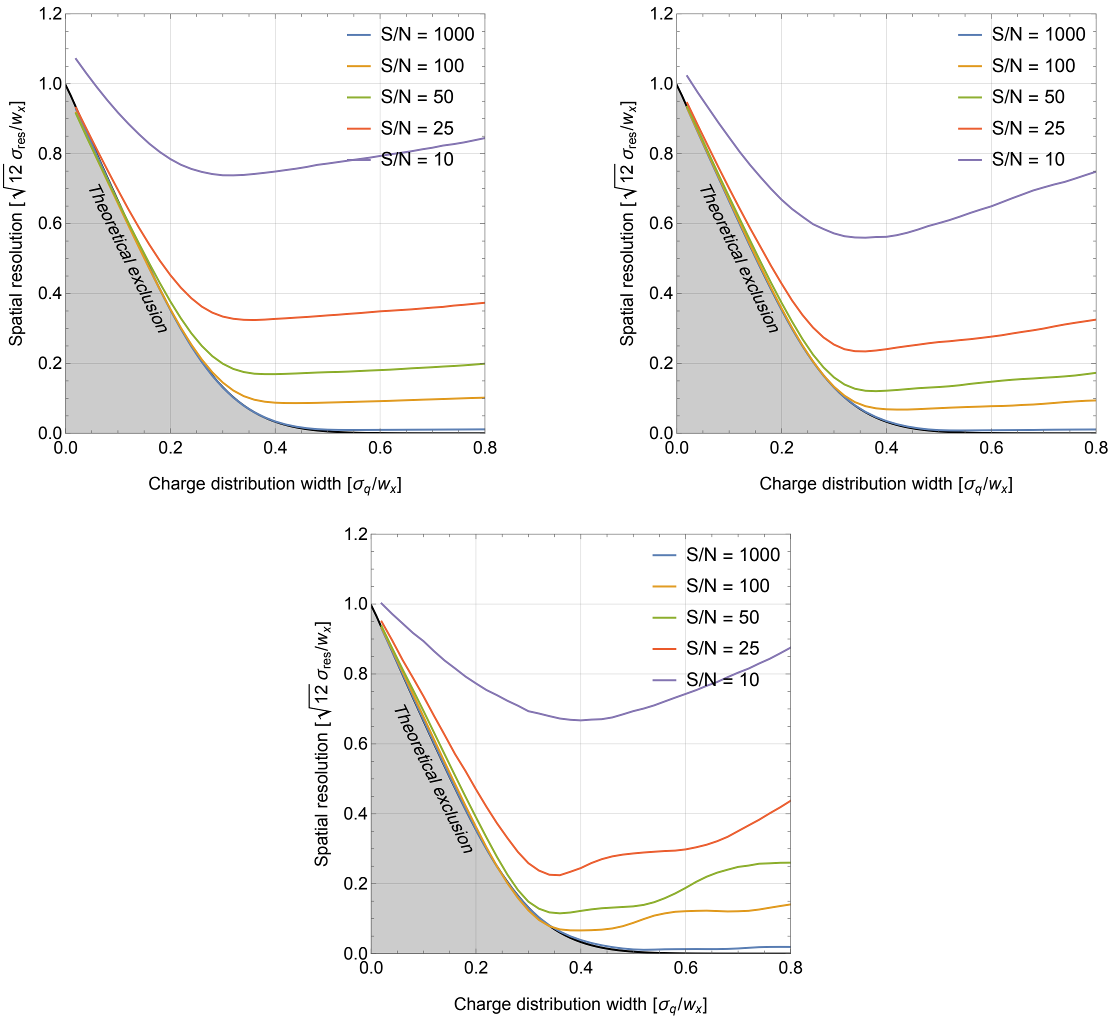

Figure 4.3: The spatial resolution is assessed in relation to the charge cloud width with respect to the pitch of a strip readout perfectly tiling the anode plane. This evaluation has been conducted using the signal on nine adjacent strips for various Signal-to-Noise ratios and channel threshold levels set at σ_n (top left), $2\sigma_n$ (top right), and $3\sigma_n$ (bottom).

pixels that have a pitch of hundreds of micrometres, can be utilized. Another approach, as illustrated in Fig. 4.5, involves using two perpendicular sets of narrow readout strips, named X and Y, positioned on top of each other and separated by insulating ridges, typically made of Kapton®. This arrangement defines two readout coordinate planes, where the collected charge is shared between them [95]. This projective coordinate readout scheme has been adopted for most GEM-based experimental setups; a comprehensive summary of which can be found in [96]. While this setup offers the advantage of requiring fewer readout channels compared to an equivalently performing pad readout structure,

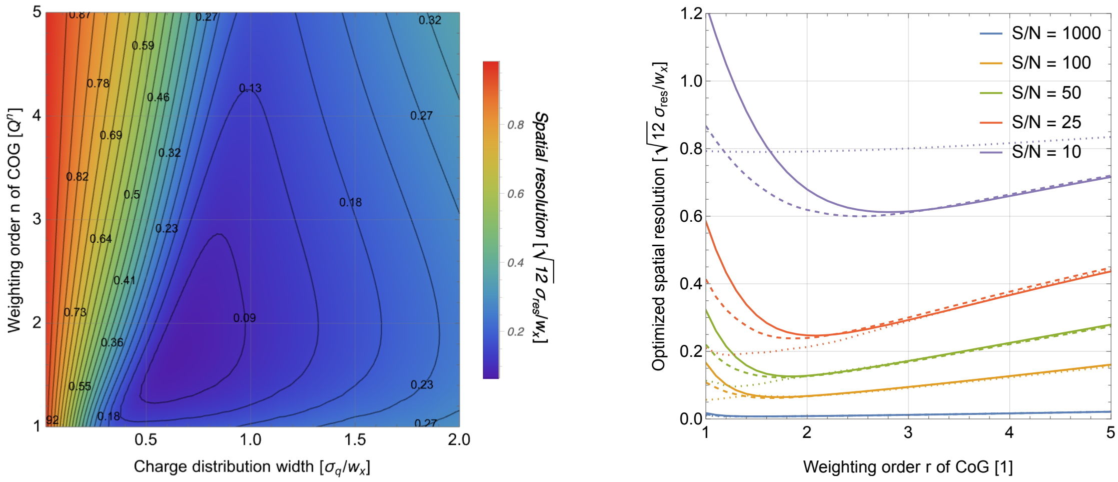

Figure 4.4: **Left:** Spatial resolution using the signal on neigh adjacent strips for a scan of the CoG weighting orders and the relative charge distribution width. Here THL $= \sigma_n$ and S/N $= 100$. **Right:** The optimal spatial resolution that can be reached using different CoG weighting orders, signal-to-noise ratios and THL of σ_n (full line), $2\sigma_n$ (dashed line), or $3\sigma_n$ (dotted line).

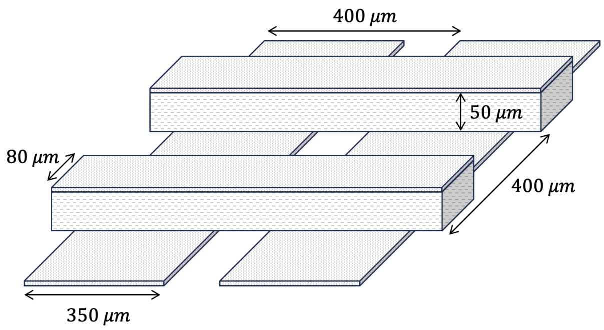

Figure 4.5: Illustration of the two-dimensional strip readout used in the induction gap a detector using a GEM foil as the amplification stage.

it may encounter limitations when operating in environments with high event rates and high particle multiplicities, as we will explore in the next section.

We will examine the induced signal of the readout structure depicted in Fig. 4.5, which is positioned within the 2 mm induction gap of a GEM detector. A cross-section image of a so-called standard GEM geometry is given in Fig. 4.6 with dimensions specified in Tab. 4.1. The electric field resulting from the potential difference between the cathode, top and bottom of the GEM foil, and anode is given in Fig. 4.7.

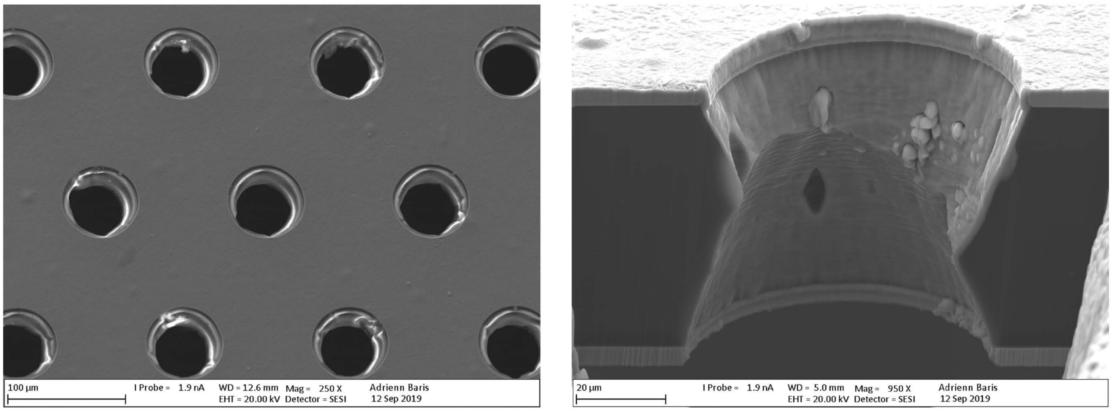

Figure 4.6: Top and cross-section image of a standard GEM foil taken with a Scanning Electron Microscope (SEG) [97]. Here the double mask technique was employed during the chemical etching manufacturing giving the characteristic double cone structure [98].

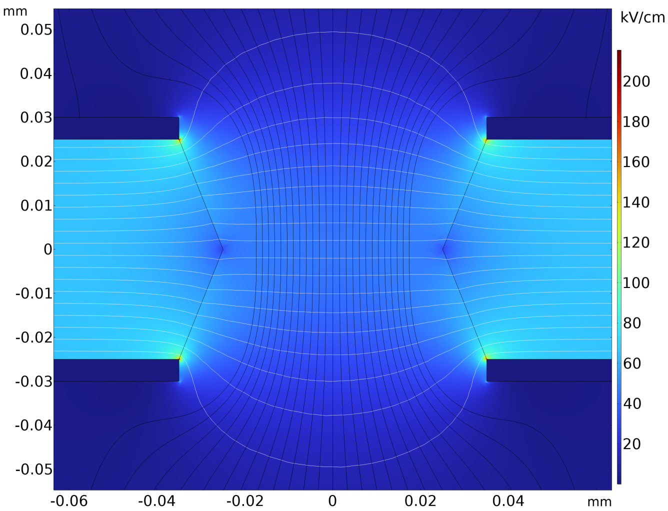

Figure 4.7: Electric field strength overlaid with streamlines (black) and potential contours (white) from an applied potential difference of 325 V across the 50 µm thick hole.

4.2.1 Charge sharing between different coordinate planes

Given a series of 10^4 primary electrons originating from the same point at the top of the 2 mm drift gap above the GEM foil, the resulting signals from the secondary charges induced on neighboring strips was calculated using Garfield++ and the weighting potential obtained using the FEM solution from COMSOL®. As a gas mixture 70% argon and 30 % CO_2 was used at atmospheric pressure and an absolute temperature of 293.15 K.

After traversing their paths, the electrons that were successfully extracted from the GEM amplification structure and that did not get lost through recombination end up

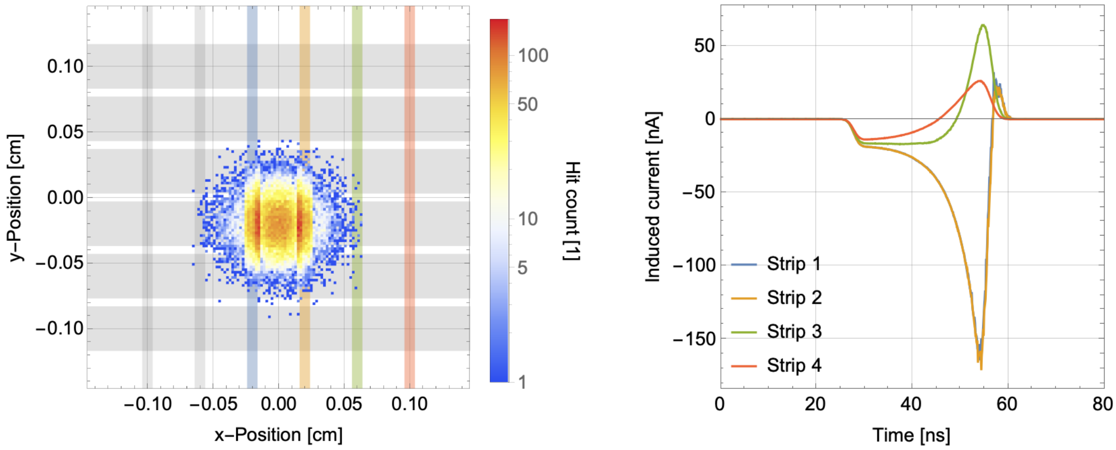

Figure 4.8: **Left:** Density plot of the hit distribution sourced by electrons form the top of the drift gap. The locations of the X and Y-strips are marked with the four coloured X-electrodes corresponding to the induced signals and charge shown in the left panel with the same colour. **Right:** Induced current on the top layer of strips color coded following the left panel.

on the grounded readout anode. The arrival position distribution of the electrons on the anode of such an event is given in Fig. 4.8. Since the integrated charge of the total induced signal is equal to the collected one, it becomes apparent that the fraction of total induced charge that is shared between the X and Y coordinate plane is not only determined through their respective coverage area of the anode surface. Instead, due to the elevated X-strips, the increased concentration of electrons along the y-direction on them is caused by the field lines locally focusing the collected charge onto the top strips. This degree of 'focusing' depends on virtually all the parameters of the strip readout structure, including the separation distance between the X and Y-layer of strips.

4.2.2 Induced signal on neighboring strips

In Fig, 4.8 (right), the induced signals are displayed for the X-strips highlighted in Fig. 4.8 (left). Since the bottom metal layer of the GEM shields the readout from the electric field

Table 4.1: Geometry parameters of the standard GEM geometry.

Parameter	Value
Cu thickness [μm]	5
Polyimide thickness [μm]	50
Outer diameter [μm]	70
Inner diameter [μm]	50
Hole pitch [μm]	140

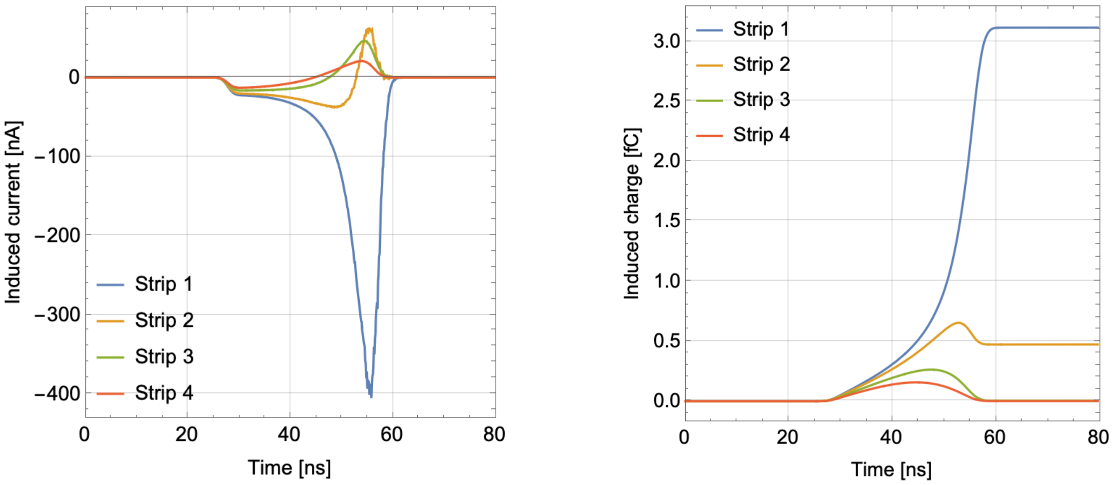

Figure 4.9: **Left:** Induced current on the bottom layer of strips with index k denoting the strip centered at $y = -600 + k400$ µm. **Right:** Cumulative induced current as a function of time.

produced by the charges moving above it, the signal starts as soon as the electrons move into the induction gap. It is worth noting that while the majority of charge amplification occurs at the bottom edge of the GEM hole, there may still be minor, albeit arguably negligible, traces of ion movement that can be observed. Similar to the observation made in Sec. 2.1.1, the signal in the readout channels collecting the bulk of the charge gets more peaked as the charge clouds move closer to it, coming from the increased weighting field strength in the region close to the strip. In addition, there is an extra feature at the end of the signal shape where it undergoes a polarity switch. This change in sign is a result of nearby electrons moving past the strip to be collected at the Y-layer, a feature that is absent from the induced currents on the bottom layer of strips, as shown in Fig. 4.9. The cross-talk current changed to a positive signal since no charge was collected on the outer strips. In the work of M. Ziegler we can find experimentally obtained signal shapes for a triple GEM detector equipped with a one-dimensional strip anode that was read out using a custom-developed amplifier with a 0.5 ns rise time [18]. An example of these waveforms, recorded during the irradiation of the detector with a ^{55}Fe X-ray source (see Sec. 4.3), is shown in Fig. 4.10.

4.3 XYU Gas Electron Amplifier

When working with a two-dimensional projective strip readout the number of channels scales linearly with the active area of the detector, instead of the quadratic scaling for pad-type electrodes. While this reduces the required electronics inventory, as one goes to large detection areas and high-rates events can overlap in time, resulting in ambiguities in the position determination with so-called *ghost hits*. An example is shown in Fig.

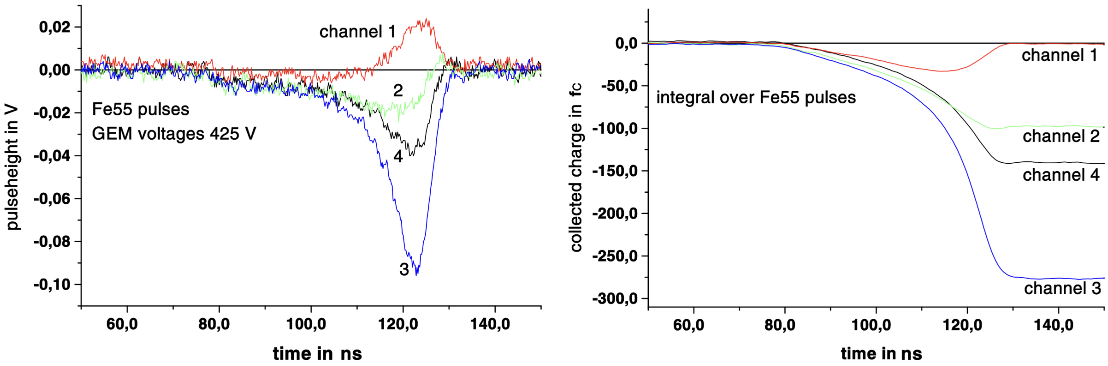

Figure 4.10: **Left:** Measured induced current in four neighboring strips sourced by an incident ^{55}Fe photon. **Right:** Integrated charge flowing from the strips to ground [18].

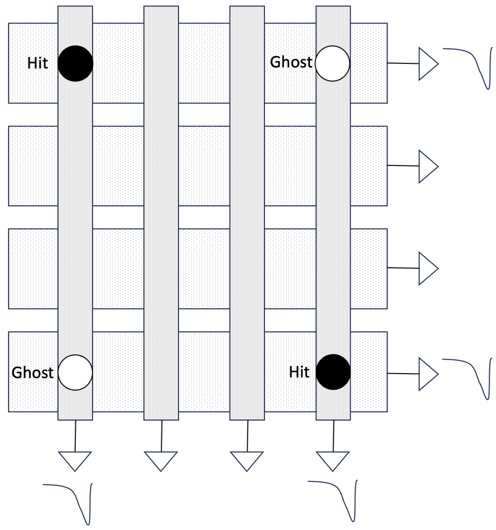

Figure 4.11: Schematic diagram of the ambiguous reconstruction from two contemporaneous events using a two-dimensional strip readout, resulting in ghost hits.

4.11. For charged particle trackers, this issue can be mitigated by amalgamating data from multiple aligned detectors, frequently installed at different angles. However, in scenarios involving neutral radiation or single photon detection, as exemplified by the COMPASS Ring-imaging Cherenkov (RICH) detectors [99], this approach is not always feasible. While many approaches are available to remedy this, we propose the use of an additional third coordinate plane equipped with one-dimensional strips. The discussion of its development in the remainder of this chapter is based on our related publication Ref. [100], outlinging our findings.

4.3.1 A three-coordinate strip readout

Various methods have been used to permit the operation of MPGDs in high-rate environments. For instance, in the central region of the upgraded GEM-based tracker within the COMPASS spectrometer, the traditional strip readout has been replaced by a grid of small pads, each with individual charge readout capability, due to its location at the highest beam flux [101]. While effective for ambiguity-free reconstruction of multiple events, this method increases the number of electrode channels from which the signals need to be retrieved and processed. In an alternative scheme, the so-called hexaboard, the anode consists of an array of hexagonal pads interconnected on the backplane in three sets of readout strips at angles of 60° from each other [102]. Permitting to reconstruct multiple events a few mm apart [103], the difficulty in manufacturing reliable multi-layer printed circuit boards with thousands of metalized holes has discouraged the adoption of the scheme for large-size detectors. In the context of R&D efforts for the ATLAS Muon System upgrade, a different method was developed for the resistive strip MicroMegas detector where a three-coordinate plane readout equipped with thin strip electrodes was embedded in the insulating layer below the resistive anode, through which the signal is coupled [104]. However, due to the resistive layout, this methodology only applies to moderate particle rates.

Driven by the increasingly demanding requirements of particle physics experiments at high luminosity colliders, we developed a modified version similar to the one described in Ref. [104], yet where direct charge collection is conducted on three projective coordinates for each detected event. Similar to the strip readout shown in Fig. 4.5, this readout structure, named the *XYU-GEM*, has two perpendicular sets of readout strips (X and Y) and an additional one below at 45° to the others (U) separated by thin insulating ridges. The active area of the detector measures 10×10 cm^2 and is equipped with a total of 256 readout strips, each with a pitch of 400 µm in both the x and y-directions, matching the pitch specified in [105]. Furthermore, there are 511 strips with a pitch of 283 µm in the U direction. As shown in Fig. 4.13, this ensures a discrete symmetry every 400 µm in the x- and y-direction, with a diagonal strip running through the vacant space of the upper two layers. Although the ideal selection would have been a 60° angle, this first prototype was made using pre-existing mechanical structures. Alongside the additional information gained from adding this bottom coordinate layer to resolve hit ambiguities or spatial resolution improvement, one can envision other applications, including the exclusive use of the U strips for triggering purposes. For the latter purpose, we can take the patterning of the third layer to be relatively coarse and are not confined to using only strip-shaped electrodes.

4.3.2 Simulation and manufacturing of readout structure

Using a standard triple-GEM amplification structure [105], a schematic of which is shown in Fig. 4.12, the detector was operated using the standard COMPASS tracker gas mixture of argon 70% and CO_2 30% at atmospheric pressure and room temperature. The high-

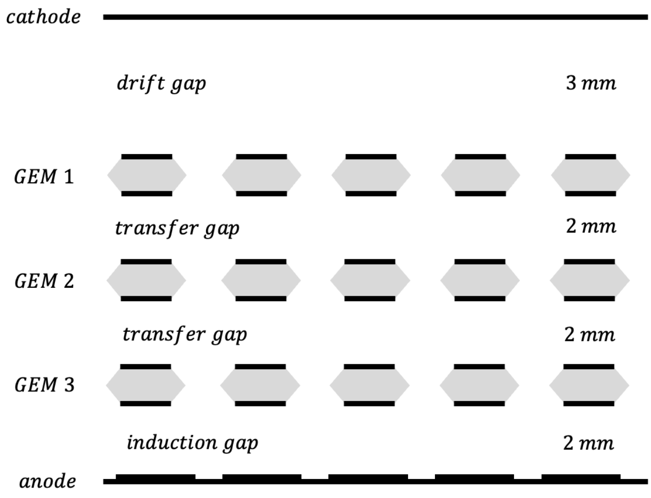

Figure 4.12: Schematic representation of the triple-GEM detector design used in this chapter. Here the total detector gain is achieved using three amplification stages . Not drawn to scale.

voltage is distributed to all electrodes through a resistor chain resulting in the fields quoted in Table. 4.2, yielding a detector gain of $\mathcal{O}\left(10^4\right)$. We have seen in the Sec. 4.2 that the distribution of the charge over the three readout plane is in part driven by the local focusing of electrons on the top layers of strips. Therefore, a Monte Carlo simulation was conducted using COMSOL®, and Garfield++ to estimate these sharing ratios across the parameter space of potential configurations to estimate the optimum design geometry for the three sets of readout strips to provide near-equal collected charge.

The bottom metal foil of GEM 3 will shield the readout from the electric field of the charge carriers propagating through the regions above it. Therefore, by approximation, we can reduce the model to that of the electrons being injected inside an induction gap bounded from above by a uniform metal plate. This is because the corrections for the

Table 4.2: Gap sizes and applied electric field strengths in the different regions of the triple GEM detector using a resistor chain.

Region	Height	$\lvert\mathbf{E}\rvert$
Drift	3 mm	2.5 kV/cm
GEM 1	50 µm	80.7 kV/cm
Transfer 1	2 mm	3.7 kV/cm
GEM 2	50 µm	73.5 kV/cm
Transfer 2	2 mm	3.7 kV/cm
GEM 3	50 µm	64.6 kV/cm
Induction	2 mm	3.7 kV/cm

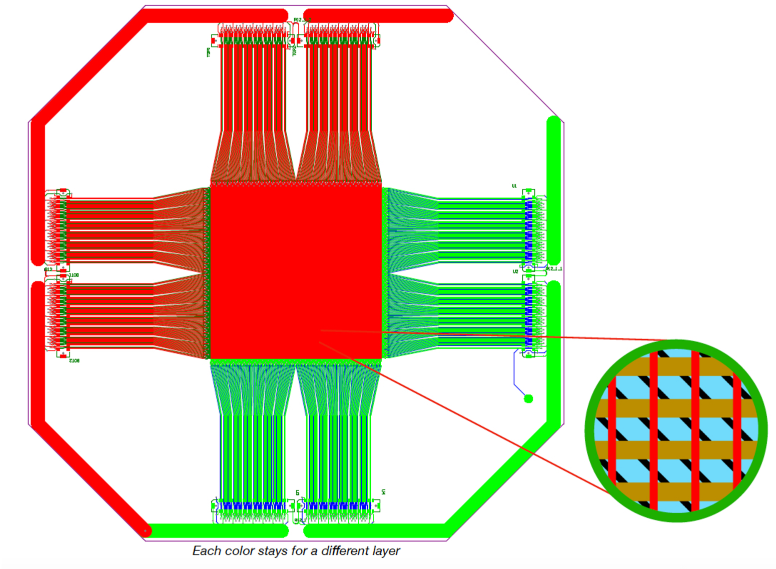

Figure 4.13: Schematic representation of the XYU anode readout board.

presence of GEM holes can be considered negligible, as the induced signals are most significant when the electron is in close proximity to the readout strips. In addition, to estimate the global charge sharing of the readout given uniform irradiation of the entire active area, we can take the initial positions of the electrons entering the induction region to be uniformly distributed over the xy-plane given the unequal pitch of the discrete symmetry of the readout and the hole pattern of GEM 3. The same steps were repeated as in Sec. 4.2 for different strip widths and separation distances between the coordinate planes. The optimized parameters are listed alongside the ones used for production in Table 4.3. Here, the optimized width of the X and Y-strips that ensure equal sharing were uncovered to be 50 µm and 150 µm, respectively. However, with the available manufacturing procedure, it was found that too fine strips would tend to detach from the insulator during the Kapton® etching process. As a result, their widths were increased to 80 µm and 180 µm, resulting in an unequal charge sharing. Better control over the manufacturing may allow the following devices to approach the optimum layout. Fig. 4.14 shows the result of the charge-sharing calculation for the optimized and manufactured design.

The XYU readout board manufacturing process was developed by CERN's Micro Pattern Technology (MPT) group aimed to overlay three overlapping sets of metallic strips at different angles, while being separated by thin insulating ridges. For the upper two layers, the insulating material between the neighboring strips in the same coordinate plane was removed, exposing the copper strips of the layer below. As can be seen in the inset in Fig. 4.13, this ensures direct collection of the shared electron charge on the three electrodes. This structure differs from those used in other devices, e.g., the resistive

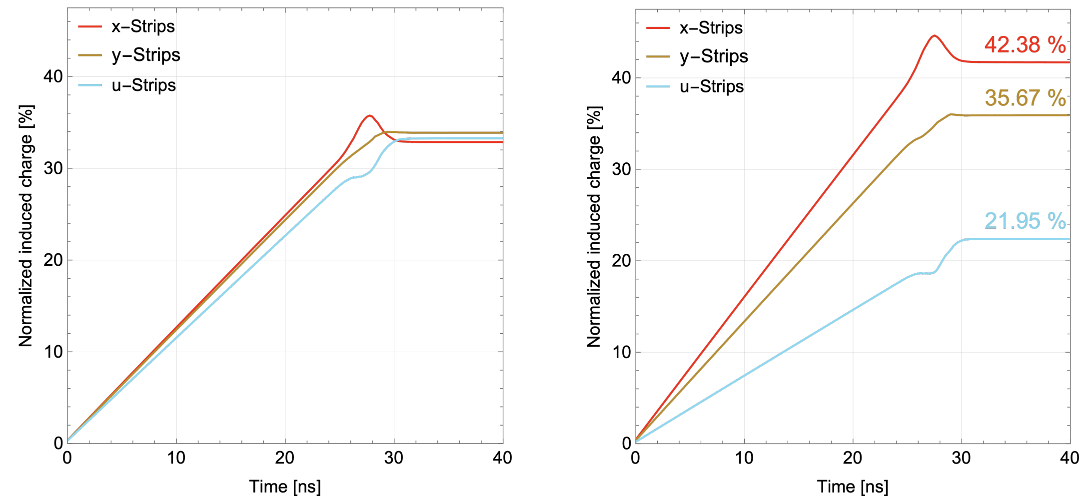

Figure 4.14: Simulated induced charge as a function of time for the optimized (left) and actually manufactured (right) XYU readout geometry.

MicroMegas to achieve two-dimensional readout exploiting capacitive couplings through insulators, that could charge up and affect the high-rate performances [34].

The production of the board involved multiple processing steps, which will be briefly outlined here:

1. The bottom layer (U) is photolithographically patterned on a single-side copper-clad 12.5 µm polyimide foil; the layer is laminated on a 1.6 mm thick fiberglass plate, that will constitute the main supporting board.

2. The middle layer (Y) is then patterned on the bottom side of a double-side copper-clad thin polyimide foil and coated with an etchable glue 10 µm thick; the U and Y layers are pasted together under pressure. To allow the realization of the metallized holes contacts for the connector, the copper layer thickness for the X strips was increased to 15 µm. Here our calculations show that this increase over the 5 µm design value slightly affects the sharing.

Table 4.3: Optimized design and practical manufactured geometry.

<table>
<tr><th></th><th colspan="3">Optimized</th><th colspan="3">Manufactured</th></tr>
<tr><th>Strips</th><th>X</th><th>Y</th><th>U</th><th>X</th><th>Y</th><th>U</th></tr>
<tr><td>Pitch [µm]</td><td>400</td><td>400</td><td>400</td><td>400</td><td>400</td><td>283</td></tr>
<tr><td>Width [µm]</td><td>50</td><td>150</td><td>350</td><td>80</td><td>180</td><td>220</td></tr>
<tr><td>Insulator</td><td colspan="2">25</td><td></td><td colspan="2">12.5</td><td></td></tr>
<tr><td>thickness [µm]</td><td></td><td colspan="2">12.5</td><td></td><td colspan="2">22.5</td></tr>
</table>

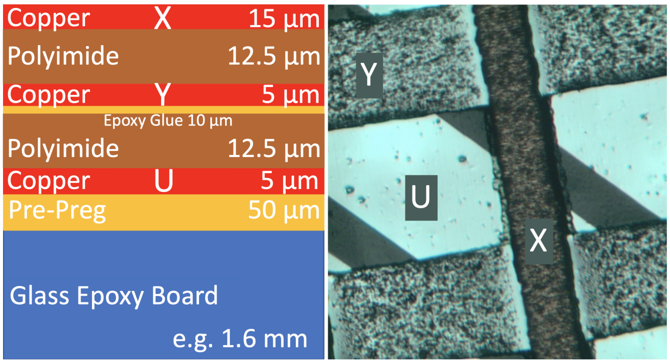

Figure 4.15: Schematic cross-section and a close-up view of the three overlapping strips.

3. An additional photolithography step is used where the top copper layer is patterned to realize the X strips. (iv) The composite structure then undergoes several stages of polymer and glue etching to open the channels for charge collection on the three layers of metal strips.

Fig. 4.15 provides a close view of the overlapping strips, and a schematic cross-section of the structure.

Based on the experience acquired with the prototype, a redesign of the geometry of strips and insulating layers could be envisaged to get closer to the desirable equal sharing of charge between the three coordinates. In addition, the strip pitch on the U projection should also be increased to the standard 400 µm to provide a more uniform response.

4.3.3 Experimental measurements

For the measurements in the laboratory the detector was equipped with strip readout electronics based on the ATLAS/BNL 64-channels VMM3a chip [106] with a peaking time set at 200 ns, and using the RD51 *Scalable Readout System* (SRS) [107] digitizing the input charge of all strips [93]. Developed by the RD51 collaboration [108], the SRS system is suitable for use with both small R&D setups and mid-sized experiments using MPGDs. For confirmation, the signal current from different layers was measured with pico-amperometers and the bottom side of the last GEM was read out with a Multichannel Analyzer. To irradiate the detector, we used X-rays from an uncollimated ^{55}Fe radioactive source[1] which, unless stated otherwise, was placed at a sufficient distance

[1] The decay process of $^{55}_{26}$Fe to $^{55}_{25}$Mn* (half-life of 2.747 years) through electron capture

$$p + e \rightarrow n + \nu_e \,,$$

leaves a vacancy in the K shell. This process leads to a relaxation chain, which results in photon emission with an energy of $E_{K\alpha} = 5.90$ keV ($E_{K\beta} = 6.49$ keV) with a probability of 24.4% (2.86%) [10]. For simplicity we will only refer to the 5.9 keV emission for what follows.

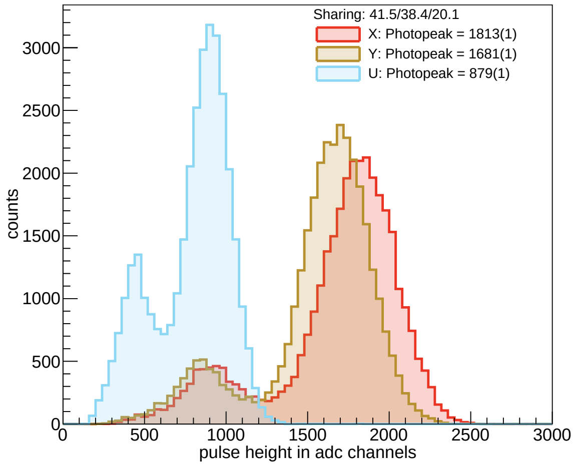

Figure 4.16: Spectra of pulse heights obtained for X-rays with an energy of 5.9 keV on the X, Y, and U projections.

to cover the full active area during the measurements.

The PH spectra recorded on the three projections on exposure to a 5.9 keV ^{55}Fe X-ray source are shown in Fig. 4.16. This well understood structure of the spectra is the result of the primary ionisation process by photoelectric absorption process with the argon atoms. Here, the photon has a probability of roughly 80% to liberate an electron from the K shell [109], leading to either radiative or non-radiative processes (Auger effect), which give rise to the emission of a fluorescence photon or an electron, respectively. Depending on the location of the initial photoabsorption, the fluorescence photon may ionize another atom or molecule within the gas or escape from the detector without interaction, giving rise to a secondary *escape peak* at lower PH values alongside the main *photo peak* [2].

As expected due to the manufacturing limitations mentioned earlier, the detector, built according to the specifications in Table 4.3, shows uneven charge distribution among the coordinate planes. Specifically, the charge sharing in the U plane is lower by about a factor of two. The relative ratios between the main peaks are, in order from the top to the bottom layer, 42%, 38%, and 20%[2], corresponding well to the simulations done using the actual production parameters. Furthermore, Fig, 4.17 shows a good correlation of the charges on X and Y and, respectively, on X and U coordinates. Since the charge sharing is significantly influenced by the higher density of field lines on the top layers of strips, the resulting sharing ratios can be modified by applying small polarization voltages to

[2]This measurement was seconded by a direct current measurement of the three coordinates resulting in ratios of 45%, 34%, and 21%.

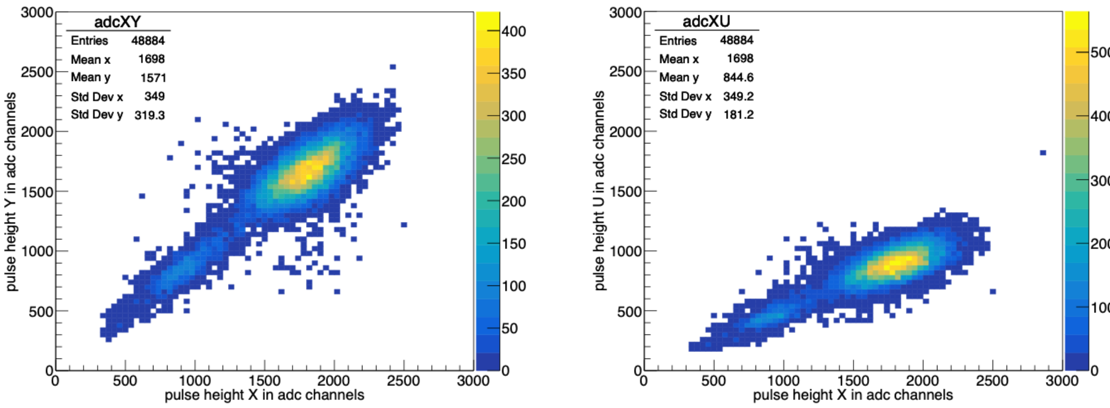

Figure 4.17: Correlation of the pulse heights between the X and Y-layer (left), and the X and U layer.

the anode strips; with +15 V on the U strips, the charge on the three coordinates is almost equal. This is was also found through simulation.

For each event contained in the main 5.9 keV peak, we have deduced the cluster size from the Root Mean Square (RMS) of the number of adjacent channels going over the threshold. After considering the strip pitches of 400 µm for X, 400 µm for Y, and 283 µm for U coordinates, the cluster size is shown in Fig. 4.18 (left) for each coordinate plane. As anticipated, the U distribution is slightly narrower due to its smaller total collected charge. However, this variance is not expected to significantly impact the localization capabilities of the detector. The average value for X and Y, around 375 µm, align with measurements previously observed in GEM detectors utilizing conventional XY projective strip readouts [105]. While the results of the three coordinates are encouragingly close, an appreciable disparity when examining the cluster size in U compared to the others, which necessitates further investigation.

Due to its intentional design, the readout system is intrinsically overdetermined, the U coordinate of an event within the photopeak can be deduced using the X and Y projections. We analysed the residual distribution of the difference between the reconstructed, U(X,Y), and measured position in U. This revealed a small distortion of the correlations, probably due to the angle of the U strips slightly deviating from 45°. After correcting for this, the result of the calculation is shown in Fig. 4.18 (right), where a Gaussian fit of the distribution estimates a Full Width at Half Maximum (FWHM) of 127 µm. To improve the event selection, by reducing the correlation between the position in U and the XY-readout, only events within this distribution that deviate by a distance of no more than a few times the strip pitch from zero are considered.

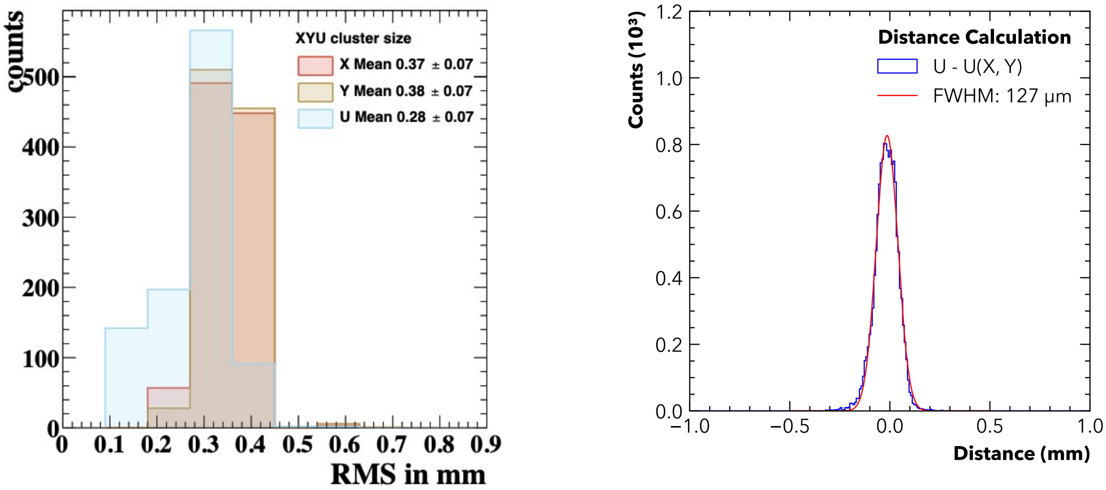

Figure 4.18: **Left:** Root Mean Square (RMS) of cluster sizes for the X, Y, and U layer. **Right:** Calculated U-projection distance relative to hit positions determined from X and Y coordinates, utilizing the formula $\mathrm{U(X, Y)} = 511 - X - Y$, with 511 representing the total count of U strips.

4.4 Summary

With the introduction of a third coordinate layer, the XYU-GEM aims for an almost ambiguity-free reconstruction of multiple coincidental tracks that can occur with high multiplicity events and increased particle fluence. Contrary to other solutions, such as pad readout structures and multi-layer strip readout capacitively coupled to a resistive anode structure, the XYU-GEM directly collects the electron cloud on three stacked layers of strips. The distribution of charge over the coordinate planes is influenced by the focusing of field lines on the electrodes in the top two layers, contingent on factors such as electrode configuration, relative pitch, width, copper thickness of the strips in different coordinate planes, and the inter-distance between the planes.

An optimal parameter set ensuring equal charge sharing was determined through simulations, informing the production of the first prototype. We have demonstrated the prototype's capability to detect and localize radiation. Due to production limitations, changes were made to the production parameters, leading to the observation of an unequal charge sharing between the layers through both PH and current measurements. This imbalance could be satisfactorily reproduced using the simulation. Based on the experience acquired with the prototype, a redesign of the geometry of strips and insulating layers could be envisioned to get closer to the desirable equal sharing of charge between the three coordinates, e.g., the strip pitch on the U projection should also be increased to the standard 400 µm to provide a more uniform response.

Chapter 5

Robust precise timing PICOSEC MicroMegas

Considering the sensitivity of timing applications to the signal's leading-edge, it remains uncertain a priori how the timing performance might be impacted when introducing a thin resistive plane with a certain surface resistivity in the readout of an MPGD. This query brings to the forefront longstanding topics, such as the rate effect and signal transparency of a resistive readout. In this chapter, we delve into the considerations that guided the development of the first multi-channel resistive plane PICOSEC MicroMegas, aiming for a sub-25 ps timing capability.

5.1 Concept and working principles

Apart from their conventional role in Time-of-Flight (TOF) systems for charged particle identification, the LHC experiments are currently upgrading or developing fast timing detectors to perform vertex separation in beam collisions with a high rate of overlapping interactions (*pileup*). On such example can be found in the hermetic timing approach of the CMS MIP[1] Timing Detector upgrade, which will be positioned between the CMS tracker and the calorimeters [28]. This is a crucial strategy to maintain the efficiencies of the LHC experiments during the upcoming HL-LHC era [110]. In an ultimate scenario, the HL-LHC will be able to achieve an instantaneous luminosity of $7.5 \cdot 10^{34}$ cm^{-2}s^{-1} with an expected average of ≈ 200 interactions per bunch crossing, spread over an RMS time range of $180 - 200$ ps. Without appropriate measures, this unparalleled increase in background is expected to result in a significant rate of misidentification of primary vertices. Meeting this challenge involves the development of high-precision timing detectors with a temporal resolution below 100 picoseconds with the ability to withstand substantial levels of radiation exposure [26]. When the additional timing information that can be gained from the integration of such detectors allows for the time-slicing of the tem-

[1]The acronym MIP stands for *Minimum Ionizing Particle*, denoting particles for which the mean energy loss per unit of length dE/dx through matter is around the minimum value.

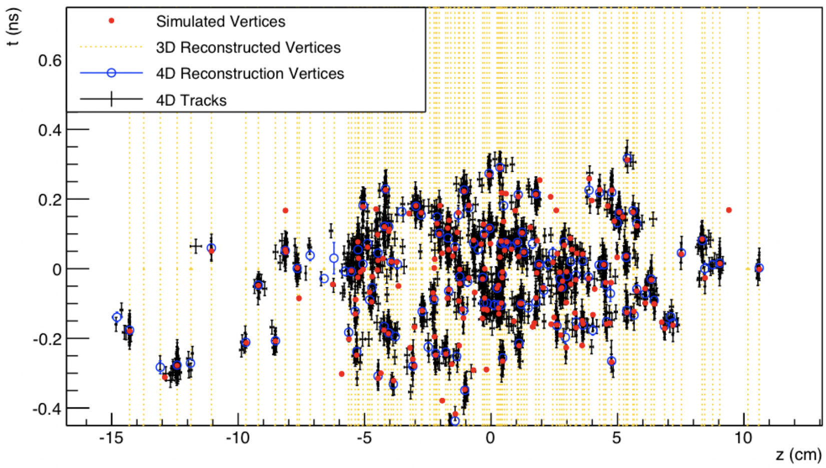

Figure 5.1: Simulated event display of the simulated and reconstructed vertex positions in space-time. Detectable vertex mergers that appear to occur when relying solely on a position information-based reconstruction (indicated by yellow lines) can be effectively resolved by incorporating MIP timing information (represented by blue markers). Here, a MIP timing detector system with a timing resolution of 30 ps that covers the end caps and the full 2π of the barrel of the CMS detector was assumed [28].

poral structures of the bunch crossings into, for example, 30-40 ps wide windows, the number of primary vertices drops to the level of the Run-2 LHC pileup levels [28]. Fig. 5.1 showcased the advantage of this four-dimensional ($3 + 1$ D) reconstruction approach from simulation. Given these stricter requirements on timing performance by upcoming physics experiments it is prudent to further explore MPGD and semiconductor-based sensors as potential fast timing detector technologies is prudent.

The *PICOSEC MicroMegas* (hereafter PICOSEC) detector concept is brought to fruition through the implementation of a two-stage MicroMegas detector [9] where the front window, typically made from a MgF_2 crystal, coated with a photocathode serves as a Cherenkov radiator [111, 112]. The gas volume is divided into two distinct regions by the woven mesh within the bulk MicroMegas [113]: a *pre-amplification region* of ≈ 200 µm that stretches above it and a 128 µm *amplification gap* mechanically defined by pillars between the mesh and the anode structure. With the thin gas volume, the probability of ionization of the gas is minimized, where the likelihood of interaction in a gas gap of size g is given by

$$P(g) = 1 - e^{-\frac{g}{\lambda}} \tag{5.1.1}$$

with λ^{-1} being the cluster density for charged particles. Rather, a relativistic charged particle traversing the Cherenkov radiator produces ultraviolet (UV) photons, which are converted into primary photoelectrons by the photocathode over an area equal to that covered by the Cherenkov cone. These photoelectrons are injected at the top of the pre-amplification stage with an RMS timing jitter of less than ten ps [114]. The presence of a

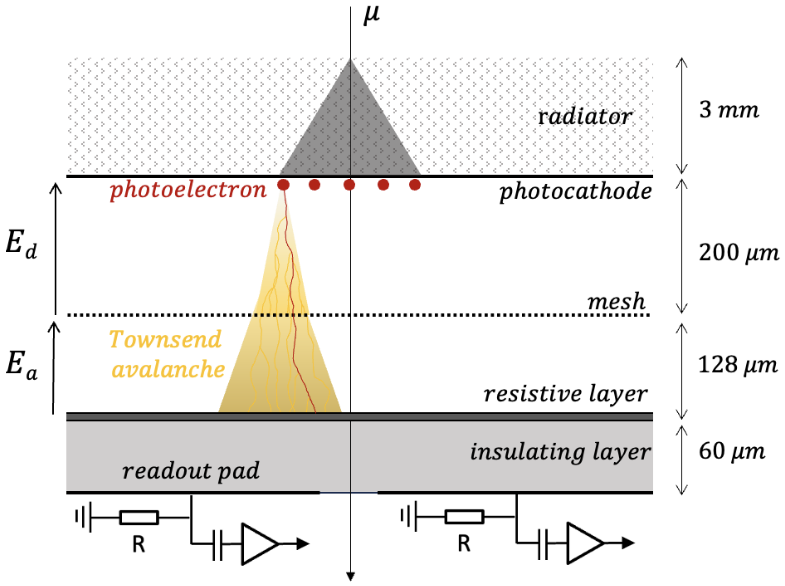

Figure 5.2: Schematic depiction of the PICOSEC detector components for a resistive plane multi-channel readout. The photoelectrons sourced by conversion of the Cherenkov radiation by the photocathode, initiate an electron avalanche in the pre-amplification gap. The fraction of electrons that traverse the micro-mesh initiate secondary avalanches in the amplification gap. The thin resistive layer decouples the high voltage application from the readout electrodes on which the signal is induced by the movement of the charge carriers in the amplification gap and the response of the resistive layer.

high electric field starts a Townsend avalanche in the pre-amplification region, resulting in a gain of $\mathcal{O}(10^4 - 10^5)$ with minimal longitudinal diffusion. A mere fraction, around a quarter, of the generated electrons will successfully navigate through the mesh into the amplification gap, where they undergo further amplification, commonly by a factor of $\mathcal{O}(10)$, and initiate the generation of current on the readout electrodes. A schematic depiction of the device's layout with a resistive readout structure and operational concept is given in Fig. 5.2. The detector is operated at atmospheric pressure and room temperature with a flammable gas mixture of 80% neon, 10% CF_4, and 10% ethane (C_2H_6), to which we will refer to as the COMPASS gas mixture in what follows[2].

As demonstrated using a single channel prototype, this detector concept pushes the boundary of the timing capability that non-resistive MPGDs can reach into the sub 25 ps regime for MIPs [111]. Successful strides have been made towards making the concept viable for large area coverage by developing a segmented anode multi-channel readout capable of maintaining the timing performance exhibited by its single-channel counterpart

[2]While being the current baseline mixture it has a relatively high global warming potential of 740 (normalized to CO_2) compared to mixtures such as Ar/CO_2 (93%/7%) that has 0.07. There is an ongoing effort to look for an alternative gas mixture that can provide a good timing performance [115]

[116]. Recently, comprehensive studies using a muon test beam with a momentum of 80 GeV/c demonstrate that a 10×10 cm^2 device equipped with 100 square pad electrodes can consistently achieve a sub-25 ps timing resolution using a CsI semitransparent photocathode [117, 118]. Informed by a Garfield++-based phenomenological model [114], this result could further be improved to 17 ps using a thinner 180 µm pre-amplification gap along with a newly developed RF pulse amplifier [117, 118].

Motivated by mitigating the destructive capability of discharges through quenching, the 100-channel multi-pad design was expanded to incorporate the resistive anode structure sketched in Fig. 5.2, where the pad electrodes are separated from a thin resistive DLC layer using an 50 µm thick insulating Polyimide lamina and a glue layer with a thickness of 10 µm. To uphold the performance of the non-resistive multi-pad prototype – a feat already accomplished on the level of single-pad prototypes with resistive plane MM [112] – several aspects needed to be considered that limit the range of possible surface resistivities R that can be employed: (i) minimal protection against violent discharges by suppressing the transition from streamer to spark, which allows for the achieving of large gains and its application in harsh environments, (ii) the operation at moderate to high fluence while retaining its timing performance by minimizing the voltage drop across the resistive layer, (iii) retaining the prompt rising edge of the signal, and (iv) minimizing Johnson-Nyquist noise from the resistive layer. The first point sets a low bound on the value R, requiring a minimal protection impedance of 10 MΩ to ground for the successful quenching of the discharges and avoid the burning of the DLC [119]. The inclusion of the final two points is driven by the imperative of upholding the timing resolution, a quantity subject to multiple contributions.

To form an intuition for these contributions, we will discuss it for the case of a constant threshold timing discriminator (CTD), while the more sophisticated method used for PICOSEC will be described in Sec. 5.5.2. For the case of a CTD, the time marker of the signal corresponds to the time when the voltage pulse crosses a fixed THL. The contribution to the attainable timing resolution can be decomposed as [120, 2]:

$$\sigma_t^2 = \left(\frac{\left(\Delta v_s^{th}\right)_{rms}}{dV/dt} \right)^2 + \frac{\langle v_n^2 \rangle}{(dV/dt)^2} + \sigma^2_{\text{arrival}} + \sigma^2_{\text{dist}} + \sigma^2_{\text{TDC}}\,, \tag{5.1.2}$$

expressed as a function of the voltage signal after the amplifier[3]. The first term denotes the uncertainty due to the *time walk*, a systematic dependence of the time marker on the pulse height variations resulting from variations in the number of primary electrons extracted from the photocathode, as well as Townsend avalanche fluctuations, which can

[3]This simplified relation is typically presented to elucidate the factors influencing the timing performance of Low Gain Avalanche Diodes (LGAD). Given the largely shared fundamental principles of timing detectors between these technologies, it will be used as a guide to introduce analogous concepts here.

be parameterised by the *Pólya distribution*[4] [122, 123, 121, 124]

$$P_n = \frac{(\theta+1)^{\theta+1}}{\bar{n}\Gamma(\theta+1)}\left(\frac{n}{\bar{n}}\right)^{\theta} \mathrm{e}^{-(\theta+1)n/\bar{n}}\,, \tag{5.1.3}$$

where n is the number of charges produced, $\bar{n}$ the mean avalanche size, and θ the shape parameter. When taking $\theta = 0$, the above relation is that of an exponential distribution, while for $\theta > 0$ the distribution becomes increasingly rounded. The most probable size and relative variance of Eq. 5.1.3 are given by $\bar{n}\theta/(\theta+1)$ and $1/(\theta+1)$, respectively [39]. Consequently, the parameter $\left(\Delta v_s^{th}\right)_{rms}$ in Eq. (5.1.2) captures the RMS of the signal height variations at the discriminator THL. As detailed in Sec. 5.5.2, this contribution can be mitigated by employing corrections based on constant fraction discrimination and amplitude information. With the noise amplitude fluctuations given by v_n, the second term signifies the time jitter coming from the noise present in the detector – to which the resistive layer will contribute as described in Chapter 3 – and the external electrical circuit connected to it. These first two terms are inversely proportional to the pulse slew rate dV/dt, underscoring the importance of maximizing this quantity. For the resistive plane readout, the delayed component of the signal is opposite in polarity to that of the prompt one found in the non-resistive detector, as elucidated in Sec. 2.3.4. Consequently, the surface resistivities needed to be taken sufficiently high such that the reaction of the thin resistive layer is slower than the time scale of the electron peak and (as such) will not impede the *leading-edge* of the signal, meaning the initial rising part of the induced current until it reaches its maximum value. The variance in arrival time of the signal $\sigma^2_{\text{arrival}}$, already minimized by the almost exclusive injection of primary charge at the photocathode, includes contributions from non-uniformities of pre-amplification gap height [116] and sensitivity to the fluctuations of the initial photoelectrons along their path before the advent of their amplification [114]. The irreducible contribution from the second to last term is the distortion from both the prompt weighting field and applied electric field from that of a homogeneous field found between two parallel plates. The digitization of the signal, denoted by the final term, also contributes to the overall uncertainty.

While the topic of resistive elements as noise sources was already covered in Chapter 3, the problem of rate-capability and the transparency of the resistive layer to the leading-edge of the signal remains to be treated. These two topics will be discussed in the case of the resistive PICOSEC design, the results of which were used to inform the design of a resistive 100 channel PICOSEC. The characterisation of the produced resistive prototype using an 80 GeV/c muon beam will be presented, and compared to the performance of its non-resistive counterpart. This will be preceded by measurements pertaining to non-resistive signal channel PICOSEC prototypes, in order to acquire familiarity with the operational principles and signal shape. This will lead us to the topic of the length of the ion tail in a MM-type device, opening a discussion when compared to simulation results.

[4]The most cited attempt to a direct proof the conformity of avalanche size variations to this distribution has been criticised, primarily due to the premise made that the energy dependence of ionization probability is solely a function of avalanche size [121]. Therefore, this characterization is appropriately regarded as a phenomenological one.

5.2 Induced signal in a non-resistive single channel device

Our initial focus will be on a single-channel non-resistive design. Our objective is to assess the signal characteristics originating from single photoelectron events through experimental measurements. This assessment will encompass two scenarios: one involving the standard COMPASS gas mixture and the other utilizing an Ar/CO_2-based mixture. Curiously, our evaluation of the standard gas mixture revealed a shorter ion tail than expected.

5.2.1 Experimental setup

The measurements were performed using two single-channel prototypes, both cylindrical bulk MM devices containing a circular anode plane with a radius of 5 mm. The 3 mm thick MgF_2 radiator crystal was coated with an 18 nm thick CsI photocathode on a 3 nm chromium, where the chromium helps with the uniform voltage distribution over the cathode area. The prototypes originate from two distinct production batches. The latest iteration, referred to as device B in what follows, demonstrates, among other points, improved PCB planarity and coverage of the calendared mesh's connection and cuts. These improvements allowed for a more uniform timing response and stable operation at narrower pre-amplification gaps compared to the initial version, designated as device A. The height of the pre-amplification gap was determined by employing Kapton® spacers, resulting in heights of 200 µm and 130 µm for devices A and B, respectively. The vessel housing these devices was equipped with a transparent (quartz) entrance window to enable the transmission of UV light. As will be specified below, the interiour of the vessel was flushed with either the COMPASS gas mixture or with 93% argon and 7% CO_2 at normal temperature and pressure (NTP), i.e., 293.15 K and 1 atm .

Fig. 5.3 shows the High Voltage (HV) voltage configuration. As will be further explored in Sec. 5.2.4, the mesh is grounded with minimal impedance to minimize the cross-coupling signal from the mesh to the anode. In contrast, the cathode and anode planes are put to HV. On both connections, two low-pass filter RC circuits were implemented to reduce the noise from the HV supply entering the system. An RF pulse amplifier read out the induced current on the anode plane [117] and digitized using a WAVERUNNER 625ZI LeCroy Digital oscilloscope [125], on which a discriminator THL was set as the trigger for the data acquisition. Using a 250 nm UV LED250J [126], the photocathode was uniformly irradiated, injecting single photoelectrons into the gas volume, which subsequently underwent amplification.

5.2.2 Fast signal measurement and ion tail duration

The measured signal shapes of device B using the COMPASS gas mixture for different voltage configuration are plotted in Fig. 5.4 where the 'fast' electron peak and 'slow' ion tail are clearly visible. At a more traditional operational point of a MM, i.e.; low cathode voltage resulting in a drift field strength E_d of $\mathcal{O}(0.1 - 1)$ kV/cm, the full

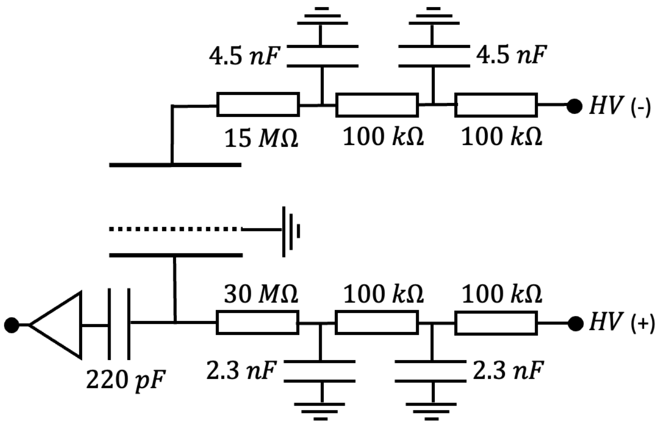

Figure 5.3: Schematic of the external circuit employed for providing high voltage (HV) to the anode and cathode, reading out the anode electrode, and noise filtering circuit.

amplification is performed below the mesh. When the amplification field E_a is decreased to prioritize additional charge production in the pre-amplification region, the charge information contained within the integral of the ion tail decreases due to the reduced effective Townsend coefficient $\bar{\alpha}$ in the amplification gap, as given by Eq. 2.3.18, alongside with a noticeable trend toward a longer ion signal with reduced amplitudes due to the lower ion velocities inside the amplification region. In addition, a more pronounced electron peak for higher E_d/E_a ratios can be observed which is beneficial for leading-edge detection of the signal in timing application.

Similarly, the chamber was filled with the Ar/CO_2 gas mixture for device A and operated in an MM-style field configuration. A recorded waveform is shown in Fig. 5.5 for −360 V and 510 V applied to the cathode and anode, respectively. While the typical MM signal structure can be observed, the length of the ion tail is found to be below 100 ns. This stands in sharp contrast with the toy-model result found in Sec. 2.3.2 that shows in Fig. 2.10 (right) more than double the total length of the signal despite the identical amplification field. Notably, the calculated result is based on the velocity of Ar^+ in a neutral argon mixture without considering the contribution of CO_2. However, as we will return to during the discussion, the contribution does not seem to result in a factor two difference in ion velocity. These measurements can, therefore, serve as a first estimation for the length of the ion tail at amplification field strengths.

The ion tail duration, here defined experimentally as the time between the electron peaking time and the back end of the ion tails in the recorded waveforms was fitted using a Sigmoid function [127] of the form

$$V(t) = \frac{c_1}{c_2 + \exp\left[c_3(t - t_0)\right]}\,, \tag{5.2.1}$$

to determine the time t_0 and the free parameters c_i, with $i \in \{1, 2, 3\}$. An example fit

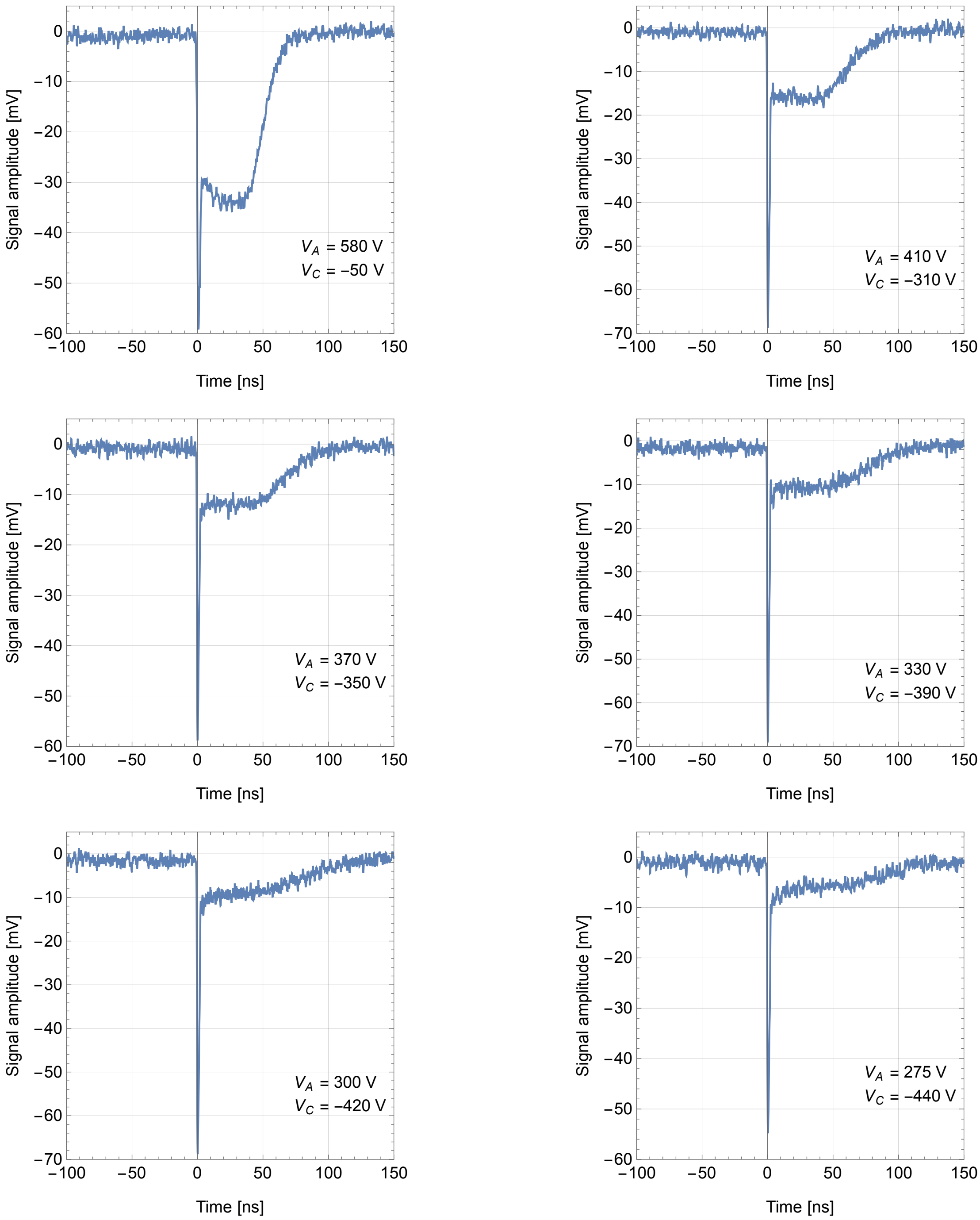

Figure 5.4: Measured signals using a PICOSEC MM (device B) going form a standard MM field configurations (top left) to a PICOSEC operation point (bottom right). Here V_C and V_A denote the applied voltages on the cathode and anode, respectively, keeping the mesh at ground.

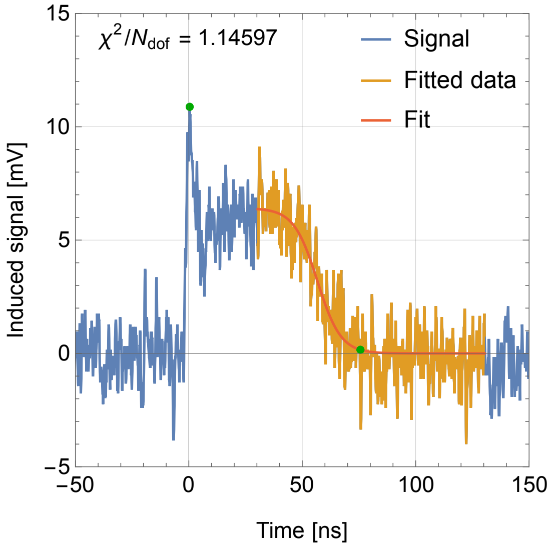

Figure 5.5: Measured signal induced on the anode of device A using a fast pulse amplifier. The tail end has been fitted using Eq. 5.2.1 giving an estimate for the ion tail duration given by the region between the green dots. Here the polarity of the signal is inverted.

can be found in Fig. 5.5 (right), where the end time when the ion is defined as the time where the above function is at 2.5% of its upper bound limit: $\lim_{t\to-\infty} S(t) = c_1/c_2$. To exclude results from subpar fits, a cut was introduced on the χ^2/N_{dof} distribution shown in Fig. 5.6 (left). Only results that satisfied $0.5 \leq \chi^2/N_{\text{dof}} \leq 2$ were used to obtain the probability distribution of the ion tail duration given in Fig. 5.6 (right), where the mean ion tail duration is estimated to be 75.32 ns for this field configuration.

A quantitative comparison of the signal duration to the one calculated using the ion velocities found in literature hinges upon several factors. The most prominent one is the maximal distance over which the moving ions induce a signal, i.e., the amplification gap height Additional factors that may play a role include (i) the uneven electric field resulting from the mesh's woven pattern affecting the average speed of the ions, (ii) the capacitive coupling between the readout electrodes altering the signal extracted from the anode, and (iii) signal shaping by the RF pulse amplifier. We will incorporate these points into a complete simulation of the current response of the detector setup which will then be compared with the measurement result presented above.

5.2.3 Precise measurement of amplification gap height

The ion tail length is a function of different parameters that come from gas properties, electric field configuration and the geometry itself. The average velocity of ions u in a

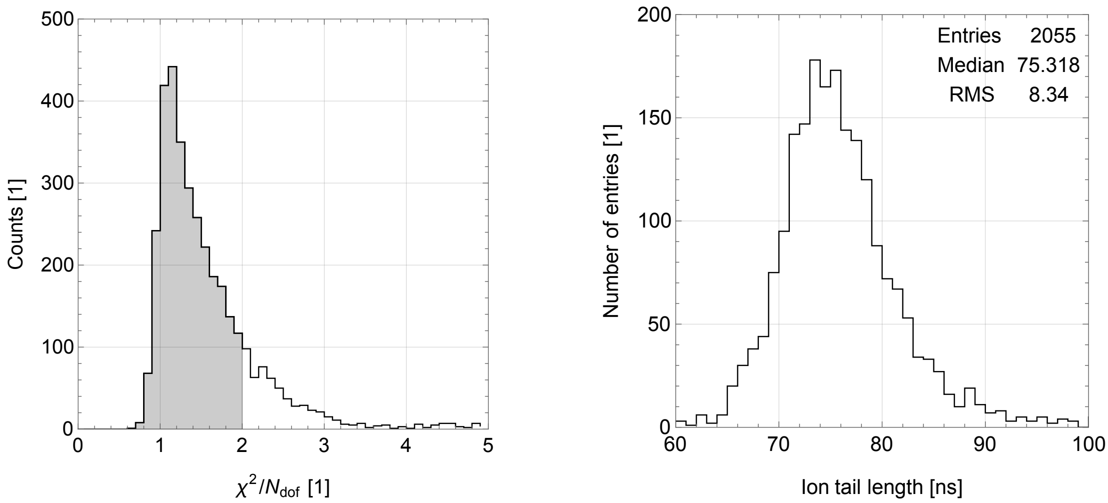

Figure 5.6: **Left:** χ^2-Distribution for the Sigmoid fits given by Eq. 5.2.1. Only events withing the gray area were accepted. **Right:** Distribution of the measured ion tail length.

given by [128]:

$$u = K\left(\frac{E}{N}\right)E\,, \tag{5.2.2}$$

with E being the electric field strength. The ion mobility K, in units of $\mathrm{cm^2V^{-1}s^{-1}}$, is dependent on the ratio of the electric field to the number density of neutral gas N in which it is moving at a given temperature. This ratio, the so-called *Townsend electric field*, governs the equilibrium between the energy ions acquire from the electric field and the energy they dissipate as a result of collisions with the neutral gas constituents. Commonly this quantity is given as a *reduced mobility*, which is the mobility scaled to 273.15 K and atmospheric pressure,

$$K_0 = K\left(\frac{P}{760\ \mathrm{Torr}}\right)\frac{273.15\ \mathrm{K}}{T} \tag{5.2.3}$$

where P is the neutral gas pressure. Given a parallel plate geometry with infinitely extending electrodes parallel to the xy-plane a distance g apart, the maximum ion tail duration is then given by

$$t_{\mathrm{tail}} = \frac{g}{K\left(\frac{E}{N}\right)E} \propto \frac{g^{3/2}}{\sqrt{\Delta V}}\,, \tag{5.2.4}$$

with ΔV being the potential difference between the two electrodes. Here we used the observation that at high fields $u \propto \sqrt{E}$ [129]. This suggests that g has an influence on both the electric field strength ($E = -\Delta V/g$) and the maximum travel distance where the ion induces a signal. While this does not yet consider the effect of the mesh structure on the electric field configuration, it does highlight the importance of having a correct value for the mesh height to accurately estimate the signal's duration.

For device A, a measurement of the distance between the anode surface and the top of the calendared mesh was performed using a Hirox RH-2000 digital microscope [130] by focusing on surface imperfections on both electrodes through the mechanical movement of the apparatus. Through multiple measurements at different positions across the active area, the height of the top of the mesh was found to be dependent on the position. This dependence was parameterized using a function of the form

$$g(r) = \frac{(g_1 - g_2)(p - r)}{p - R}\Theta(r - p) + g_2\,, \tag{5.2.5}$$

where r is the radial coordinate taking the center of the active area as the origin, R is the radius of the active area, p is the radial position of the pillar. The parameters g_1 and g_2 were found to be 119.56 ± 1.37 µm and 131.53 ± 1.19 µm, respectively. The above equation describes a sloping mesh going from g_1 at the outer ridge of the active area till g_2 at the pillar positions, while the mesh's top between the pillars is at a constant height of g_2. For $R = 0.5$ mm and $p = 1.7 \pm 0.1$ mm the geometric mean $\bar{g}$ is 127.58 ± 0.92 µm.

5.2.4 Calculated ion tail duration for Ar/CO_2

Aside from the contribution from the smaller amplification gap, the non-uniformity of the field due to the structure of the mesh results in a varying ion mobility over the ion's trajectory. Furthermore, the signals induced in the three electrodes exhibit some degree of capacitive coupling with the other electrodes due to external impedance elements present in the experimental setup (Fig. 5.2.1). Finally, the anode signal is shaped and amplified by the RS pulse amplifier. These three contributions could collectively impact the accuracy of the calculated signal duration, and are therefore taken into account in the simulation of the induced signal on device A's anode plane presented in this subsection.

Using Garfield++, the trajectories of the electrons and ions can be simulated through the microscopic tracking and Monte Carlo integration method, respectively, provided the electric field map for the operational voltages where for the electrons, the parameters used for their drift, diffusion, amplification, and attachment were provided by MAGBOLTZ [39]. The solution for the electric field in the parallel plate geometry, which includes a calendared woven mesh composed of 18 µm thick wires, was determined using the Finite Element Method (FEM) approach with the COMSOL® toolkit. The top of the mesh was situated at a distance of $z = \bar{g}$ above the anode located at $z = 0$. Fig. 5.7 shows the field configuration in the mesh region, with the most intense fields being concentrated at the lower section of the wires. The same observation can be made for the numerically calculated prompt weighting field solution of the anode, resulting in an increased sensitivity in this area for the induced signal calculation using the basic form of the Ramo-Shockley theorem through Eq. (2.2.22). We performed identical calculations for the induced currents on the mesh and cathode electrodes.

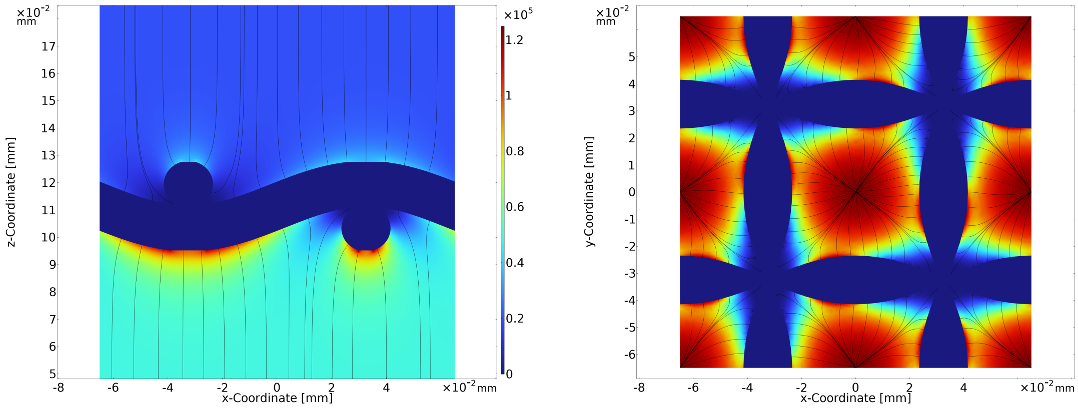

Figure 5.7: Cross-section cut of the FEM electric field solution around the mesh area. **Left:** Electric field strength [V/cm] for $y = 32.5$ µm. **Right:** Electric field strength [V/cm] along the central axis of the mesh within the xy-plane.

The trajectories of all charge carriers involved in a single photoelectron event are shown in Fig. 5.8 (left). Notably, a slight amplification can be observed above the mesh, while the bulk of the charge production occurs within the amplification region. Illustrated in Fig. 5.8 (right) are the projected end points of the ion tracks onto the xy-plane. In this configuration, the low E_a/E_d ratio leads to reduced transparency for both electrons and ions, with approximately three-quarters of the drifting ions being collected on the mesh. The resulting induced signals for this single photoelectron event are presented in Fig. 5.9 (left) for all three electrodes. Since the amplification gap closely resembles a parallel plate chamber, the weighting fields of both the mesh and the anode are, by approximation, the same, with the exception of their sign.

The incorporation of the circuit illustrated in Figure 5.3, along with the amplifier model, allowed us to calculate the cross-coupling of the electrodes and the amplifier's response in LTSpice. To include the equivalent circuit of the detector itself into the network, the capacitance between the anode, mesh, and cathode (designated as electrodes 1, 2, and 3, respectively) was determined through the FEM, yielding the Maxwell capacitance matrix:

$$\begin{aligned}\hat{C}_{ij} &= \begin{pmatrix} \sum_n C_{1n} & -C_{12} & -C_{13} \\ -C_{21} & \sum_n C_{2n} & -C_{23} \\ -C_{31} & -C_{32} & \sum_n C_{3n} \end{pmatrix} \\ &= \begin{pmatrix} 6.69785 & -6.67702 & -0.0208369 \\ -6.67701 & 10.2697 & -3.59272 \\ -0.0208369 & -3.59272 & 3.61356 \end{pmatrix} \text{pF}\,. \end{aligned} \tag{5.2.6}$$

for a circular active area with a radius of $R = 5$ mm. The value for C_{12}, i.e., the capacitance between the anode and mesh, is encouragingly close to the one of a parallel

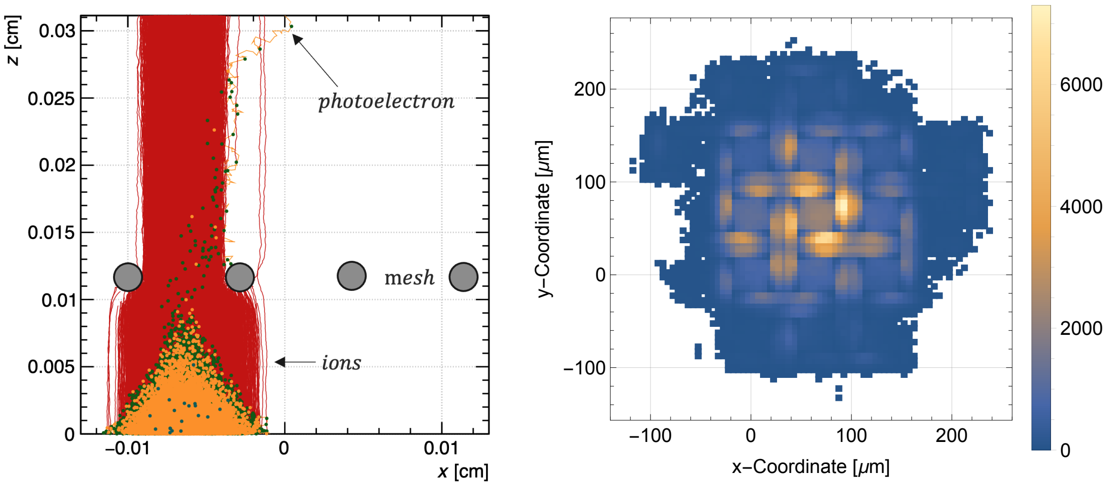

Figure 5.8: **Left:** Trajectories of the electrons (yellow) and ions (red) in the gas medium for a single photoelectron event. The positions of ionization and excitation are indicated by yellow and green dots, respectively. **Right:** Density map depicting the number of entries of the projection of the endpoints of ion tracks, which result from 94 individual photoelectron events.

plate capacitor

$$C = \frac{\varepsilon_0 \pi R^2}{\bar{g} - 2r_w} = 6.34611 \text{ pF}\,, \tag{5.2.7}$$

with the radius of the wire r_w being 18 µm. Following the reasoning of Sec. 2.5.4, the induced signals on the electrodes are treated as ideal current sources, resulting in the voltage pulse after the amplifier shown in Fig. 5.8. Compared to the directly induced current, the voltage pulse's electron peak at the amplifier's output terminal is broader. Furthermore, it reduces in amplitude compared to the ion tail amplitude. This is even more exacerbated when introducing a non-zero resistance R_{mesh} between the mesh connection and ground, resulting in the mesh's current being, in part, coupled out through the anode. Due to its opposite sign, the amplitude of the current on the anode is reduced and increases the signal rise time. This is a significant incentive to minimize the mesh's impedance to ground for timing applications. Despite the above considerations, the total length of the signal still exceeds 200 ns.

In summary, the observed length of the ion tail in an MM amplification stage, with an amplification field of 39.8 kV/cm and utilizing a gas mixture consisting of 97% argon and 7% CO_2, was measured to be 75.32 ns. This is shorter by more than a factor two compared to the calculated length using the ion mobilities found in the literature, even when considering the correct height of the mesh, cross-coupling between electrodes and the shaping of the amplifier.

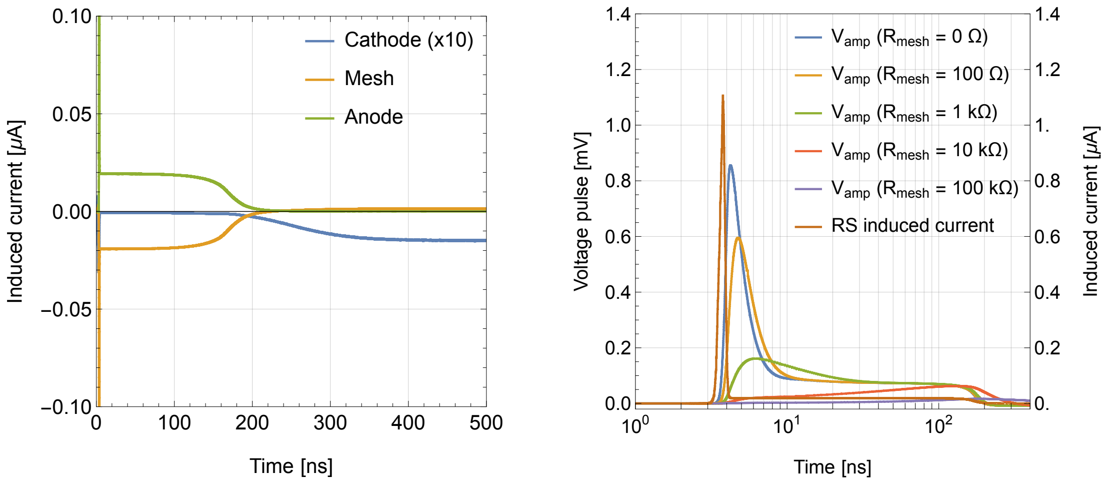

Figure 5.9: Ideal induced current on all three electrodes for a single photoelectron event, absent of any cross-coupling between the terminals. **Left:** Electric field strength [V/cm] for $y = 32.5$ µm. **Right:** The theoretical induced current on the anode, overlaid with the voltage pulses at the amplifier's output terminal for different termination resistors for the mesh.

5.2.5 Discussion

Since we have been using the mobilities found in a pure argon gas some discrepancy between the calculated and measured ion tail is to be expected. Indeed, when going to an Ar/CO_2 mixture, there are three notable changes: (i) the Ar^+ mobility will be dependent on the CO_2 content of the gas [131, 132], (ii) the creation of CO_2^+ that likewise will drift in the medium either though direct ionisation or the Penning effect [133, 134, 135, 136], and (iii) through ion chemistry there is a transfer of charge from the noble gas ions to CO_2 that will form slower $CO_2^+ \cdot (CO_2)_n$ cluster together with CO_2 molecules [137]. Less numerous are the $Ar^+ \cdot Ar$ dimers, unless for high fractions of Ar and pressures significanlty higher then 1 atm. This chemistry most likely increases in complexity when considering gas impurities, although the addition of water of the gas mixture tends to result in a lower mobility [132]. As a result, after less then 10 ns the main contributors to the ion tail signal are $CO_2^+ \cdot (CO_2)_n$ clusters which tend to move slower than the CO_2^+. This would result in a longer predicted ion tail, and thus not seem to resolve the discrepancy.

When dealing with amplification level field strengths, the natural difficulties of measuring mobilities of different ion species leaves us reliant on those obtained at low pressures of $P \lesssim \mathcal{O}(0.1 - 10)$ Torr. These measured reduced mobilities (5.2.3) can be scaled for the use at ambient pressure. For Ar/CO_2 measurements at ambient pressure have been performed field strengths of $\mathcal{O}\left(10^2 - 10^3\right)$ V/cm in the absence of any Townsend avalanches using a triple GEM detector [132], yet no measurements are reported in literature for $E = \mathcal{O}\left(10^4\right)$ V/cm. Hence, the problem of this striking discrepancy remains unresolved and stands as an open question necessitating further investigation.

5.3 Impact of a thin resistive layer on the leading edge

Incorporating a resistive layer into the readout structure of the robust PICOSEC design introduces an impact on the overall signal shape coming from the resistive layer's finite conductivity and the insulating laminate's presence. Crucial for timing measurements, this influence can adversely affect both the shape and amplitude of the leading-edge of the signal induced on the pad electrodes. The subject of the 'transparency' of the resistive layer to a signal generated by charges moving above it and the induction on the readout electrodes located below has been a longstanding topic in detector research [138]. A classic example is the contribution to the timing performance from the graphite layers, which form an integral part of contemporary (M)RPCs designed for the HV application and avalanche charge dissipation. Due to the finite conductivity of these layers, the reaction of this resistive element will result in the emergence of a delayed component to the signal, which negatively contributes to the signal amplitude due to its opposite polarity to the prompt current. It is now well understood that this contribution is negligible for the typical value of $\mathcal{O}(300)$ k$\Omega/\Box$ of this material. A seminal study on this topic was performed by G. Battistoni et al. in 1982 [138] who utilized a lumped element equivalent circuit to estimate the signal transparency of a thin resistive cathode layer, which divides the gas volume of a MWPC from an insulating layer containing AC-coupled closely spaced strip electrodes. As described in Sec. 2.4, this approach hinges on the ability to define a capacitance between the resistive layer and ground, which only holds at late times. Instead, we rely on the numerical framework developed in Chapter 2 to apply the extended form of the Ramo-Shockley theorem to estimate the delayed component's contribution to the electron peak amplitude found in the resistive PICOSEC design.

We consider the geometry sketched in Fig. 5.2, where a thin resistive layer with a surface resistivity R positioned between the amplification gap of size g and the insulating layer with thickness d is terminated around its entire outer edge situated at $x = 0, 10$ cm and $y = 0, 10$ cm. Since we are exclusively interested in the formation of the signal on the 1 cm^2 square pad electrodes on the readout plane, only the movement of the charges below the micro-mesh will contribute to this. Therefore, we approximate the amplification gap structure as a parallel plate geometry as given in Fig. 2.15. While the analytical solution is given by Eq. 2.2.29, we have opted to use the numerical recipe found in Sec. 2.5.2. Given a Towsend avalanche that occurs in the amplification region, we aim to assess the contribution of the delayed component to the electron peak as a function of the parameter R and the relative position of the avalanche with respect to the pad electrode. The dynamic weighting potential was calculated for the central pad, i.e., $x_p = y_p = 5$ cm, for different surface resistivities and subsequently integrated into our Garfield++ model. An example prompt signal I^p and delayed signal I^d from a Townsend avalanche is shown in Fig. 5.10 (left) for three different surface resistivities.

Although the ion tail is indeed accounted for, its amplitude is significantly smaller in comparison to the electron signal, causing the ion tail to be nearly imperceptible due to the fine signal binning. The amplitude of the prompt component resulting from the instantaneous induction of signal from the movement of both the electrons and ions below the mesh is subject to the relative permittivity ε_r and thickness of the insulating layer. Compared to the non-resistive design where this laminate is absent, this results in a fundamental signal reduction by a factor f_p, which in the limit of $w_x \gg g$ can be written as

$$f_p = \frac{E^p(d)}{E^p(0)} = 1 - \frac{d}{d + \varepsilon_r g}\,, \tag{5.3.1}$$

where we used Eq. (2.3.22) with ε_r reestablished. In our scenario, this corresponds to a value of $f_p = 0.89$. The response of the resistive layer, as captured by the delayed component of the signal, occurs over a longer time as R grows, such that for large surface resistivities this contribution can be neglected inside the initial ≈ 1 ns time range of the electron peak.

As an indicator for the contribution of the resistive layer to the electron peak amplitude, we define the *relative peak amplitude* as the ratio between the prompt signal and the total signal: $\mathrm{Min}\left[I^p(t) + I^d(t)\right]/\mathrm{Min}\left[I^p(t)\right]$. This is plotted as a function of different surface resistivities in Fig. 5.10. We observe heightened sensitivity to the resistive layer's behavior at the periphery of the pad electrode due to the more immediate signal spreads over the adjacent channels. As $R \gtrsim 100$ k$\Omega/\square$, we enter a regime where the electron peak of the induced signal is virtually unaffected by the delayed component of the signal. This outcome remains consistent even when accounting for the response of the pulse amplifier that reads out the channels. Similar to Sec. 5.2.4, this was accomplished by utilizing an LTSpice amplifier model, treating the induced signals as ideal current sources.

In conclusion, due to the occurrence of avalanches in the amplification region over the several mm wide area covered by the radiator's Cherenkov cone, coupled with the lack of prior knowledge regarding the particle's hit position, it is imperative to reduce the impact of the DLC layer's response on the leading-edge of the signal across the entire surface of the readout pad. We have found that for surface resistivities exceeding 100 k$\Omega/\square$, the electron peak is unaffected by the delayed component on the signal. However, we need to contend with an overall amplitude reduction of around 11% due to the presence of the 60 µm thick insulating layer between the amplification gap and the readout plane. This model can be further developed in order to describe the relation between the temporal resolution for the case of surface resistivities below 100 kΩ. Furthermore, it has the potential to quantify the extent of enhancement in spatial resolution attributable to signal propagation to neighboring channels by including the weighting potentials of the adjacent pads in the calculation.

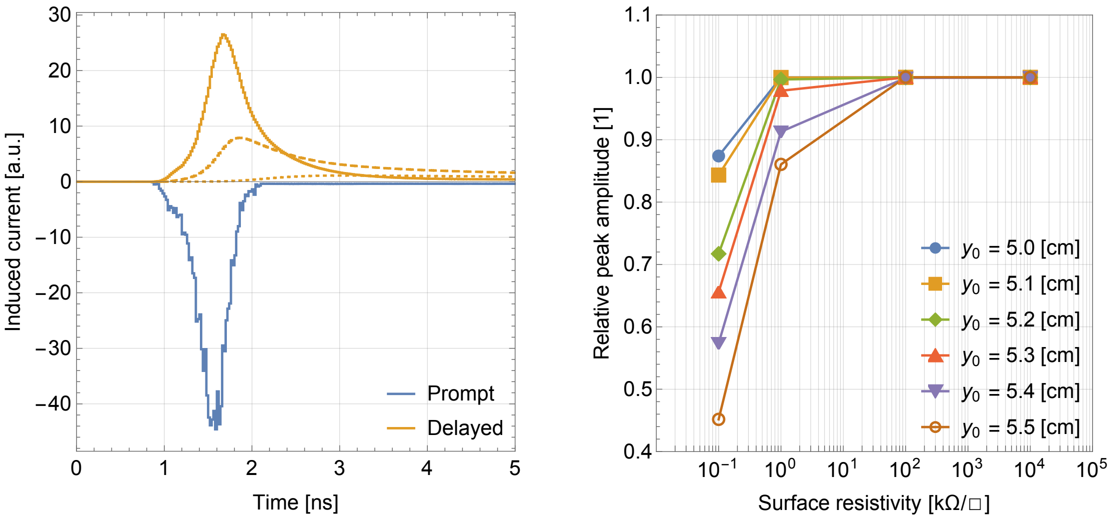

Figure 5.10: **Left:** The prompt and delayed components of the induced signal on the 1 cm wide square pad, which is positioned at the center of the active area ($x_p = y_p = 5$ cm), are determined for a Townsend avalanche initiated at the top of the amplification gap, specifically at the point centered at $x_0 = 0$ and $y_0 = 5.4$ cm. The result is given for $R = 100\ \Omega/\square$ (full line), $R = 1\ k\Omega/\square$ (dashed line), and $R = 100\ k\Omega/\square$ (dotted line). **Right:** The relative peak amplitude as a function of the surface resistivity for different avalanche positions on the pad where $x_0 = 0$. The plot markers represent the calculated values, while the lines are to guide the eye.

5.4 Rate-capability estimation

Because of its non-zero resistance to ground, the resistive layer of our readout causes an ohmic reduction of the electric field within the amplification gap when high gains or high event rates are encountered. The decrease in gain that follows adversely affects the efficiency and timing performance of our device, the degree of which is dependent on the surface resistivity and precise grounding scheme of the resistive layer. For resistive MPGDs, the *rate effect*, here referring to a device's ability to maintain its gain under a certain event rate per unit area, has been theoretically assessed using various methods. For resistive plane configurations like the one discussed in this chapter, previous work estimated the gain reduction as a function of the particle flux Φ [Hz cm^{-2}] for different surface resistivities [139]. This estimation was achieved by taking the limit of the solution (2.4.6) of the Telegraph equation (2.4.1) in the case of a current being imposed on an infinitely extending resistive layer. While this approach captured the qualitative behavior observed in experimental data, it does not account for the boundaries of the resistive readout. Another approach, focusing on the μ-Resistive WELL (μ-RWELL) detector, was presented by G. Bencivenni et al. [140]. They provided the average resistance to ground $\bar{\Omega}$ given the irradiated current over a circular area with a radius r at the center of a circular resistive layer. This resistance could be expressed in terms of the layer's radius c as $\bar{\Omega}(c) \simeq R(2c - r)/2\pi r$, where the voltage drop can then be calculated using Ohm's first law. A numerical approach was employed in another study conducted by Z. Fang et al. [141]. They represented the resistive layer as a discrete electrical system, thus enabling the assessment of the local voltage drops and rate effects for the more complex charge evacuation schemes found in various μ-RWELL prototypes [72] resulting from a position dependent irradiation current density. Our work presents an alternative numerical method based on the FEM, where the Maxwell equations are solved under the quasi-static limit. This method provides the flexibility to handle systems with greater complexity that are technically more challenging to represent using a circuit-based approach, e.g., vertical charge evacuation through embedded resistors [142, 143], or multiple DLC layers [72, 73, 144].

First, we will review the concept of the voltage drop across our resistive layer given an externally impressed direct current (DC) source. After this, the gain reduction will be estimated using precise numerical solutions of the potential in the design of the resistive anode on which a current density from the particle flux is imparted. Using this, we estimate the maximum surface resistivity value that allows the resistive PICOSEC design to be effectively operated within a π beam at the H4 Secondary Beam Line facility of the CERN Super Proton Synchrotron (SPS).

5.4.1 Voltage drop across a thin resistive layer

In this part, we will reexamine the configuration depicted in Figure 2.15. This configuration involves a thin resistive layer electrically connected to the ground and situated along its entire outer boundary at coordinates $x = 0, a$ and $y = 0, b$, which is positioned between the gas gap and the insulating layer. In addition, let us apply an amplification field in the gas gap of strength E_a. Given a charge q deposited on the resistive layer at $t = 0$, currents will start flowing in the resistive layer to compensate for this newly arrived charge, resulting in its seeming decay. As seen in Sec. 2.3.4, the dynamics are governed by the infinite number of time constants given by Eq. (2.3.34), the largest of which, τ_{11}, dictates the time scale over which the charge is horizontally drained by the resistive layer to the ground frame. This happens at a rate set by the maximal time constant of the system, e.g., for $g = 128$ µm, $d = 60$ µm, $a = b = 10$ cm, $\varepsilon_1 = 3.7$, and $R = 10$ M$\Omega/\square$ we have $\tau_{11} = 3.12$ ms. As indicated by Equation (2.3.37), when the endpoint of the resistive layer is shifted to a greater distance, this time constant increases.

Given several charges deposited in the same region in rapid succession, the combined effects of their electric fields within the amplification gap will lead to a localized reduction in E_a. In the limit, we can apply a constant DC-current, represented as $q(t) = I_0 t$, to the resistive layer, rather than introducing a single charge of $q(t) = q\Theta(t)$ [145]. Working in the quasi-static limit, we can reuse the methods outlined in Sec. 2.1.2 in addition to noting that $q(s) = \mathcal{L}(I_0 t) = I_0/s^2$. The steady-state solution can then be found through

$\lim_{t\to\infty}\phi(\mathbf{x},t) = \lim_{s\to 0} s\phi(\mathbf{x},s)$, resulting in the potential on the resistive layer to be

$$\begin{aligned}\phi_3(x,y,z=0) &= \frac{4I_0R}{ab}\sum_{l,m=1}^{\infty}\frac{\sin\left(\frac{\pi lx}{a}\right)\sin\left(\frac{\pi lx_0}{a}\right)\sin\left(\frac{\pi my}{b}\right)\sin\left(\frac{\pi my_0}{b}\right)}{\pi^2\left(\frac{l^2}{a^2}+\frac{m^2}{b^2}\right)}\\ &= 2I_0R\sum_{l=1}^{\infty}\frac{\sinh\left(l\pi\left(a-x_>\right)/b\right)\sinh\left(l\pi x_</b\right)}{\pi l\sinh(l\pi a/b)}\sin\left(\frac{l\pi y_0}{b}\right)\sin\left(\frac{l\pi y}{b}\right),\end{aligned} \tag{5.4.1}$$

where we employ the following notation

$$x_> := \begin{cases} x_0 & x < x_0 \\ x & x \geq x_0 \end{cases}, \qquad x_< := \begin{cases} x & x < x_0 \\ x_0 & x \geq x_0 \end{cases}. \tag{5.4.2}$$

We find back the Ohmic relation between the voltage drop, resistance to ground and the injected current. It is worth noting that the dependence on the size and dielectric constants of the gas gap and insulating layer are absence in the steady-state solution, which is fully determined by the properties of the resistive layer.

5.4.2 Simulated gain drop at high particle fluxes

Due to spatial constraints on the Printed Circuit Board (PCB), the final design of the resistive anode layer uses eight termination points as shown in Fig. 5.11, instead of connecting it along its entire outer edge as was the premise before. A 10 MΩ resistor is connected to each of these points to ensure the minimal impedance at every point on the active area to avoid destructive capabilities of the discharges resulting in the burning of the DLC layer. These additions resulted in us opting for a FEM approach to determine the steady-state solution of the voltage drop across the resistive layer given a circular π beam profile with a rate of 1.9 MHz. Given the exponential relation between the amplification gain and the voltage difference of the mesh and anode, we could deduce the resulting decrease in gain.

Given the 10×10 cm^2 geometry shown in Fig. (5.2), we empress a constant boundary DC-current source $\mathbf{j}_e(x,y,t)$ on the resistive layer starting at $t=0$. As an ansatz, we took the beam spot as circular with a radius of r_b centered in the active area. In polar coordinates, the externally applied current density can be expressed in terms of the particle flux per surface area Φ as

$$\mathbf{j}_e(r,t) = -e_0 n_p G_e \Phi\Theta(r_b - r - a)\Theta(t)\hat{\mathbf{z}}\,, \tag{5.4.3}$$

where e_0 denotes the electron charge, and G_e is the effective detector gain given an applied voltage V_a on the anode. The number of primary charges n_p depends on the quantum efficiency of the photocathode used, and for what follows will be taken as $n_p = 5$, which is a conservative overestimation for a DLC photocathode [112]. In addition, we fix the beam's radius to $r_b = 7.5$ mm. Solving Maxwell's field equations using the electrical

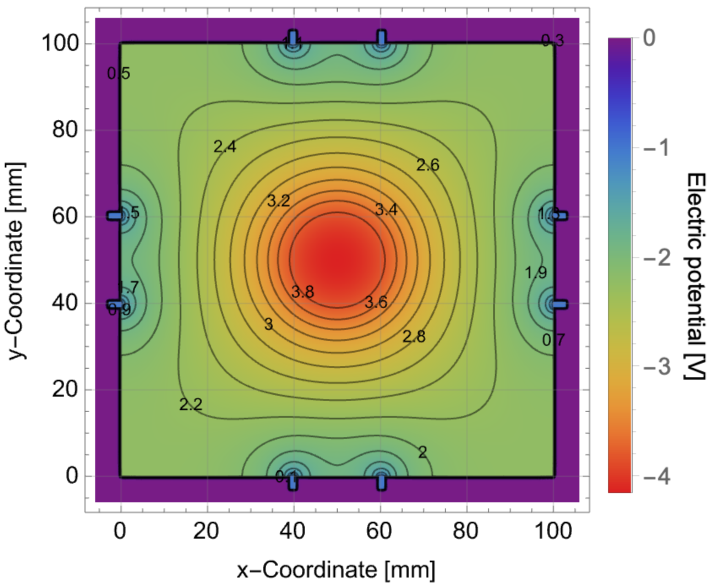

Figure 5.11: Electric potential $\phi(x, y)$ across the resistive layer due to the injection of a current density coming from a 15 mm wide circular beam with a flux of $\Phi = 5.66 \cdot 10^5$ $\mathrm{cm}^{-2}\mathrm{s}^{-1}$ and effective detector gain $G_e = 10^6$.

currents module within the COMSOL® toolkit, the steady-state solution was obtained for various values of G_e, Φ, and R. An example of the potential value across the resistive layer is shown in Fig. 5.11. The voltage drop caused by the constant charge deposition on the resistive readout structure is at its highest at the center of the beam profile on the active area. Subsequently, it gradually tapers as it extends towards the periphery of the beam spot, and its impacts can be detected throughout the entire resistive layer. Due to the presence of the termination resistors, the potential does not reach zero at the connection points of the resistive layer. Following Ohm's law, this sets a lower bound to the rate capabilities that can be achieved as $R \to 0$, since a global voltage drop will occur over the entire layer due to the constant current flowing through the 1.25 MΩ equivalent resistor. What is more, due to the symmetry of the system, the current is equally drained over all connection points, while shifting the position of the beam towards the corners of the active area, an increase in the voltage drop was found proportional to the increased current that flowing over the two neighboring resistors.

Given an amplification field resulting from the potential difference between the grounded mesh and the anode plane set at a voltage V_a we can sum to this the average voltage drop in the beam spot $\bar{\phi} := \int_A \phi(x, y)\, dA/\pi r_b^2$. The result in the irradiated circular area for fixed Φ, and V_a is shown in Fig. 5.13, where G_e is plotted as a function of the average voltage in the beam spot $V_a + \bar{\phi}$ that it causes. Until now, we have treated G_e as independent of the local alteration of the anode voltage due to the charge deposition on the resistive layer, while in truth, it will be coupled

$$G = \exp\left[c_1(V_a + \bar{\phi}) + c_2\right] \,, \tag{5.4.4}$$

where the parameters c_1 and c_2 depend on the gas properties and detector field configuration. As sufficient time passes, an equilibrium state G is established where the surface current density impressed on the resistive layer leads to a voltage reduction in the irradiated area, ultimately resulting in an effective gain that matches the generated surface current density as given by Eq. (5.4.3). To find this stable point, we need to estimate the free parameters in the above relation between the effective gain G_0 and V_a, i.e., the *gain curve* of the detector, in the absence of any rate effects.

The gain curve of the amplification region for our detector can be either obtained through simulation or experiment by varying the amplification field and counting the arrived charge per event. Going with the experimental approach, we employed the configuration discribed in Sec 5.2.1, using a resistive single-channel prototype featuring a pre-amplification gap size of 200 µm. The current I_a on the anode plane resulting from a uniform and $\mathcal{O}(1)$ kHz low-intensity UV LED irradiation was measured using a picoampere meter. Knowing the single photoelectron event rate f_{pe} through the areas of the PH spectra for a fixed exposure time using an MCA, the gain could be estimated using $G_0 = f_{pe}/e_0 I_a$ for different (pre-)amplification fields. The results for two different cathode voltages are plotted in Fig. 5.12 alongside the fitted curves of Eq. (5.4.4) to estimate the trends. We do observe the anticipated exponential relationship where the fit adequately describes the data.

Following Eq. (5.4.3) when $G_e = G_0$, j_e constitutes the expected current density after irradiating over a long time scale, i.e., when the system is in equilibrium. Consequently, the steady-state solution for voltage drop and gain can be estimated by identifying the point of intersection between the two curves. In Fig. 5.13 the gain drop curve is shown as a function of the anode voltage given a 1.9 MHz event rate. For operational voltages of $V_c = 475$ V and $V_a = 275$ V the expected gain is reduced by 5.24% and 8.87% for $R = 10$ M$\Omega/\square$ and $R = 20$ M$\Omega/\square$, respectively. While in this model, an ideal beam of pions is considered, in truth, there will be contamination with particle showers from the interaction of the meson with the material of the experimental setup. This results in a significant increased energy deposit inside the detector geometry, yielding a temporary higher current density on the resistive layer, the degree of which is a function of the rate at which these showers occur. Hence, the results presented here can be regarded as the most favorable scenario.

5.4.3 Conclusion

Incorporating a resistive layer into the readout structure of a robust PICOSEC design will lead to a reduction of the gain within the amplification region when exposed to continuous high particle fluxes. To estimate this rate effect for a 1.9 MHz π beam at the

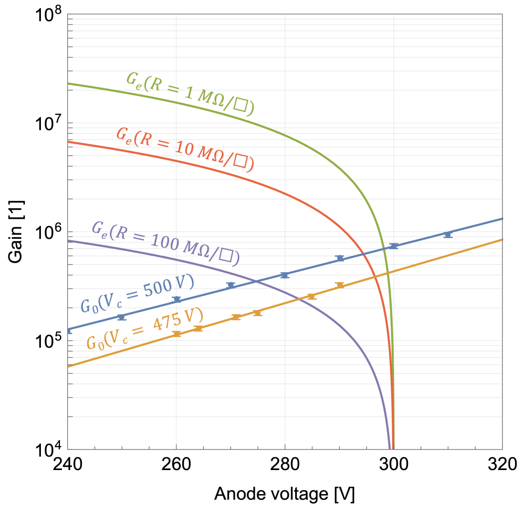

Figure 5.12: Computed relation between the gain G_e of the externally applied current density j_e on the resistive layer as a function of the average voltage drop $V_a - \bar{\phi}$ on the anode. Furthermore, we have depicted the measured gain, represented as G_0, for diverse (pre-)amplifications, indicating the data points with markers, where a 5% error is assumed. The full lines signify the exponential fits for the two gain curves, employing Eq. (5.4.4). The equilibrium state can be identified as the point of intersection between G_0 and G_e.

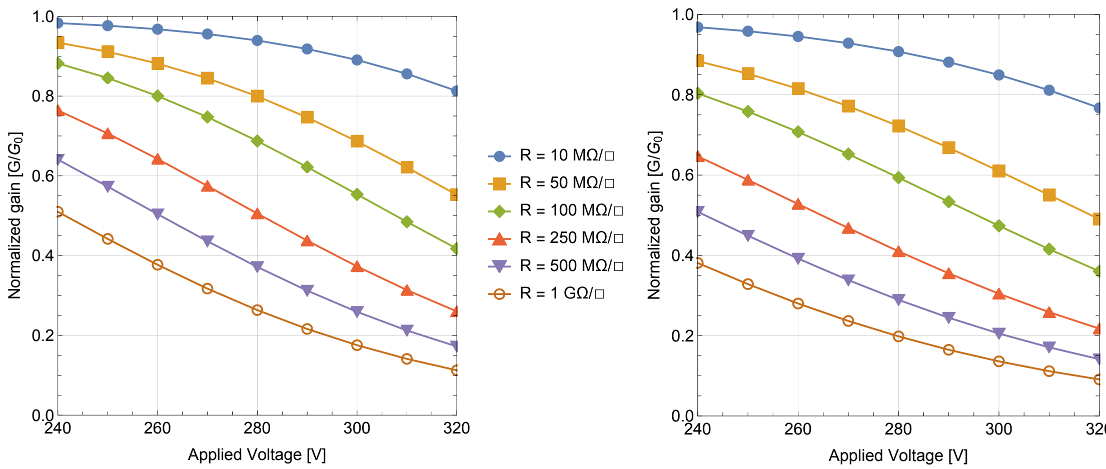

Figure 5.13: Calculated normalized gain for the resistive PICOSEC as a function of the applied anode voltage V_a for different surface resistivities an cathode voltate of -475 V (left panel) and -500 V (right panel),

CERN SPS H4 Beam Line, we obtained the steady-state solution for different surface resistivities by combining the FEM numerical results of the simulated potential drop on the anode layer and the measured gain curve using low rate single photoelectron events. As a result, a below 20% gain drop is found for a surface resistivity of 20 $M\Omega/\square$. Considering the spatial variation of the voltage drop, denoted as $\phi(x, y)$, across the readout plane, implementing gain compensation via an increase in the applied anode voltage will uniformly elevate the amplification field. This elevation can lead to undesirably high gains in regions beyond the beam profile. Furthermore, in cases of non-constant event rates at intermittent intervals without incoming particles, the system will relax to its initial state, leading to an amplification field that surpasses the desired level.

Depending on the final HEP application requirements, this calculation can be repeated with the beam-relevant parameters. This outcome was taken into account, along with the minimal discharge protection prerequisites and a negligible reduction to the rising edge of the electron peak due to the delayed component of the signal, and the final surface resistivity value for production was fixed at 20 $M\Omega/\square$.

This simple resistive layout only allows the evacuation of the deposited charge along the edges of the geometry. Therefore, this design is not scalable for high-rate applications requiring extensive surface area coverage. Within the development of resistive layer-based readout structures within the MPGD family, more sophisticated 'local' charge evacuation schemes have been devised that are suitable for large area coverage [72]. One such structure is realized through the implementation of draining vias in a double resistive layer layout, with the bottom layer ensuring minimal protective impedance [142, 143, 72, 73, 144]. These types of rapid grounding techniques hold the potential to overcome the typical rate limitations associated with large-area resistive readout structures and could be applied to following resistive PICOSEC designs.

5.5 Timing performance

Informed by the theoretical considerations covered in the previous sections, an initial prototype of the resistive PICOSEC has been manufactured and subjected to testing, both in a laboratory setting and in the context of the μ-beam experiments during RD51 test beam campaigns [146]. An image of the readout board is shown in Fig. 5.14. During the production process, particular attention was given to maintaining excellent planarity throughout the active area. This was done to preserve a consistent drift gap size, which, in turn, ensures uniform signal-arrival times (SAT) across the readout. In comparison to the non-resistive counterpart, however, which achieved a deviation below 10 µm [118], the resistive prototype exhibits a roughly threefold higher deviation.

In this section, we aim to experimentally assess the timing performance of both the resistive multi-pad prototype, specifically in the context of MIPs. These measurements were conducted during the RD51 test beam campaigns at the H4 Secondary Beam Line facility of CERN SPS, involving the use of 80 GeV/c muons.

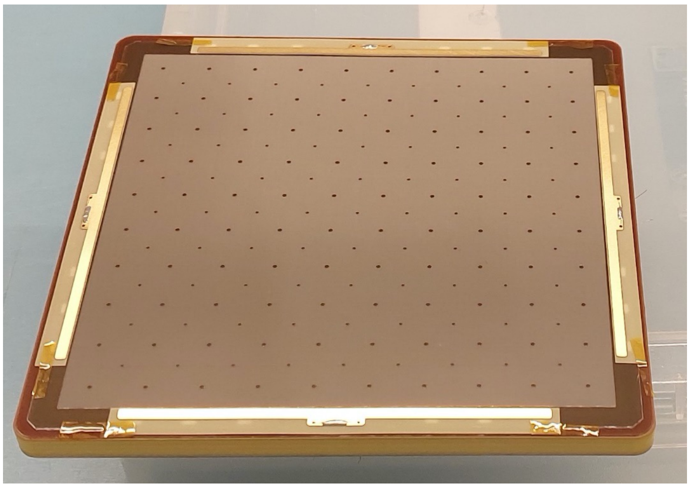

Figure 5.14: Image of the readout board covered by the bulked mesh, for which the distance to the readout is mechanically defined by the pillars positioned above the center and shared corners of the readout pads.

5.5.1 Experimental setup

As shown in Fig.5.15, the North Area – holding both physics experiments and test beam facilities – forms part of the accelerators complex of CERN. The PICOSEC test beams campaigns took place in the H4 beam line positioned downstream of the T2 target.

The experimental arrangement, depicted in Fig. 5.16, consisted of a tracking telescope designed for ascertaining the impact positions of incoming particles. This setup featured three triple GEM detectors[5] with two-dimensional strip readout structures, whose signal was shaped using the APV25 front-end ASICs and subsequently digitized it using the SRS system for all electrode channels. Two Microchannel Plate Photomultiplier Tubes[6] (MCP-PMTs) with quoted time resolutions below 6 ps, served as the timing reference and trigger source [111, 148, 149, 116, 118]. As the data acquisition system, the signal induced by the detector was amplified using the aforementioned high-bandwidth RP pulse amplifier before it was digitized by a LeCroy WR8104 oscilloscope at a sampling rate of 10 GS/s. The tracker and timing data were correlated by means of the event ID, which was generated by the SRS system as a serial bitstream that subsequently was recorded by the oscilloscope and thereby included in the timing data set [118]. While the setup was used to study a multitude of PICOSEC designs, we will focus on the 100 channel multi-pad resistive and non-resistive designs as the *detector under test* (DUT).

The (resistive) PICOSEC prototype was configured with a 180 µm pre-amplification gap, which was mechanically established using polyimide spacers situated between the

[5]The gas mixture used was 70% argon and 30 % CO_2 at NTP.
[6]Hamamatsu MCP-PMT R3809U-50

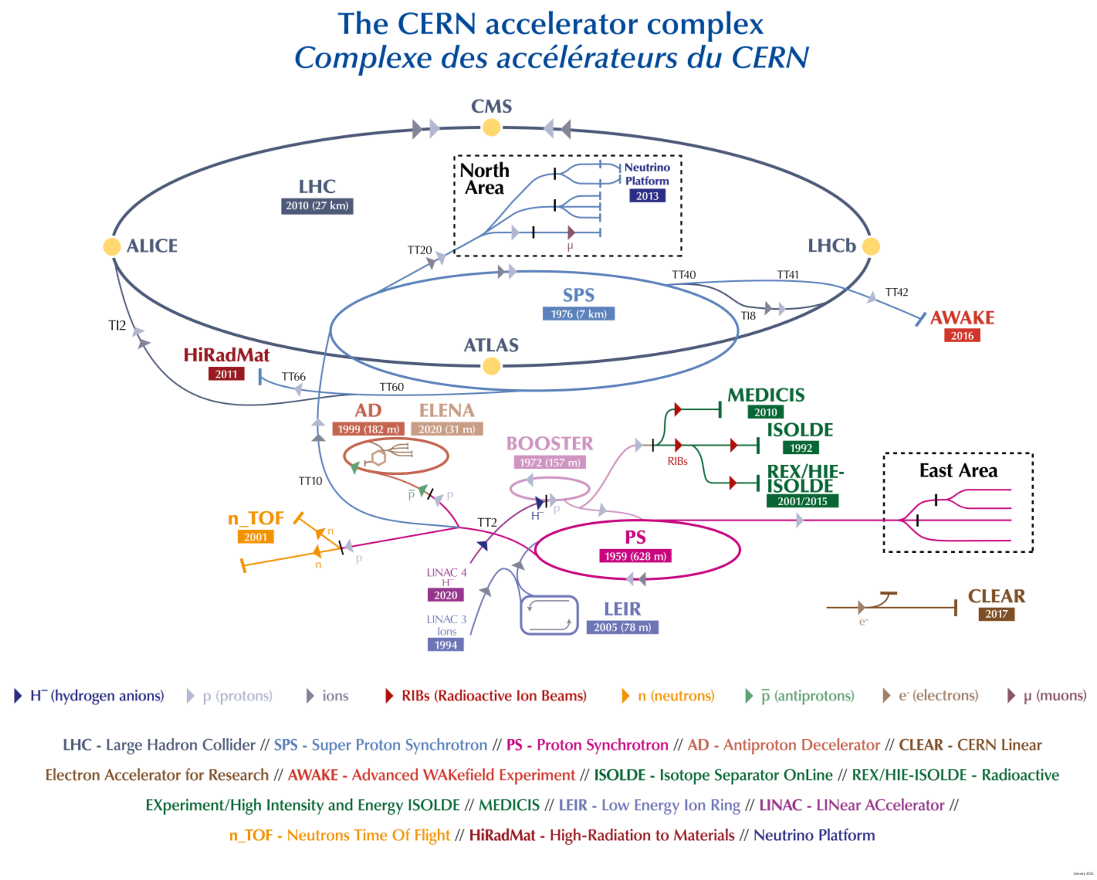

Figure 5.15: Schematic overview of CERN's accelerator complex [147].

CsI photocathode (deposited on a thin chromium layer) and the calendared micro-mesh. These components were situated within a detector housing, which was continually flushed with the COMPASS gas mixture. The housing chamber is illustrated in Fig. 5.17, the design details of which can be found in Ref. [118]. Square pads measuring 9.82×9.82 mm^2 were arranged in a 10×10 readout grid on the readout plane with a 1 cm pitch. To obtain the timing resolution on a pad located on row i and column j, denoted as pad ij for what follows, where $i, j \in \{0, 1, \dots, 9\}$, both MCP-PMTs were aligned to its center as projected on xy-plane. In both prototypes, the mesh was grounded, whereas the anode [7] and the cathode were connected to a CAEN HV supply. Each HV line had a low-pass filter to reduce the noise originating from the HV supply.

[7]In the robust design, the resistive layer is subjected to HV, while the readout plane is grounded. Conversely, in the non-resistive multi-pad configuration, each readout electrode was maintained at HV, and the readout electronics were capacitively decoupled in the amplifier's input stage.

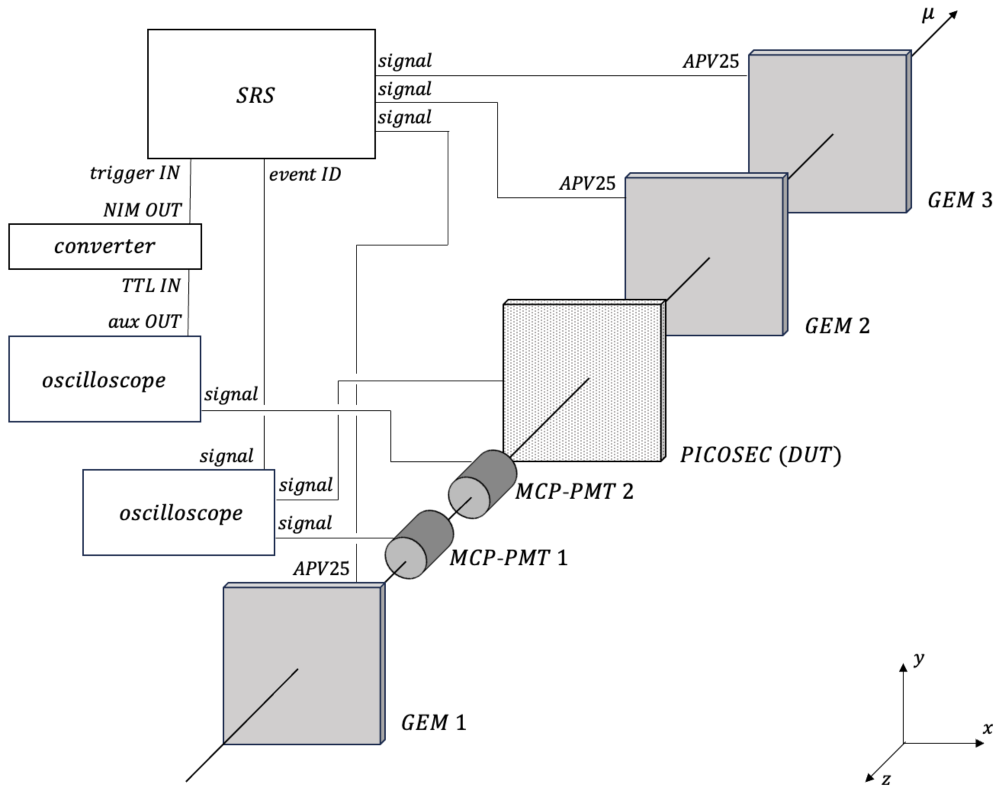

Figure 5.16: Diagram of the test beam telescope and data acquisition chain used during the RD51 SPS test beam campaigns. Here MCP-PMT 2 is used to trigger the acquisition system though the use of a discriminator THL on the signal, while MCP-PMT 1 is used as the absolute time reference to which the PICOSEC DUT is compared. For track reconstruction of the incident muon three triple GEM detectors are employed.

5.5.2 Data analysis methodology

For time sensitive application the implementation of leading-edge discrimination using a fixed THL leads to the problem of *time walk* when dealing with signals of varying heights. As depicted in Fig. 5.18 (left), signals of different amplitudes are associated with different *signal arrival times* (SAT) [2]. Notably, pulses with greater amplitudes are observed to arrive earlier. In the best-case scenario, this approach typically yields timing resolutions within the range of 400-500 ps [150]. Considering the insufficiency of this level of precision for our specific requirements, a more sophisticated methodology must be used where the response time is corrected given the amplitude of the signal. To this end, the method of *constant fraction discrimination* (CFD) is employed, in which the time stamp is determined as the moment when the signal reaches a predefined fraction k of its peak amplitude [2]. This is shown in Fig. 5.18 (right). If the rise time is independent of the signal height, this is expected to fully correct for the time walk.

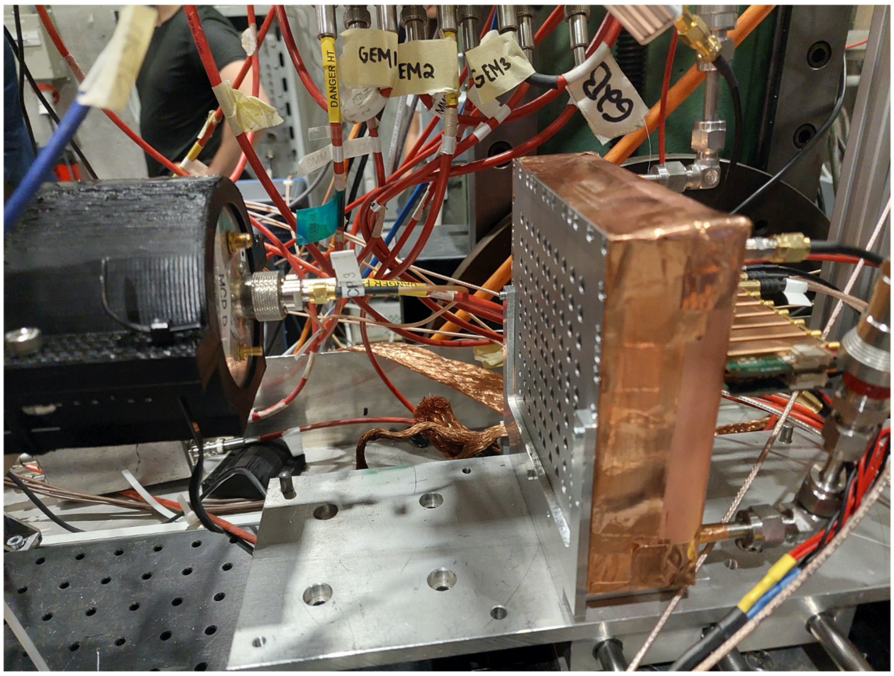

Figure 5.17: Image of the resistive PICOSEC equipped with an pulse amplifier card in the test beam setup. The muons pass through the detector from left to right.

The expected signal structure is comprised of an electron peak[8] and ion tail, as shown in Fig. 5.4. In the case of both the MCP-PMT 1 and PICOSEC signals, the recorded 200 ns of the signal waveform preceding of the event was used to determine the noise level and baseline offset. The amplitude of the electron peak V_{amp} was subsequently determined by calculating the difference between the electron peak's minimum value and the established baseline level. Given linearity between the charge produced and the size of the signal, the distribution of V_{amp} was fitted using a Pólya function of the form given in Eq. 5.1.3. A related quantity is the *electron peak charge*, i.e., charge contained within the electron peak, which is determined through integration of from the start of the signal until the end of the electron peak structure. Note that here, the term electron peak charge is not synonymous with the fraction of the induced charge contributed by the electron signal as given by Eq. 2.3.16. To minimize the noise contribution in the determination of the timing of the event through CFD, a logistic function of the form

$$V(t) = \frac{c_1}{1 + c_2 \exp\left[c_4(c_3 - t)\right]^{c_5}}\,, \tag{5.5.1}$$

was used to fit the rising edge. The to be free parameters c_i, with $i \in \{1, 2, , 3, 4, 5\}$, can be understood as the supremum of the function, the scaling factor for $t = c_3$, the time shift

[8]While labeled as the electron peak this part of the signal already has contributions form the ions drifting in the amplification gap (Fig. 2.10), especially after shaping of the amplifier (Fig. 5.9).

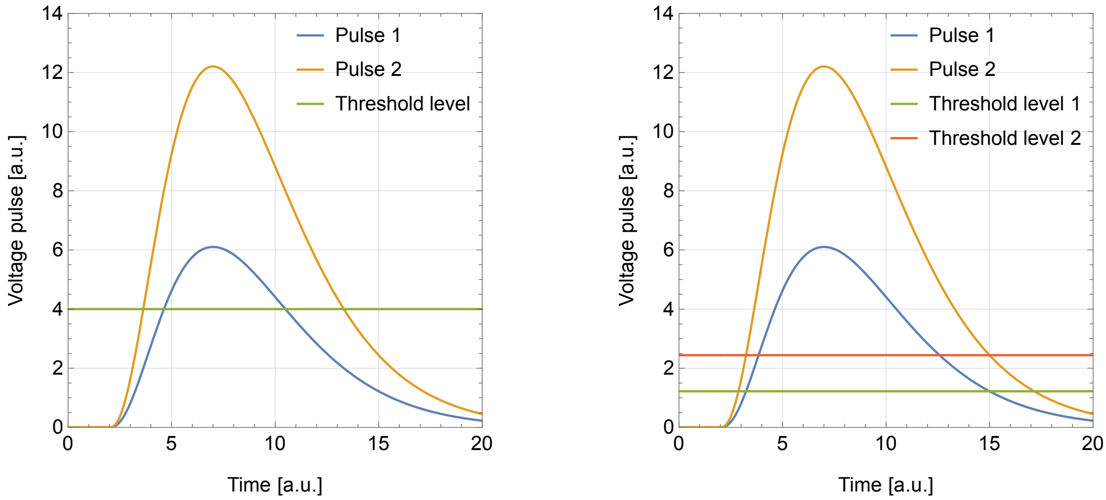

Figure 5.18: Time walk illustration given a fixed discriminator threshold level (THL) for two signals with different peak amplitude. The response time is determined as the point at which the signal crosses the THL value for two methods: the constant threshold discriminator (left) and the constant fraction discriminator (right). For the latter the THL is set to 20% of the maximum signal amplitude.

of the signal, the speed of the function change, and the asymmetry of the growth rate, respectively [112]. The time of the pulse is then taken as the time corresponding where the fitted curve reaches $k = 20\%$ of the max value c_2. The DUT's timing performance in the center of the pad is determined through the residual distribution of the signal arrival time (SAT) difference between the reference (MCP-PMT 1) and the DUT signal. Using the tacking data, a geometric selection criterion was applied to the hit position of the muons, ensuring that the 6 mm-wide Cherenkov cones remained entirely within the pad's area. Furthermore, we only considered events within the effective photocathode diameter of 11 mm in the central region of MCP-PMT 1, given its documented timing performance degradation at its periphery [148, 149]. Finally, the rise time of the leading-edge of the DUT was ascertained by estimating the time it takes for the fitted Sigmoid curve (Eq. 5.5.1) to transition from 10% to 90% of its maximum value.

5.5.3 Results

In what follows, we will present the outcomes of the measurements for two pad electrodes, one for the resistive PICOSEC readout and the other for the non-resistive configuration. The signal rise time and timing performance will be compared at operating voltages that produce comparable signal-to-noise ratios for both systems.

For what follows, the results are discussed for the resistive PICOSEC when operated at −470 V and 290 V for the cathode and anode, respectively. The waveforms obtained

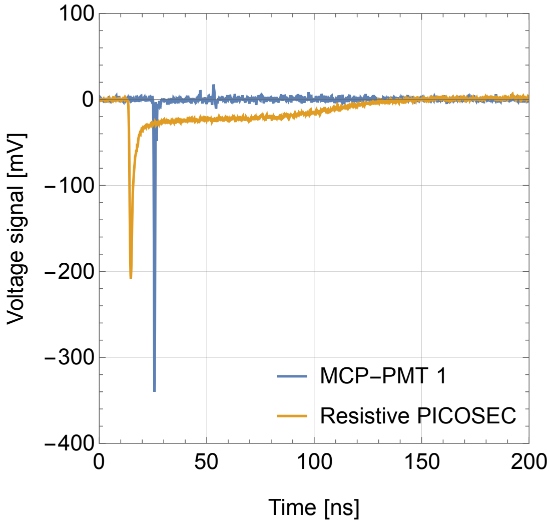

Figure 5.19: Signal waveforms for the reference timing MCP-PMT and the resistive PICOSEC MM operated at −470 V and 290 V for the cathode and anode, respectively.

with pad 17 in the prototype and MCP-PMT 1 for a single muon event are shown in Fig. 5.19, where the duration of the former is significantly shorter compared to the latter due to the absence of any ion tail. The average electron peak amplitude for the resistive PICOSEC across this pad is shown in Fig. 5.20 (left), where lower amplitudes on the edges of the pad result from the sharing of signal with adjacent pads. For the events where the Cherenkov cone is contained within the confines of the pad the distribution of V_{amp} is given in Fig. 5.20 (right), where the distribution was fitted using a Pólya distribution resulting in an estimated average signal amplitude of 130.4 ± 1.5 mV on a background noise an RMS of 1.24 ± 0.49 mV.

The residual distribution of the SAT difference is depicted in Figure 5.21 (left). It was subjected to a Gaussian fit with mean μ and standard deviation σ, which corresponds to the estimated timing resolution of 20.5 ± 0.5 ps. Despite the CFD, it shows an asymmetric tail on the right-hand side of the measured distribution. This phenomenon can be attributed to the presence of relatively diminutive electron peak signals with delayed arrival times, which represent only a minor portion of the overall event dataset. Consequently, as shown in Fig. 5.21 (right), this gives rise to a correlation between the SAT and the charge associated with the electron peak $\tilde{q}$. The relation between the two was phenomenologically gauged using a parametric function of the form

$$\langle \mathrm{SAT}(\tilde{q}) \rangle = \frac{c_1}{\tilde{q}^{c_2}} + c_3 \tag{5.5.2}$$

where c_i for $i \in \{1, 2, 3\}$ are the free parameters that were estimated through the fitting of the data [111]. As shown in Fig. 5.21 (right), this function adequately describes the

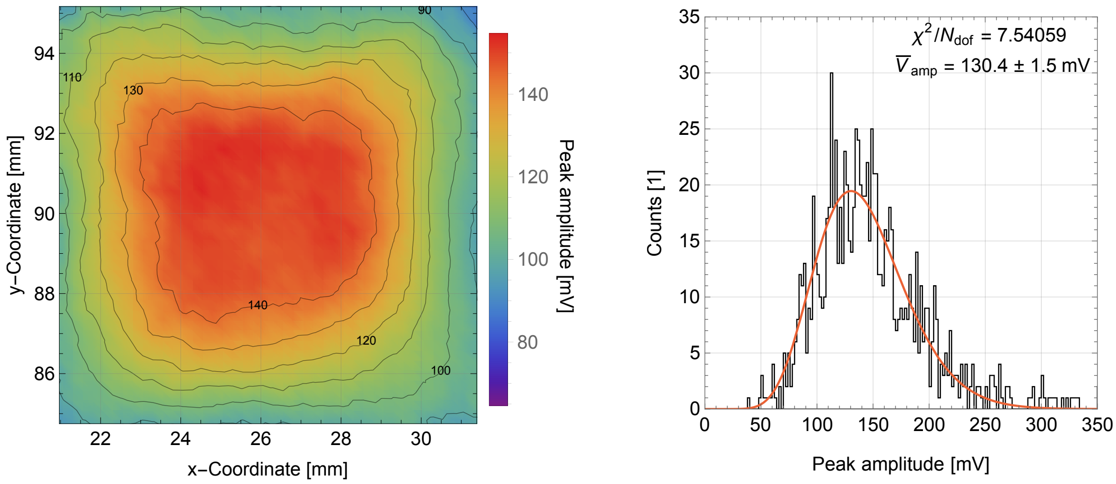

Figure 5.20: **Right:** Peak amplitude as a function of the hit location of the muon track across the pad electrode. **Left:** Distribution of the peak amplitue of the signal pulses in the central area the pad. The mean is determined though fitting with the Pólya distribution.

trend. Similarly, the rise time of the signal is plotted as a function of $\tilde{q}$, resulting in the correlation shown in Fig. 5.22. The notable increase in rise time observed at lower electron-peak charge valuesis ascribed to events occurring outside the central region of the pad.

An identical analysis was performed for pad 27 of the non-resistive multi-pad device. When operated with a cathode voltage of −445 V and an anode voltage of 275 V, we attained a S/N comparable to that observed in the previously mentioned measurement. In this configuration, we determined the mean peak amplitude to be 116.31 ± 1.58 mV, with a baseline noise fluctuation with an RMS of 1.20 ± 0.09 mV. The residual distribution on the difference in SAT between the DUT and reference MCP-PMT is shown in Fig. 5.23, resulting in an improved timing resolution compared with the resistive readout structure of 18.3 ± 0.6 ps. The leading-edge rise time was measured to be 0.747 ± 0.03 ns, which is consistent within the margin of error with the values depicted in Fig. 5.22 for the resistive readout.

In summary, these results indicate that the resistive multi-pad PICOSEC MM retains its the timing performance of below 25 ps at the center of the pads. We note that variation in the timing performance may be ascribed to the inclusion of a DLC layer and Kapton® laminate, alterations in the signal routing and grounding arrangement on the PCB - necessary for accommodating the resistive readout within the detector housing - could also make a non-negligible contribution to the device's sensitivity.

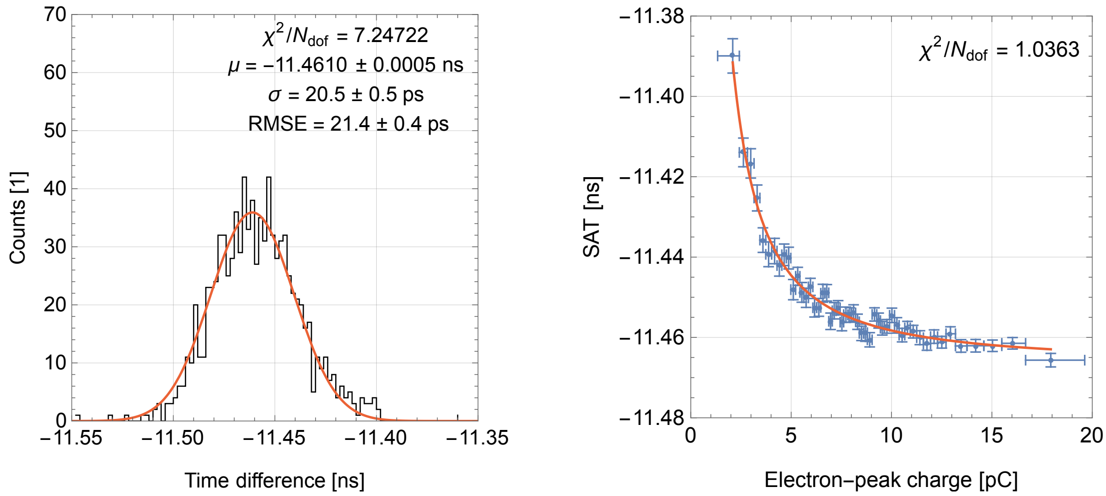

Figure 5.21: **Right:** Residual distribution of the measured time difference between the timing reference and pad 17 in the resistive PICSEC. The distribution was fitted using a Gaussian function (full red line) to determine the timing resolution σ. **Left:** Mean of the SAT as a function of the electron-peak charge. The presented data was fitted (full red line) using Eq. (5.5.2).

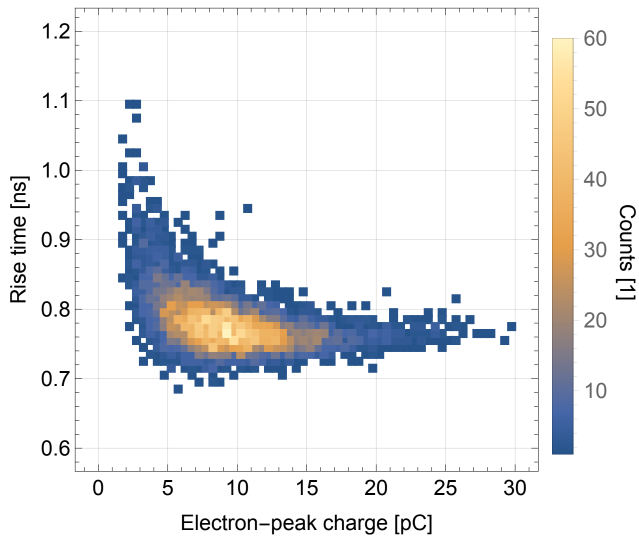

Figure 5.22: Correlation plot between the leading-edge rise time of the signal and the electron-peak charge.

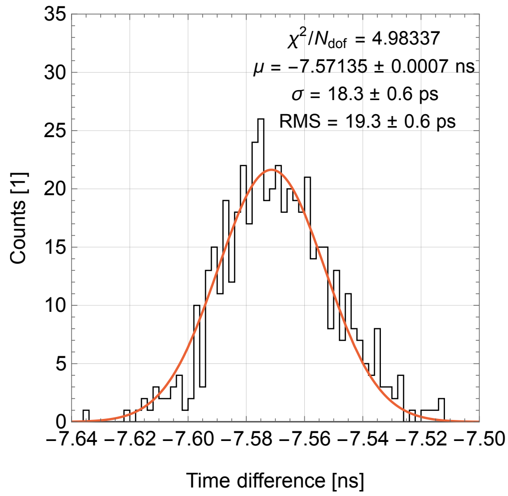

Figure 5.23: Gaussian-fitted residual distribution for the SAT difference between the reference MCP-PMT and pad 27 in the non-resistive multi-pad PICOSEC.

5.6 Summary

The fast timing PICOSEC MM concept successfully pushes the timing resolution with MPGDs below 25 ps for MIPs by employing a two-stage amplification structure alongside a virtually-simultaneous injection of primary photoelectrons at the top of the gas volume. Building upon the encouraging results obtained from the most recent 100-channel prototypes, we have conducted simulation studies to better understand how performance may evolve during the transition to a robust design. In this updated configuration, the readout pads are situated below a thin Kapton® layer, positioned beneath a resistive DLC sheet with a surface resistivity R. A key observation was that the delayed component of the induced current leaves the rising edge of the signal unaffected if $R \geq 100$ k$\Omega/\Box$. To asses the rate-capability, we used FEM calculations to estimate the potential drop across the resistive layer given a specific beam intensity and profile. By incorporating data from effective gain measurements, the expected gain drop was calculated for a wide range of surface resistivities and event rates. In conjunction with the requirement of sufficient quenching of sparks, this lead us to fixing the surface resistivity at $R = 20$ M$\Omega/\Box$ across the 10×10 cm^2 area.

After production, the new multi-pad prototype was extensively tested in the laboratory and test beam. In this chapter, we reported a first comparison between the single-pad response of the resistive and non-resistive multi-pad. We have found that the timing performance remains below 25 ps and that the signal's rise time is preserved.

Part III

Detectors dominated by delayed signal induction

Chapter 6

Resistive 2D interpolation readout structure

In the preceding chapters, specifically in Chapters 2 and 4, we explored the utilization of segmented anode structures for achieving one or two-dimensional localization of an incident particle's position. In the context of Part II, we delved into a method where the location information was derived directly from the sampling of the charge distribution, relying on the prompt component of the signals. Chapter 2 introduced an alternative strategy involving a thin resistive layer AC-coupled in the readout plane. This innovative approach aims at dispersing the signal across neighboring channels, thereby increasing the cluster size of the event.

The discussion in this chapter will shift towards a DC-coupled resistive readout method, wherein the position information is discerned through a charge sharing mechanism between distinct electrodes. As with the AC-coupled readout, this approach significantly reduces the required number of readout channels without sacrificing spatial resolution. The concept of position-sensitive readout using resistive materials has a rich history, spanning over half a century, with its origins tracing back to the one-dimensional case of a wire, which was adopted in numerous experiments [151].

First, we will briefly examine the basic principles of the one-dimensional case before delving into the intricacies of position-sensitive resistive readout schemes, which offer two-dimensional spatial reconstruction. For the latter, the correction maps required for linear position interpolation will be numerically calculated. This computation involves applying the extended form of the Ramo-Shockley theorem for conductive media to the readout electrodes and simulating the device's response using Garfield++. We will account for possible non-homogeneous surface resistivity after production on the level of the time-dependent weighing potential calculation to describe its effect on the spatial performance.

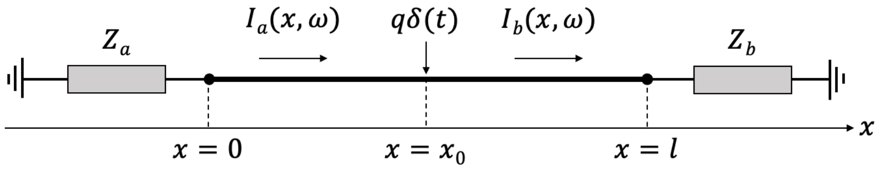

Figure 6.1: Schematic representation of a perturbed transmission line connected to two external impedance elements.

6.1 Charge sharing on a transmission line

In Sec. 2.4 of Chapter 2, the Gaussian solution to the Telegraph equation – depicting the diffusion of a point charge within an infinitely extending thin resistive layer – was discussed. This solution represents the late-time limit of the complete solution that satisfies the Maxwell's equations in the quasi-static regime over the entire time domain. From Eq. 2.4.11 is could be deduce that when a point charge travels through the parallel plate gap above the resistive layer, the induced current on and AC-coupled readout can be calculated using the basic form of the Ramo-Shockley theorem. This calculation uses the static weighting field a parallel plate chamber, effectively treating the resistive layer as if it were perfectly conducting. Subsequently, this computed current 'on' the resistive layer by the movement of the charge can be applied to the layer as an ideal current source at a position $(x, y) = (x_0, y_0)$. The layer's dynamics at late times are then governed by the solution of the Telegraph equation. A similar result regarding a transmission line is detailed in Ref. [57]. Deriving the dynamics of the transmission line following a perturbation at a specific location along its length is, therefore, sufficient to describe the characteristic behavior of such a one-dimensional system. For this case, it can be shown that there is a linear dependence between the position of collection on the wire and the charge read out on both ends [151, 152]. In this section, we will derive this practical property, alongside providing the general relation that will serve as a reference point for the following chapters. What follows is based upon Ref. [153].

6.1.1 Equations of motion

The transmission line model can be represented by an repeating series of lumped components formed out of the circuit shown in Fig. 2.21. In the continuous limit where this segments are taken to be infinitesimally short, the line voltage $V(x,t)$ and the current $I(x,t)$ are related by

$$\begin{aligned} \frac{\partial V(x,t)}{\partial x} &= -RI(x,t) - L\frac{\partial I(x,t)}{\partial t} \\ \frac{\partial I(x,t)}{\partial x} &= -GV(x,t) - C\frac{\partial V(x,t)}{\partial t} \end{aligned} \tag{6.1.1}$$

where the parameters R, L, C and G are the distributed resistance, inductance, capacitance and conductance, respectively, expressed per unit of length of the transmission line. For the system found in Fig. 6.1 where a current source $I_0(t) = q\delta(t)$ has been placed on $x = x_0$ the general solution in the frequency domain is given by

$$\begin{aligned} V_a(x,\omega) &= V_{a+}e^{-\gamma x} + V_{a-}e^{\gamma x} \\ I_a(x,\omega) &= \frac{1}{Z_0}\left(V_{a+}e^{-\gamma x} - V_{a-}e^{\gamma x}\right) \\ V_b(x,\omega) &= V_{b+}e^{-\gamma x} + V_{b-}e^{\gamma x} \\ I_b(x,\omega) &= \frac{1}{Z_0}\left(V_{b+}e^{-\gamma x} - V_{b-}e^{\gamma x}\right) \end{aligned} \tag{6.1.2}$$

where the propagation constant γ and the characteristic impedance Z_0 are expressed as

$$\gamma := \sqrt{(R+i\omega L)(G+i\omega C)}\,, \quad Z_0 := \sqrt{\frac{R+i\omega L}{G+i\omega C}}\,. \tag{6.1.3}$$

The constants $V_{a\pm}$ and $V_{b\pm}$ found in Eq. (6.1.2) must be determined by imposing of boundary conditions. Assuming that the two sides a, b are terminated by frequency-independent impedances $Z_{a,b}$, the boundary conditions of the system sketched in Fig. 6.1 read:

$$\begin{aligned} V_a(0,\omega) &= -Z_a I_a(0,\omega) \\ V_a\left(x_0,\omega\right) &= V_b\left(x_0,\omega\right) \\ I_a\left(x_0,\omega\right) &= I_b\left(x_0,\omega\right) - q \\ V_b(l,\omega) &= Z_b I_b(l,\omega)\,. \end{aligned} \tag{6.1.4}$$

As a result, the constants of the solution are then given by

$$\begin{aligned} V_{a+} &= -\frac{qZ_0\left(Z_0-Z_a\right)\left(Z_b\cosh\left(\gamma\left(l-x_0\right)\right)+Z_0\sinh\left(\gamma\left(l-x_0\right)\right)\right)}{2\sinh(\gamma l)\left(Z_aZ_b+Z_0^2\right)+2Z_0\left(Z_a+Z_b\right)\cosh(\gamma l)} \\ V_{a-} &= \frac{qZ_0\left(Z_a+Z_0\right)\left(Z_b\cosh\left(\gamma\left(l-x_0\right)\right)+Z_0\sinh\left(\gamma\left(l-x_0\right)\right)\right)}{2\sinh(\gamma l)\left(Z_aZ_b+Z_0^2\right)+2Z_0\left(Z_a+Z_b\right)\cosh(\gamma l)} \\ V_{b+} &= \frac{qZ_0e^{2\gamma l}\left(Z_b+Z_0\right)\left(Z_a\cosh\left(\gamma x_0\right)+Z_0\sinh\left(\gamma x_0\right)\right)}{e^{2\gamma l}\left(Z_a+Z_0\right)\left(Z_b+Z_0\right)-\left(Z_0-Z_a\right)\left(Z_0-Z_b\right)} \\ V_{b-} &= -\frac{qZ_0e^{-\gamma x_0}\left(Z_0-Z_b\right)\left(e^{2\gamma x_0}\left(Z_a+Z_0\right)+Z_a-Z_0\right)}{2\left(e^{2\gamma l}\left(Z_a+Z_0\right)\left(Z_b+Z_0\right)-\left(Z_0-Z_a\right)\left(Z_0-Z_b\right)\right)}\,. \end{aligned} \tag{6.1.5}$$

The consequent solutions for the current read out on both ends of the wire are therefore

$$\begin{aligned} I_a(0,\omega) &= -\frac{qZ_0\left(Z_b\cosh\left(\gamma\left(l-x_0\right)\right)+Z_0\sinh\left(\gamma\left(l-x_0\right)\right)\right)}{\sinh(\gamma l)\left(Z_aZ_b+Z_0^2\right)+Z_0\left(Z_a+Z_b\right)\cosh(\gamma l)} \\ I_b(l,\omega) &= \frac{qZ_0\left(Z_a\cosh\left(\gamma x_0\right)+Z_0\sinh\left(\gamma x_0\right)\right)}{\sinh(\gamma l)\left(Z_aZ_b+Z_0^2\right)+Z_0\left(Z_a+Z_b\right)\cosh(\gamma l)}\,, \end{aligned} \tag{6.1.6}$$

while the voltage is given by

$$\begin{aligned} V_a(0,\omega) &= \frac{qZ_0Z_a\left(Z_b\cosh\left(\gamma\left(l-x_0\right)\right)+Z_0\sinh\left(\gamma\left(l-x_0\right)\right)\right)}{\sinh(\gamma l)\left(Z_aZ_b+Z_0^2\right)+Z_0\left(Z_a+Z_b\right)\cosh(\gamma l)} \\ V_b(l,\omega) &= \frac{qZ_0Z_b\left(Z_a\cosh\left(\gamma x_0\right)+Z_0\sinh\left(\gamma x_0\right)\right)}{\sinh(\gamma l)\left(Z_aZ_b+Z_0^2\right)+Z_0\left(Z_a+Z_b\right)\cosh(\gamma l)}\,. \end{aligned} \tag{6.1.7}$$

These general solutions will be of use in subsequent chapters to cover a multitude of different types of resistive readout structures.

6.1.2 Position and timing

Setting the conductance G to zero, the current is confined to the wire and flows though the terminals on its ends. The resulting total charge flowing through Z_a and Z_b is then given by

$$\begin{aligned} Q_a &= \int_0^\infty I_a(0,t)\,dt = \lim_{i\omega\to 0} I_a(0,i\omega) = q\frac{Z_b + R\,(l - x_0)}{Z_a + Z_b + Rl} \\ Q_b &= \int_0^\infty I_b(l,t)\,dt = \lim_{i\omega\to 0} I_b(l,i\omega) = q\frac{Z_a + Rx_0}{Z_a + Z_b + Rl} \end{aligned} \tag{6.1.8}$$

where we can see that we have conservation of charge: $Q_a + Q_b = q$. This constitutes a crucial outcome resulting from the sharing of charge between the two connections. The linearity of the charge flowing from the contacts of the wire with the location of the charge deposition allows for the reconstruction of the event position through

$$x_0 = \frac{lQ_bR - Q_aZ_a + Q_bZ_b}{Q_aR + Q_bR}\,. \tag{6.1.9}$$

This reduces further to

$$x_0 = \frac{lQ_b}{Q_a + Q_b}\,, \tag{6.1.10}$$

when taking the case were both ends are perfectly grounded ($Z_a = Z_b = 0$). The concept of position-sensitive readout, which translates position into corresponding analog signals in a linear manner, has been employed in numerous designs [151]. Compared with pure pixel devices, this leads to a significant reduction of electronic channels with comparably good spatial resolution at the same time.

A similar feat can be achieved using the timing of the signals. When $Z_a = Z_b = 0$, the current flowing from end point B to ground is given by

$$I_b(l,\omega) = q\frac{\sinh\left(x_0\sqrt{iC_lR_l\omega}/l\right)}{\sinh\left(\sqrt{iC_lR_l\omega}\right)}\,, \tag{6.1.11}$$

where $C_l := Cl$ and $R_l := Rl$ are the total capacitance and resistance of the wire, respectively. In Fig. 6.2 (left) the signals are plotted in the time domain for different initial depositions of the charge, using

$$I_b(l,t) = \frac{1}{2\pi}\int_{-\infty}^{\infty} I_b(l,\omega)e^{i\omega t}d\omega\,. \tag{6.1.12}$$

As the charge is deposited further from $x = l$ the current on side b will not only be attenuated due to the sharing of the charge with connection A, but also be delayed in time. This delay can be characterised using the Center of Gravity time of both side A

$$
\begin{aligned}
t_a^{cog}(x_0) &= \frac{\int_0^\infty t I_a(0,t)\, dt}{\int_0^\infty I_a(0,t)\, dt} \\
&= -\lim_{i\omega \to 0} \frac{I_a'(0,i\omega)}{I_a(0,i\omega)} \\
&= \frac{1}{6} CR(2l - x_0)x_0\,,
\end{aligned}
\tag{6.1.13}
$$

and connection B

$$
\begin{aligned}
t_b^{cog}(x_0) &= -\lim_{i\omega \to 0} \frac{I_b'(l,i\omega)}{I_b(l,i\omega)} \\
&= \frac{1}{6} CR\left(l^2 - x_0^2\right)\,.
\end{aligned}
\tag{6.1.14}
$$

Expressed in terms of C_0 and R_0, these quantities are plotted as a function of x_0 in Fig. 6.2 (right), where we find a non-linear dependence on the initial location of q. However, linearity can be restored when taking the difference between the CoG time on both sides

$$
t_b^{cog}(x_0) - t_a^{cog}(x_0) = \frac{1}{6} ClR(l - 2x_0)\,,
\tag{6.1.15}
$$

allowing for a linear reconstruction capability using the time difference between the signal measured on both ends of the wire. This is the basic principle behind some contemporary detector designs, such as the improved RPC (iRPC) [154] of the foreseen upgrade to the CMS Muon system [14] where the strip electrodes are read out on both sides. In addition, this allows for the scaling of the strip-based readout structures to larger areas without impeding the timing capability of the device due to the finite propagation speed of the signal through the electrodes.

6.2 Two-dimensional interpolation readout

Given the interpolation capability of the one-dimensional case of a wire, it is natural that this would be extended to the case of two-dimensional reconstruction using a resistive readout. In this section the basic concepts and merit of these type of position sensitive structures will be discussed before going into the modeling efforts of the next section.

The longstanding concept of charge sharing between electrodes connected to a resistive layer has prompted numerous theoretical approaches to describe its characteristics. Predominantly, these approaches focus on numerically solving the Telegraph equation (2.4.1) to capture the diffusion of the charge. For the square thin resistive layer grounded on each side by a separate electrode depicted in Fig. 6.3 (left), the dependency of the charge sharing between the edge electrodes on the position of a deposited point charge q was described by the work of E. Mathieson [155][1]. Fraser et al. later proposed a description for more complex interpolation structures, including one where four "L"-shaped

[1] In the recent work of W. Riegler [61], the current distribution across the four borders is given in the quasi-static limit of Maxwell's equations.

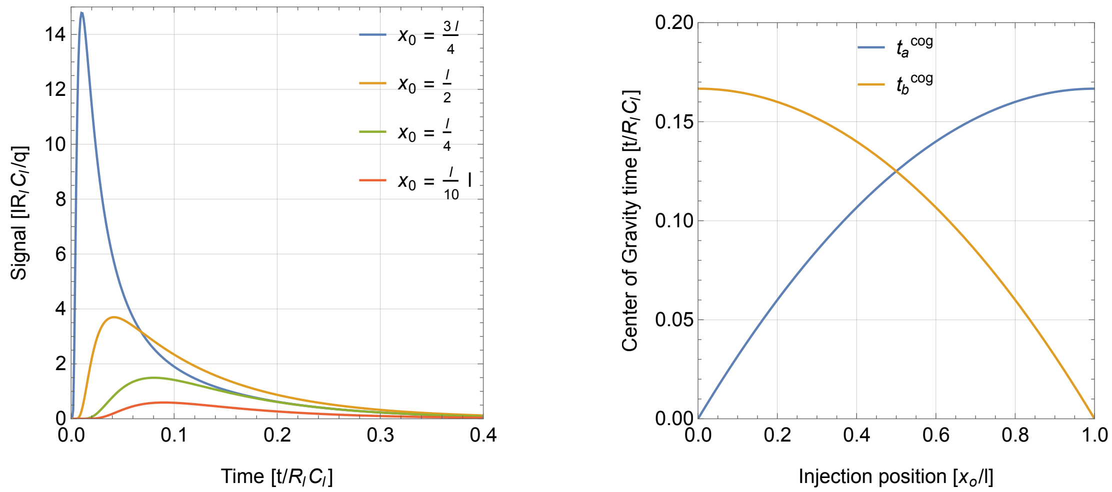

Figure 6.2: **Right:** Current flowing through connection B ($x = l$) to ground form a charge q being deposited at a position x_0. **Left:** Center of Gravity time as a function of the hit position.

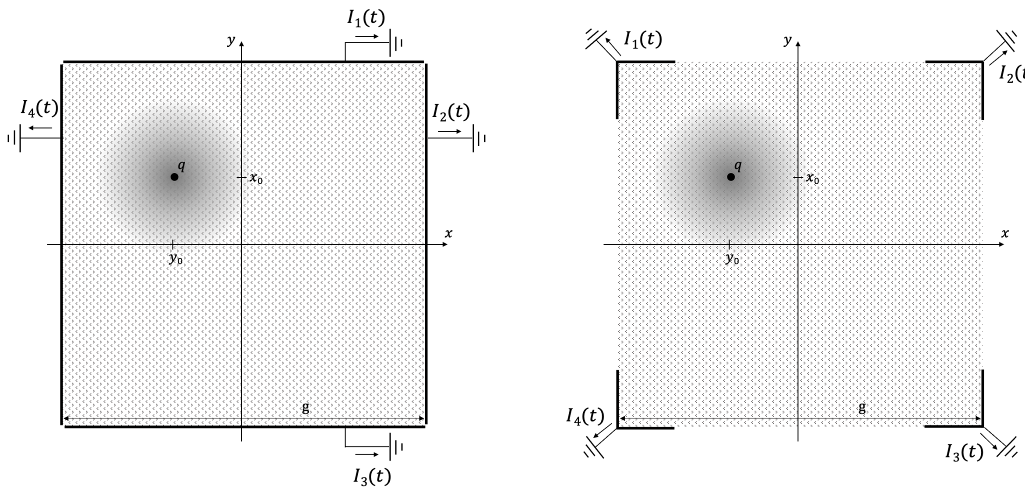

Figure 6.3: **Right:** Position sensitive readout cell using a thin layer material with a finite surface resistivity to share the collected charge between the four strip electrodes placed at the edges of the cell. **Left:** resistive readout cell using L-shaped electrodes to enable hit position dependent charge division.

anodes are located at the corners of a square resistive layer [156, 157], as shown in Fig. 6.3 (right). Let us consider that $x_0, y_0 \in [-g/2, g/2]$ and Q_i for $i \in \{1, 2, 3, 4\}$ are the total collected or induced charge on the four nodes. When performing a linear interpolation using a linear four-node algorithm, alternatively called Anger-logic [158],

$$
\begin{aligned}
x &= \frac{g}{2}\frac{(Q_2+Q_4)-(Q_1+Q_3)}{\sum_{i=1}^{4} Q_i} \\
y &= \frac{g}{2}\frac{(Q_3+Q_4)-(Q_1+Q_2)}{\sum_{i=1}^{4} Q_i} ,
\end{aligned}
\tag{6.2.1}
$$

a non-negligible position dependent reconstruction offset on the edge of the resistive cell from the true collection point can be observed. This issue is a recognized challenge that is inherent in resistive readouts of this family. While sub-optimal, a good understanding of the distortion through theoretical or experimental means allows for the construction of a *correction map* which can subsequently be used to correct the position obtained by the linear interpolation using the measured charge ratios.

The linearity observed in the one-dimensional case can be restored in two dimensions by adopting the specific geometry illustrated in Fig. 6.4. In this configuration, a resistive layer with surface resistivity R_1 is surrounded by concave thin strips with a lower surface resistivity R_2, the values of which are related through

$$
\frac{R_1}{R_2} = \frac{a}{w} , \tag{6.2.2}
$$

assuring the linearity of the interpolation [159, 160]. One can show that when applying a (unit) potential to nodes $N1$ and $N2$ while keeping $N3$ and $N4$ at ground that the steady-state electric potential is linearly dependent on the position [76]. Given Eq. (2.2.14), this explicitly proofs the linear position sensitivity of the readout. Recent applications of this principle can be found in the advancement of position sensitive MCPs [161]. Although practical, this solution leads to issues of incomplete tiling of the readout plane when aiming to cover a larger active area.

Motivated to cover the active area of a detector completely using a resistive anode cell with no dead area, the two-dimensional resistive interpolation readout found in Fig. 6.5 was developed [162]. To minimize linear interpolation distortions it incorporates the idea of a square resistive readout cell adjoined by low resistivity strips with node electrodes placed on its four corners. Using the charge sharing between these corner nodes, the CoG position of the collection position of avalanches inside a readout cell can be reconstructed [76, 163]. An analytical solution for charge division in a position-sensitive silicon detector utilizing this readout was obtained by solving the Telegraph equation for a deposited charge [164]. Nevertheless, this model comes with limitations stemming from the assumption that the border strip resistance is zero. To address this, an RC-circuit approach was employed to better describe the charge sharing phenomenon [165]. In the context of the development of the Micro-Compteur à Trous (MicroCAT)[2] MPGD [166, 167], this two-dimensional interpolation readout structure was proposed by H.J. Besh et al. [168]. For this technology the surface resistances of the low resistivity

[2]Similar to the MicroMegas gas amplification structure the (Micro)CAT separates a drift and amplification region (≈ 200 µm) with a mesh-type structure with circular holes.

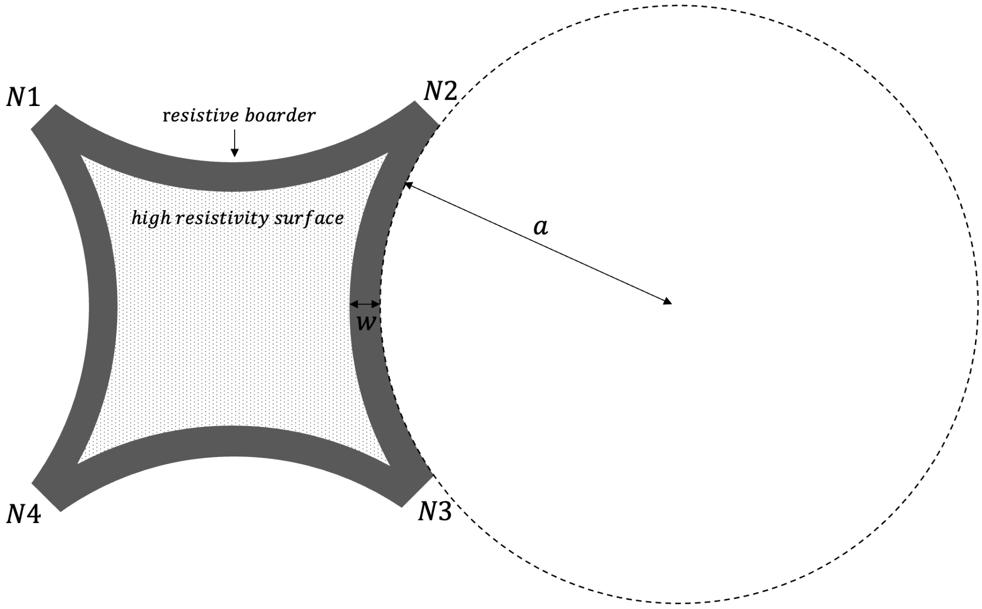

Figure 6.4: Gear's resistive position-sensitive readout concept using four readout nodes, $N1$, $N2$, $N3$ and $N4$, that ensures linear hit position interpolation capability in two dimensions.

strips and the bulk of the high resistivity cell typically range from 1–10 k$\Omega/\square$ and 0.1-1 M$\Omega/\square$, respectively [76]. Within its rate capacity, the resistive positions sensitive anode realizes the performance of a pixel detector, offering a spatial resolution of approximately 200 µm. Notably, this is achieved while reducing the required number of electronic channels per unit area by two orders of magnitude compared to a pixel detector with the same resolution [168]. This concept has recently gained renewed attention in the context of developing a DC-Coupled Low Gain Avalanche Diode (LGAD) device [169, 170], where the signal shape is used for both timing and position measurements. In addition, a recently development on a resistive anode design employes discrete metal electrodes rather than planar resistive layers to capture the induced signal and utilizing an resistor chain for charge division [171].

From Eq. (6.2.2), we deduce that in the limit $R_1/R_2 \to \infty$, the charge sharing between the nodes holds a perfect linear relation with the CoG position of an charge cloud. However, event rate considerations put an upper bound on R_1 since it dominates the time of the charge draining of the system. Simultaneously, the parallel resistive noise of the resistive border imposes a lower limit on the value of R_2 [163]. Due to the finite ratio R_1/R_2, deviations of the position reconstruction from the actual collection point are anticipated when using the linear four-node-encoding algorithm. This is because the collected charge is not entirely confined within the cell structure; instead, a portion of it flows into adjacent cells making the distortion more pronounced in the area near the low

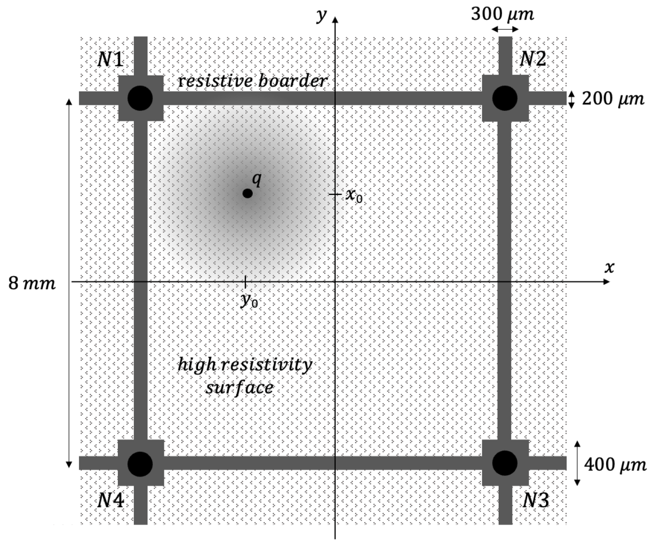

Figure 6.5: Schematic depiction of a 8×8 mm^2 (MicroCAT-type) resistive readout cell within the collective readout structure. The readout nodes, represented by black circles, are positioned at the intersections of the low resistivity strips indicated by the dark gray color.

resistivity border. Alternative interpolation methods are available that try to capture the lost charge information by using the neighboring cells' readout nodes or overcome the distortion through a mixed or weighted interpolation algorithm [163, 172, 173]. Even so, non-uniformity in both R_1 and R_2 during production results in additional distortions that can significantly affect the reconstruction capability of the detector. Therefore, thoroughly assessing this non-uniformity contribution in the design stage before manufacturing resistive position-sensitive anodes is prudent.

6.3 Simulation of the correction map

To enhance the position performance of the resistive position-sensitive anode and align it with the dimensions required for the intended detector technology implementation, it is crucial to employ sound physical and numerical methods. Until now, this was only achieved though the numerical solving of the Telegraph equation. In this section, we will utilize the extended form of the Ramo-Shockley theorem to analyze the MicroCAT resistive position-sensitive anode. This analysis aims as calculating the correction map under both the scenarios of uniform and non-uniform distribution of surface resistivity across the cell.

6.3.1 Model of the readout structure

The MicroCAT operates with a 250 kV/cm drift field in the $\mathcal{O}(1)$ mm drift region and performs gas gain below the mesh structure using a field of 30 kV/cm for an amplification gap of 200 µm using a gas mixture of 90% argon and 10% CO_2 at NTP. To take the MicroCAT structure into account these regions are smoothly connected though the mesh's opening over a region of length ≈ 150 µm across the structure, according to the modeling presented in Ref. [174]. In this work we have treated the mesh as a perfect shield between both regions, and we have exclusively focused on the movement and amplification of charge in a 200 µm parallel plate-like amplification structure yielding a uniform amplification field. Considering that the aim was to calculate the induced signals resulting from moving charges in a gas and the reaction of the resistive material, the Garfield++ toolkit is used. Using the dynamic weighting potential of the device, the induced charge for each electron and ion track could be calculated independently and summed up giving the full signal shape of each node over time.

The response of the central cell – shown Fig. 6.5 – in a 5×5 grid of 8×8 mm^2 resistive cells has been calculated in a parallel plate setup, similar to the ones found in Telegraph equation based simulation work of H. Wagner et al. [76]. Unless stated otherwise, the values of R_1 and R_2 are taken as 100 k$\Omega/\square$ and 1 k$\Omega/\square$, respectively. Added to this is a 1 mm thick ceramic substrate below the anode [163, 174, 175]. In which, resistors R_d were embedded directly below the readout nodes to represent the impedance to ground due to external electronics. This approach of implementing the contribution of external discrete elements into the time-dependent weighting potentials is distinct from the circuit-based approach described in Sec. 2.5.4, yet equivalent.

6.3.2 Dynamic weighting potential

The dynamic weighting potential $\Psi_1(\mathbf{x}, t)$ of the resistive position-sensitive anode is shown in Fig. 6.6 for $R_d = 50$ Ω. The localized nature of the prompt component – it rapidly decays when moving radially away from the node – suggests that the contribution of the delayed component dominates the induced signal. As time progresses, the reaction of the low resistivity border strips becomes apparent due to their small surface resistivity compared to the one hundred times larger value found in the interior of the cell. For practical considerations, a numerical solution of the steady-state of Ψ_i is obtained at a time slice for a finite time, where the solution has already closely converged to its final value. This steady-state solution reveals a non-vanishing weighting potential outside the adjacent cells. This indicates that the draining of charge is not fully contained in one cell since, in general, the node's contribution located in next to adjacent cells will be non-zero.

As the overall induced charge resulting from the motion of a point charge is connected to the steady-state solution through Eq. 2.2.14, and considering that the ions' end points align with the "mesh" plane where $\forall t \in \mathbb{R}$, $n \in \{1, 2, 3, 4\}$: $\Psi_n = 0$, the proportion of the electron's charge induced on the readout nodes is determined by its impact position

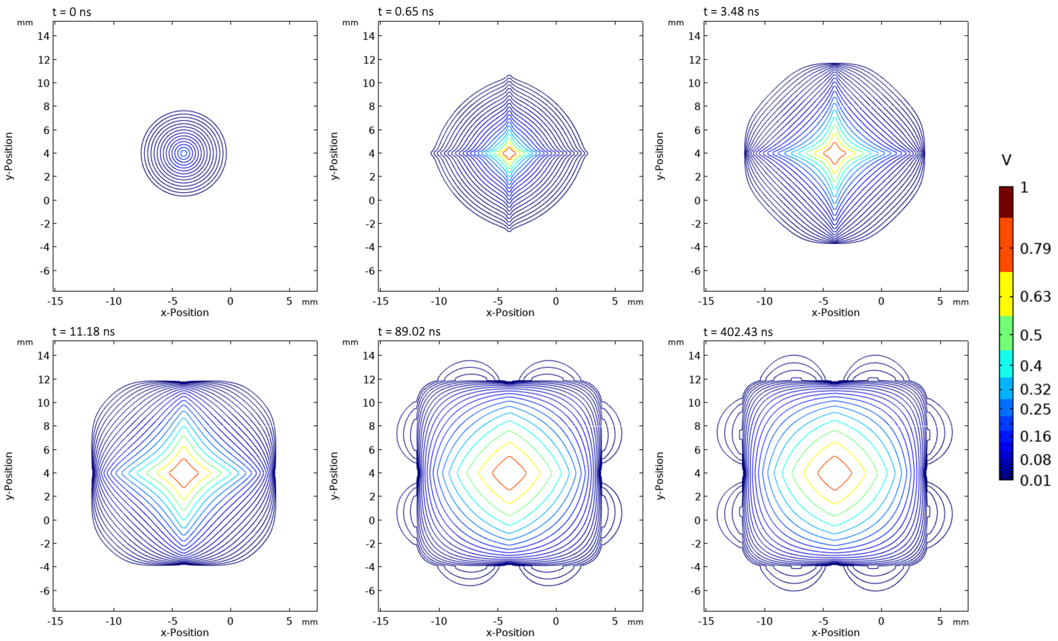

Figure 6.6: Four logarithmic scaled contour plots of the numerically obtained dynamic weighting potential of the upper left readout node of the central cell of the resistive anode for different time slices. Here the upper left plot, taken at $t = 0$ represents $\psi_1^p(\mathbf{x})$ while the steady-state solution is given by the last panel.

according to the steady-state solution of the electrodes. As a result, the total induced charge on node n given the impact position $\mathbf{x}_1 = (x_1, y_1, 0)$ of electron is given by

$$Q_n = \frac{e_0}{V_w} \lim_{t\to\infty} \Psi_n(\mathbf{x}_1, t)\,, \tag{6.3.1}$$

to which the ions do not contribute. To reconstruct the CoG position of a Townsend avalanche containing L electrons, the four-node interpolation algorithm of Eq. (6.2.1) then reads

$$\begin{aligned} x &= \frac{g}{2} \lim_{t\to\infty} \sum_{l=1}^{L} \frac{[\Psi_2(\mathbf{x}_l, t) + \Psi_4(\mathbf{x}_l, t)] - [\Psi_1(\mathbf{x}_l, t) + \Psi_3(\mathbf{x}_l, t)]}{\sum_{i=1}^4 \Psi_i(\mathbf{x}_l, t)} \\ y &= \frac{g}{2} \lim_{t\to\infty} \sum_{l=1}^{L} \frac{[\Psi_3(\mathbf{x}_l, t) + \Psi_4(\mathbf{x}_l, t)] - [\Psi_1(\mathbf{x}_l, t) + \Psi_2(\mathbf{x}_l, t)]}{\sum_{i=1}^4 \Psi_i(\mathbf{x}_l, t)}\,, \end{aligned} \tag{6.3.2}$$

where $\mathbf{x}_l$ is the end position of electron $l \in \{1, 2, \ldots, L\}$.

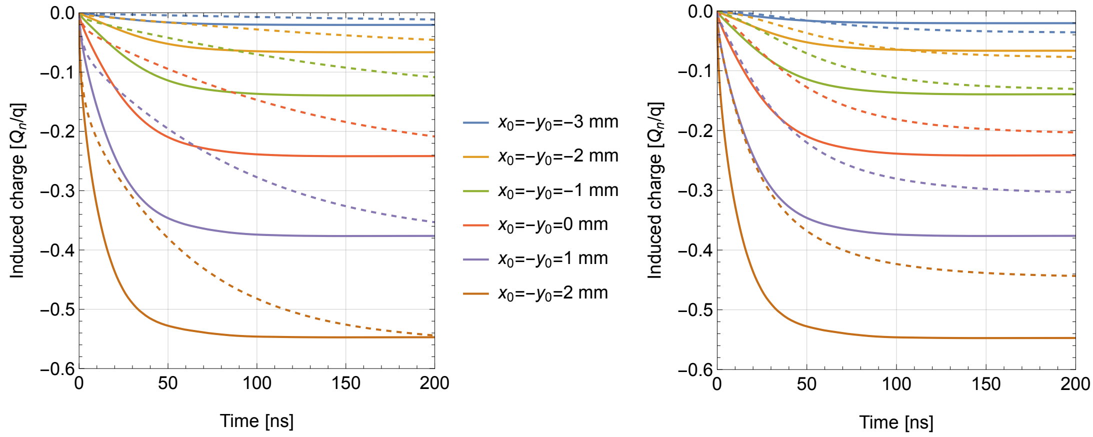

Figure 6.7: Induced charge $Q_3(t)$ on node $N3$ for a point charge q being injected at $(x, y) = (x_0, y_0)$ at $t = 0$ and $R_d = 0\ \Omega$. **Right:** The induced charge for $R_2 = 1\ k\Omega/\square$ are indicated by the full and dashed lines for $R_1 = 100\ k\Omega/\square$ and $R_1 = 500\ k\Omega/\square$, respectively. **Left:** The full and dashed lines illustrate the induced charge for $R_1 = 100\ k\Omega/\square$, with distinct cases of $R_2 = 1\ k\Omega/\square$ and $R_2 = 10\ k\Omega/\square$, respectively.

6.3.3 Induced charge on readout node

From the discussion on the relation of R_1/R_2 and the problem of distortion we can already devise that both R_1 and R_2 play a role in the precise charge sharing between the four nodes. In addition, the higher their respective values, the longer the required integration time of the signal to obtain the collected charge on each channel, as shown in Fig. 6.7 for the case of a point charge being deposited at different points in the central readout cell at time $t = 0$. The early-time spreading of the charge appears to be primarily influenced by the lower surface resistivity of the border strips. In contrast, the duration required to accumulate the total amount of charge is determined by R_2. However, both R_1 and R_2 play pivotal roles in the eventual convergence to the total induced charge.

The cumulative induced charge on the four readout nodes located at the corners of the central cell has been computed for a sequence of avalanches initiated by a single electron at the cathode. These initial electrons were positioned above the central readout cell at distinct positions, which were then reconstructed through the calculated total induced charge on the corner nodes. As a result, the resulting correction map has been calculated by virtue of expression (6.3.2) for the start and end points of all electrons. Using the same coordinate system as in Fig. 6.5 the resulting plot given in Fig. 6.8 shows a distortion-free center of the readout cell which degrades when approaching its border. The same has been observed using the Telegraph equation based models found in literature [76, 163, 173]. In Fig. 6.9 our result is directly compared to the one found in the work of H. Wagner et al. [76], where we find good agreement for a terminator resistors value of $R_d = 100\ \Omega$.

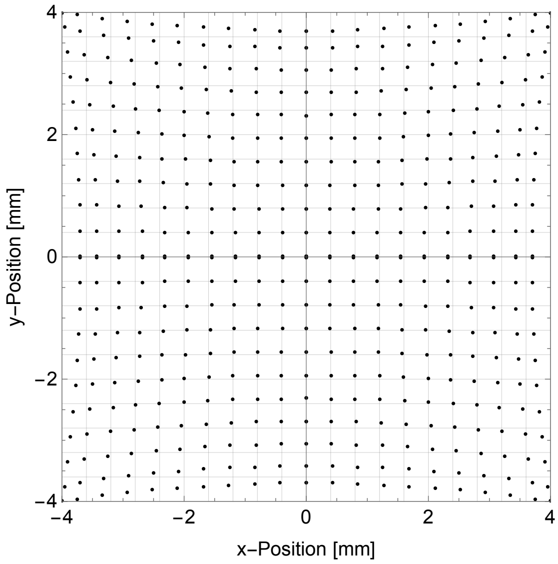

Figure 6.8: Correction map of the central cell in the resistive readout due to linear interpolation. The coordinate system is taken such that the center of the cell corresponds to the origin. The lattice nodes indicate the point of the initial position of a single electron at the cathode. The dots show the reconstructed Center of Gravity positions due to linear interpolation.

To validate the theoretical calculations, we compare our results with measurements conducted by H. Wagner et al. [76]. In their experiment, a predefined quantity of charge was directly injected onto the surface of the low resistivity strip using a needle placed on its surface. Given the manual placement, and the mechanical hysteresis of the needle a uncertainty of ± 50 µm is assumed. The experimentally observed distortions are plotted alongside the theoretical curves in Fig. 6.9, where we find a good agreement with the experimental data.

6.3.4 Non-uniform surface resistivity

Given constraints on the precision of the manufacturing procedure of the resistive anode, non-homogeneity in the surface resistivity can degrade the position capability of the device. An example of this can be found in a GEM-based prototype where a variation of around 20% was observed in surface resistivity [176]. Here, we propose a novel way to calculate the effects of varying surface resistivity using the dynamic weighting potential.

To emulate a relatively severe case of non-uniformity within one readout cell, a map of surface resistivity was generated using Perlin noise, a gradient noise function used in computer graphics to create natural-looking random patterns [177]. The method em-

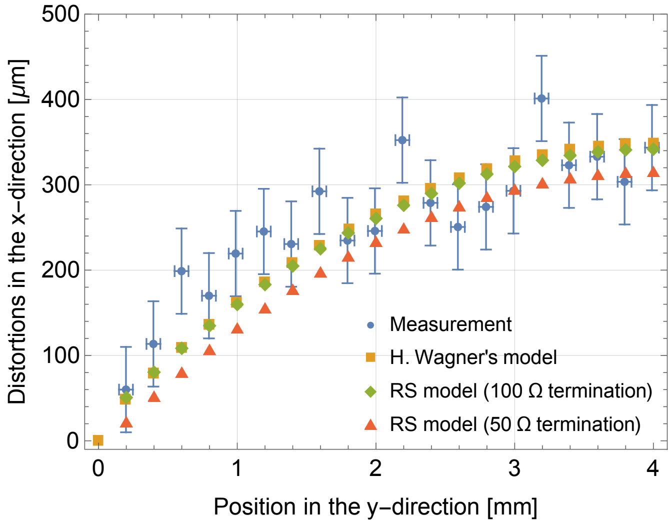

Figure 6.9: Comparison between the experimental distortions in the x-direction at the edge of the resistive cell ($x_0 = \pm 4$ mm) with the simulated results from both our study and the Telegraph equation-based approach detailed in [76].

ploys a grid of gradient vectors that are smoothly interpolated to produce the random pattern shown in Fig. 6.10 (left). By adjusting the initial settings of the noise generator, various aspects of the noise pattern can be controlled, including amplitude and the rate of variation across the cell. The surface resistivity distribution $R_1(x, y)$ on the central high resistivity pad was utilized to calculate the dynamic weight potentials of the four nodes, which broke the system's symmetry. Following the procedures described in the previous subsections, this asymmetry could be observed in the correction map displaying the reconstructed positions of the event's CoG, as shown in Fig. 6.10 (right). The more pronounced deviations from the ideal correction map are observed in the region around the peaks and valleys of $R_1(x, y)$. In these areas, the reconstructed positions appear to be either repelled or attracted to the center of the feature, respectively.

While applied to the case of the MicroCAT, the methodology of incorporating the effect of non-homogeneous surface or volume resistivity in the modeling efforts through a randomly generated Perlin noise map can be applied to any resistive detector. Specific technologies can be highly sensitive to these variations, such as the case of the 4D tracking RSDs where an expected roughly factor two degradation in spatial resolution is reported for a 2% variation in surface resistivity [178]. Hence, simulations of this nature can be employed to estimate the sensitivity of the performance of the designed structure to anticipated non-uniformity in the resistive elements during production.

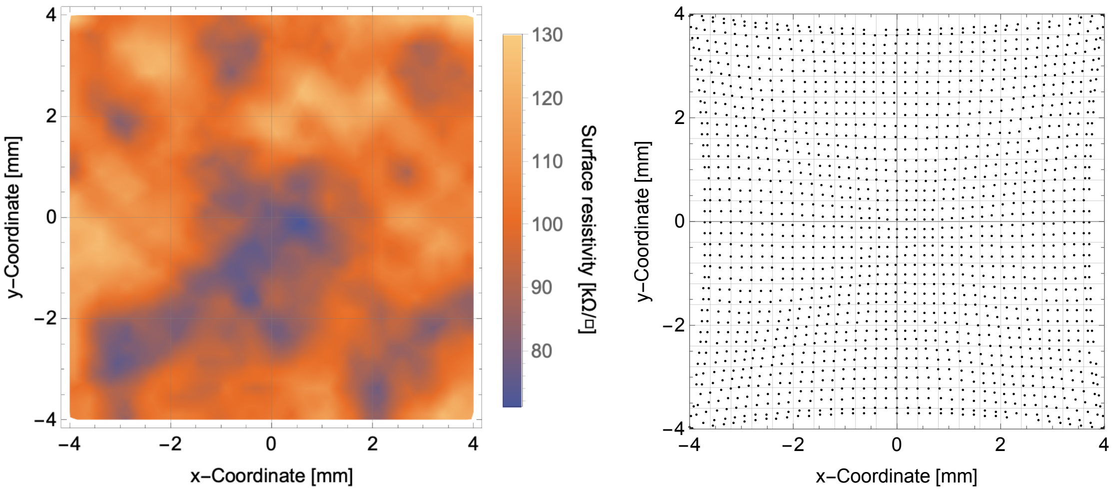

Figure 6.10: **Right:** The surface resistivity distribution $R_1(x, y)$ across the central readout cell as randomly generated using Perlin noise. The variation in values is around the central value of 100 kΩ/□. **Left:** Theoretical correction map form linear interpolation in the presence of a non-uniform resistive readout cell for $R_d = 50\ \Omega$.

6.4 Summary

Within their rate capabilities, resistive positive-sensitive readouts can be used to significantly reduce the required number of readout channels without loss of localization precision. While the linearity of the position interpolation can be preserved going from the one-dimensional case of a wire to a two-dimensional readout, this is only the case when adopting a specific concave configuration that does not allow for fulll tiling of the readout plane. Consequently, this limitation led to the development of alternative readout structures, exemplified by the MicroCAT readout. This structure utilizes a tiling arrangement of square resistive cells, each equipped with readout nodes at the corners. As a result, employing a linear position reconstruction using the total charge induced on readout nodes would result in deviations of the reconstructed position from the CoG position of an event. To study the accuracy of the implementation of the extended form of the Ramo-Shockely theorem in Garfield++, we calculated the correction map of the readout for Townsend avalanches in the amplification region. The resulting map captures the measured interpolation distortions within the experimental uncertainty. Additionally, these results are found to be consistent with those from previous simulation studies using RC networks. Furthermore, the effect of non-uniformity in surface resistivity within a readout cell was addressed by incorporating a surface resistivity map, generated using Perlin noise, into the correction map.

Chapter 7

3D Diamond detectors

Following the stringent requirements of future hadron machines, the 3D diamond detector adopts a novel resistive readout architecture to overcome the anticipated challenges. The response of the resistive electrodes will be characterized using a transmission line description of the system, which will subsequently be compared to the full-time-dependent weighting potential approach. Given pion hits, the current response will be calculated, the shape of which will be analyzed.

7.1 Concept and working principle

As highlighted in Chapter 5, the design of detectors for upcoming high-luminosity hadron machines, such as the HL-LHC, encounters the significant challenge of reconstructing the trajectories of an unparalleled density of charged particles. In addition to this is the expected increase in flux of ionizing particle leads to a higher level of radiation exposure for the detectors. For instance, the sensors positioned closest to the interaction points in the vertex locator of the LHCb experiment, scheduled for installation in 2032, are expected to withstand a radiation dose of $\mathcal{O}(10^{17})$ 1 MeV $\mathrm{n_{eq}}$ cm^{-2} over a ten year period [179]. This engenders concerns regarding potential radiation damage to sensors and front-end electronics throughout their operational lifespan [180].

Semiconductor sensors comprised of diamond have demonstrated exceptional radiation tolerance compared to contemporary silicon devices [181, 182]. This resilience is further enhanced by adopting the innovative three-dimensional readout structure illustrated in Fig. 7.1, where the electrodes run parallel with one another inside the bulk of the sensor [183, 184, 30]. The columns used as the signal readout are interleaved with biasing columns, where a potential difference is applied between them to generate the motion of the free electron-hole (e-h) pairs. Compared to the more traditional planar sensors, this approach shortens the charge carrier path within the material, significantly improving both the response speed and charge collection efficiency [185]. This characteristic proves especially valuable in detectors with substantial charge-trapping mechanisms, as seen in diamond or silicon sensors exposed to high radiation levels. In contrast to their silicon

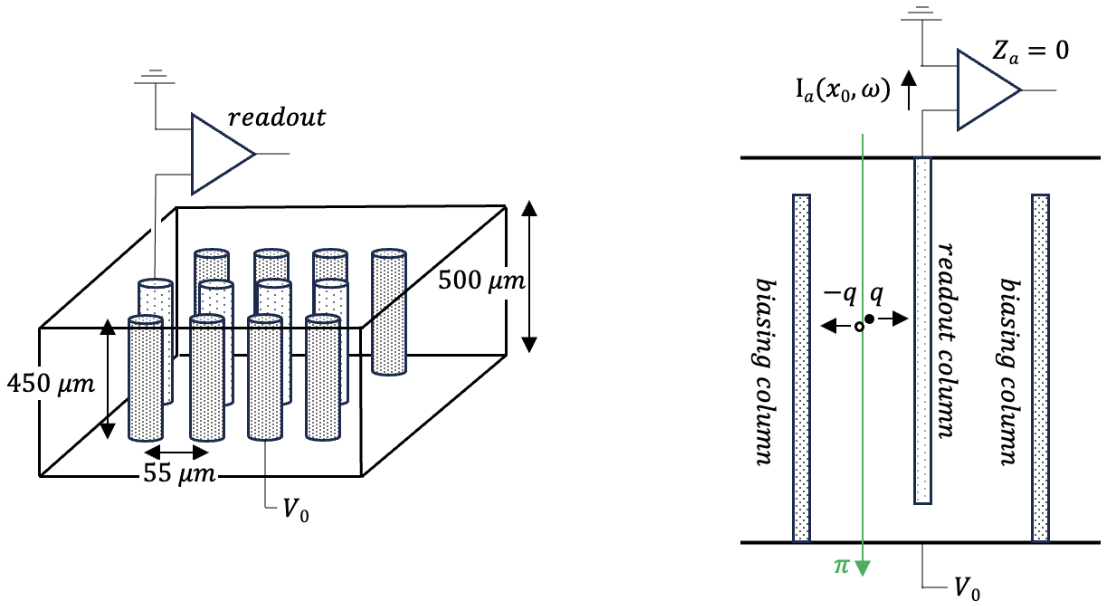

Figure 7.1: Schematic depictions of the 3D diamond sensor's geometry. **Right:** Dimensions of the sensor with a pixel cell size of 55×55 μm^2 comprised of a central readout pillar (light gray) and four biasing pillars (dark gray) placed at the corners. **Left:** Projected view of a electron-hole pair form the primary interaction of a incident pion. The applied potential difference guides the oppositely charged carriers to the readout and biasing columns.

counterparts, the columnar electrodes comprising the 3D architecture are obtained by focusing a femtosecond laser within the bulk domain to cause a local phase transition to a resistive composite of DLC, amorphous carbon, and graphite [186, 187]. Depending on the production parameters, the resulting electrodes have a total end-to-end resistance in the range of $\mathcal{O}(10^5 - 10^6)$ Ω over their 450 − 500 μm length [188], categorizing them as resistive electrodes. Further details on this innovative fabrication process can be found in Ref. [180, 188]. Additionally, diamond exhibits a low leakage current owing to its large energy gap, possesses a small dielectric constant leading to low capacitance, and its carriers demonstrate high mobility and saturation speed compared to silicon [189]. The latter characteristic makes it appealing for timing applications by reducing the spread in the collection times of charges. However, the drawbacks of using diamond include the generation of low signal amplitudes from energy deposition by passing particles owing to its sizable energy gap [189], as well as the existing challenge of large-scale production [190].

Within the INFN TIMESPOT[1] R&D project framework, the manufactured 3D diamond devices use single-crystal chemical vapor deposited (sCVD) diamond samples with

[1]TIME and Space real-time Operating Tracker.

a engraved pixel size of 55 × 55 µm^2. Typically, rows of columns are connected together in a single readout channel. The overall device thickness is 500 µm, and the resistive pillars run to approximately 50 µm from the opposite surface. For these sensors a sub-100 ps timing resolution hase been demonstrated for MIP [180] with good detection efficiency, making them a good candidate for tracking applications in future experiments.

7.2 Transmission line description

Considering the ohmic composition of the pillar electrodes, we will first cover the working principle of the 3D Diamond detector concept using a transmission line description by arguing that the resistive readout columns can be approximated as such. As the electrons and holes propagate in the bulk diamond, the induction of signal on these columns can then be seen as ideal currents — calculable using the basic Ramo-Shockley theorem with a static weighting potential — that propagates through a wire after injection [57]. This method, coupled with KDetSim [191] for charge transport, has been used by L. Anderlini et al. [188] to enhance the understanding of experimental findings and explore potential optimizations, while circumventing the more involved TCAD simulations (e.g. [192]). The details of this strategy for the 3D diamond sensor was worked out by G. Passaleva and W. Riegler [193], the results of which will be the topic of this section. The aim is to derive the response of the transmission line to rapid signal injections and provide a toy model example of how these ideal currents look like for this readout architecture.

7.2.1 Transfer function from injection of charge

For the following derivation we will rely on the results already obtained in Sec. 6.1, where we studied the system depicted in Fig. 6.2 perturbed by the injection of charge q at position $x = x_0$ along the transmission line's length. By adopting appropriate boundary conditions, this will provide us with a delta response function for the terminal reading out the transmission line.

If taking one of the sides to be perfectly insulating, i.e., $Z_b \to \infty$, the current flowing through Z_a, as given by Eq. (6.1.6), can be written as

$$I_a(0,\omega) = qZ_0 \frac{\cosh(\gamma(l - x_0))}{Z_0 \cosh(\gamma l) + Z_A \sinh(\gamma l)} \, . \tag{7.2.1}$$

Here, we have reversed the sign of the current to be compliant with the conventional direction of the induced current. When assuming that there is a vanishing impedance to ground on side A (Z_a=0), the above equations reduces to

$$I_a(0,\omega) = q \frac{\cosh(\gamma(l - x_0))}{\cosh(\gamma l)} \, . \tag{7.2.2}$$

As depicted in Fig. 7.2, a set of four bias columns encircle a single readout column, with the separation between the bias pillars measuring 55 µm. This system can be

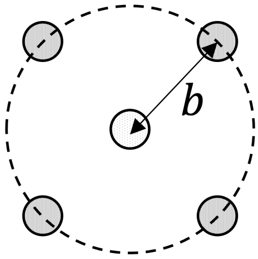

Figure 7.2: Approximation of the readout pixel by a cylindrical chamber.

approximated by situating the readout pillar within a cylindrical chamber of a radius $b = 55/\sqrt{2} \approx 40$ µm, as depicted in Fig. 7.2. For this system, the capacitance and inductance per unit of length of the readout pillar are given by

$$C = \frac{2\pi\varepsilon_0\varepsilon_r}{\ln\left(\frac{b}{a}\right)}\,, \quad L = \frac{\mu_0}{2\pi}\ln\left(\frac{b}{a}\right)\,, \tag{7.2.3}$$

respectively. Here a denotes the radius of the readout pillar, ε_r the relative permittivity of the bulk diamond, and μ_0 the permeability of free space. Taking $a = 6$ µm, $l = 450$ µm and $\varepsilon_r = 5.7$, the total capacitance and inductance of this electrode is

$$C_l = Cl \approx 75.2 \text{ fF}\,, \quad L_l = Ll \approx 0.17 \text{ nH}\,. \tag{7.2.4}$$

The impedance resulting from the inductance is expressed as $Z = i\omega L_l$, equating to 1.07 Ω at a frequency of 10^9 Hz. This value is inconsequential compared to the overall resistance of $R_l = 300$ kΩ of the pillar and can, therefore, be disregarded. Furthermore, we make the assumption of a negligible transconductance $G \approx 0$. As a result, Eq. (7.2.2) equates to

$$H(x_0,\omega) := \frac{I_a(0,\omega)}{q} = \frac{\cosh\left[\sqrt{i\omega R_l C_l}(1 - x_0/l)\right]}{\cosh\sqrt{i\omega R_l C_l}}\,, \tag{7.2.5}$$

which is written in the form of a transfer function $H(x_0,\omega)$; capturing the dynamics of the graphitic pillar. The characteristic time constant that governs the system's dynamics is $\tau := R_l C_l \approx 2.26$ ns. Fig. 7.3 (left) shows the bandwidth of the transfer function of different signal induction points. Given a general injection current $I_{\text{ind}}(t)$ at $x = x_0$ instead of $q\delta(t)$, this current needs to be convoluted with the normalized impulse response function

$$H(x_0,t) = \frac{1}{2\pi}\int_{-\infty}^{\infty} H(x_0,\omega)e^{i\omega t}\,d\omega\,, \tag{7.2.6}$$

in the time domain to deduce the current observed at terminal A. Since for small and large values of ω Eq. (7.2.5) is exponentially suppressed the above integral can be evaluated numerically, with the exception of $x_0 = 0$ where $H(0,\omega) = 1$. The result of this is shown in Fig.7.3 (right), where the signal is delayed in its arrival time and reduced in amplitude as the injection distance from the terminal is increased. In the case of our

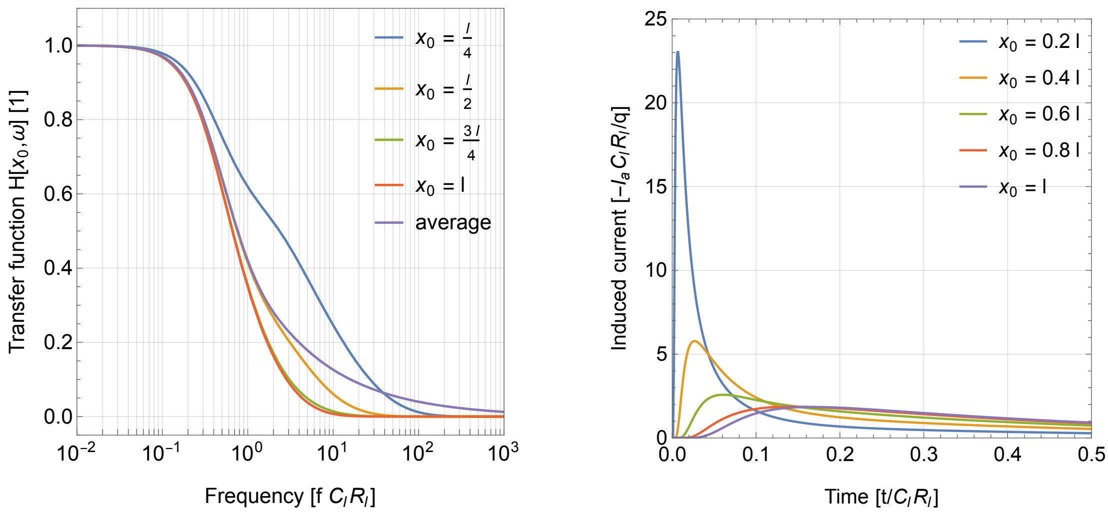

Figure 7.3: **Right:** Transfer function of the response of the transmission line readout electrode. **Left:** Signal on terminal A form the injection of charge q at different locations x_0.

diamond sensor, $I_{\text{ind}}(t)$ denotes the current induced on the pillar from the movement of the electron-hole pairs as if the readout electrode was a perfectly conducting metal rod. This calculation can be achieved by applying the basic form of the Ramo-Shockley theorem, wherein the static weighting potentials are computed for N azimuthally symmetric ring electrodes, dividing the readout column along its length. The resultant currents can then be introduced into the transmission line at positions corresponding to the centers of their respective rings by utilizing Eq. (7.2.6). By aggregating all contributions, this process produces the measured current read out from the end of the resistive pillar.

Electron-hole pairs are generated in clusters throughout the path of the incident particle. When the trajectory of this particle is assumed to be parallel to the readout column, then, on average, this results in a uniform distribution of primary charge along a line. With the injection of this constant line charge on the transmission line, the average transfer function is given by

$$\tilde{H}(\omega) = \frac{1}{l}\int_0^l H(x_0, \omega)\, dx_0 = \frac{\tanh\left(\sqrt{i\omega R_l C_l}\right)}{\sqrt{i\omega R_l C_l}}\,, \tag{7.2.7}$$

which is shown in Fig. 7.3 (left). In the time domain it reads

$$\tilde{H}(t) = \frac{1}{2\pi}\int_{-\infty}^{\infty} \tilde{H}(\omega) e^{i\omega t}\, d\omega\,. \tag{7.2.8}$$

One can show that, for late times $t > 0.2 R_l C_l$ the expression $\bar{H}(t) \propto \exp\left(-2.5t/R_l C_l\right)$ emerges. This result aligns with the distinctive exponential decay pattern observed in the solution of the Telegraph equation, as discussed in Sec. 2.4.

According to Eq. (6.1.13), one can calculate the Center of Gravity (CoG) time of the transfer function through

$$t_{\text{cog}}(x_0) = R_l C_l \frac{x_0(2l - x_0)}{2l^2}\,, \tag{7.2.9}$$

which is shown in Fig. 7.4. Unsurprisingly, as the signal is injected further away form the readout point of the pillar, the arrival of the signals becomes progressively later, to the point where it converges to $t_{\text{cog}} \to R_l C_l/2$ at the end of the line. The average value of $t_{\text{cog}}(x_0)$ is $R_l C_l/3$, meaning that half of the signal comes later than 0.752 ns. Likewise, the expression for the second moment of the CoG time is given by

$$\begin{aligned} \overline{t^2}_{\text{cog}}(x_0) &= \frac{\int_0^\infty t^2 H(x_0,t)dt}{\int_0^\infty H(x_0,t)dt} \\ &= \lim_{i\omega\to 0} \frac{H''(x_0,\omega)}{H(x_0,\omega)} \\ &= R_l C_l \frac{8l^3 x_0 - 4l x_0^3 + x_0^4}{12l^4}\,. \end{aligned} \tag{7.2.10}$$

With these expression we can write the RMS of the pulse width as

$$\begin{aligned} \text{RMS}(x_0) &= \sqrt{\overline{t^2}_{\text{cog}}(x_0) - t_{\text{cog}}(x_0)^2} \\ &= R_l C_l \frac{\sqrt{\left(4l^3 - 6l^2 x_0 + 4l x_0^2 - x_0^3\right) x_0}}{\sqrt{6}l^2}\,, \end{aligned} \tag{7.2.11}$$

which is presented in Fig. 7.4. As expected, the signals become wider as the injection point is further removed form the readout terminal. Given the stochastic process of the energy lost by the particle and the energy deposited in the material i.e., Landau fluctuations, the fluctuations of the CoG time can be written as [194]

$$\sigma_t = w(l)\sqrt{\frac{1}{l}\int_0^l \bar{t^2}_{\text{cog}}(x_0)\,dx_0 - \left(\frac{1}{l}\int_0^l t_{\text{cog}}(x_0)\,dx_0\right)^2} = \frac{\sqrt{7}w(l)}{3\sqrt{5}} R_l C_l\,, \tag{7.2.12}$$

where in its general form the function $w(l)$ is defined as

$$w(l)^2 := \int_0^\infty \left[\frac{d}{\lambda}\int_0^\infty \frac{n_1^2 p_{\text{clu}}(n_1)}{(n_1+n)^2} dn_1\right] p(n,l)\,dn\,, \tag{7.2.13}$$

with $p(n,l)$ being the probability for a relativistic particle to deposit n e-h pairs along a path of length l, $p_{\text{clu}}(n)$ the cluster size distribution, and λ the average distance between primary interactions. As a result, the timing performance is linearly related to $R_l C_l$, such that a factor 10 decrease in resistance of the column would yield an improved σ_t by one order of magnitude.

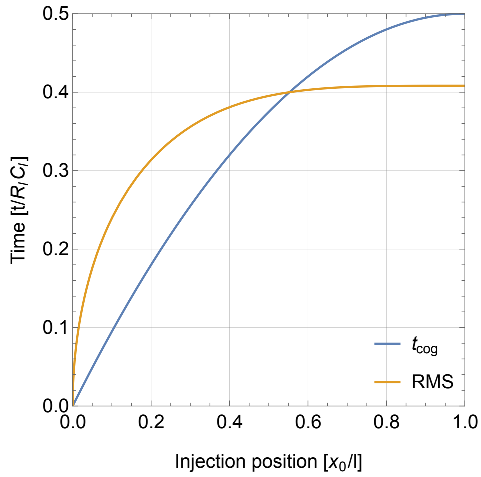

Figure 7.4: Timing characteristics of the signal pulls at the readout terminal for different charge injection positions.

7.2.2 Induced signal from electron-hole pair movement

With the transmission line description of the readout column, the dynamics of the resistive electrode are captured in the derived impulse response function. This can be directly used in conjunction with a numerical simulation framework, such as Garfield++, where the movement of the carriers can be calculated for each event. The simulation flow would then include the computation of the induced current on the electrodes as if they were perfectly conducting, after which the resulting current would be convoluted with Eq. (7.2.6). In order to gain a comprehensive understanding of the signal's structure, we will confine our analysis in this section to the trajectory of a singular electron-hole pair within the cylindrical chamber, as a description of the pixel cell.

The velocities of electrons and holes, when subjected to an electric field of magnitude $|E|$, will reach a saturation point under sufficiently high field strengths. To get a realistic estimate of their trajectories we use the following parametrization for their velocities [195, 196, 197]:

$$|v_e(E)| = \frac{\mu_e|E|}{1+\frac{\mu_e|E|}{v_{se}}}\,, \qquad |v_h(E)| = \frac{\mu_h|E|}{1+\frac{\mu_h|E|}{v_{sh}}}\,, \tag{7.2.14}$$

where μ_e (μ_h) and v_{se} (v_{sh}) are the mobility and saturation velocity for the electron (hole), respectively. Their exact values are influenced by the purity of the diamond, yet for illustrative purposes, we employ the following set of values for the mobility [198]

$$\mu_e = 1266\,\frac{\mathrm{cm}^2}{\mathrm{Vs}}\,, \qquad \mu_h = 1992\,\frac{\mathrm{cm}^2}{\mathrm{Vs}}\,, \tag{7.2.15}$$

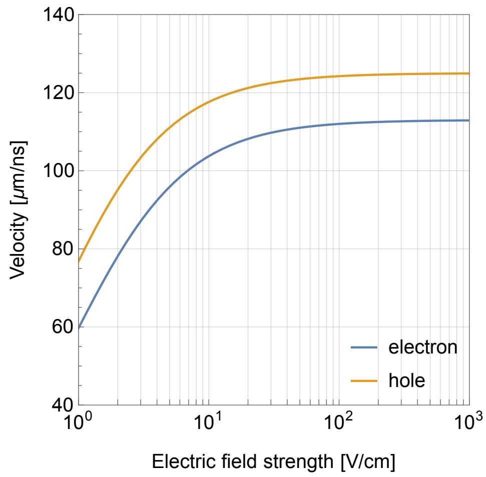

Figure 7.5: Drift velocity of the electrons and holes in the CVD diamond.

and saturation velocity

$$v_{se} = 1.13 \times 10^7 \ \frac{\text{cm}}{\text{s}} \,, \qquad v_{sh} = 1.25 \times 10^7 \ \frac{\text{cm}}{\text{s}} \,, \tag{7.2.16}$$

which are in the same range as the ones found in Ref. [199, 200]. The velocities obtained are depicted as a function of electric field strength in Fig. 7.6, where it is noteworthy that, unlike silicon sensors, the hole's movement can be faster than that of the electron[2]. It has been found that diamond detectors have a high intrinsic breakdown voltage which allows for its operation at high electric field configurations. This, coupled with the elevated electron and hole mobility, has the potential to lead to a reduction of the impact of the temporal spread of the charge collection on the time resolution of the sensor [180].

To gather the holes at the readout electrodes we apply a biasing potential. To do so the central pillar is virtually grounded, while the outer edge of the chamber is put at $V_0 > 0$, resulting in the electric field

$$\mathbf{E}(r) = -\frac{V_0}{r \ln\left(\frac{b}{a}\right)} \hat{\mathbf{r}} \,, \qquad a < r < b \,, \tag{7.2.17}$$

with r being the radial coordinate. Plugging this into Eq. 7.2.14 and placing the appropriate signs to indicate the direction of motion, the radial trajectories of the electron

[2]This is not always the case, as it is contingent on the properties of the CVD diamond.

and hole being created as a pair at position $r = r_0$ and time $t = 0$ are given by

$$
\begin{aligned}
r_e(t) &= \frac{\sqrt{v_{se}\ln\left(\frac{b}{a}\right)\left(r_0^2 v_{se}\ln\left(\frac{b}{a}\right) + 2\mu_e V_0(r_0 + tv_{se})\right) + \mu_e^2 V_0^2} - \mu_e V_0}{v_{se}\ln\left(\frac{b}{a}\right)} \\
r_h(t) &= \frac{\sqrt{v_{sh}\ln\left(\frac{b}{a}\right)\left(r_0^2 v_{sh}\ln\left(\frac{b}{a}\right) + 2\mu_h V_0(r_0 - tv_{sh})\right) + \mu_h^2 V_0^2} - \mu_h V_0}{v_{sh}\ln\left(\frac{b}{a}\right)} ,
\end{aligned}
\tag{7.2.18}
$$

respectively. The electron reaches its endpoint at $r = b$, while the hole reaches its endpoint at $r = a$, at a time

$$
\begin{aligned}
t_e &:= \frac{b - r_0}{v_{se}} + \frac{\left(b^2 - r_0^2\right)}{2\mu_e V_0}\ln\left(\frac{b}{a}\right) \\
t_h &:= \frac{r_0 - a}{v_{sh}} + \frac{\left(r_0^2 - a^2\right)}{2\mu_h V_0}\ln\left(\frac{b}{a}\right) ,
\end{aligned}
\tag{7.2.19}
$$

giving the time range in which they induce a signal on the readout pillar.

To calculate the signal on the central column from the movement of the e-h pair we apply the basic form of the Ramo-Shockley theorem. Following Eq. 2.2.22 the contribution from each charge carrier is given by

$$
\begin{aligned}
I_e(t) &= \frac{e_0}{r_e(t)\ln\left(\frac{b}{a}\right)}\dot{r}_e(t)\Theta(t_e - t) \qquad t > 0 \\
I_h(t) &= -\frac{e_0}{r_h(t)\ln\left(\frac{b}{a}\right)}\dot{r}_h(t)\Theta(t_h - t) \qquad t > 0 .
\end{aligned}
\tag{7.2.20}
$$

In Fig. 7.6 (left), the signals are depicted for various initial positions of the pair. As the pair creation takes place farther from the readout pillar, the signal composition changes based on the contribution of different charge carriers. When r_0 is in proximity to a, the total signal is predominantly comprised of the electron signal. This observation is also apparent in the respective contributions of each carrier to the induced charge, illustrated in Fig. 7.6 (right). Alongside this, the CoG time of the total signal, given by

$$
t_{\text{cog}} = \frac{\int_0^{t_e} tI_e(t)\,dt + \int_0^{t_h} tI_h(t)\,dt}{\int_0^{t_e} I_e(t)\,dt + \int_0^{t_h} I_h(t)\,dt} , \tag{7.2.21}
$$

is dependent on this, as shown in Fig. 7.7. This leads to a dependence of the SAT to the primary interaction position, adding to the overall timing resolution of the sensor in conjunction with the signal's propagation speed along the resistive column, and the fluctuation in the primary ionisation pattern.

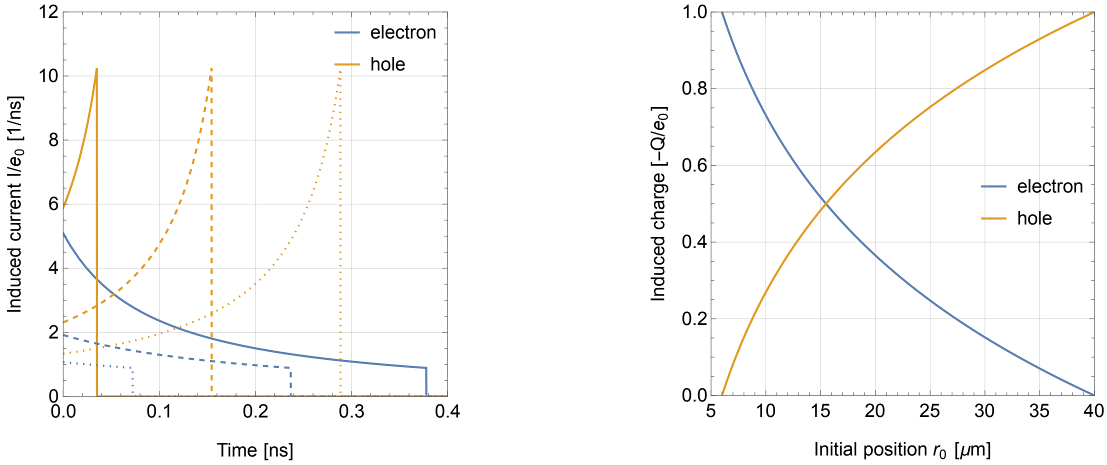

Figure 7.6: **Right:** Induced signal form an electron-hole pair on the readout column taken to be perfectly conducting. The initial positions are $r_0 = 10$ µm (full line), $r_0 = 22.5$ µm (dashed line), $r_0 = 35$ µm (dotted line). **Left:** Contributions to the total induced charge from the different carriers given different initial distances form the readout column.

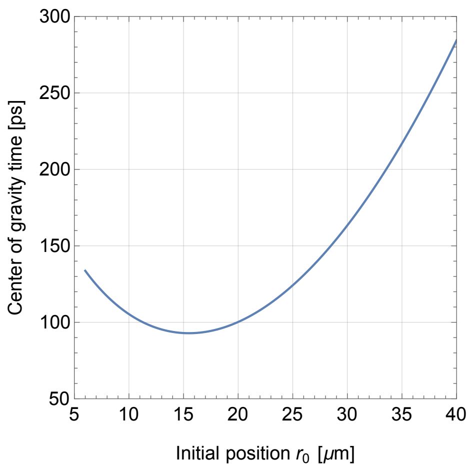

Figure 7.7: Center of Gravity time of the signal as a function of the initial distance of the e-h pair form the central readout column.

7.3 Dynamic weighting potential of a readout column

For a more detailed description of the current response exhibited by the 3D readout structure, we return to the numerical dynamic weighting potential approach. This methodology will be employed for various resistive pillars, from which the resulting signals will be computed using Garfield++ resulting from pion tracks. To conclude, a comparative analysis with the transmission line description will be provided.

7.3.1 Simulation setup

The calculated current response of the detector to an incident MIP has been obtained through the use of Garfield++. This involved the calculation of the primary charge deposition pattern, charge carrier transport driven by the applied electric field and the determination of the induced signal. The latter was achieved through the use of the extended form of the Ramo-Shockley theorem for conductive media by convoluting the velocity vectors of the drifting charges with time-dependent weighting vectors of the readout electrodes (i.e., Eq. (2.2.18)). One benefit of adopting this method is its consideration of electrons and holes as point particles in the calculation. In certain TCAD simulations, it is necessary to represent charge deposition as a continuous distribution, resulting in the unrealistic behavior of individual charge carriers seemingly 'diffusing' [49].

The simulation of the primary ionization pattern of a charged particle tracking through a gas or solid-state medium can be performed with the widely used High Energy Electrodynamics (Heed) toolkit [201], developed by I. Smirnov. The computations presented in this thesis were conducted using the C++ iteration of Heed [202]. For this work, the simulation will be reported for 180 GeV/c pions with a normal incidence direction to the sensor's orientation, as depicted in Fig. 7.1 (left), for which the primary ionization structure was calculated on an event-by-event basis. The general characteristics of these interactions are given in Fig. 7.8, where both the calculated average cluster density and cluster size distribution are presented for the diamond medium at an absolute temperature of 296.15 K.

The modeled 3D architecture is comprised of resistive readout columns interleaved with the biasing columns. Integrating these resistive electrodes into sCVD diamond involves the production of graphitic buried electrodes using femtosecond laser pulses [203]. The resulting columns exhibit variations in column diameter due to the inherent tolerance of the production process [192]. Additionally, graphite possesses a significantly lower density compared to diamond, introducing mechanical stress within the diamond lattice during the graphitization process [188], which may lead to local imperfections in the sensor. Since representing these intricacies directly in a FEM environment was not straightforward and would have required a detailed study of these irregularities, the pillars were represented as cylindrical electrodes with a diameter of 12 µm [204] and a height of 450 µm. As shown in Fig. 7.9, they were arranged in a 3×3 grid for the readout columns, alternating with the 4×4 biasing columns within a $275 \times 275 \times 500$ µm^3 sensor. The electrode's resistance was taken to be 30 kΩ [188], corresponding to a volume resistivity of $\rho \approx 0.75$ Ωcm. This geometry was implemented into the COMSOL® toolkit, focusing particularly on refining the meshing near the pillar areas due to their curvature and the higher gradient of the electric (weighting) potential. This has been done to enhance the accuracy of the subsequent Monte-Carlo integration method employed by Garfield++ for modeling charge carrier transport in that region.

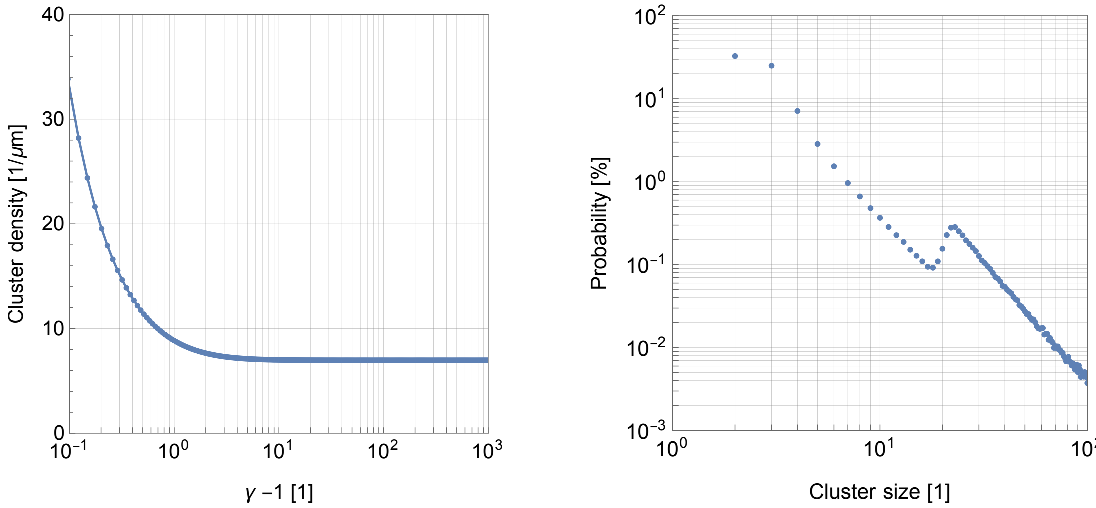

Figure 7.8: Primary interaction pattern characteristics of a relativistic pion tracking through the diamond material, as calculated by Heed. **Right:** Average number of clusters per unit of distance for different Lorentz factors. **Left:** The probability to have n electron-hole pairs per primary interaction for a pion with a momentum of 180 GeV/c.

For the applied electric field, the biasing columns were placed at $V_0 = 100$ V, including the backplane to which they were connected, while the readout pillars were perfectly grounded. While applied to the terminal points at the outer end of the electrodes, the applied potential propagates along the entire length of the pillars given sufficient time due to their non-zero volume resistivity. To streamline the numerical computation, we assumed that the electric field remained static throughout the entire charge collection process and that any variation resulting from the signal current could be neglected. Fig. 7.10 shows the resulting electric potential and field solutions. The inhomogeneity of the electric field strength can result in variable speeds of charge carriers below their saturation velocities for a portion of their paths. This variability, in turn, can lead to a non-uniform-induced current response based on the position of primary ionization. A variation in the range of $|E| \approx 10^3 - 10^5$ V/cm can be observed in the region between two adjacent readout columns, with the minimum occurring at the midpoint. This range appears sufficient to attain saturation velocities throughout the volume.

The preceding results were amalgamated with the outcomes of the calculation of the propagation of the e-h pairs generated from the primary interactions of the pion with the medium. An example of the paths of the charge carriers is given in Fig. 7.11, where the holes and electrons are collected on the readout and biasing pillars, respectively. Due to the insulating gap between one end of the pillars and the edge of the sensor, charges in this region must traverse a greater distance resulting in a longer collection time.

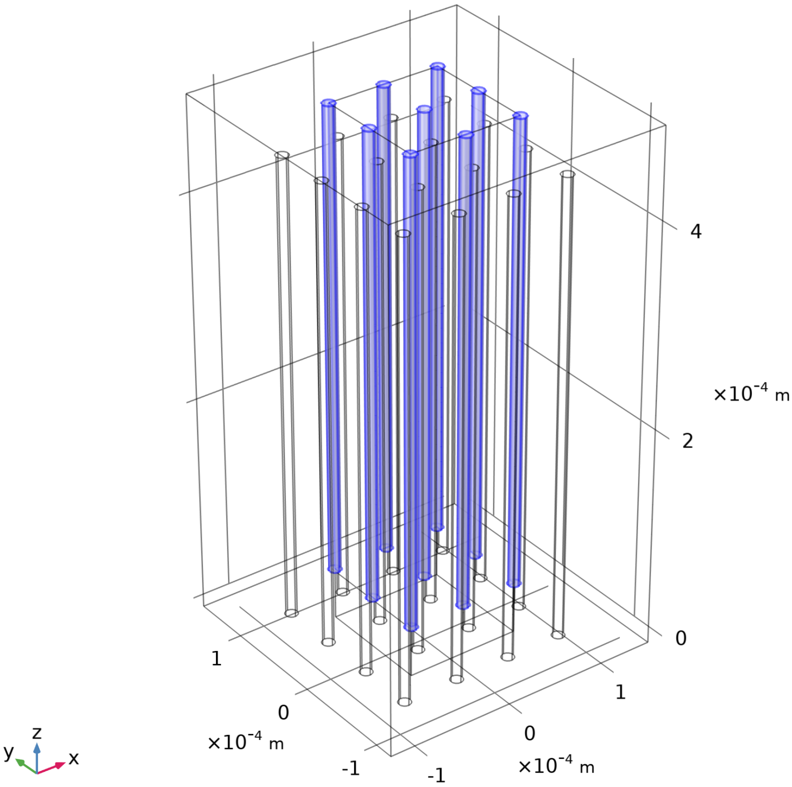

Figure 7.9: Simulated 3D readout architecture with graphitic pillar for the purpose of signal readout (highlighted in blue) and biasing (unmarked). The inner region, delineated by the outer readout electrodes, features denser meshing, owing to the fact that it serves as the area of interest in the simulation.

7.3.2 Weighting potential and induced signals

Given an event, the signal from the central pillar has been calculated for the direct induction from the motion of the charge carriers (prompt component) and the reaction of the graphetic column (delayed component). The delayed weighting potential of the readout electrode was calculated through the FEM following the recipe outlined in Sec. 2.5.2. A potential step of $V_w = 1$ V was applied on the connection terminal, while taking all other electrodes to be perfectly grounded, thereby considering all external impedance elements to be negotiable. The resulting dynamic weighting potential $\Psi(\mathbf{x}, t)$ solutions at different time slices are presented in Fig. 7.12 and Fig. 7.13. The prompt component of the potential $\psi^p(\mathbf{x}) = \Psi(\mathbf{x}, 0)$ is, while relatively localized around the connection point of the electrode, non-vanishing in the detector volume. Nevertheless, as time progresses, the delayed component's contribution ($\psi^d(\mathbf{x}) = \Psi(\mathbf{x}, t) - \psi^p(\mathbf{x})$) to the overall weighting

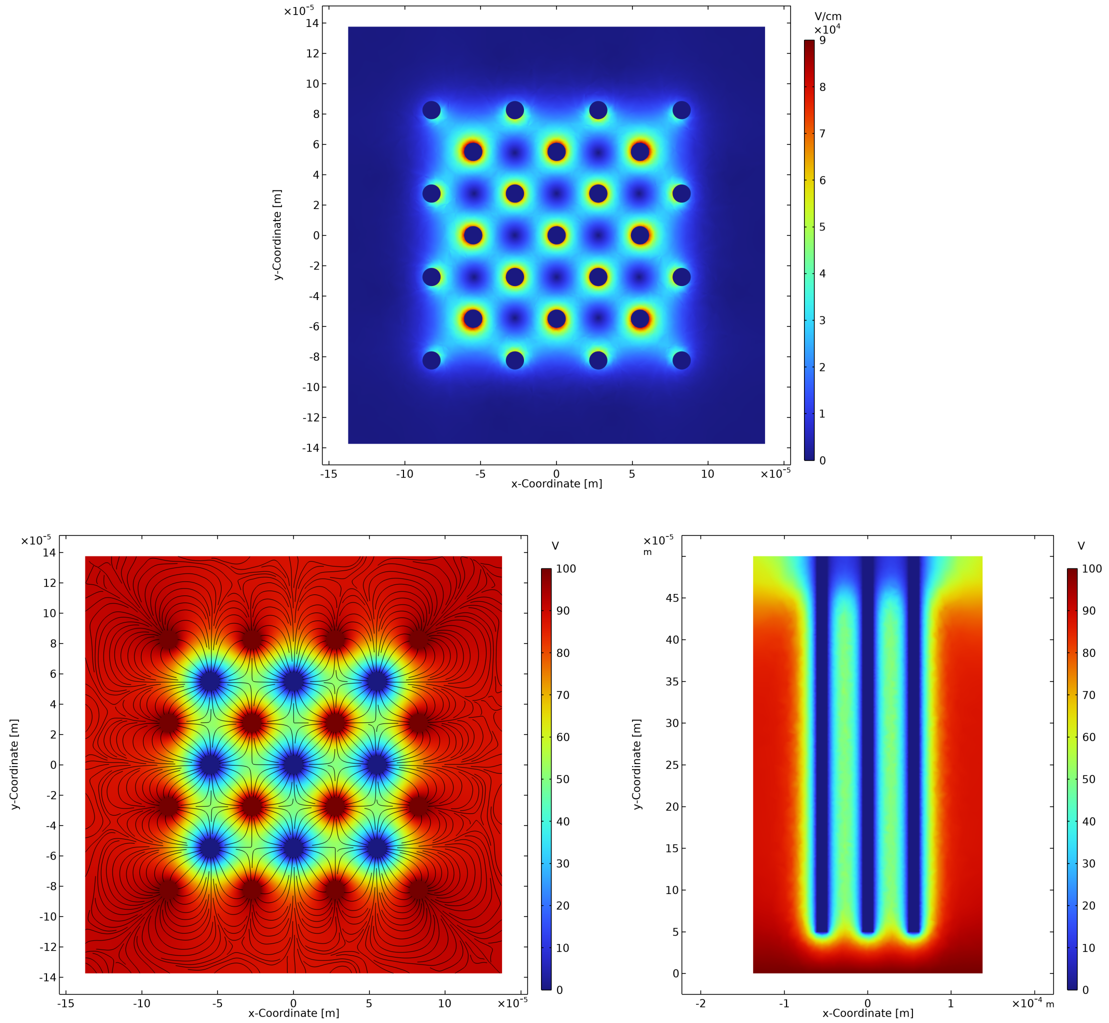

Figure 7.10: Applied electric field and potential for the pixel matrix as calculated by the COMSOL® toolkit. **Upper:** Cross-section view of the electric field strength at $z = 250$ µm. **Bottom left:** Potential solution for constant $z = 250$ µm with streamlines. **Bottom right:** Potential solution in the xz-plane ($y = 0$).

potential far outweighs the one from $\psi^p(\mathbf{x})$. Hence, the majority of the signal will be caused by the resistive nature of the electrode. Notably, both components do not vanish in the volume of the neighboring pixel, suggesting signal sharing from direct induction. In the limit $t \to \infty$, the solution will reach its steady-state where the pillar will act as a perfectly conducting metal rod, perfectly propagating the applied voltage pulse over its entire extent.

In Fig. 7.14 a comparison is made between the signals induced on the central electrode for different positions of the incident pion. As detailed in Sec. 7.2.2, the nuanced compo-

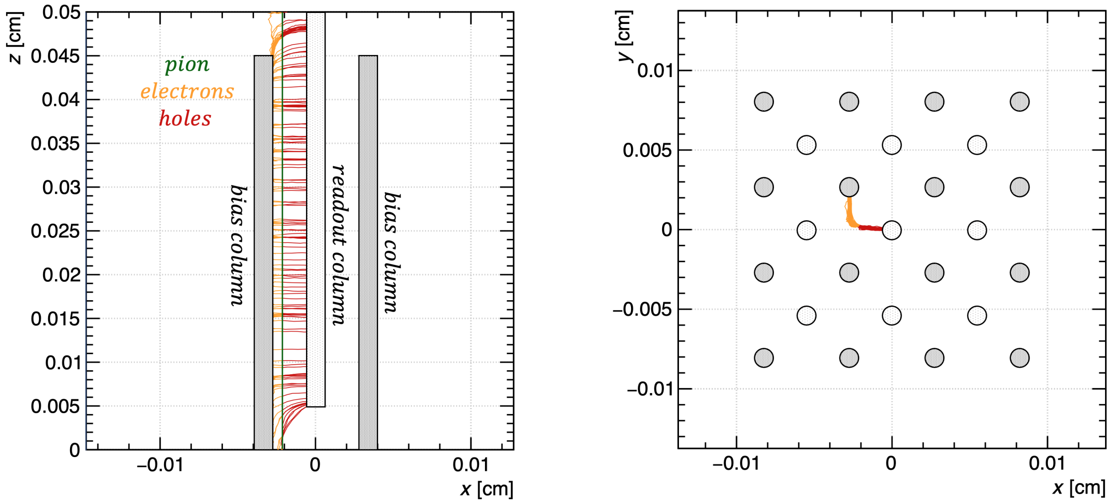

Figure 7.11: Drift lines of the free electron-hole pairs of a randomly selected simulated event. **Right:** Projected view in the xz-plane. **Left:** Projected drift lines on the xy-plane.

sition of the signal, involving contributions from both electrons and holes, is contingent upon the precise location of primary ionization. In instances where events occur in close proximity to the electrode under examination, the signal is predominantly shaped by the influence of electrons as they traverse toward the biasing pillars (see event 2). Conversely, this pattern is reversed for events occurring near the biasing columns (see event 5). Due to the delayed reaction of the biasing column, they do not perfectly shield readout electrodes from events occurring in adjacent pixel regions (as demonstrated by event 3). Given our assumption that the electrodes possess negligible external impedance, this cross-talk is present without factoring in the cross-coupling between the electrodes.

While the delayed component of the signal is dominant, there is a minor contribution from the direct induction signal from the movement of the electrons and hole, mainly coming from the vicinity of the top part of the electrode. This prompt part has the expected shape compared to the ones found in Fig. 7.6 (left). The propagation of the signal along the resistive column gives rise to the relaxation tail in the late-time behavior of the signal. In this region, a wavy artifact emerges from the interpolations between the time-slicing of the weighting potential maps (see Sec. 2.5.2). These maps are spaced further apart in time during late times to mitigate the memory load of the simulation.

The complete readout chain would include the convolution of the induced signals with the impulse response function of the electronics. For this, the BFP842ESD RF bipolar transistor[3] is used, the simulated impulse response function of which is given in Fig. 7.15

[3]Produced by Infineon Technologies: www.infineon.com

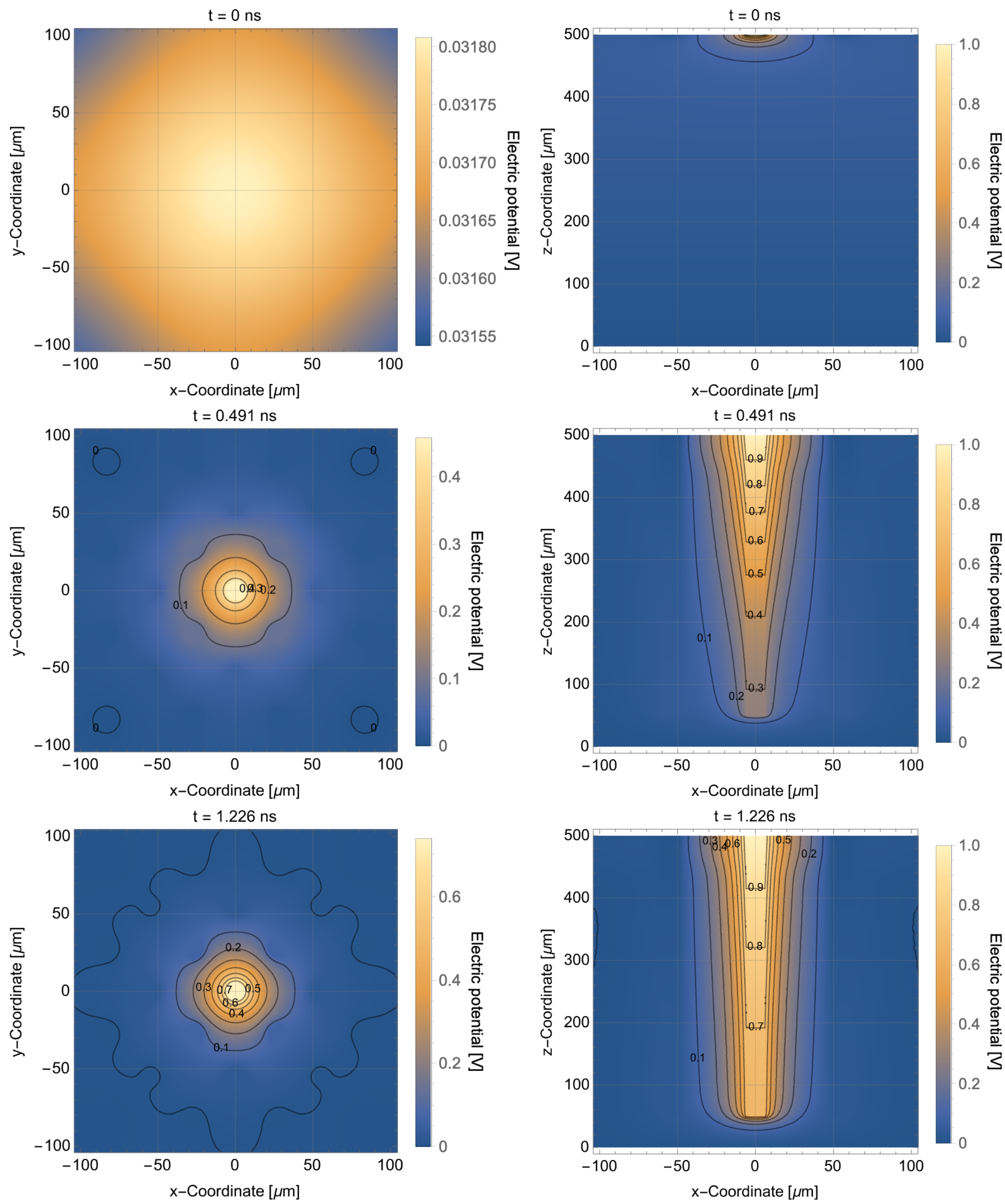

Figure 7.12: Time-sliced weighting potential solutions for the central resistive readout pillar at constant $z = 250$ μm (left column) and $y = 0$ (right column).

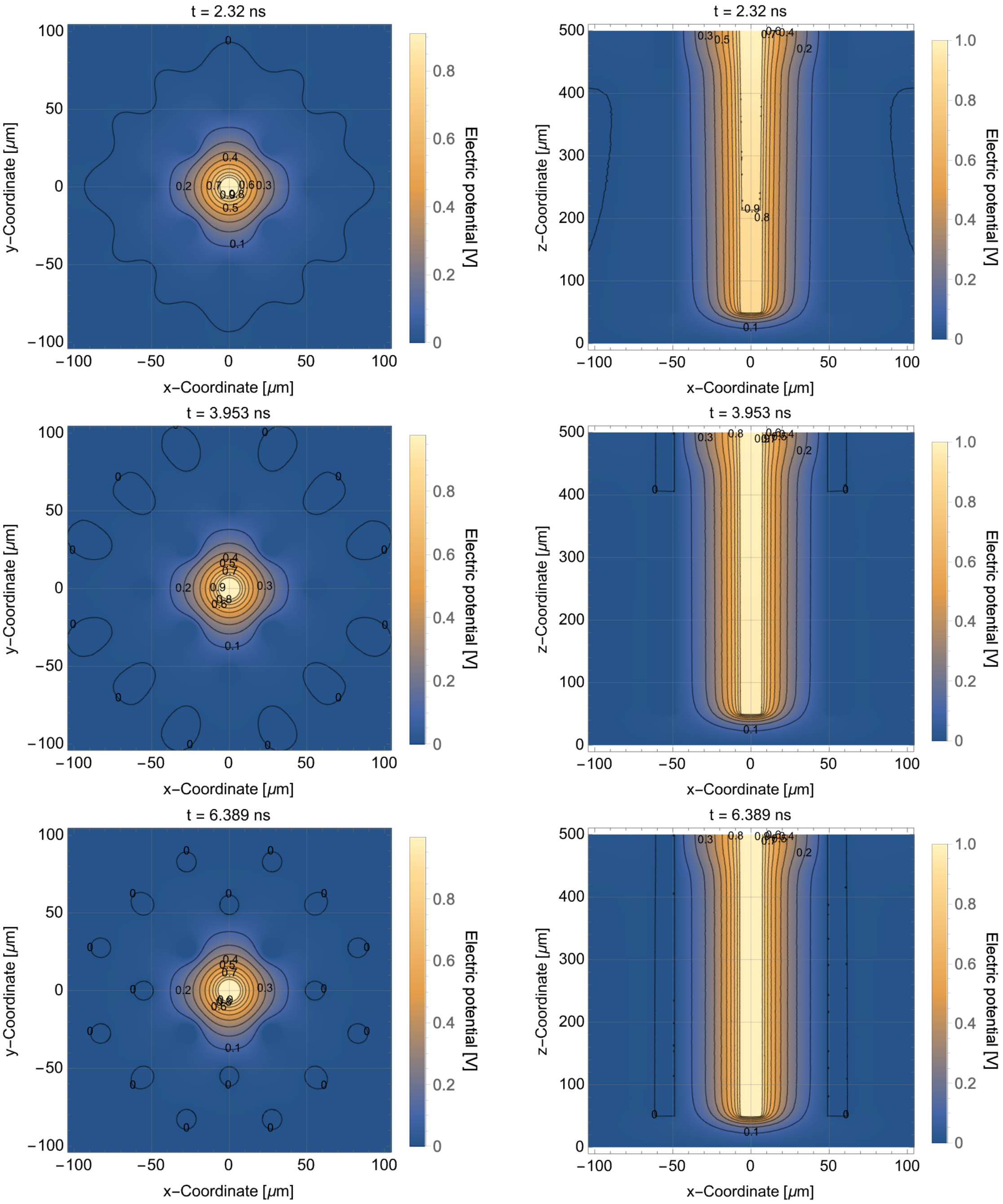

Figure 7.13: (Continued) Time-sliced weighting potential solutions for the central resistive readout pillar at constant $z = 250$ μm (left column) and $y = 0$ (right column).

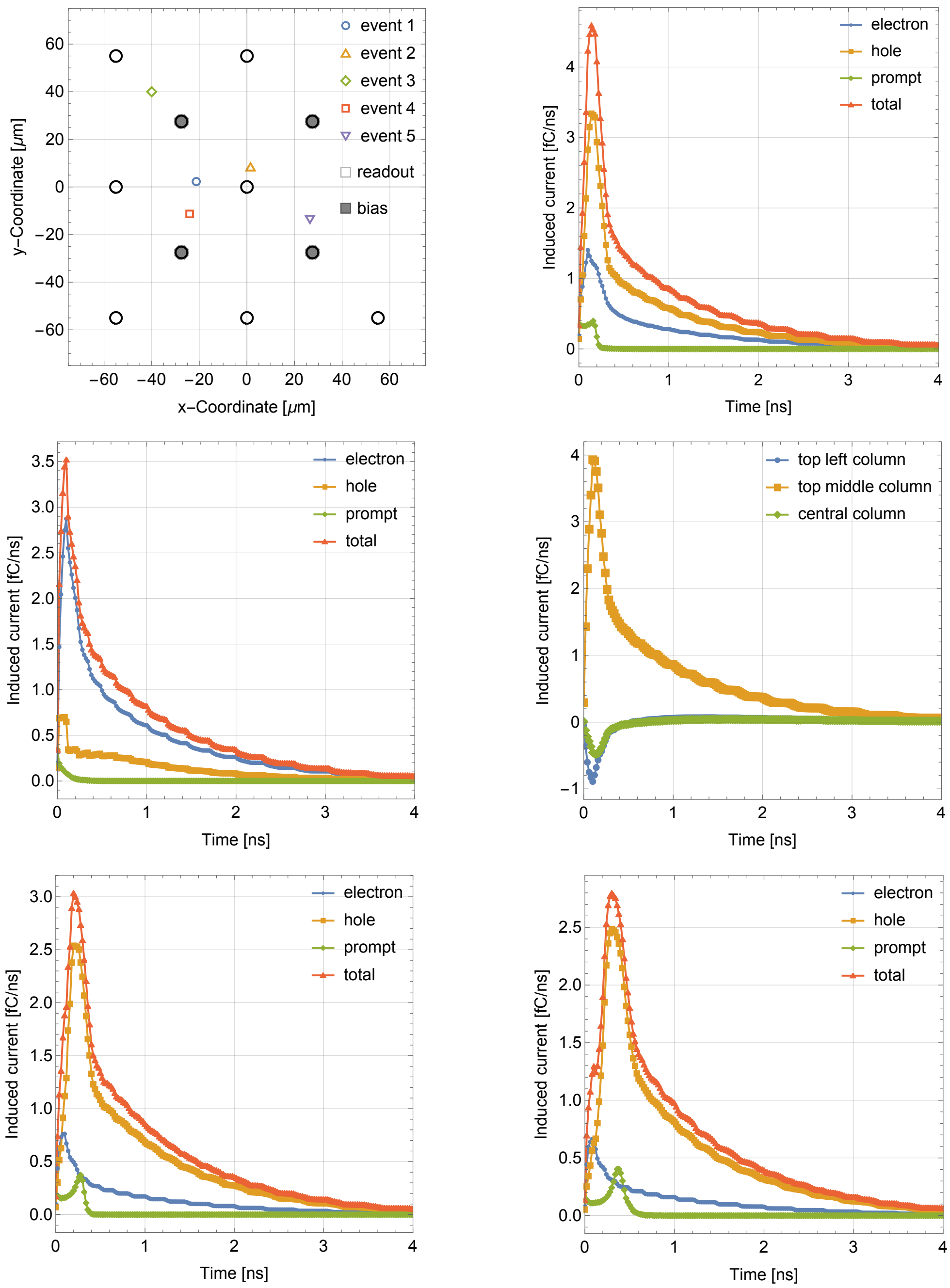

Figure 7.14: Induced signal for different events. **Top left:** Hitmap of the pion track position for the different events. **Top right:** Event 1, for which the charge trajectories are plotted in Fig. 7.11. **Center left:** Event 2. **Center right:** Event 3, showing the cross-talk between three pillars. **Bottom left:** Event 4. **Bottom right:** Event 5.

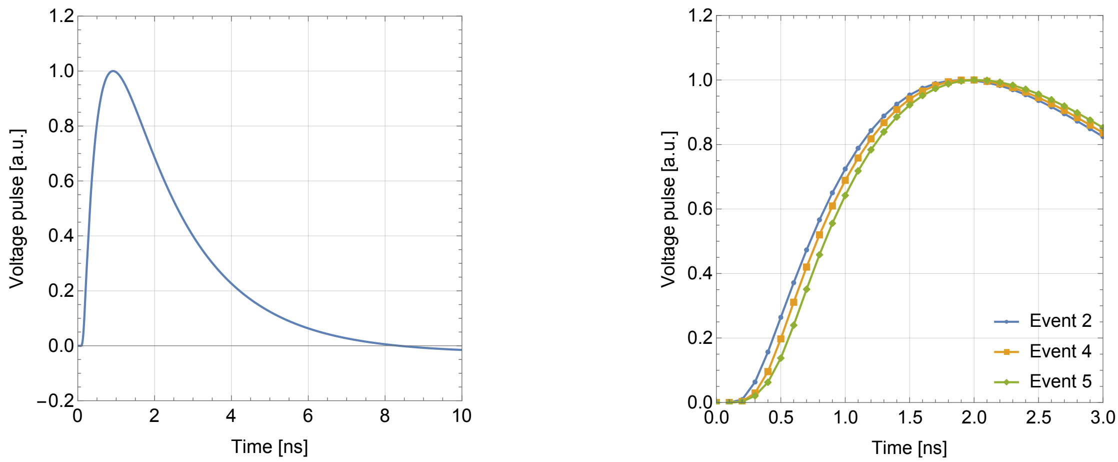

Figure 7.15: **Right:** Normalized impulse response function of the readout transistor. **Left:** Normalized voltage pulses at output of the shaper.

(left)[4]. The voltage pulses after the shaping for events from Fig. 7.14 are given in Fig. 7.15, where the pulses are normalized on the premise that during analysis the time-walk due to Landau fluctuations is mitigated through CFD. From the leading-edge, we observe a time jitter when comparing the three signals at a fixed THL.

7.3.3 Comparison with transmission line approach

In this chapter, two techniques were introduced to compute the current response of the resistive readout pillars in the 3D readout structure: (i) the analytical approach, which approximates the system dynamics as that of a transmission line, and (ii) the numerical calculation of the dynamic weighting potential within the framework of the Ramo-Shockley theorem. While the former provides valuable insights through its equations, aiding in the comprehension of experimental and numerical observations, the latter, with its more accurate representation of the early-time behavior (see Sec. 2.4) and geometry, offers a more complete description of the system.

A direct comparison between the two methods is provided in terms of their solutions for the induced charge readout at the terminal of the electrode, considering the injection of a point charge q at a specific point on its surface. The results are superimposed in Fig. 7.16, showing a convergence of solutions to each other at late times. In qualitative terms, the curves from both computations demonstrate similar behavior, with the most significant deviations observed in the initial part of the signal. This initial deviation can be attributed to the fact that, unlike in the transmission line calculation, the initial value of the induced charge is not zero. This is due to the consideration to the presence of the prompt contribution to the signal within the Ramo-Shockley theorem approach.

[4] Courtesy of G. Passaleva and by extension the INFN TIMESPOT project.

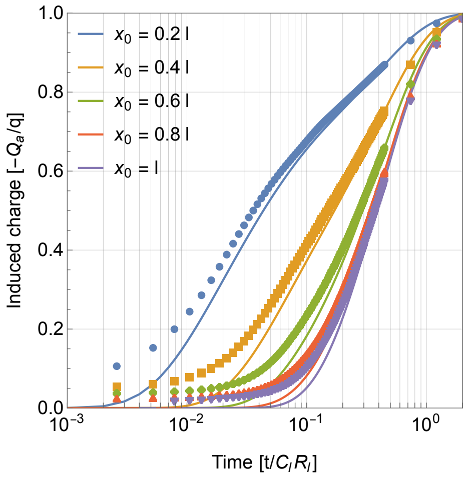

Figure 7.16: Comparison between the induced charge using the transmission line equation (full line) and the dynamic weighting potential (dotted lines) from deposited charges q on the resistive column's surface at different point along its length.

7.4 Summary

The case of signal formation in the 3D readout structure has been treated using two distinct methods: a transmission line description and the dynamic weighting potential methodology outlined in Chapter 2. We discussed the application of both methodologies and their respective merits. While the analytical approach using the transmission line approximation provides us with an intuitive way of calculating the signal, the arguments in favour of using the extended form of the Ramo-Shockley theorem are three-fold:

- The formulation of the problem in terms of a transmission line works under the premise that the local line density is related to the potential via the capacitance, i.e., $\sigma(x,t) = CV(x,t)$. As discussed in Sec. 2.4, this relation only holds for the late-time behavior of the signal; failing to capture the initial portion of the signal shape accurately. Given the importance of the rising edge of the signals in timing applications, this can be reflected in the simulated temporal performance. However, the extent to which this is manifested in the final 'recorded' signal depends on the shaping times of the ASICs. When the shaping time is long enough compared to the signal length, is is expected that the difference between the results of two methods will decrease. This happens because for a longer shaping time the signal shape at the output terminal of the shaper will increasingly resemble its delta response function.

- With the FEM approach, the precise structure and materials of the full pillars are resolved in the model. This not only introduces the prompt component into the signal calculations but also directly provides us with the cross-talk between neighboring readout pixels from due to the partial transparency the resistive columns given their finite reaction times. When adding external impedance elements before solving the EM system for the weighting potentials, the cross-coupling between the electrodes can be added. This last effect can, however, be added to the transmission line model by using the admittance matrix between the columns.

- This brings us to a more pragmatic viewpoint: when employing the dynamic weight potential strategy, quantities such as the electrode's capacitance automatically follow from the geometry and material definitions and, therefore, are directly folded into the weighting potential formalism. This relieves us from the need to estimate these lumped parameters through analytical, numerical, or experimental means.

With this, we do not wish to diminish the critical role of toy models in building our intuition and understanding of the signal induction mechanisms underpinning the system by distilling the complexity of the problem into its core constituents. However, when greater precision is needed from the theoretical predictions, the system's complexity invariably increases, often then requiring numerical methods to solve it.

The propagation of the signal through the resistive columns introduces a dependence of the SAT of the signal from different clusters based on their respective positions along the length of the pillar. As is already stated in literature, this results in the timing performance of the device being closely linked with the volume resistivity of the ohmic mixture comprising the readout electrodes. Intensive R&D into the manufacturing of the resistive pillars has already resulted in the lowering of the resistance of the column down to 30 kΩ, which poses a lower bound of the attainable resolutions. The discussed modeling strategies are being employed by the TIMESPOT collaboration, where the currently the dynamic weighting potential strategy is being benchmarked [205].

Part IV

Detectors with superimposed prompt and delayed signal induction

Chapter 8

Resistive strip bulk MicroMegas

In this chapter we systematically build up a complete Monte Carlo model for the response of a resistive strip bulk MicroMegas (MM) equipped with a two-dimensional strip readout structure. To determine the numerical precision of the techniques described in Chapter 2 and the accuracy of the implementation into Garfield++, we conducted a benchmarking study using experimental data taken with MIPs during the 2022 RD51 test beam campaign.

8.1 Introduction

In the preceding chapters, we have encountered several resistive MM detectors that feature readout electrodes embedded in an insulating layer bellow a thin resistive layer. While this represents a commonly used design for a resistive MM detector, an alternative layout can be found in the layout of the ATLAS MM. As part of the NSW upgrade of the ATLAS muon system, this design features a series of readout strips covered by a thin Kapton® foil, upon which are resistive strips that run perpendicular with the readout electrodes. The design choice to utilize individual resistive strips instead of a continuous resistive layer was was motivated by the minimizing the affected area in the event of a discharge and preventing the spread of charge across multiple readout strips [34]. For this detector layout, it has been demonstrated that when equipped with two-dimensional strip electrodes, signal spreading becomes distinctly visible across adjacent channels that run perpendicular to the resistive strips [104]. Motivated by this observation, we used two prototypes, each featuring a distinct surface resistivity — specifically, nominal surface resistivities of 100 k$\Omega/\square$ and 1 M$\Omega/\square$ – to measure their respective current responses. Fig. 8.1 shows a cross-section schematic of the geometry, which is supplemented by an image of the top of the amplification structure in Fig. 8.2. The average induced current response of the two devices for MIPs has been measured at the H4 beamline at the CERN SPS. This enables us to experimentally assess the effect of the surface resistivity on the signal shape. The result is subsequently compared with a detailed Monte Carlo simulation in order to gauge the accuracy of the numerical approach explored and implemented during this project.

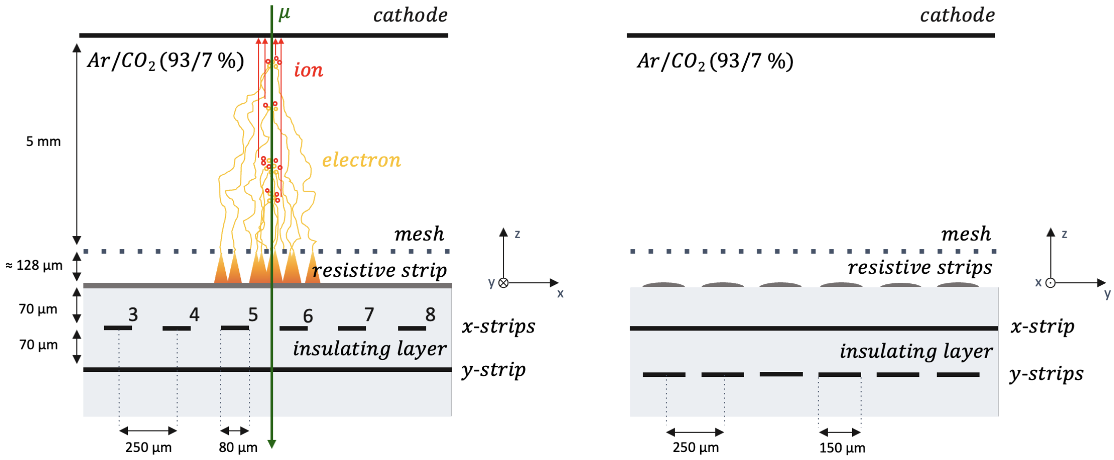

Figure 8.1: Schematic overview of the layout of the two-dimensional resistive strip bulk MicroMegas. The primary electrons sourced by a muon are shown in yellow while the positive ion tracks are truncated to the red arrows and absent for the secondary ions. Indicating the respective indices of the x-strips, the numbering shown will be the convention used throughout the chapter. This drawing is not to scale.

In addition to intricate Monte Carlo simulations, simplified models such as the transmission line model of Chapter 7 serve as valuable tools for cultivating an intuition of the way signals are formed in resistive readout structures. That being the case, we first develop a toy model using the previously derived transmission line descriptions to capture leading principles of the signal's behavior for the resistive strip readout structure. This is followed by the setup and results of the Monte Carlo simulation, which considers the measured height of the mesh. Specific care was placed in the accurate representation of the boundary condition of the relatively long resistive elements. The estimations of the induced current response for MIPS will subsequently be compared to the measured values for the 1 M$\Omega/\square$ following a general discussion of the experimental results.

8.2 Transmission line description

Given that the anode is divided into long, relatively thin resistive strips, we can treat the resistive elements as a set of transmission lines by approximation. In this scenario, the readout electrodes are AC-coupled with the resistive strip, and we can depict this coupling using the circuit shown in Fig. 8.3. Here, the capacitor C_s represents the coupling between the voltage pulses $V(x,\omega)$ on transmission lines and the resulting current $I_s(x,\omega)$ on the readout electrodes that we take to be terminated to ground through a resistor R_s. We will work under the premise that the readout electrodes have a negligible effect on the response of the transmission line, making them 'passive observers'. Without loss of generality, these can be taken as strips (denoted by the subscript s) intersecting

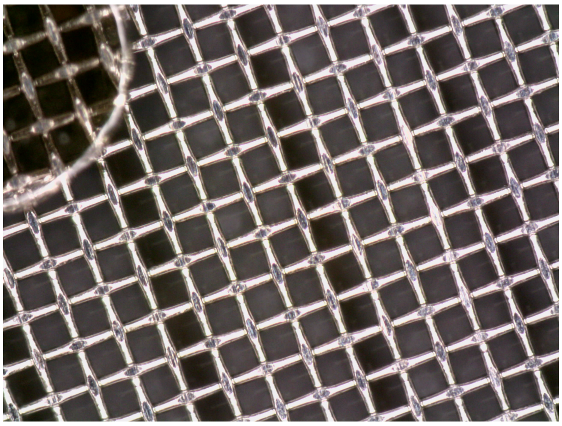

Figure 8.2: Optical microscope image showcasing the amplification structure situated atop the readout architecture. A pillar mechanically determining the size of the amplification gap positioned at the upper left corner of the image,, while the resistive strips are discernible through the micro-mesh.

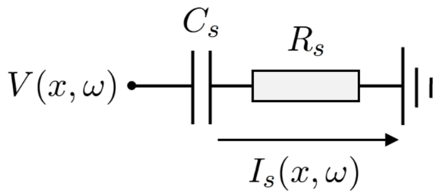

Figure 8.3: Circuit representing the AC-coupling of the readout electrodes, terminated with resistor R_s, to the resistive lines using a capacitor C_s.

the transmission line at a right angle. Given a set of transmission lines and readout electrodes, the system will contain cross-coupling between the elements. However, for simplicity, we can focus on the case of a single resistive strip. A numerical solution for a perturbed RC-line was already pursued in Ref. [206] through discretization of the line. In this section, we will provide an analytical expression for this response by elaborating on the findings presented in Sec. 6.1.

8.2.1 Delta response function

To discuss the solution to a perturbed transmission line, we revisit the system depicted in Fig. 6.1. The solution for the voltage pulse on the line is given by Eq. (6.1.2) and Eq. (6.1.5). Given that the resistive strips are usually connected to ground or high voltage at only one side, while the other side is left floating, we evaluate the equations for the conditions $Z_a = 0$ and $Z_b \to \infty$.

If we take the coupling described in Fig. 8.3 such that $C_s \gg R_s$, then the current flowing from the readout electrode to ground is given by

$$\begin{aligned} I_s(x,\omega) &= \frac{V(x,\omega)}{R_s + 1/\left(i\omega C_s\right)} \\ &\approx i\omega C_s V(x,\omega) \\ &= i\omega q C_s \sqrt{R}\frac{\sinh\left(x_< \sqrt{iCR\omega}\right)\cosh\left((l-x_>)\sqrt{icR\omega}\right)}{\sqrt{iC\omega}\cosh\left(l\sqrt{iCR\omega}\right)}\,. \end{aligned} \tag{8.2.1}$$

Here, the subscripts a and b indicating the solution left and right of the injection point is truncated in favor of writing the solution in terms of

$$x_> := \begin{cases} x & \text{for } x \geqslant x_0 \\ x_0 & \text{for } x < x_0 \end{cases}, \quad x_< := \begin{cases} x_0 & \text{for } x > x_0 \\ x & \text{for } x \leqslant x_0 \end{cases}. \tag{8.2.2}$$

To obtain the solution in the time domain, we note that the above equation has poles ω_n lying along the positive imaginary axis:

$$\omega_n := \frac{i(2\pi n + \pi)^2}{4cRl^2}\,, \quad \text{for} \quad n \in \mathbb{Z}\,. \tag{8.2.3}$$

Then the current measured from the electrode as a function of time is given by

$$\begin{aligned} I_s(x,t) = \frac{q\pi^2 C_s}{2C^2 R l^3}\sum_{n=0}^{\infty}(-1)^{n+1}(2n+1)^2 \sin\left(\pi\frac{(2n+1)x_<}{2l}\right) \\ \times\cos\left(\pi\frac{(2n+1)(l-x_>)}{2l}\right)e^{-\frac{t}{\tau_n}}\,, \end{aligned} \tag{8.2.4}$$

where we have defined an infinite number of characteristic time constants

$$\tau_n := \frac{4C_l R_l}{(2\pi n + \pi)^2}\,, \qquad n \in \mathbb{N}\,. \tag{8.2.5}$$

Consequently, the signal amplitude is directly proportional to the capacitance between the pickup electrode and the resistive strip. Moreover, the temporal characteristics of the signal are entirely dictated by the value of $R_l C_l$, with the amplitude exhibiting an inverse proportionality to $R_l C_l^2$, meaning that for lower surface resistivities the signals will be faster but lower in amplitude. In Fig. 8.4 the solution is shown for various electrode positions, considering an initial injection of charge at a fixed location. The anticipated bipolar shape due to the AC-coupling is recovered, leading to the absence of charge collection on the readout electrodes. Indeed, the total charge flowing from the electrodes vanishes:

$$\begin{aligned} Q_s(x) &= -\int_0^{\infty} I_s(x,x_0,t)\,dt \\ &= \frac{2qC_s}{Cl}\sum_{n=0}^{\infty}(-1)^n \sin\left(\pi\frac{(2n+1)x_<}{2l}\right)\sin\left(\pi\frac{(2n+1)x_>}{2l}\right) \\ &= 0\,. \end{aligned} \tag{8.2.6}$$

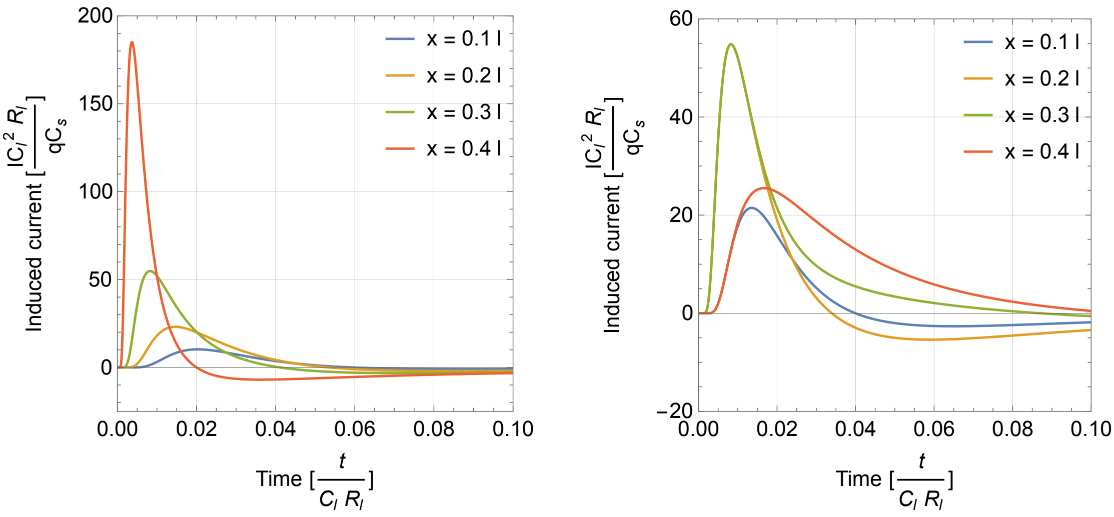

Figure 8.4: Signal on an electrode at position x that is capacitively coupled to a transmission line on which a charge q was injected at position $x_0 = 0.6l$ and $x_0 = 0.5l$ for the left and right panel, respectively.

Instead, all the charge is flowing to the ground frame through the connection of the transmission line: $\int_0^\infty I_a(0,t)\,dt = q$. Fig. 8.4 (right) highlights the asymmetric response of the readout due to the termination of the resistive strips on only one side. While this effect is present in the delayed response – particularly at the ends of the transmission line – it is not expected to be a significant factor for the electrodes that are in close proximity to the event along for large enough values of l. At late times, the dominating term in the sum is given by $n = 0$, yielding an exponential relaxation that follows

$$I_s(x,t) \approx -\frac{q\pi^2 C_s}{2C_l^2 R_l} \sin\left(\frac{\pi x}{2l}\right) \sin\left(\frac{\pi x_0}{2l}\right) e^{-\frac{\pi^2 t}{4C_l R_l}} . \tag{8.2.7}$$

Following the arguments of Chapter 7, to find the signal from an injected MM current such as the one given in Sec. 2.3.2, it should be convoluted with the delta response function $h(x,t) := I_s(x,t)/q$.

8.3 Precise measurement of the amplification gap size

The amplification structure of the resistive strip MM has a mesh suspended above the readout plane at a nominal distance of 128 µm as defined from the center of the mesh. Depending on the production, this gap size can differ from the quoted one, as was the case in Chapter 5. To get the modeling as accurate as possible, the gap was measured using a Hirox RH-2000 digital microscope following the procedure outlined in Sec. 5.2.3. The imperfections on both the anode plane and the top of the mesh serve as reference

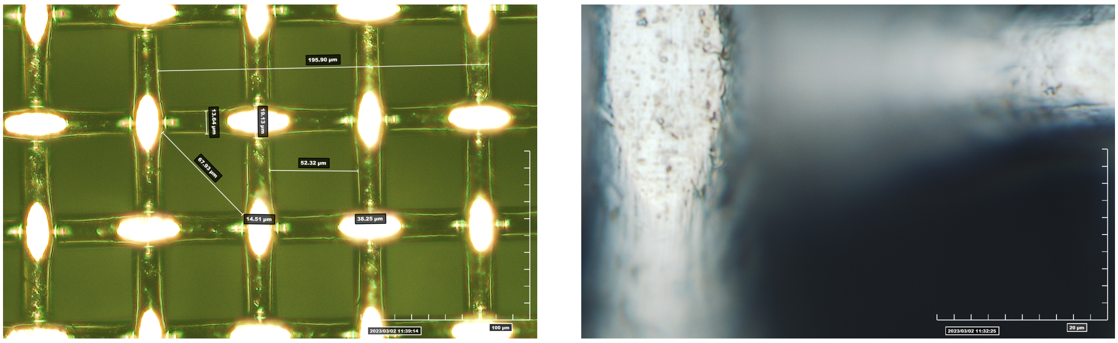

Figure 8.5: Photograph of the calendared mesh taken with the optical microscope during the amplification gap height measurement. Imperfections on the top of surface of the wires were used as a reference point for the focusing of the microscope.

points for microscope focus. In Fig. 8.5, images from the mesh during the data taking reveal its noticeable flatness, indicating calendaring of the mesh. On the left panel, the measured dimensions of the woven micro-mesh-structure are given. The distance between the top of the mesh and the anode plane was measured at various points across the active area, resulting in an average distance of 138.23 ± 1.42 µm. With a wire radius of 9 µm, we determine an amplification gap height of 120.23 ± 1.42 µm, significantly smaller than the nominal height.

8.4 Simulations of a resistive strip bulk MicroMegas

To apply the extended form of the Ramo-Shockley theorem for conductive media numerically to the geometry under investigation, the weighting potential is computed with COMSOL® using the techniques described in Sec. 2.5.2. Subsequently, we used this solution in Garfield++ to calculate the induced signal on five adjacent readout strips in the x-coordinate plane for events caused by muon tracks running perpendicular to the readout plane, as indicated in Fig. 8.1 (left). Our publication [77] gives a concise description of the simulation setup and first results, upon which this chapter will expand.

8.4.1 Weighting potential solution

The resistive strips generally adhere to the same overarching arrangement as the y-strip electrodes, with a few additional characteristics. As shown in Fig. 8.6, neighboring resistive strips are interconnected repeatedly after 4 mm, a pattern that is shifted by 2 mm from one strip to the next. This network was designed to drain the deposited charges over a series of neighboring strips instead of a solitary one, thereby equalizing the effective resistance to the ground frame across the active area. This also results in a decreased effectiveness of defects in the resistive pattern that could otherwise have severed the path to evacuate the collected electrons, which would have resulted in a local buildup of charge [207]. There is also a vertical structure to these resistive elements, the

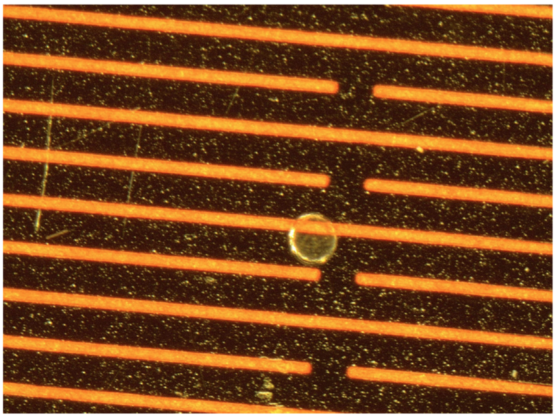

Figure 8.6: Image depicting the sputtered resistive anode structure. The resistive strips, along with their interconnections, are shown as the dark brown lines. Additionally, parts of the underlying layer featuring bright readout strips, and a singular pillar, are also discernible [207].

precise nature of which is subject to the manufacturing process, i.e., through sputtering or screen printing [208]. For example, with the screen printing technique, the resistive strips have a domed structure roughly 15 µm in height [200], as depicted in Fig. 8.1 (right). To simplify the calculations, we treat the resistive anode architecture as a series of separated two-dimensional resistive strips with a homogeneous surface resistivity. With this approach, we assume that the local response of the readout can be adequately approximated using this simplified layout. In practice, however, the surface resistivity value can vary across the active area of the detector coming from the manufacturing procedure, such as non-uniform temperatures and pressures during the gluing stage of the board. Variations around a factor two have been observed over a 10×10 cm^2 anode [209]. These fluctuations are around a mean value that is known to drift throughout the production steps, e.g., during the curing of the ohmic polymer past. As a result of many production and environmental parameters, the final surface resistivity can be different from the target value to an appreciable degree, as seen in the ATLAS MM production [210]. As the resistive strip MM detectors used in this study were manufactured before the project's initiation, we could not measure their surface resistivities given the presence of the fixed micromesh preventing access to the anode structure. This introduces a systematic uncertainty to our simulation study, the magnitude of which will be discussed in Sec. 8.5.3 during the final comparison with the measurements.

In the y-direction, the discrete symmetry in the geometry enables a reduction of the system to the configuration depicted in Fig. 8.7, without loss of generality. This representation includes a singular resistive strip and y-strip readout electrode within the geometry, featuring periodic boundaries at the edges at $y = \pm 125$ µm. However, the resistive strips run a finite distance in the x-direction, the length of which is reflected in the time-dependent reaction as indicated by Eq. 8.2.4. Hence, the size of the active area

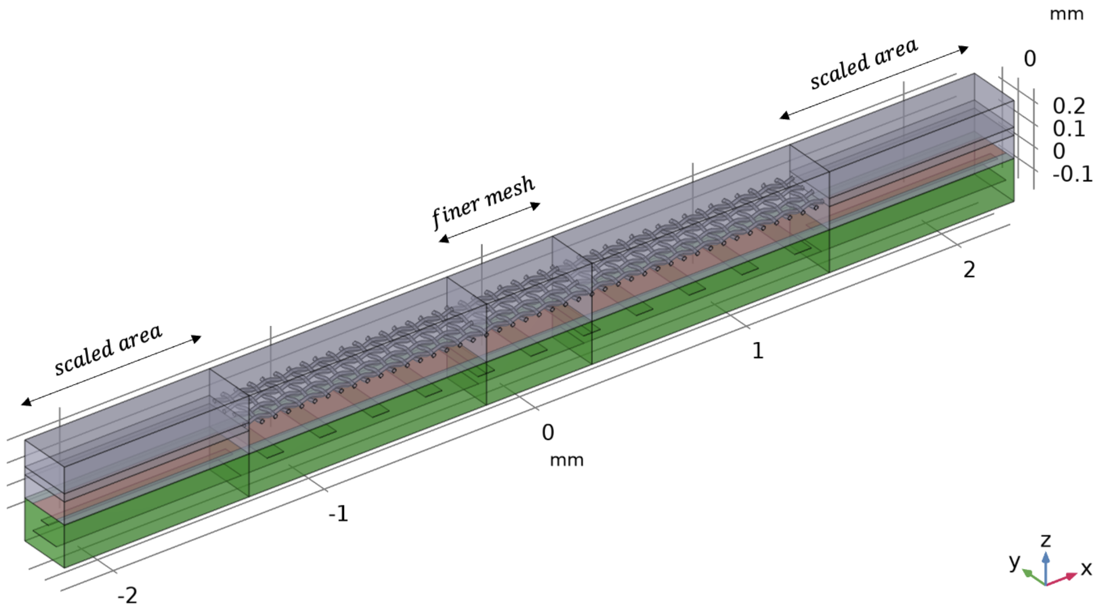

Figure 8.7: Input geometry of the simulated cell of the amplification and readout architecture of the resistive strip MM. A central region includes twelve x-strip electrodes and one y-strip within the insulator (highlighted in green), above which a resistive strip is positioned (highlighted in red). The micro-mesh is suspended above the anode structure. Two adjacent regions are coordinate mapped to align with the appropriate length of the resistive strip.

in the x-direction needs to be considered with an accurate set of boundary conditions. In addition, we aim to acquire signals from multiple neighboring x-strip electrodes, each of which must be individually represented in the geometry. Consequently, a central area of interest is defined, comprising twelve x-strips, in which the events will be simulated, while an outer region is coordinate scaled to span the width of the active area. The focus was placed on the central region of the active area; therefore, we take the scaling to be equal on both sides. Within this region, the micro-mesh structure is fully resolved and suspended above the readout at the measured height quoted in the preceding section; in the scaled regions, it is coarsely approximated by a metal plate of 36 µm thickness.

The weighting potential has been calculated for the central x-strip electrode, in close proximity of which the gradient of the weighting potential is expected to be the highest. Hence, a higher local density of finite elements was utilized to improve the accuracy of the numerical computation, as indicated in Fig. 8.7. Since typically the resistive strips are connected to ground or HV on one side, the boundary conditions of this element read

$$\Psi(\mathbf{x},t) = 0\,, \qquad \text{for } \mathbf{x} = \left(-\frac{l}{2}, y, 0\right) \text{ cm}\,, \tag{8.4.1a}$$

$$\frac{\partial \Psi(\mathbf{x},t)}{\partial x} = 0\,, \qquad \text{for } \mathbf{x} = \left(\frac{l}{2}, y, 0\right) \text{ cm}\,. \tag{8.4.1b}$$

where $l > 0$ is the length of the resistive strip taken to be 10 cm, unless stated otherwise. On the remaining outer edges parallel to the xy and xz-plane we imposed insulating boundary conditions. The system was solved for the nominal surface resistivities of $R = 100$ k$\Omega/\square$, $R = 1$ M$\Omega/\square$ and $R = 2$ M$\Omega/\square$ for a finite number of time points $t \in [0, 1.1]$ µs.

Four time slices of the solution of the weighting potential of the central strip are shown in Fig. 8.8. At time $t = 0$, the prompt weighting potential instantaneously permeates the detector volume, as if all resistive elements were perfect insulators. As time progresses, the resistive strips gradually disperse the potential across their surfaces, resulting in all conducting materials behaving like ideal conductors as $t \to \infty$. In this steady-state solution – taken to be the final frame shown in Fig. 8.8 – the amplification gap is not fully shielded from the weighting potential of the readout electrode due to the opening between the resistive strips. As the area above these openings is minimally affected by the delayed component, signals induced from charge carriers drifting in this region will predominantly exhibit a prompt response, unlike the rest of the amplification volume, where a significant contribution arises from the reaction of the resistive material. Consequently, based on Eq. (2.2.14), we can infer that electrons concluding their drift on this perfectly insulating material will contribute a non-zero value to the total induced charge measured upon signal integration[1].

To increase the quenching of discharges that develop in close proximity to the connection points, the resistive strips are connected to the HV supply through an intermediate resistor $R_t = \mathcal{O}(10)$ MΩ to provide a minimal impedance to ground[2]. This addition alters the boundary condition presented in Eq. 8.4.1a, the effect of which on the signal formation was gauged by extending the FEM model by virtually terminating the edge of the resistive element with a total resistance R_t to the ground frame. In Fig. 8.9, the potential on the terminated side of the strip is shown for varying lengths of the strip and different values of R_t. As the system is disrupted by the sudden change of conditions through the voltage step on electrode one at $t = 0$, this change propagates via the resistive strip to the system's boundary as a voltage 'pulse.' As the length of the resistive strip is increased, the pulse arrives later and is more defused at the edge. At the same time, it is shorter and more attenuated for a reduced termination resistance. This can be interpreted as the system more efficiently draining deposited on the strip if it is shorter

[1] In actuality, the material possesses non-zero volume and surface conductivities. Consequently, the accumulated charge will eventually dissipate or be offset by the system.

[2] The subscript denotes the termination of the element.

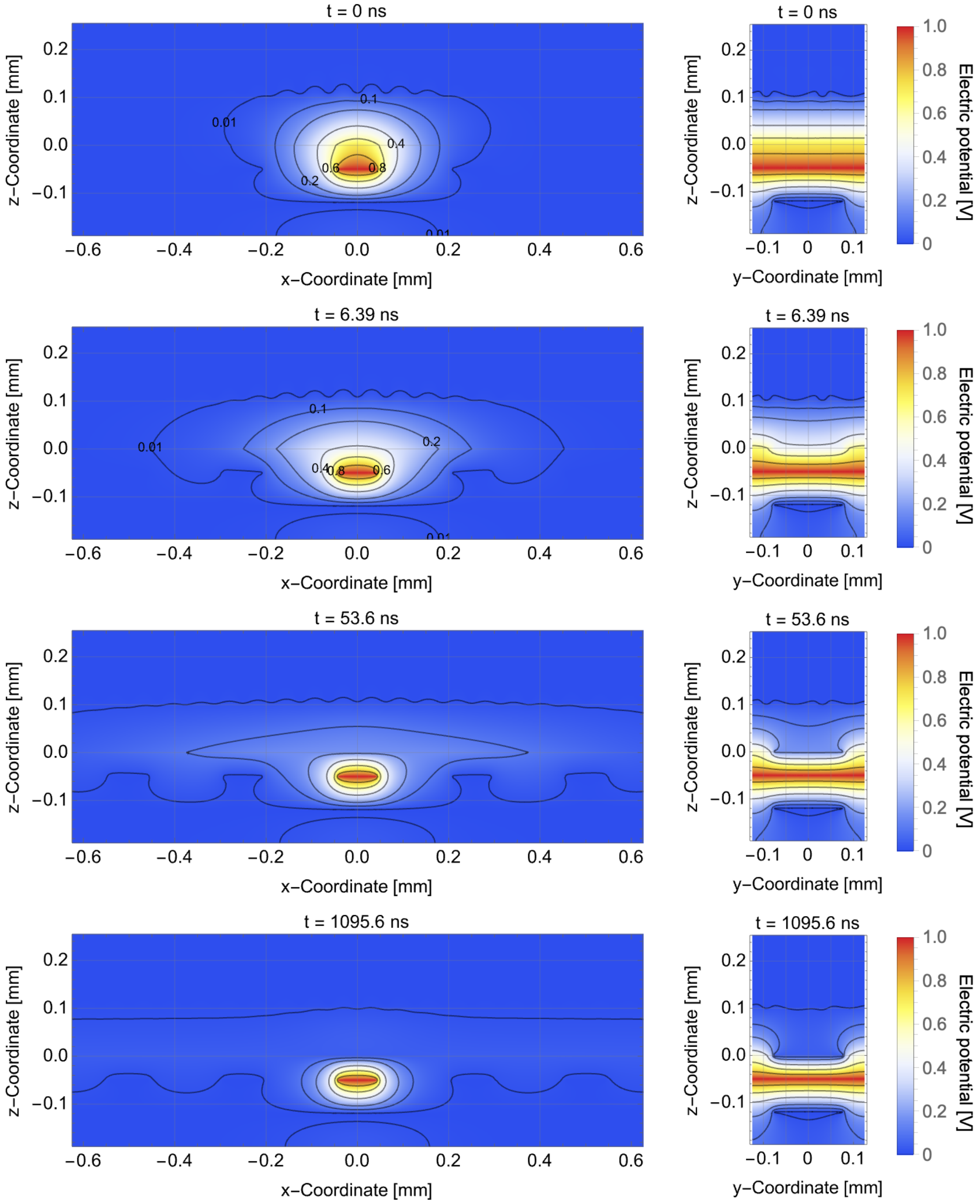

Figure 8.8: Time sliced cross-section weighting potential maps for x-strip number 5 with resistive strips of 1 M$\Omega/\square$. The right and left columns are cross-sections of the solution at $y = 0$ and $x = 0$.

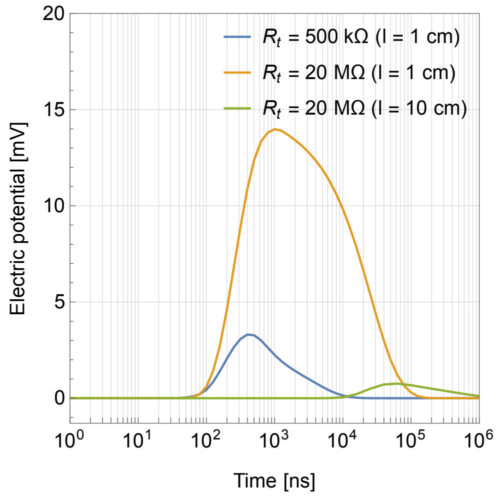

Figure 8.9: Weighting potential at the connection point of a 1 MΩ/□ resistive strip positioned at $x = -l/2$ for different termination resistor values R_t.

and has a reduced impedance to ground. Looking at the magnitude the contribution of a 20 MΩ resistor to the weighting potential at the termination point, we did not expect any significant changes compared to the solution found for an ideally grounded case. This was confirmed when looking at the weighting potential in the region around the readout strip under study, where the contribution was found to be negligible. As a result, for what follows, we use the solution presented in Fig. 8.8 where $R_t = 0$ Ω.

8.4.2 Description of Monte Carlo model

The complete response of the detector was modeled using a series of independent calculations: (i) the primary ionization pattern in the drift gap due to a relativistic muon and subsequent motion of the electrons until they reach the amplification structure, (ii) the avalanche development in the amplification region and the resulting signal induction on the readout electrodes, and (iii) the convolution of the induced currents with the delta response function of the ASIC. The final signal waveform was then analyzed and averaged over different muon hit positions.

Given the the deviations of the drift field from a uniform field are located close to the mesh structure, we can approximate the drift gap as a parallel plate chamber with a gap size of 5 mm. For this volume filled with an Ar/CO_2 93/7% gas mixture at NTP, the energy transfer from a muon with a momentum of 150 GeV/c to this medium, leading to the creation of electron-ion pairs, was calculated through a Monte Carlo simulation with Heed. The simulated average cluster density and cluster size are shown in Fig. 8.10, which leads to the Landau distribution of the number of pairs given in Fig. 8.11. For what follows we take the time of the muon crossing the detector to be $t = 0$. The

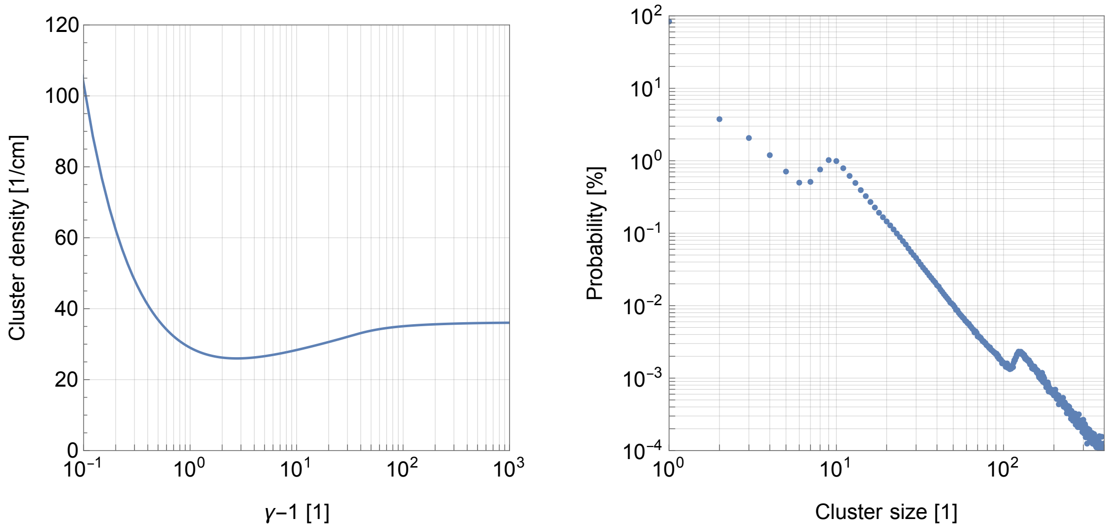

Figure 8.10: **Left:** Average cluster density for tracking muon though the Ar/CO_2 93/7% binary gas mixture as calculated by Heed. **Right:** Simulated cluster size distribution for a 150 GeV/c muon using Heed.

parameters governing the drift, diffusion, amplification[3], and attachment of electrons were computed using MAGBOLTZ. These parameters were then used to microscopically simulate the trajectories of electrons towards the amplification structure, driven by a uniform electric field of 550 V/cm. Fig. 8.12 (left) shows the drift lines of the charge carriers of one such event where the position of the incident muon runs along the z-axis. The distribution of the electrons at the bottom of the drift gap is shown in Fig. 8.12 (right), which follows the distribution of Eq. (4.1.9).

After reaching the amplification structure, the electrons were transferred to a second simulation where they were placed ≈ 150 µm above the mesh. Here, a FEM solution of the electric field was used for the final portion of the drift field and the amplification field between the mesh and anode structure. As a result, we included the mesh transparency, as the electrons were guided through or onto the mesh wires. The avalanche dynamics were simulated microscopically, given a 550 V potential difference between the mesh and resistive strips. Taken from Fig. 2.11, the ion mobility was adjusted to align with the values previously measured in Sec. 5.2. The resulting trajectories of the positive and negative charge carriers were used in conjunction with the dynamic weighting potential solution to calculate the total induced signal on the x-strips.

Finally, the impulse response function of the ASIC was convoluted with the total induced signal of the electrodes. We approximated the electronics by an idealized uni-

[3]The effective Townsend coefficient was modified based on an expected penning rate of $r = 0.40477$.

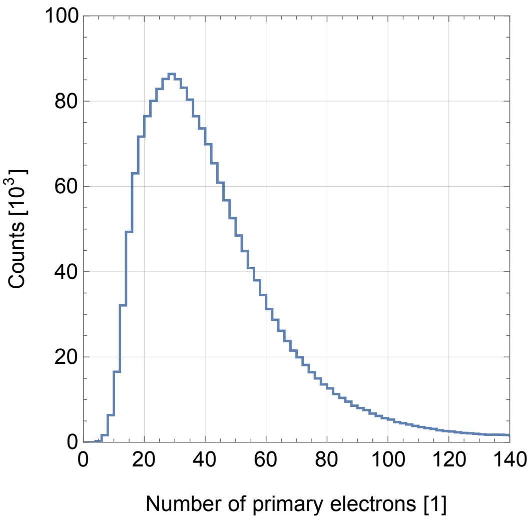

Figure 8.11: Distribution of the number of primary electrons in a 5 mm drift gap filled with Ar/CO_2 93/7% for a 150 GeV/c muon.

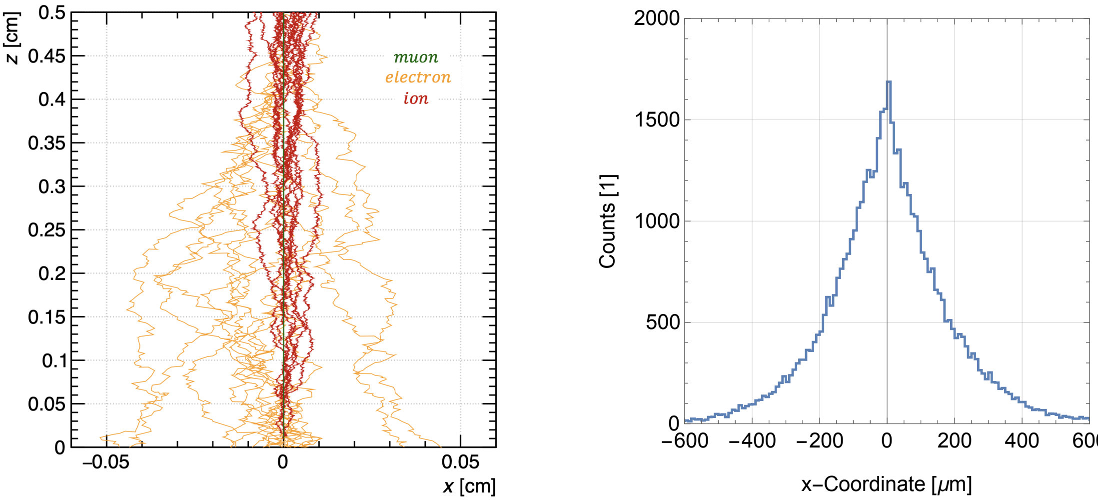

Figure 8.12: **Left:** Drift lines of the primary charge carriers in the drift gap for a muon event. **Right:** Simulated distribution of the endpoints of the electrons.

polar shaper:

$$f(t) = ge^{n}\left(\frac{t}{t_p}\right)^{n} e^{-\frac{t}{\tau}}\,, \tag{8.4.2}$$

where the peaking time is defined as $t_p = n\tau$ [6]. The above expression is normalized such that at time $t = t_p$ it reaches the value of the gain factor g. To emulate the response of the APV25 ASIC we assumed a peaking time of $t_p = 50$ ns, and a first order shaping

$n = 1$, while keeping the amplification to $g = 1$ [211, 212]. Since this chip is sampling at 40 MHz, the bulk of the simulations were performed using 25 ns wide time bins.

8.4.3 Results

The total induced signal before shaping is shown in Fig. 8.13 for the $R = 1$ M$\Omega/\square$ configuration and a muon going though of the origin of the xy-plane. The different initial vertical positions of the clusters in the drift gap in conjunction with the transversal diffusion of the primary electrons result in different arrival times at the mesh that can be ≈ 120 ns at the latest. With the mesh mostly shielding the drift gap from the dynamic weighting potential, the signal is induced as soon as electrons have propagated through the mesh and are being amplified. This variation in time is visible in the signal structure as the multiple electron peaks that are distributed over the part of the induced current. For the strips below and those directly neighboring the CoG of the event, both the prompt and delayed components significantly influence the overall current profile. As we move away from this point, the primary contribution will be from the response of the time-dependent resistive strips. Notably, the ion tail amplitude is reduced due to the persistent positive signal polarity of the delayed component. Once the bulk of the ions are collected, a polarity switch will occur, possibly preceded by other short ones triggered by the electron current from large Townsend avalanches. For the case of $R = 100$ k$\Omega/\square$ (see Fig. 8.14), the delayed component is significantly faster in time. Consequently, the ion tail experiences shows suppression. For the sake of comparison, we have used the identical set of arrival positions and times of the primary electron from a simulated event in the drift gap for both Fig. 8.14 and Fig. 8.13.

While the charge of electrons arriving on the resistive strips, as can be seen in the top panel of Fig. 8.13, will be directly drained from the anode structure, the accumulation of charge on the insulating material results in the modification of the shape and strength of the amplification field. This charging-up effect results in variations in gain over time [213], which would require a separate simulation such as the one found in Ref. [214].

For our eventual comparison with the experimental results, the induced current is averaged over events where the muon tracks were uniformly distributed over the first half between electrode 5 and 6: $0 \leq x_\mu \leq 125$ µm. After convolution with the impulse response function of the APV25, the average response is given for $R = 100$ k$\Omega/\square$ and $R = 1$ M$\Omega/\square$ in Fig. 8.15. As anticipated, the strip closest to the muon track, being electrode 5 and henceforth referred to as the *leading strip*, exhibits the highest signal amplitude. The adjacent channels display time-shifted peak amplitudes that are progressively decreasing in magnitude, illustrating the signal's spread in the resistive strips and yielding the distinctive V-shape of the peak position in the time [104]. Owing to the rapid response of the resistive strips at $R = 100$ k$\Omega/\square$, the average pulse height is lower than that observed for $R = 1$ M$\Omega/\square$.

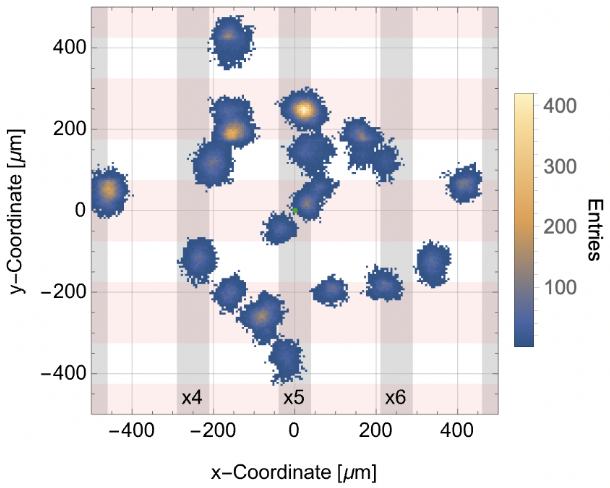

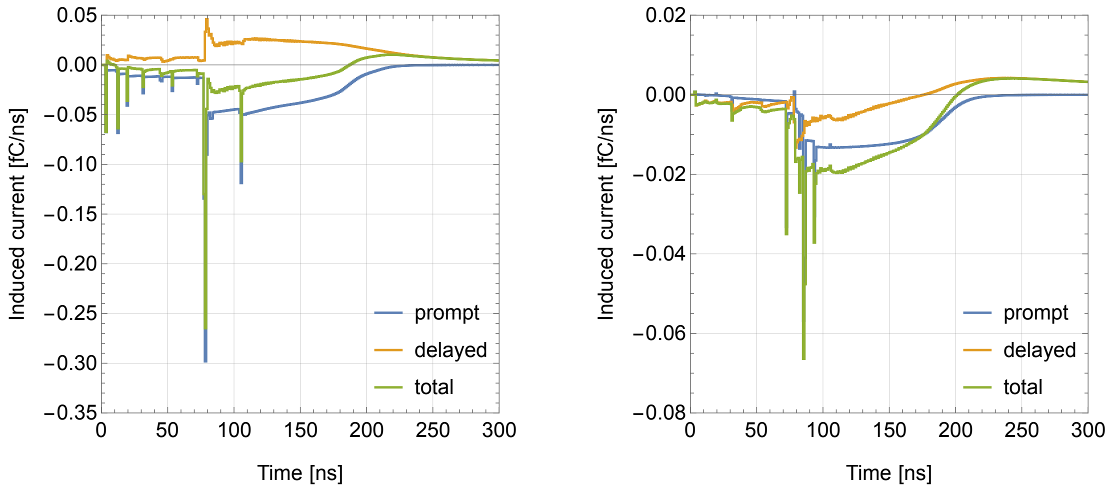

Figure 8.13: Induced current response on the x-strips from a generated muon event for $R = 1\,\mathrm{M}\Omega/\square$. **Top:** Endpoint distribution of the electrons collected by the resistive anode. Superimposed is the location of the readout strips (marked in gray) and the resistive strips (marked in red). The position of the muon track is marked in green. The indices of the strips are marked at the bottom of the figure, while to hit position of the muon is marked in green. **Bottom left:** Prompt, delayed and total induced signal on x-strip 5. **Bottom right:** Induced signal on our neighboring readout x-strip 6.

8.5 Signal induction measurement

To assess the accuracy of the implementation of the extended form of the Ramo-Shockley theorem in Garfield++, the induced current response of the x-strip electrodes in two resistive strip MM detectors with different surface resistivities has been measured using MIPs. The data was collected during the common RD51 SPS test beam campaigns at

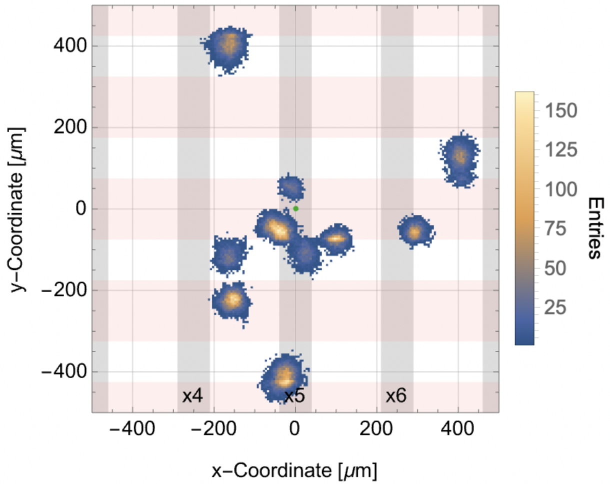

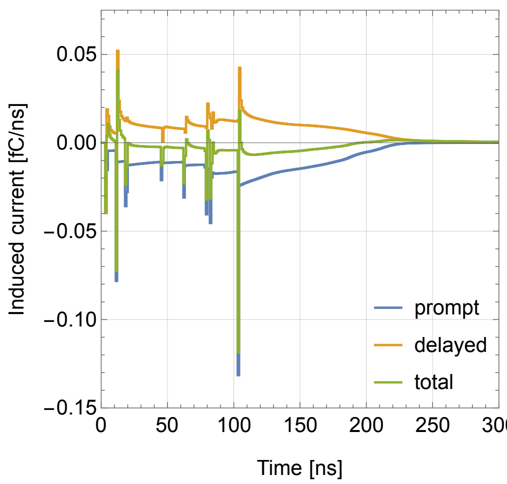

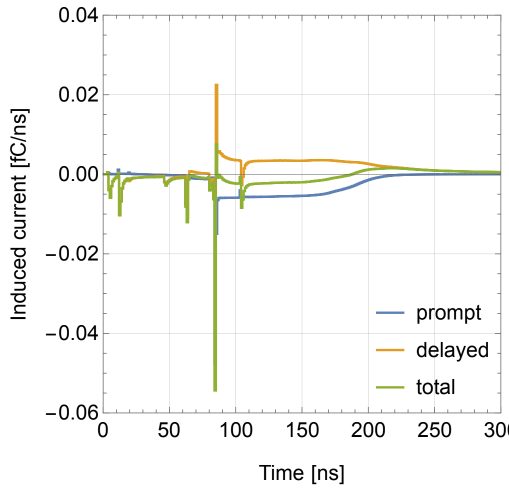

Figure 8.14: Induced current response on the x-strips from a generated muon event for $R = 100\,\mathrm{k}\Omega/\square$. **Top:** Endpoint distribution of the electrons collected by the resistive anode. Superimposed is the location of the readout strips (marked in gray) and the resistive strips (marked in red). The position of the muon track is marked in green. **Bottom left:** Prompt, delayed and total induced signal on x-strip 5. **Bottom right:** Induced signal on our neighboring readout x-strip 6.

the CERN SPS H4 beam line using the MM-based tracking telescope sketched in Fig. 8.16. For specifics on the test beam infrastructure we will refer to Sec. 5.5. The subsequent discussion will focus on the measurements performed with 150 GeV/c muons.

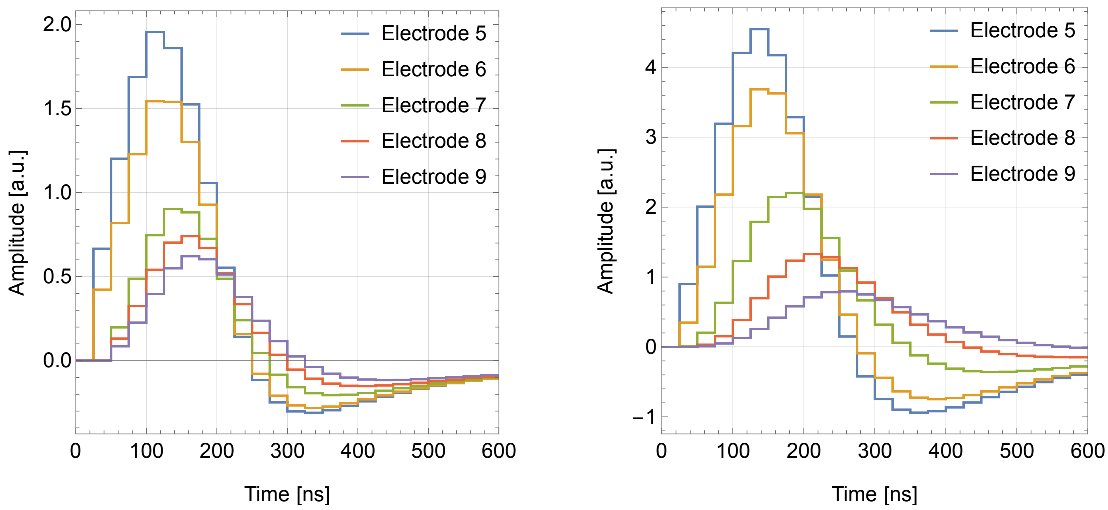

Figure 8.15: Averaged induced current response on the x-strips from a generated muon track between electrode 5 and 6 for $R = 100\,\mathrm{k}\Omega/\Box$ (left panel) and $R = 1\,\mathrm{M}\Omega/\Box$ (right panel).

8.5.1 Experimental setups

The setup incorporated three bulk MMs, which included one DUT. These contained a 1 M$\Omega/\Box$ resistive strip anode and a two-dimensional strip-based readout structure. These functioned as our tracking detectors, the recorded signals of which were used for the offline track reconstruction of the incident muons. To this ensemble, another DUT was added featuring a 100 k$\Omega/\Box$ resistive strip bulk MM readout structure. All four devices had an active area of 10×10 cm^2 and adhered to the same layout depicted in Fig. 2.5. Their orientation in the setup was such that the resistive strips were aligned parallel to the x-axis, as illustrated by the right-handed coordinate system in Fig. 8.16. Additionally, we positioned the connection points to HV on the same side. In this way, the sole difference between the two DUTs was their surface resistivities: 1 M$\Omega/\Box$ and 100 k$\Omega/\Box$ respective to the beam direction. Both of these detectors were positioned at the center of the tracker. As depicted in Fig. 8.17, the detectors were affixed to support frames that allowed for alignment adjustments in the xy-plane. The cathode and resistive anode of the MMs were connected to HV, while the micro-mesh was put at zero potential. Filtering circuits were placed between the HV modules and the detectors to minimize the noise from the HV supply entering the system. The operation field configurations[4] and resulting effective gains[5] are given in Tab. 8.1, with the premise that all devices have

[4]Prior to the test beam period, we performed laboratory measurements that indicated that the drift field was within the plateau of the maximum mesh transparency.

[5]The effective gains were determined for the 100 k$\Omega/\Box$ MM through current measurements during irradiation with a ^{55}Fe source. Given the four MMs share the same amplification architecture, it is assumed that the gain is consistent across all of them.

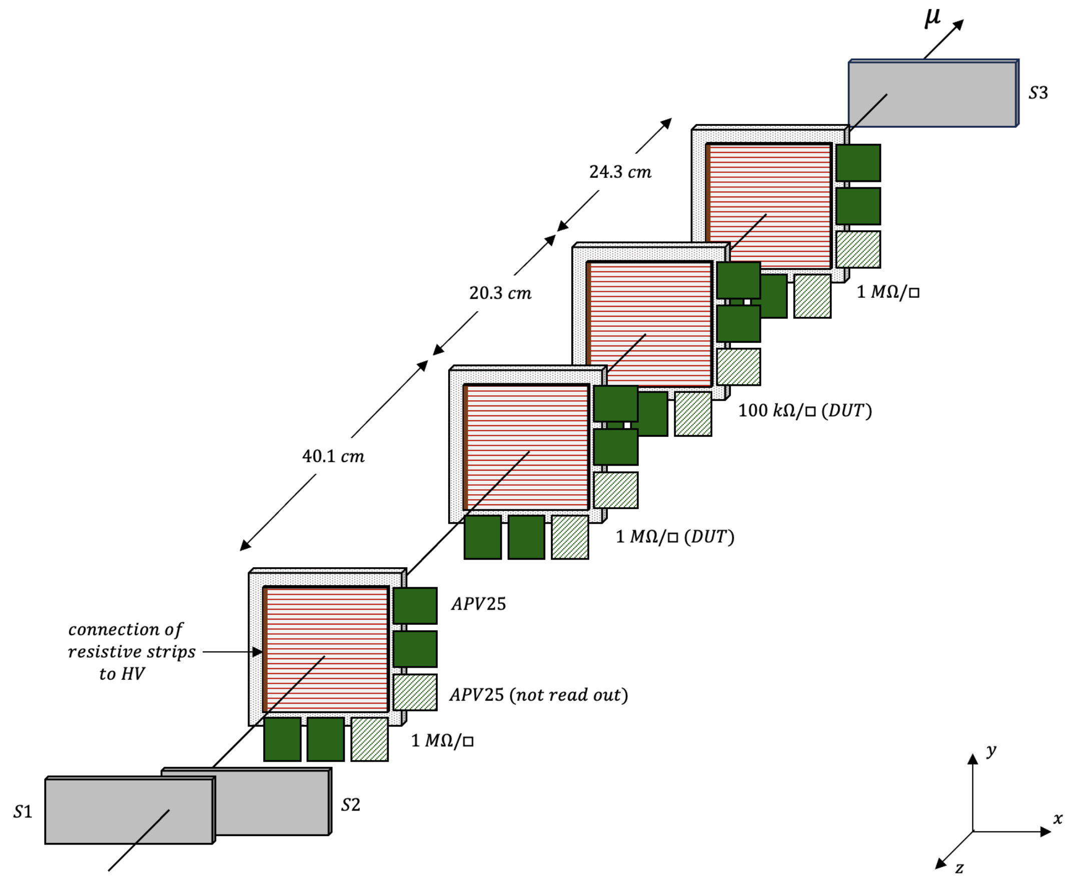

Figure 8.16: Schematic representation of the test beam setup used at the CERN SPS H4 beam line. Four resistive strip bulk MMs with two sets of surface resistivities form the tracking telescope containing two DUTs. The resistive strips (horizontal red stripes) and their connection point to HV (vertical brown stripe) are indicated. For triggering, three scintillators (S1, S2, and S3) linked to PhotoMultiplier Tubes are positioned at the front and rear of the telescope.

an amplification gap size as the one found in Sec. 8.3. Throughout the data taking, the detectors were operated with a binary gas mixture of 93% argon and 7% CO_2 at NTP.

The MM signals was extracted using mounted hybrid cards that housed APV25 chips, facilitating analog data transmission through HDMI cables to a front-end card in the RD51 SRS. At this juncture, the signal is digitized and transmitted via Ethernet to a Data Acquisition (DAQ) PC. The amplitude of the signal over time was digitized using 12-bit Analog-to-Digital Converters (ADCs), representing the signal digitally. The APV25 is a 128-channel chip sampling at 40 MHz that is constructed using radiation-hard 0.25 µm CMOS technology. It incorporates a charge-sensitive amplifier, a CR-RC shaper with a 50 ns time constant, and a 192-cell pipeline. Following the reception of the trigger, the

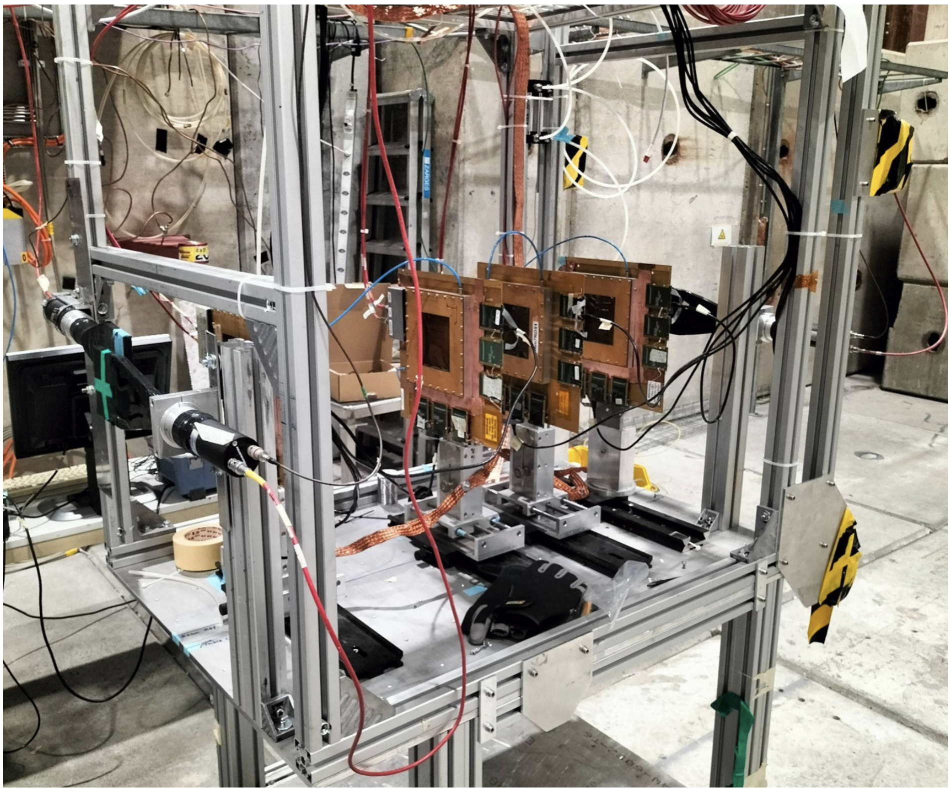

Figure 8.17: Photograph of the test beam setup used in the RD51 test beam containing four resistive strip bulk MicroMegas devices and three scintillators.

signals undergo processing by an analog circuit with three possible operation modes: *peak mode*, where single sample are read out, *deconvolution mode*, where the amplitudes of three successive time bins are combined in a weighted sum [215], and a *multi-mode*, where for each trigger the signals of three consecutive time slots are recorded and then read out separately as with peak mode [216]. The results presented in this chapter are based on data collected with the multi-mode. In every coordinate plane, we installed three such cards, yet only two were actively read during the setup's operation. This was a deliberate choice to reduce the number of channels needing processing. Consequently, just four-ninths of the detectors' area was fully read out, while the rest remained unprocessed.

Owing to the inherent background noise of the system, the output signal from the APV25s delivers a continuous stream of low-amplitude pulse fluctuations. When a particle hit generates signals on strip electrodes, the raw waveforms are recorded into the dataset, while the waveforms from the unaffected strips undergo rejection through an online *zero-suppression*. This algorithm ensures that the integrated waveform of a strip must surpass a predefined THL based on the standard deviation from the recorded noise distribution (pedestal variation) to be considered a part of the event; otherwise, it is re-

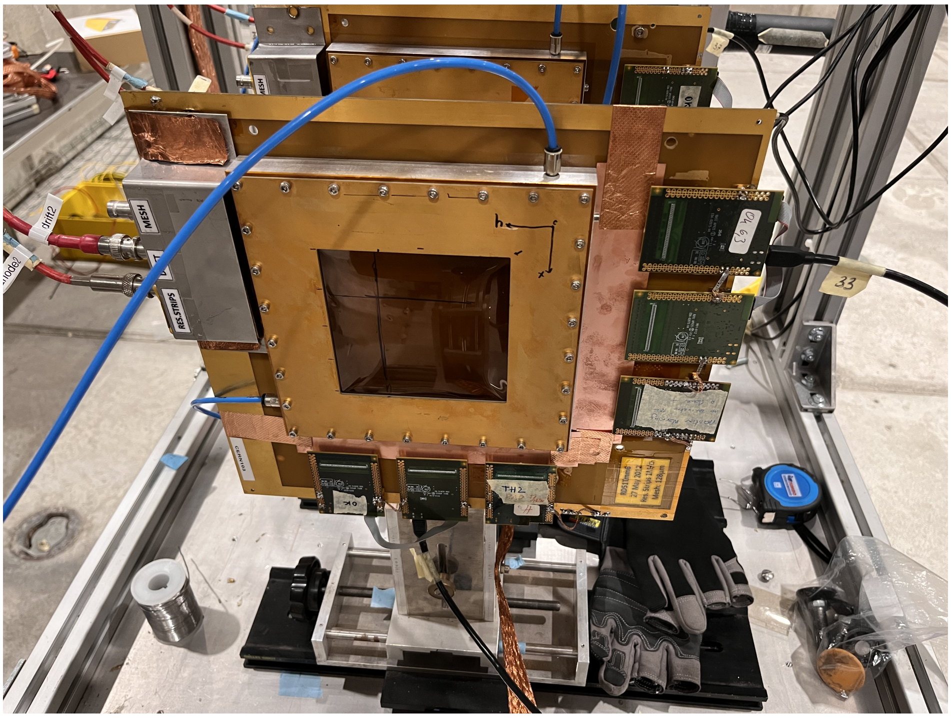

Figure 8.18: Photograph of the 1 M$\Omega/\square$ detector under test mounted in the tracking telescope.

garded as a noise channel. In the subsequent offline reconstruction process, we estimated the PHs of pedestal-corrected signal waveforms by determining the maximum ADC count above the baseline by fitting the leading-edge using a logistic function. The difference between the constant offset and the maximum of the function is taken as the maximum amplitude of the signal [6], which is propagated to the track reconstruction processing.

The DAQ system was triggered by NIM signals originating from a coincidence unit, which in turn received signals from three scintillators (S1, S2, and S3) linked to Photo-Multiplier Tubes (PMTs). Mounted on the overarching frame of the tracker, two scintillators labeled S1 and S2 were positioned in front of the MMs, with a third scintillator S3 situated at the telescope's end. Different modules, e.g., threshold discriminators, were employed to pre-process the signals from the PMTs before going to a coincidence unit that formed an *AND* gate. The coincidence unit would then send out a signal in case a particle interacted with all three scintillators. These modules were housed, alongside the CAEN SY5527 HV supply mainframe, in a rack placed next to the telescope.

[6] As pointed out in Sec. 2.3.4 this quantity is not synonymous with the total induced charge of the signal due to the relatively short shaping time compared to the length of the signal, and as such is a more convoluted indicator of the number and relative position of charge carriers involved in the event.

Table 8.1: List of the operational drift and amplification fields for the MM detectors in the test beam setup, along with their corresponding effective gain G_{eff}.

	E_{drift} [kV/cm]	E_{amp} [kV/cm]	G_{eff} [10^3]
MM1	0.45	44.91	9.67 ± 0.31
MM2	0.55	45.75	13.34 ± 0.59
MM3	0.45	45.75	13.34 ± 0.59
MM4	0.45	44.91	9.67 ± 0.31

8.5.2 Signal shape comparison

A selection of pedestal-corrected signal waveforms are shown in Fig. 8.19 (left) for 1 MΩ/□ and in Fig. 8.20 (left) for 100 kΩ/□, for which the recorded PHs are plotted in the respective right panels as a function of the strip index. This PH distribution has been fitted using the function

$$f(x) = a\frac{|x - x_0|\left(\operatorname{erf}\left(\frac{|x-x_0|}{\sqrt{2}\sigma}\right) - 1\right) + \sqrt{\frac{2}{\pi}}\sigma e^{-\frac{(x-x_0)^2}{2\sigma^2}}}{\sigma^2}, \tag{8.5.1}$$

where the amplitude a, position x_0 and width σ are the free parameters. The result superimposed on the measured peak amplitudes is shown in Fig. 8.20 (right) and Fig. 8.20 (right) for the 1 MΩ/□ and 100 kΩ/□, respectively. Despite having comparable diffusion in the drift region, the lower surface resistivity case shows a significantly wider spread of the signal over the local set of strips. This is reflected in the value of the estimated for σ, which is around a factor four higher in the case of the 100 kΩ/□. Another quantity indicating that the spreading of the signal is indeed driven by surface resistivities is the cluster size distribution in the readout, as shown in Fig. 8.21[7].

As for the simulated response, the recorded waveforms of the events were averaged to get the mean current response of the x-strips. In accordance with the convention of Sec. 8.4, electrodes $i \in \{1, 2, \ldots, 9\}$ are arranged in ascending order along the positive x-axis. The electrode with the maximum amplitude, i.e., the leading strip, is labeled as electrode 5. Signals are then averaged around electrode 5, including the eight closest neighboring electrodes. The maximum amplitude for the leading strip for each event is shown in Fig. 8.22, where a noise spike can be observed at low ADC counts. To filter out these noise hits, a fixed THL of 100 ADCs is employed for each readout channel. In addition, to avoid the saturation of the ADCs for large signal amplitudes that are observed during the operation of the APV25 ASIC, we require the maximum ACD count to be below 1800 in order not to distort the average signal shape. However, the APV is non-linear below zero and saturates the signal below -200 ADC counts, resulting in the negative polarity of the signal being distorted for large signals. To mitigate potential edge effects, we exclusively consider events situated within the central region of the

[7] In this figure, events were chosen based on the criterion that the maximum amplitudes of the leading strip should fall within the range of 300 to 1800 ADC counts.

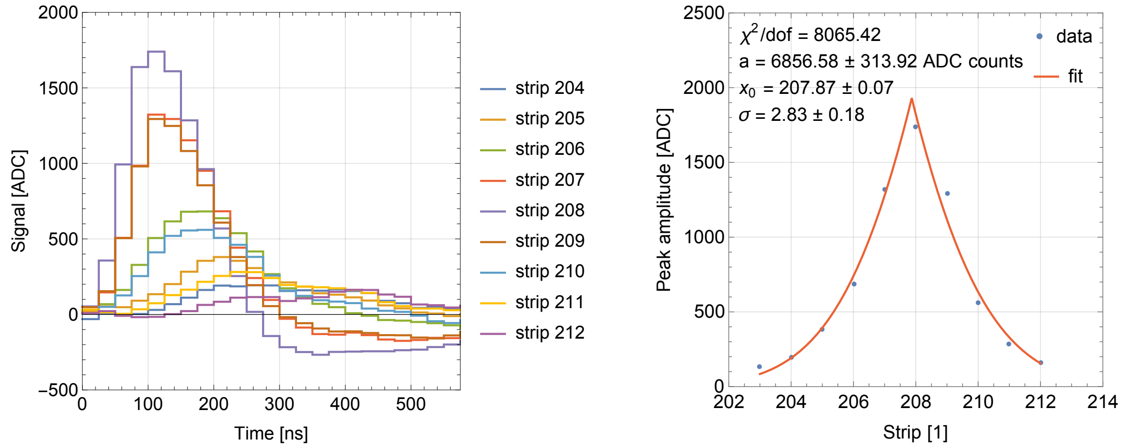

Figure 8.19: Example of a recorded event with the 1 MΩ/□ DUT **Left:** Signal shapes on the x-strip electrodes. For clarity, only a reduced number of channels are displayed compared the total amount that were recorded over the threshold level. **Right:** Pulse heights for triggered channels, fitted using the function 8.5.1.

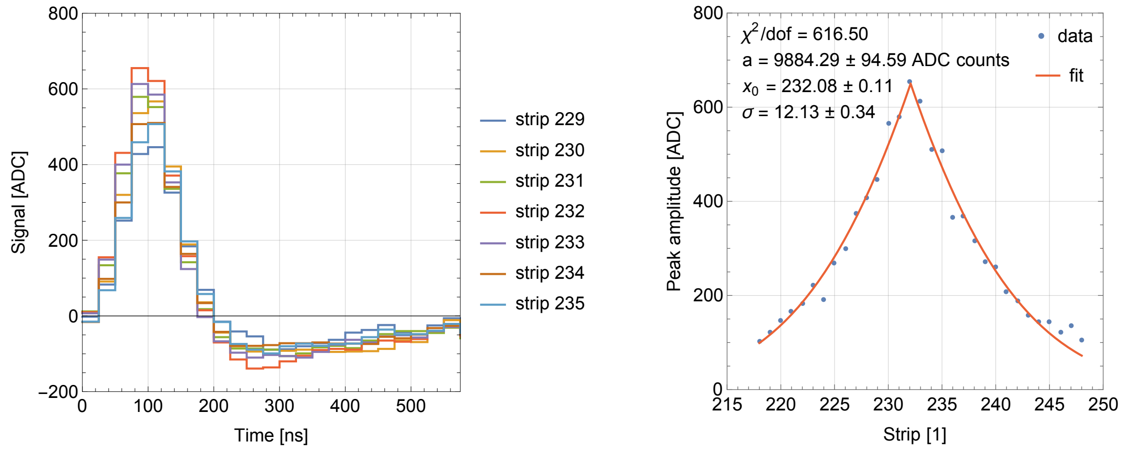

Figure 8.20: Single recorded event of the 100 kΩ/□ DUT. **Left:** Digitized induced signal for seven x-strips, where the remaining of the fourty triggered channels are omitted form this plot for clarity. **Right:** Pulse heights distribution over the triggered channels, fitted with function 8.5.1.

DUTs based on their position information. Additionally, we selected events for which the reconstructed position x_r was located in the first half between the center electrode of 5 $(x_{s,5})$ and 6, i.e., $x_{s,5} \leq x_r \leq x_{s,5} + 125$ µm. The resulting average signal shapes for the 1 MΩ/□ are shown in Fig. 8.23, where the spreading of the characteristic signal over neighboring channels can be observed. The uncertainties of the measurements are driven by systematic errors pertaining to the zero-suppression cut, PH cuts, and response

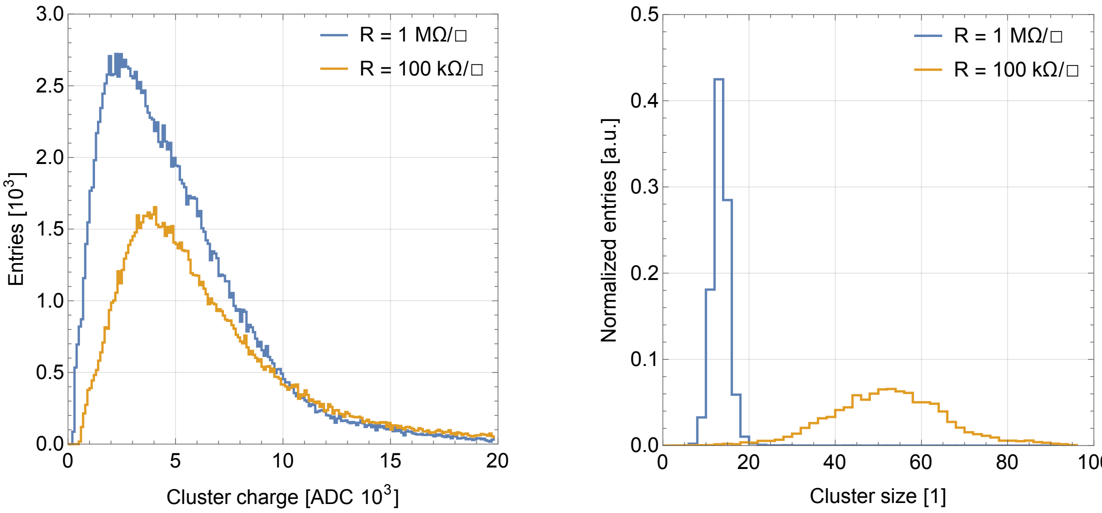

Figure 8.21: **Left:** Measured distribution of the cluster charge, i.e., the sum of the pulse heights off all the strips in the neighboring strips. **Right:** Cluster size distributing for both surface resistivities.

variations across the active are, e.g., due to gain non-uniformity. Compared with the 100 kΩ/□ prototype (Fig. 8.24), the 1 MΩ/□ one shows a slower reaction of the resistive strip, resulting in a more delayed signal in the neighboring channels.

Even though the signal induced on the y-strips also includes a substantial contribution from the delayed component, the change in surface resistivity affects the amplitude signal distribution across the x and y-coordinate plane, resulting in a shift in the signal sharing between them. The ratio of the cluster charge on two planes is $q_{\text{clu,x}}/q_{\text{clu,y}} = 2.782 \pm 0.005$ and 3.748 ± 0.002 for the 100 kΩ/□ and 1 MΩ/□ MM, respectively. To optimise the design, numerical optimisation studies along the line of Chapter 4 could be conducted.

8.5.3 Comparison with simulation

In order to test the viability of the simulation method, we benchmark the calculation results of Sec. 8.4 against the above measured current response.

For the purpose of comparison we need to account for the conversion chain from the unamplified CR-RC shaped signal to the ADC counts after digitization. This was done by scaling the amplitude of simulated responses to ensure that the pulse height of the leading strip corresponds to that of the measured value. The calculated responses for the 1 MΩ/□ and 2 MΩ/□ resistive strip MM through the Monte Carlo simulation are overlaid with the measured data in Fig. 8.23. While both simulation configuration provide a good description of the signal, doubling the surface resistivity yields an appreciable difference in the overall shape of the signal by changing the PH, peaking time and zero-crossing

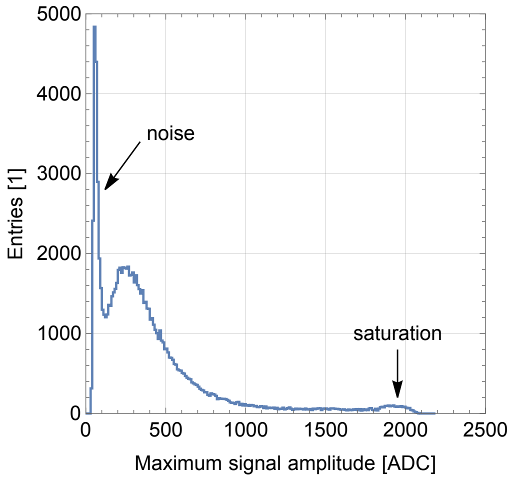

Figure 8.22: Distribution of the maximum pulse height found in the triggered x-strip channels for the 1 M$\Omega/\Box$ DUT.

time. For example, for electrode 7 (8) this results in an $\approx$ 15% ($\approx$ 40%) reduction in its mean maximum amplitude and an $\approx$ 15% ($\approx$ 35%) increase in its zero-crossing time. This provides an indication of the systematic uncertainty associated with the possible values the surface resistivity can take after production. In addition, since variations up to a factor two can be expected across the active are, it would be more accurate to an appropriate mixing of the responses coming from the Monte Carlo calculations using a range of surface resistivities. Nevertheless, the simulated current response for the 2 M$\Omega/\Box$ shows the best agreement with the experimental data, falling within three sigma of the measured values for most time bins. Computing the χ^2/N_{dof} we obtain a value of 14.5, 7.0, 2.6, 2.9, and 7.5 for strip number five to nine, respectively. The largest deviations can be observed for values below zero. This can be attributed to the nonlinear response of the ASIC for the negative polarity which is not taken into account in our model or the experimental errors.

The zero-crossing times of the signals were estimated by employing an linear interpolation between the closest sampling point around zero, and looking at the intersection point. The binned distributions of both simulated and measured values are presented in Fig. 8.25. It is observed that, on average, the simulated values using 2 M$\Omega/\Box$ resistive strips tend to underestimate the zero-crossing time. In addition to the systematic impact of surface resistivity, using the precise delta response function of the ASIC – either computed using a general-purpose circuit simulation program or measured by injection of charge pulses on at the input terminal – could provide a better matching of the two distributions. However, further investigation is needed to explore this possibility.

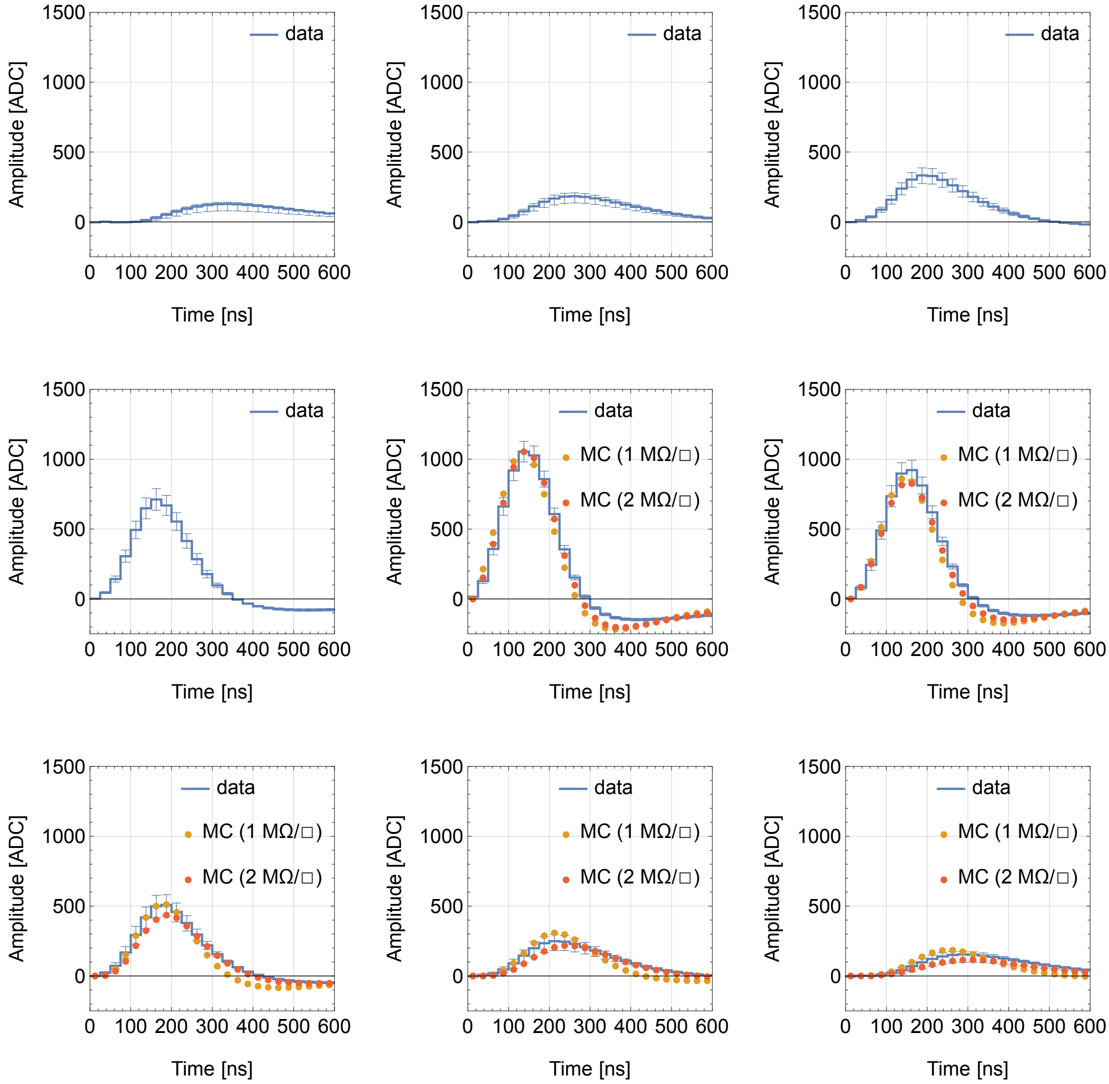

Figure 8.23: Induced currents of nine neighboring x-strips in the two-dimensional readout of a 1 MΩ/□ resistive strip bulk MicroMegas. Following the convention of Fig. 8.1, the result for electrode 1 and 9 are given by the upper left and bottom right panel, respectively. The electrode indices of the remaining panels follow the reading direction. The response is averaged over incident muon tracks reconstructed to be between electrodes 5 and 6 in the first half. The results from the Monte Carlo (MC) calculations for R =1 MΩ/□ and R = 2 MΩ/□ are superimposed on the experimental data.

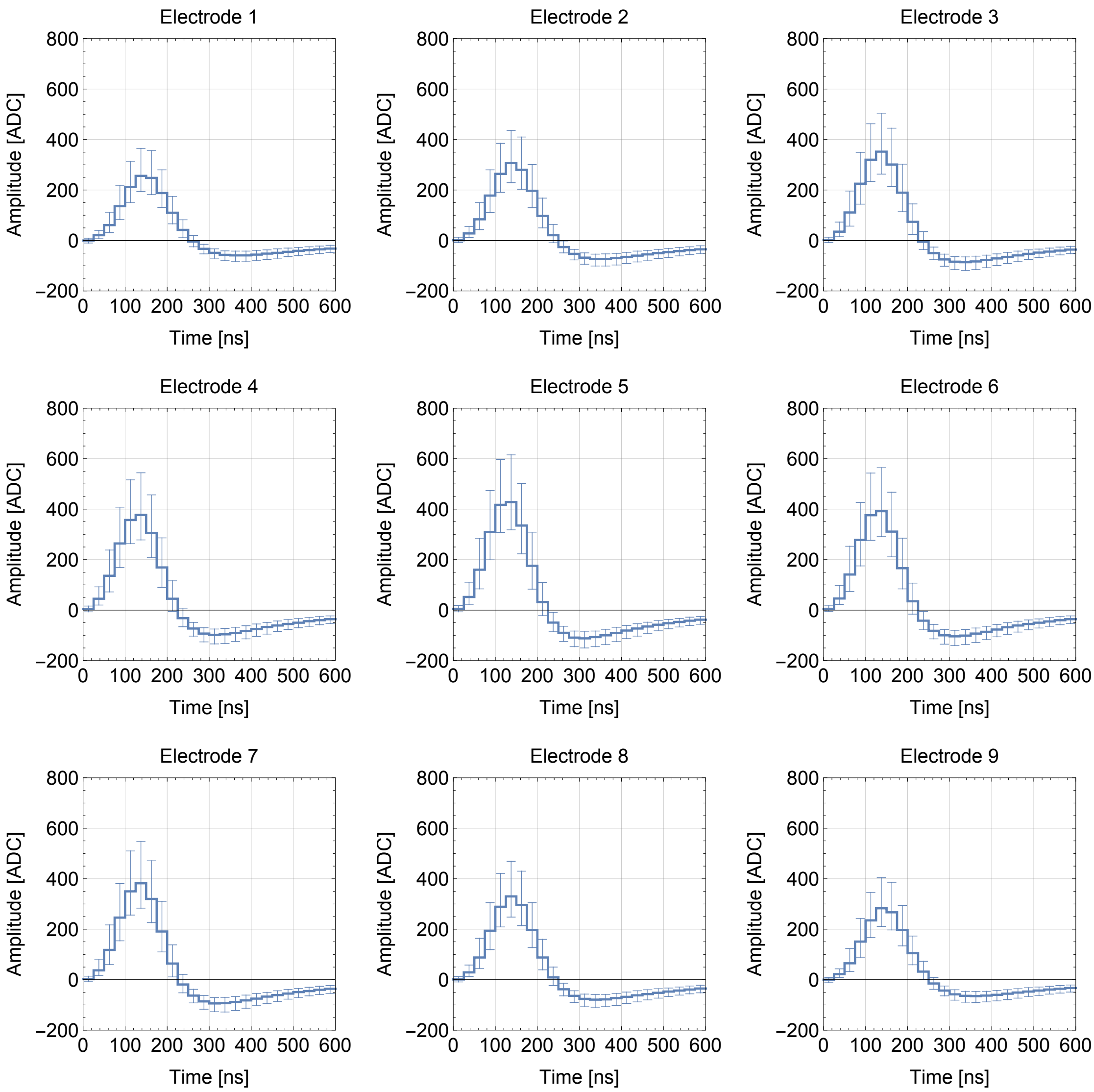

Figure 8.24: Induced currents of nine neighboring x-strips in the two-dimensional readout of a 100 kΩ/□ resistive strip bulk MicroMegas. The response is averaged over incident muon tracks reconstructed to be between electrodes 5 and 6 in the first half.

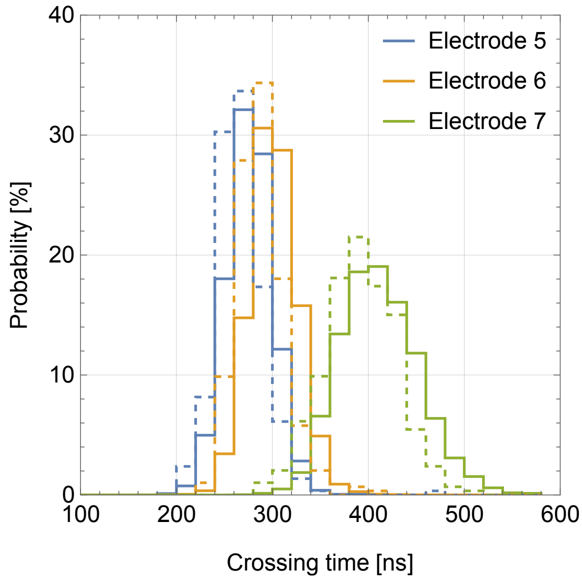

Figure 8.25: Measured and simulated (2 MΩ/□) zero-crossing times for three neighboring strips indicated by the full and dashed lines, respectively.

8.6 Summary

To enhance the operational stability of the MM design, the ATLAS MMs installed in the NSW were fitted with an innovative AC-coupled one-dimensional readout structure that incorporates resistive strips with a surface resistivity of $\approx$ 300 kΩ/□. The formation of the signals on the readout electrodes contains a sizable contribution from the delayed component in addition to the fast prompt component of the signal. The role of the delayed component was found to be especially prominent with the addition of a second set of readout strips, which sample the 'spreading' of the signal along the length of the resistive elements. We successfully observed this phenomenon for two different surface resistivities using the APV25 ASIC. We found that the signals induced in the 100 kΩ/□ setting are faster and more attenuated than those observed in the 1 MΩ/□ configuration, reflected in an increased cluster size for the former.

Similar findings were also noted in the simulation outcomes. During the computation of the time-dependent weighting potential via the FEM, particular care was taken to ensure the mesh structure and height were accurately implemented, in addition to faithfully representing the boundary conditions of the system to reflect the length of the resistive strips. Additionally, the influence of a resistor at the end of the resistive strips was evaluated, which showed to have a negligible effect on the localized signal development.

The two sets of results were compared using the overall signal shape and zero-crossing times. Within the systematic uncertainty of the calculation – mainly driven by the uncertainties regarding the precise surface resistivity value – the simulation results are in agreement with the experimental data.

Part V

Epilogue

Chapter 9

Summary

Incorporating resistive elements into contemporary detector designs has become increasingly prevalent in research and development (R&D) projects in order to meet the stringent requirements set by current and upcoming particle physics experiments. In this thesis, a numerical framework for calculating induced signals numerically in resistive detector layouts was implemented in Garfield++, which enables the application of the extended form of the Ramo-Shockley theorem for conductive media to arbitrary grounded electrodes and resistive media arrangements. The dynamic weighting potential is the key quantity in these calculations, capturing both the direct induction of current on metal electrodes from the motion of free charge carriers in the detector (prompt component) and the time-dependent reaction from the resistive elements (delayed component). Making use of the established finite element method, solutions for the weighting potential for geometries that could not be solved using analytical methods were found. To allow for the applicability of this approach to a wide range of scenarios, different techniques were explored:

- The weighting potential could be obtained for systems containing electrodes that are connected to external impedance elements, instead of being perfectly grounded, by representing the elements either physically or via a lumped element circuit.

- Without the need to represent the full active area, the boundary conditions for resistive elements stretching over a large detection area were accurately represented in the calculation of the dynamic weighting potential using coordinate mapping.

- The impact of non-uniform conductive properties of resistive layers on the readout response was incorporated by creating Perlin noise maps to represent the varying surface resistivity. These maps were then used to compute the time-dependent weighting potential, effectively capturing these non-uniformities of the resistive layer, which affect the signal formation.

Over the course of this thesis, the application of the methodology evolved from accurately replicating outcomes of toy model examples to being a part of more intricate simulations to describe the macroscopic response of a broad class of detector technologies.

The viability of this implementation was demonstrated through two comparisons with experimental data. The first validation study was conducted using empirical data from literature, focusing on the position interpolation correction map for a two-dimensional position-sensitive readout in a MicroCAT Micro-Pattern Gaseous Detector (MPGD). Using COMSOL® in conjunction with Garfield++, this map was generated using the simulated total charge induced on the readout nodes by Townsend avalanches inside the amplification gap. The result accurately captured the measured interpolation distortions within the experimental uncertainty. Moreover, the findings were consistent with those from an earlier published RC-circuit-based simulation study. The second comparison was performed using a resistive strip bulk MicroMegas detector for which the spreading of the signal in the resistive strips could be observed. Using nominal surface resistivities of 100 k$\Omega/\square$ and 1 M$\Omega/\square$, the current response was measured using minimum ionizing particles at the SPS H4 beam line at CERN. The shape of the signals induced on the readout strips running normal to the resistive strips showed a clear dependence on the value of the surface resistivity. In the case of the 100 k$\Omega/\square$, the bipolar signals waveforms showed greater attenuated, shorter duration, and more rapid spreading over neighboring channels – resulting in an increased cluster size – compared to the 1 M$\Omega/\square$ configuration. Informed by measurements of the ion tail duration in a non-resistive MicroMegas device for Ar/CO_2 93/7%, a simulation of the induced signal was performed. A one-to-one comparison between data and simulation of the average signal shapes for the nominal surface resistivity showed that the simulation could reproduce the average signal shape within the systematic uncertainty.

Another aspect of resistive elements is their adverse effect on the noise background of a detector system. This is due to the generation of Johnson-Nyquist noise resulting from the thermal fluctuations of charges within the material. A FEM-based approach was developed for obtaining the noise power density spectrum for electrodes in resistive readout structures by calculating the self-impedance of the electrodes. After benchmarking the method against toy model examples, it was applied to the case of the resistive plane MicroMegas. With this, the relation was found between surface resistivity values, the peak time of the shaper, and equivalent noise charge. More specifically, as surface resistivity values increase, the equivalent noise charge at the output terminal of an amplifier decreases.

Serving as a proof-of-principle demonstration of the suitability of the numerical methodology for semiconductor sensors, the case of the 3D diamond detector was treated. The weighting potential of the resistive pillar electrodes was compared with a toy model representation using a perturbed transmission line, where the solutions converge at late times. The TIMESPOT collaboration has previously employed the latter approach for their ongoing R&D on 3D diamond detectors and are currently in the process of incorporating and assessing the numerical application of the extended form of the Ramo-

Shockley theorem within their simulation efforts, using the presented solution of the dynamic weighting potential.

To enhance the operational stability of the 10×10 cm^2 100-channel precise timing PICOSEC MicroMegas, the readout structure underwent a modification by incorporating a resistive Diamond-Like Carbon (DLC) layer. To arrive at an informed decision regarding the surface resistivity value R, two studies were conducted to prevent a substantial timing performance deterioration resulting from the redesign:

- By performing induced current calculations with Garfield ++ for the approximately ≈ 1 cm^2 square readout pads situated below the insulating Kapton® laminate which separates the readout from the resistive anode, it was determined that the leading-edge of the signal is virtually unaffected by the delayed component when $R > 100$ k$\Omega/\square$.

- Using a FEM simulation, the rate capability degradation was due to an ohmic potential drop on the DLC was estimated for a pion flux of around $1 \cdot 10^6$ cm^{-2}s^{-1}. For $R = 20$ M$\Omega/\square$ an estimated gain drop of around 20% was found.

Based on these findings and the required minimal protection from the destructive capabilities of discharges, a surface resistivity of 20 M$\Omega/\square$ was selected for the DLC. Using 80 GeV/c muons at the SPS H4 beam line at CERN, it was shown that the performance on the pad level was retained with a timing resolution below 25 ps.

As a final simulation study, the charge collection sharing between three-coordinate layers comprised of strip electrodes in the novel non-resistive XYU-GEM was calculated numerically using Garfield++ using the basic form of the Ramo-Shockley theorem. Various readout configurations within the parameter space were examined, leading to the identification of a configuration where charge sharing was estimated to be uniform. Although these insights guided the initial prototype development, practical constraints during manufacturing resulted in the use of suboptimal parameters. Consequently, this led to uneven charge sharing between the layers, an observation that was accurately replicated through simulation. Nevertheless, the prototype's capability to detect and localize radiation was successfully demonstrated.

With a numerical approach for applying the exerted form of the Ramo-Shockley theorem for conductive media developed, implemented in Garfield++, and benchmarked, it can be used in future detector R&D projects. The discussion in this work outlines examples highlighting the merits of this method across various resistive detector technologies. For instance, these calculations can inform the design of resistive detectors by performing simulation-based optimization studies of their layout tailored to specific physics applications. This can be used not only to determine, for example, the optimal surface resistivity to share the signal over enough channels for enhanced spatial reconstruction but also to explore different electrode shapes. In addition, it can be employed for the design of the readout electronics with which the detector would be equipped since it provides the induced signals at its input terminal. Beyond detector geometry, current research focuses on finding alternative gas mixtures with a low global warming potential for the resistive pate chamber currently installed in the LHC experiments, which often operated with a mixture containing $C_2H_2F_4$ and SF_6 [217]. Efforts in this doctoral project to simulate resistive plate chambers are being expanded to identify suitable alternatives and validate new cross-section data for candidate molecules such as R134a [218]. Finally, past simulation efforts have elucidated puzzling experimental results and provides tools to form a deeper understanding of the underlying physics of these devises. We hope this work can be found useful in this ongoing effort.

Appendix A

FEM calculations of dynamic weighting potentials

Given that one of the central methods of this dissertation is the calculation of the dynamic weighting potential for electrodes in various resistive detector structures using the FEM, this appendix will outline the procedure taken during these calculations in more detail. More specifically, while the general approach is outlined in Sec. 2.5.2, we will go over the practice steps needed to execute them in COMSOL®. As an example that covers most techniques used throughout this work, we will take the time-dependent weighting potentials of a pad electrode in the toy model representation of the amplification gap of the 10×10 cm^2 resistive plane MicroMegas shown in Fig. 2.14. The result is compared to the corresponding analytical solution in Fig. 2.23 of Sec. 2.5.2. While the structure of this appendix follows the traditional COMSOL® workflow, it is advisable to have a passing knowledge of the basic workings of this software tool. For this, we will refer to Ref. [79]. The central aim is to obtain the weighting potential of a pad electrode in the readout plane and make the exported solution compatible with the import function of the *ComponentCOMSOL* class in Garfield++. Both the project file and an up-to-date version of the contents of this appendix can be found on the Garfield++ webpage [38].

Method and modules

To import the model's results into Garfield++, we need to calculate two sets of potentials: (i) the static potential used to perform the calculation of the drift (and amplification) of the charge carriers in the detector medium and (ii) the weighting potential of the electrodes. Accordingly, using the *Model Wizard*, we can set up a three-dimensional model that includes both the *Electrostatics (es)* and *Electrical Currents (ec)* physic interfaces for the static potential and dynamic weighting potential, respectively. A *Stationary* and *Time Dependent* study is needed to solve for both sets of potentials. At the time of writing, the *ComponentCOMSOL* class of Garfield++ only supports importing three-dimensional solutions that are solved using second-order tetrahedral mesh elements.

Table A.1: List of parameters used in the FEM model.

Name	Expression	Description
g	128 [µm]	Thickness of the amplification gap
b	100 [µm]	Thickness of the insulation layer
pitch	0.5 [mm]	Pitch of the pads
$\mathrm{w_x}$	0.5 [mm]	Width of the pads in the x-direction
$\mathrm{w_y}$	0.5 [mm]	Width of the pads in the y-direction
$\mathrm{d_R}$	1 [pm]	Thickness of the resistive layer
a	5 [mm]	Size of the central area of interest
l	a + 1.5 [mm]	Size of the MM in the model in the xy-plane
$\mathrm{f_{scaling}}$	63.33	Coordinate scaling factor for outer region
R	1 [MΩ/□]	Surface resistivity of resistive layer
σ	$(d_R R)^{-1}$	Surface resistivity of resistive layer
ε_1	4	Relative permittivity of the insulator
ε_3	1	Relative permittivity of the gas gap
V_A	510 [V]	Applied voltage to the resistive layer
t_{rise}	10^{-18} [s]	Rise time of the voltage ramp function
dn	0.1	Step size for the time slices
N	8	Used indicate the last time slice

Detector geometry

The parallel plate structure depicted in Fig. 2.14 can be represented by two sets of cuboid-shaped domains, one for the induction gap with a size presented in Table A.1 and another for the amplification gap. As we will see later, there is no need to physically represent the resistive layer using a thin volume. In addition, due to the impracticality of solving the system for the full 10×10 cm^2 active area, we only fully resolve the detector structure in an 'active region' of 5×5 mm^2. To later accurately represent the Dirichlet boundary conditions at the edges of the resistive layer, this region is surrounded by a border consisting of 16 domains with a width of 750 µm as shown in Fig. A.1, which will later be coordinate mapped to yield the correct size. In the active region, a 9×9 grid of square pad electrodes is added to the readout plane at the bottom of the insulating layer.

Material properties

This toy model example contains three sets of materials:

- The gas gap with a unit relative permittivity ε_3 and zero volume conductivity.
- The perfectly insulating layer characterised by ε_1 and zero volume conductivity.
- The resistive layer with a volume conductivity given by σ.

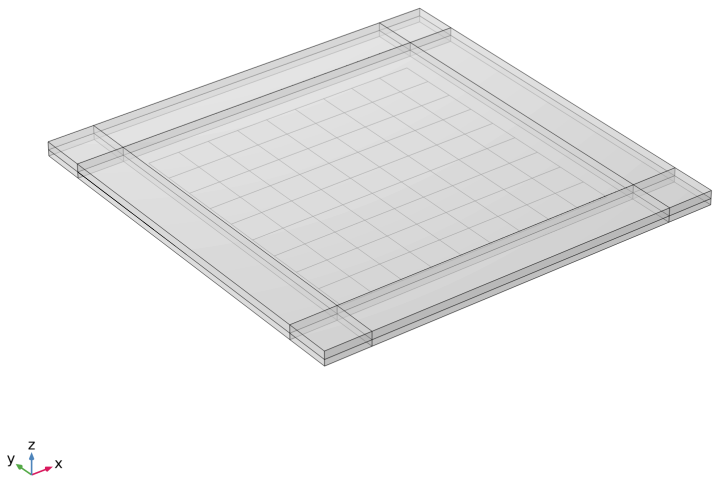

Figure A.1: Detector geometry in used for the FEM calculation.

While the former two are used for their respective domains, the latter is applied to the interfacing surface between the amplification gap and the insulating layer using the *Boundary* geometry entry level.

Boundary conditions and coordinate mapping

In order to make our small geometry equivalent to one with the fully sized resistive layer, we need to perform coordinate mapping on the outer region of the model. For this, we use three instances of *Scaling System* function that can be found under *Coordinate Systems* in the *Definitions* option. To perform a linear coordinate stretching, we can multiply the x-coordinate with the scaling factor f_{scaling} for the four domains positioned left and right of the active region, while the same can be done for the y-coordinate for those above and below it. The remaining eight domains positioned at the corners require the coordinate scaling to be applied to both coordinates. This will result in the representation of the device's entire active region when solving the system's field equations without the need to use a large number of mesh elements.

To obtain a unique solution to the field equations of the *Electrostatics* and *Electrical Currents* systems we need to provide two sets of boundary conditions. Starting with the static potential, we can apply the Dirichlet conditions

$$\phi(\mathbf{x})|_{z=g} = 0\,, \qquad \phi(\mathbf{x})|_{z=-b} = 0\,, \qquad \phi(\mathbf{x})|_{z=0} = V_A\,, \tag{A.0.1}$$

to the 'mesh' cathode (using the *Ground* function), readout plane, and the resistive layer (using the *Electric Potential* function), respectively. To the remaining boundaries we apply the Neumann boundary condition

$$\hat{\mathbf{n}} \cdot \mathbf{j}(\mathbf{x}) = 0\,, \tag{A.0.2}$$

with $\hat{n}$ the normal to the boundary. This condition on the vanishing of the flux through the surface can be achieved by using the *Electric Insulation* option.

To solve for the dynamic weighting potential using the *Electrical Currents* module, we impose the following Dirichlet boundary condition on the readout plane:

$$\Psi_k(\mathbf{x})|_{z=-b} = \begin{cases} 0 & \mathbf{x} \notin S_k \\ V_w(t) & \mathbf{x} \in S_k \end{cases}\,, \tag{A.0.3}$$

with S_k being the surface of the pad under study and $V_w(t)$ the ramping function shown in Fig. 2.22. The ramping function $V_w(t)$ can be implemented through the *Electric Potential* boundary condition and the introduction of a *Step* function under the *Definitions* option with the size of transition zone set to t_{rise} and the location to $-t_{\text{rise}}/2$. The surface condition *Electric Shielding* can be applied to the resistive layer, i.e., the interfacing surface between the amplification region and the insulating layer. The parameters for this setting involve using relative permittivity and volume conductivity obtained *From Material*, with the surface thickness set to equal d_R. To ground the borders of the layer, we use the one-edge version of the *Ground* condition. To satisfy the remaining boundary conditions outlined in Sec. 2.3.4, we impose grounding Dirichlet boundary conditions on the remaining outer surfaces.

Meshing

One should adhere to particular guidelines when it comes to meshing a geometry. One such point that is of particular relevance here is that the quality of the solution is reduced when using tetrahedral elements with needle-like corners. This leads us to avoid needing to mesh the thin resistive layer and discourages us from using it as the element of choice for the outer region of the model. Instead, we can use pentahedral elements without loss of precision when performing the coordinate stretching. As a result, we mesh the active region using tetrahedral elements and subsequently use the *Swept* function on the outer domains to continue the mesh to the outer surfaces. Using the *Distribution* option, we can increase the number of elements to five. The final mesh is shown in Fig. A.2.

Solving

We use the two study options chosen while preparing the model to solve for the static and dynamic weighting potential. The former is relatively straightforward, where before computing the solution, we select the *Electrostatics* in the physics and variables section of the study. The time-dependent solver for the *Electrical Currents* interface requires us to

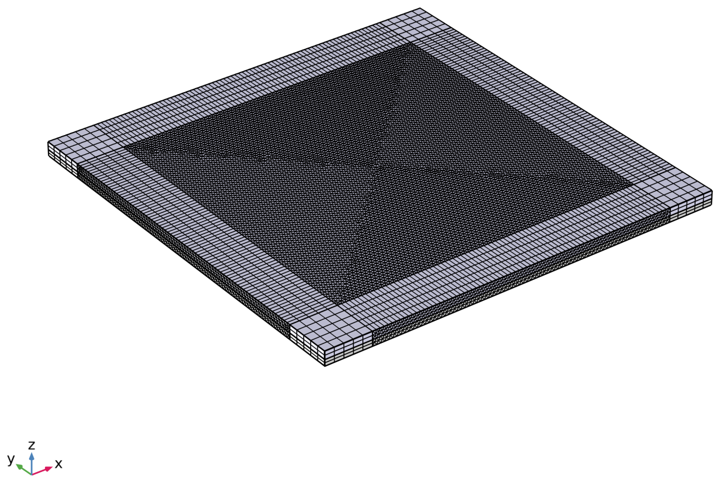

Figure A.2: Meshing of the model using tetrahedral and pentahedral elements for the inner part of interest and the outer scaling region, respectively.

define the set of time slices t_n for which the solution will be evaluated and saved. Given the typically rapid change of the weighting potential at early times and its gradually slowing down as time progresses, we can reflect this by setting the output times to:

$$t_n = e^n - 1 \text{ ns} \tag{A.0.4}$$

with $n \in \{0, dn, \ldots, N - dn, N\}$, dn the step size, and N the maximum value of n. Now, we can calculate the delayed weighting potential and utilize the plotting functions available in COMSOL® to visualize it.

Data exporting

Specific export settings need to be used to extract the data for COMSOL® toolkit in a way that makes it suitable to be imported into Garfield++. These settings depend on the type of file that is being exported. In general, the *ComponentCOMSOL* class needs four files to set up the simulation: *mesh.mphtxt*,*Potential.txt*, *WPotential.txt*, and *dielectrics.dat*.

mesh.mphtxt: This file contains information on the types of mesh elements being used, in which domain they are located, and in what position their nodes are placed. While under *Results/Export*, there is the option to export the *Mesh*. However, it does not seem to provide adequate information for second-order elements. Instead, we need to go to the *Mesh* object where between the options to define the mesh is an *Export* option. On the following window, under output settings, there is the option to *Export second-order elements*, which needs to be enabled. Following this, the mesh data can be exported as a COMSOL Multiphysics text file.

Potential.txt: In the function of the *Export* section in Results, there is the *Data* option. With this, the potential map containing the scalar field values on each mesh node can be exported. To include the values on the second-order nodes, we need to go into the advanced options in the settings window and set the resolution to *Costume*, at which point the option to change the Lagrange-element node-point order from one to two becomes available. With this, the data can be exported as a Text file.

WPotential.txt: Similar to the previous file, this file contains a list of weighting potential values on the nodes of the elements, but now for all time slices (when setting the time selection to *All*). Consequently, the same steps can be followed. However, the exporting will require significantly more time, memory, and disk space due to the larger number of potential maps being exported.

dielectrics.dat: The final file needs to be created manually, as it contains information on the relative permittivity of the material of each domain. This allows Garfield++ to know which domains need to be imported since only the one containing a medium in which the electrons and ions (holes) drift are required during the calculation. These regions are indicated by a unit relative permittivity. Since only domains containing tetrahedral elements will be imported, it results in only the gas volume in the active region being used.

The .dat file follows a particular structure that should be followed for the data to be read correctly by Garfield++. Starting with the first three lines:

- The first line indicates the number of relative permittivities are used.
- The second line list the values of these relative permittivities.
- The third line indicates the total number of domains in the geometry.

This is followed by the list of domains, represented by their respective numbers, and which relative permittivity it has, indicated by the index (starting at zero) of the entries of the list defined in line two. The resulting file should look as follows:

```
2
1 4
18
1 1
2 0
3 1
4 0
5 1
```

```
6 0
7 1
8 0
9 1
10 0
11 1
12 0
13 1
14 0
15 1
16 0
17 1
18 0
```

Here, we have two different relative permittivity values, one and two, and 18 domains in the geometry. Further instructions on proceeding with the simulation in Garfield++ are provided in Sec. 2.5.3.

Appendix B

Overview of student's contributions

In presenting the results within this thesis, it is important to acknowledge that these achievements were not accomplished in isolation. The journey through this research has been enriched and made possible through collaborations with a number of skilled and knowledgeable individuals. However, in the interest of transparency and to provide a clear understanding of my individual contributions, I would like to outline the specific aspects of the work that can be directly attributable to my efforts. In the subsequent sections, it should be noted that these accomplishments were overseen by Prof. Dr. Jorgen D'Hondt, Dr. Eraldo Oliveri, Dr. Werner Riegler, Dr. Heinrich Schindler, and Dr. Rob Veenhof. Additionally, the success of these efforts was made possible through discussions and support from the members of the EP-DT-DD GDD team.

Chapter 2

- While most examples in the first half of the chapter can be found in the cited literature, I give an alternative toy model derivation for the signal shape in a MicroMegas amplification structure (Sec. 2.3.2).

- The discussion of Sec. 2.4 is based on the work of Dr. Werner Riegler, in particular Ref. [61] which is presented in this work in more detail and extend by me with Eq. (2.4.11).

- The development of the equations behind the numerical implementation was performed in collaboration with Dr. Werner Riegler and Dr. Heinrich Schindler. Both the actual implementation of the strategy and the subsequent benchmarking against analytical examples was performed by me.

Chapter 3

- Together with Dr. Werner Riegler, the outlined strategy for calculating the thermal noise power spectrum was developed, tested against toy model examples, and applied to the case of a resistive plane MicroMegas.

Chapter 4

- Sec. 4.1 is based on the cited work of P. Fischer, where a systematic study was performed of the spatial resolution for a strip electrode readout with respect to varying charge cloud widths, signal-to-noise ratios, and threshold levels. These results were extended with Eq. (4.1.10) and the discussion on the weighted CoG method.

- The XYU-GEM concept was proposed by Prof. Dr. Fabio Sauli. Together with the co-authers of the related publication, in particular Karl Jonathan Floethner, the prototype was designed and characterised in the laboratory, where the signal sharing calculations were performed by me using Garfield++ and I contributed to the data taking and analysis.

Chapter 5

- As a member of the PICOSEC MicroMegas collaboration, I actively participated in data collection for various prototypes across three RD51 test beam campaigns. The measurements discussed in this chapter stem from the collected data sets, which I analyzed using analysis code created by the collaboration.

- The experimental measurements for Device A were conducted solely by me, while the measurements for Device B were carried out together with Dr. Antonija Utrobicic.

- The discussed simulation work was the result of my individual efforts.

Chapter 6

- The comparison of the simulated correction map with data and published RC circuit modeling results, including those for a non-uniform surface resistivity, were my individual efforts.

Chapter 7

- The simulation of the signal formation on the resistive columns was developed in collaboration with members of the TIMESPOT project.

Chapter 8

- The results presented in the chapter were achieved by me. The experimental data was collected over two separate two-week periods. During one of these periods, I collaborated with and supervised Marthe Azzi as part of the Summer Student Program.

Appendix C

Acknowledgments

The realization of this project stands as a testament to the support, contribution, and kindness from numerous individuals. Their collective influence weaves seamlessly through the tapestry of this manuscript, enriching its narrative with diverse perspectives and shared experiences. Thus, it is with heartfelt appreciation that I reserve the closing pages of this thesis to honor and express gratitude to each of these remarkable individuals.

First and foremost, I extend my deepest gratitude to Prof. Dr. Jorgen D'Hondt for his pivotal role in ensuring that the project could conclude on time. Despite his demanding schedule, he generously dedicated his time to closely monitor my progress, provide guidance and support me throughout the duration of this project.

I extend my sincere appreciation to Prof. Dr. Freya Blekman for her invaluable guidance and supervision during the initial stages of this doctoral journey. Even before embarking on my Ph.D. project, her openness to discuss possible research directions after having obtained my master's degree played a pivotal role in shaping the trajectory that I am currently on. For this, I will always be grateful.

I am deeply grateful to Dr. Heinrich Schindler for his outstanding guidance as my supervisor at CERN. His unwavering support kept me focused and on track throughout the project, while his meticulous proofreading of numerous draft versions of this manuscript ensured its scientific rigor, clarity, and coherence. Our collaborative brainstorming sessions over coffee, exploring potential new features for implementation into Garfield++, were not only enjoyable but also profoundly enriching. The invaluable impact Dr. Schindler has had on my professional growth, fostering my development as a scientist, cannot be overstated.

With profound gratitude, I extend my heartfelt thanks to Dr. Eraldo Oliveri for his encouragements and mentorship, which continuously propelled me beyond my perceived limits. His infectious enthusiasm kept me going back to the lab, eager to explore or validate the ideas I had developed through simulations in the comfort of my office. Our spontaneous discussions in the laboratory were instrumental in deepening my understanding of detector physics and helped grow the flame of curiosity in me. I am deeply grateful for Dr. Oliveri's steadfast belief in my abilities, his honesty, and support throughout the duration of this project.

I want to express my immense gratitude to Dr. Rob Veenhof for introducing me to the field of detector physics. As a CERN summer student, I could not have asked for a better mentor to guide me through my first tentative steps into this subject, an experience that has left a lasting impact on me. It was under his guidance that I first felt the aspiration to delve deeper into calculations regarding the behavior of particle detectors and to pursue a career as a detector physicist. Dr. Veenhof's extensive knowledge of both the physics underlying these devices and the community surrounding them has been awe-inspiring. I am truly thankful that he always kept his office door open for me, welcoming with a warm smile my questions ranging from the complex to the trivial. Thank you, Dr. Veenhof, for exemplifying what it means to be an expert in your field.

I extend my sincere gratitude to Dr. Werner Riegler for generously sharing his wealth of knowledge with me through our numerous conversations and private notes, which helped me grasp the subject matter more deeply. His guidance, encouragements, and contributions to this doctoral project are unmistakable, significantly elevating its quality, for which I am profoundly grateful. Dr. Riegler's remarkable precision in understanding complex topics sets a standard for me to aspire to and exemplifies the essence of a great researcher. It was an honor to collaborate with him.

I am genuinely grateful to Dr. Antonija Utrobicic and Dr. Marinko Kovacic for their unwavering support and availability throughout this project. Without fail, they made time for me, whether it was to indulge my curiosity, share my enthusiasm, or alleviate my concerns. Their willingness to engage in discussions and offer guidance, even during challenging times, has been invaluable and deeply appreciated.

My thanks and appreciation go to Dr. Leszek Ropelewski for welcoming me into the CERN EP-DT-DD GDD team. His efforts in assembling and running the team have resulted in an environment conducive to research driven by curiosity and scientific interest. Dr. Ropelewski has curated a group comprised of talented individuals with complementary expertise, fostering a stimulating and dynamic working environment. I am truly grateful for the opportunity to be part of such a team.

This brings me to the members of the GDD team itself, with whom I spent almost every working day exchanging ideas, working through difficulties, and celebrating successes. I am deeply grateful to each and every individual in this group for the support and guidance they have provided me over the past years. The working environment you provided has been a privilege to work in and far exceeded my hopes when I first came to CERN. A special acknowledgment goes to the "Ph.D. council" for not only being incredible colleagues, but also such good friends with whom I have developed many cherished memories.

A heartfelt acknowledgment goes out to all the members of the RD51 collaboration for their invaluable contributions. The insightful discussions and the opportunity to regularly present the progress of my work at the RD51 Collaboration meetings were instrumental in shaping my research journey. These meetings provided a crucial reflection point, allowing for constructive feedback and collaboration with many talented people.

I would like to express my gratitude to Prof. Dr. Michael Tytgat for his role as chair of the defense committee. Additionally, I extend my thanks to Prof. Dr. Thierry Gevaert, Dr. Inna Makarenko, Dr. Victor Coco, and Prof. Dr. Paulo Fonte for graciously accepting to be part of the defense committee and for dedicating their time to review this work. Your expertise and insights have been invaluable contributions to the refinement of this thesis.

I acknowledge the support of the CERN EP R&D Strategic Programme on Technologies for Future Experiments (https://ep-rnd.web.cern.ch/).

To my parents, Hilde van Lierde and Cesar Janssens, and my sister, Gisia Janssens: Your unwavering belief in me, unconditional support, and boundless love have been a guiding light throughout this journey, even as any miles separated us for much of the past three years. Thank you for your understanding during all the family outings and dinners I missed these past years while I was studying in my room, doing research abroad, or being mentally absent, consumed by thoughts of work. You instilled in me the value of hard work and the importance of pursuing my dreams, encapsulated in our family motto: "We gaan dat varkentje wassen", a sentiment I hope I have honored. I am deeply grateful for the foundation you provided on which I continue to build today and enabling me to pursue a career in science. The depth of gratitude and love I feel towards you is immeasurable and will remain with me always.

Finally, I would like to dedicate these closing words to Julie Vonck. It is one thing to decide for oneself to pursue a career in physics abroad for years; it is another to ask one's partner to support it. I consider myself incredibly fortunate to share my life with a woman who understands so deeply what it means to me to embark on this journey, go to CERN, and realize my dream of working there. She supported me during the challenges of pursuing a Ph.D. and actively helped me carry this burden, together, even while she was immersed in her own doctoral studies. It is a blessing to have a partner by my side who understands the sacrifices and dedication required to complete a Ph.D., to whom I can look and smile while she smiles back, knowing it will be okay. Countless moments spent laboring side by side stirred a determination within me to work late into the night, secure in the knowledge that you stood steadfast beside me, working together to build the foundations of our shared future. I am grateful to you for bringing so much joy into my life and making the universe brighter.

Bibliography

[1] O.S. Brüning, P. Collier, P. Lebrun, S. Myers, R. Ostojic, J. Poole et al., *LHC Design Report*, CERN Yellow Reports: Monographs, CERN, Geneva (2004), 10.5170/CERN-2004-003-V-1.

[2] H. Kolanoski and N. Wermes, *Particle Detectors: Rundamentals and Applications*, Oxford University Press, USA (2020).

[3] Special issue: Advances in detectors and applications for medicine,*Nuclear Instruments and Methods in Physics Research Section A: Accelerators, Spectrometers, Detectors and Associated Equipment* **809** (2016) 1.

[4] D. Poulson, J. Durham, E. Guardincerri, C. Morris, J. Bacon, K. Plaud-Ramos et al., *Cosmic ray muon computed tomography of spent nuclear fuel in dry storage casks*, *Nuclear Instruments and Methods in Physics Research Section A: Accelerators, Spectrometers, Detectors and Associated Equipment* **842** (2017) 48.

[5] K. Morishima, M. Kuno, A. Nishio, N. Kitagawa, Y. Manabe, M. Moto et al., *Discovery of a big void in Khufu's Pyramid by observation of cosmic-ray muons*, *Nature 2017 552:7685* **552** (2017) 386.

[6] L. Rolandi, W. Riegler and W. Blum, *Particle Detection with Drift Chambers*, Springer Berlin Heidelberg (2008), 10.1007/978-3-540-76684-1.

[7] G. Charpak, R. Bouclier, T. Bressani, J. Favier and Č Zupančič, *The use of multiwire proportional counters to select and localize charged particles*, *Nuclear Instruments and Methods* **62** (1968) 262.

[8] F. Sauli, *GEM: A new concept for electron amplification in gas detectors*, *Nuclear Instruments and Methods in Physics Research Section A: Accelerators, Spectrometers, Detectors and Associated Equipment* **386** (1997) 531.

[9] Y. Giomataris, P. Rebourgeard, J.P. Robert and G. Charpak, *MICROMEGAS: a high-granularity position-sensitive gaseous detector for high particle-flux environments*, *Nuclear Instruments and Methods in Physics Research Section A: Accelerators, Spectrometers, Detectors and Associated Equipment* **376** (1996) 29.

[10] Particle Data Group, R.L. Workman et al., *Review of Particle Physics*, *Progress of Theoretical and Experimental Physics* **2022** (2022) 083C01.

[11] The ATLAS Collaboration, *The ATLAS Experiment at the CERN Large Hadron Collider*, *Journal of Instrumentation* **3** (2008) S08003.

[12] T. Kawamoto, S. Vlachos, L. Pontecorvo, J. Dubbert, G. Mikenberg, P. Iengo et al., *New Small Wheel Technical Design Report*, CERN-LHCC-2013-006, ATLAS-TDR-020, CERN, Geneva (2013).

[13] The CMS Collaboration, *The CMS experiment at the CERN LHC*, *Journal of Instrumentation* **3** (2008) S08004.

[14] The CMS Collaboration, *The Phase-2 Upgrade of the CMS Muon Detectors*, CERN-LHCC-2017-012, CMS-TDR-016, CERN, Geneva (2017).

[15] The ALICE Collaboration, *The ALICE experiment at the CERN LHC*, *Journal of Instrumentation* **3** (2008) S08002.

[16] The ALICE Collaboration, *Upgrade of the ALICE Time Projection Chamber*, CERN-LHCC-2013-020, ALICE-TDR-016, CERN, Geneva (2013).

[17] The LHCb Collaboration, *The LHCb Detector at the LHC*, *Journal of Instrumentation* **3** (2008) S08005.

[18] M. Ziegler, *Development of a triple GEM detector for the LHCb experiment*, Dissertation, University of Zurich (2002).

[19] F. Sauli, *Gaseous Radiation Detectors: Fundamentals and Applications*, Cambridge Monographs on Particle Physics, Nuclear Physics and Cosmology, Cambridge University Press (2014), 10.1017/9781009291200.

[20] F. Sauli, *Micro-Pattern Gaseous Detectors*, World Scientific (2020), 10.1142/11882.

[21] M. Titov and L. Ropelewski, *Micro-pattern gaseos detector technologies and RD51 colaboration*, *Modern Physics Letters A* **28** (2013) 1340022.

[22] L.S. Scharenberg, *Next-Generation Electronics for the Read-Out of Micro-Pattern Gaseous Detectors*, Ph.D. thesis, Rheinische Friedrich-Wilhelms-Universität Bonn (2023).

[23] G. Lutz, *Semiconductor Radiation Detectors*, Springer Berlin, Heidelberg (1999).

[24] H. Spieler, *Semiconductor detector systems*, Oxford Univ. Press, Oxford (2005).

[25] O. Aberle, I. Béjar Alonso, O. Brüning et al., *High-Luminosity Large Hadron Collider (HL-LHC): Technical design report*, CERN Yellow Reports, Geneva (2020), 10.23731/CYRM-2020-0010.

[26] ECFA Detector RD Roadmap Process Group, *The 2021 ECFA detector research and development roadmap*, CERN-ESU-017, CERN, Geneva (2020).

[27] V. Sola, R. Arcidiacono, N. Cartiglia, M. Ferrero, M. Mandurrino and A. Staiano, *Fast timing detectors towards a 4-dimensional tracking*, *Proceedings of Science* **340** (2019) 594.

[28] T.C. Collaboration, *A MIP Timing Detector for the CMS Phase-2 Upgrade*, CERN-LHCC-2019-003, CMS-TDR-020, CERN, Geneva (2019).

[29] M. Tornago, R. Arcidiacono, N. Cartiglia, M. Costa, M. Ferrero, M. Mandurrino et al., *Resistive AC-Coupled Silicon Detectors: Principles of operation and first results from a combined analysis of beam test and laser data*, *Nuclear Instruments and Methods in Physics Research Section A: Accelerators, Spectrometers, Detectors and Associated Equipment* **1003** (2021) 165319.

[30] F. Bachmair, L. Bäni, P. Bergonzo, B. Caylar, G. Forcolin, I. Haughton et al., *A 3d diamond detector for particle tracking*, *Nuclear Instruments and Methods in Physics Research Section A: Accelerators, Spectrometers, Detectors and Associated Equipment* **786** (2015) 97.

[31] A. Abada, M. Abbrescia, S.S. AbdusSalam, I. Abdyukhanov, J.A. Fernandez, A. Abramov et al., *FCC Physics Opportunities*, *The European Physical Journal C 2019 79:6* **79** (2019) 1.

[32] O. Brunner, P. Burrows, S. Calatroni, N.C. Lasheras, R. Corsini, G. D'Auria et al., *The CLIC project*, CERN-ACC-2022-005, CLIC-Note-1174, CERN, Geneva (2022).

[33] C. Aimè, A. Apyan, M. Attia Mahmoud, N. Bartosik, A. Bertolin, M. Bonesini et al., *Muon Collider Physics Summary*, *arXiv e-prints* (2022) arXiv:2203.07256 [2203.07256].

[34] T. Alexopoulos, J. Burnens, R.D. Oliveira, G. Glonti, O. Pizzirusso, V. Polychronakos et al., *A spark-resistant bulk-micromegas chamber for high-rate applications*, *Nuclear Instruments and Methods in Physics Research Section A: Accelerators, Spectrometers, Detectors and Associated Equipment* **640** (2011) 110.

[35] S. Agostinelli, J. Allison, K. Amako, J. Apostolakis, H. Araujo, P. Arce et al., *Geant4—a simulation toolkit*, *Nuclear Instruments and Methods in Physics Research Section A: Accelerators, Spectrometers, Detectors and Associated Equipment* **506** (2003) 250.

[36] J. Allison, K. Amako, J. Apostolakis, H. Araujo, P. Arce Dubois, M. Asai et al., *Geant4 developments and applications*, *IEEE Transactions on Nuclear Science* **53** (2006) 270.

[37] R. Veenhof, *Garfield*, *https://garfield.web.cern.ch/garfield* (2023) .

[38] H. Schindler and R. Veenhof, *Garfield++*, *https://garfieldpp.web.cern.ch/garfieldpp* (2023) .

[39] H. Schindler, *Microscopic simulation of particle detectors*, Technischen Universität Wien (2012), https://cds.cern.ch/record/1500583.

[40] H. Schindler, *Garfield++: status and plans*, Presented at: The 16the Vienna Conference on Instrumentation, 21-25 February 2022.

[41] W. Riegler, *Signals in particle detectors*, Presented at: CERN Academic Training Lecture Regular Programme, 2 December 2019.

[42] J. Jeans, *The Mathematical Theory of Electricity and Magnetism*, Cambridge University Press (1908).

[43] R. Fano, L. Chu and R. Adler, *Electromagentic Fields, Energy, and Forces*, Wiley (1963).

[44] H.A. Haus and J.R. Melcher, *Electromagnetic Fields and Energy*, Prentice Hall Inc. (1989).

[45] T. Heubrandtner, B. Schnizer, C. Lippmann and W. Riegler, *Static electric fields in an infinite plane condenser with one or three homogeneous layers*, *Nuclear Instruments and Methods in Physics Research Section A: Accelerators, Spectrometers, Detectors and Associated Equipment* **489** (2002) 439.

[46] W. Riegler, *Induced signals in resistive plate chambers*, *Nuclear Instruments and Methods in Physics Research Section A: Accelerators, Spectrometers, Detectors and Associated Equipment* **491** (2002) 258.

[47] W. Shockley, *Currents to conductors induced by a moving point charge*, *Journal of Applied Physics* **9** (1938) 635.

[48] S. Ramo, *Currents Induced by Electron Motion*, *Proceedings of the IRE* **27** (1939) 584.

[49] W. Riegler, *An application of extensions of the Ramo–Shockley theorem to signals in silicon sensors*, *Nuclear Instruments and Methods in Physics Research, Section A: Accelerators, Spectrometers, Detectors and Associated Equipment* **940** (2019) 453 [1812.07570].

[50] G. Cavalleri, E. Gatti, G. Fabri and V. Svelto, *Extension of Ramo's theorem as applied to induced charge in semiconductor detectors*, *Nuclear Instruments and Methods in Physics Research Section A: Accelerators, Spectrometers, Detectors and Associated Equipment* **92** (1971) 137.

[51] E. Gatti, G. Padovini and V. Radeka, *Signal evaluation in multielectrode radiation detectors by means of a time dependent weighting vector*, *Nuclear Instruments and Methods in Physics Research* **193** (1982) 651.

[52] L.-A. Hamel and M. Julien, *Comments on Ramo's theorem*, *Hard X-Ray and Gamma-Ray Detector Physics III* **4507** (2001) 255.

[53] L.A. Hamel and M. Julien, *Generalized demonstration of Ramo's theorem with space charge and polarization effects*, *Nuclear Instruments and Methods in Physics Research Section A: Accelerators, Spectrometers, Detectors and Associated Equipment* **597** (2008) 207.

[54] W. Riegler, *Extended theorems for signal induction in particle detectors vci 2004*, *Nuclear Instruments and Methods in Physics Research, Section A: Accelerators, Spectrometers, Detectors and Associated Equipment* **535** (2004) 287.

[55] W. Riegler, *An application of extensions of the Ramo–Shockley theorem to signals in silicon sensors*, *Nuclear Instruments and Methods in Physics Research Section A: Accelerators, Spectrometers, Detectors and Associated Equipment* **940** (2019) 453 [`1812.07570`].

[56] D. Janssens et al., *Induced signals in particle detectors with resistive elements: Numerically modeling novel structures (VCI 2022)*, *Nuclear Instruments and Methods in Physics Research Section A: Accelerators, Spectrometers, Detectors and Associated Equipment* **1040** (2022) 167227.

[57] W. Riegler and P. Windischhofer, *Signals induced on electrodes by moving charges, a general theorem for maxwell's equations based on lorentz-reciprocity*, *Nuclear Instruments and Methods in Physics Research, Section A: Accelerators, Spectrometers, Detectors and Associated Equipment* **980** (2020) .

[58] H.A. Lorentz, *Het theorema van poynting over de energie in het electromagnetisch veld en een paar algemeene stellingen over de voortplanting van het licht*, *Verslagen der Afdeeling Natuurkunde van de Koninklijke Akademie van Wetenschappen 4: 176-187* (1895) .

[59] R. Santonico and R. Cardarelli, *Development of resistive plate counters*, *Nuclear Instruments and Methods in Physics Research* **187** (1981) 377.

[60] E.C. Zeballos, I. Crotty, D. Hatzifotiadoua, J.L. Valverde, S. Neupane, M.C. Williams et al., *A new type of resistive plate chamber: The multigap rpc*, *Nuclear Instruments and Methods in Physics Research Section A: Accelerators, Spectrometers, Detectors and Associated Equipment* **374** (1996) 132.

[61] W. Riegler, *Electric fields, weighting fields, signals and charge diffusion in detectors including resistive materials*, *Journal of Instrumentation* **11** (2016) [`1602.07949v1`].

[62] M.R. Spiegel, *Theory and problems of complex variables with an introduction to conformal mapping and its applications*, New York (1964).

[63] S. Biagi, *MAGBOLTZ 11*, *https://magboltz.web.cern.ch/magboltz/* (2023) .

[64] S.F. Biagi, *Monte carlo simulation of electron drift and diffusion in counting gases under the influence of electric and magnetic fields*, *Nuclear Instruments and Methods in Physics Research Section A: Accelerators, Spectrometers, Detectors and Associated Equipment* **421** (1999) 234.

[65] J.A. Hornbeck, *The drift velocities of molecular and atomic ions in helium, neon, and argon*, *Physical Review* **84** (1951) 615.

[66] E. Beaty, *Contribution*, *5th conference on ionization phenomena in gases* (1961) .

[67] E. Basurto, J. de Urquijo, I. Alvarez and C. Cisneros, *Mobility of* He^+, Ne^+, Ar^+, N_2^+, O_2^+, *and* CO_2^+ *in their parent gas*, *Physical Review E* **61** (2000) 3053.

[68] W. Riegler, C. Lippmann and R. Veenhof, *Detector physics and simulation of resistive plate chambers*, *Nuclear Instruments and Methods in Physics Research Section A: Accelerators, Spectrometers, Detectors and Associated Equipment* **500** (2003) 144.

[69] M.S. Dixit, J. Dubeau, J.P. Martin and K. Sachs, *Position sensing from charge dispersion in micro-pattern gas detectors with a resistive anode*, *Nuclear Instruments and Methods in Physics Research, Section A: Accelerators, Spectrometers, Detectors and Associated Equipment* **518** (2004) 721.

[70] D. Attié, M. Batkiewicz-Kwasniak, J. Boix, S. Bolognesi, S. Bordoni, D. Calvet et al., *Performances of a resistive micromegas module for the time projection chambers of the T2K Near Detector upgrade*, *Nuclear Instruments and Methods in Physics Research Section A: Accelerators, Spectrometers, Detectors and Associated Equipment* **957** (2020) 163286.

[71] P. Fonte, N. Carolino, L. Costa, R. Ferreira-Marques, S. Mendiratta, V. Peskov et al., *A spark-protected high-rate detector*, *Nuclear Instruments and Methods in Physics Research Section A: Accelerators, Spectrometers, Detectors and Associated Equipment* **431** (1999) 154.

[72] G. Bencivenni, R. de Oliveira, G. Felici, M. Gatta, M. Giovannetti, G. Morello et al., *The μ-RWELL layouts for high particle rate*, *Journal of Instrumentation* **14** (2019) P05014.

[73] M. Iodice et al., *Small-pad resistive micromegas: Comparison of patterned embedded resistors and dlc based spark protection systems.*, *Journal of Physics: Conference Series* **1498** (2020) 012028.

[74] G. Bencivenni, R.D. Oliveira, G. Felici, M. Gatta, M. Giovannetti, G. Morello et al., *The surface resistive plate counter: An RPC based on resistive MPGD technology*, *Nuclear Instruments and Methods in Physics Research Section A: Accelerators, Spectrometers, Detectors and Associated Equipment* **1046** (2023) 167728.

[75] D. Attié et al., *Characterization of resistive Micromegas detectors for the upgrade of the T2K Near Detector Time Projection Chambers*, *Nuclear Instruments and Methods in Physics Research Section A: Accelerators, Spectrometers, Detectors and Associated Equipment* **1025** (2022) 166109 [`2106.12634`].

[76] H. Wagner, H. Besch, R. Menk, A. Orthen, A. Sarvestani, A. Walenta et al., *On the dynamic two-dimensional charge diffusion of the interpolating readout structure employed in the MicroCAT detector*, *Nuclear Instruments and Methods in Physics Research. Section A, Accelerators, Spectrometers, Detectors and Associated Equipment* **482** (2002) 334.

[77] D. Janssens et al., *Studying signals in particle detectors with resistive elements such as the 2D resistive strip bulk MicroMegas*, *Journal of Instrumentation* **18** (2023) C08010 [`2304.01883`].

[78] H.R. Skullerud, *The stochastic computer simulation of ion motion in a gas subjected to a constant electric field*, *Journal of Physics D: Applied Physics* **1** (1968) 1567.

[79] COMSOL® 6.1, *Software for multiphysics simulation*, *https://www.comsol.ch* (2023) .

[80] C.F. Curtiss and J.O. Hirschfelder, *Integration of stiff equations*, *Proceedings of the National Academy of Sciences* **38** (1952) 235.

[81] C.W. Gear, *The numerical integration of ordinary differential equations*, *Mathematics of Computation* **21** (1967) 146.

[82] R. Veenhof, *Numerical methods in the simulation of gas-based detectors*, *Journal of Instrumentation* **4** (2009) P12017.

[83] Analog Devices, *LTspice®*, *https://www.analog.com/en/design-center/design-tools-and-calculators/ltspice-simulator.html* (2023) .

[84] D. Janssens and W. Riegler, *Noise in detectors containing distributed resistive elements*, *Submitted to Nuclear Instruments and Methods in Physics Research Section A: Accelerators, Spectrometers, Detectors and Associated Equipment* (2023) .

[85] A. Einstein, *Zur theorie der brownschen bewegung*, *Annalen der Physik* **324** (1906) 371.

[86] J.B. Johnson, *Thermal agitation of electricity in conductors*, *Physical Review* **32** (1928) 97.

[87] H. Nyquist, *Thermal agitation of electric charge in conductors*, *Physical Review* **32** (1928) 110.

[88] P. Fischer, *Spatial resolution of pad/strip structures*, Presented at: HighRR BiWeekly-Seminar, 8 April 2018,.

[89] I.B. Smirnov, *Algebraic methods for reconstruction of coordinates in strip detectors*, *Journal of Instrumentation* **18** (2023) C06001.

[90] J. Tu, Q. Fu and D. Zhong, *CMS phase-II upgrade with GEM detector*, *Journal of Physics: Conference Series* **1498** (2020) 012054.

[91] J. Merlin, *Study of long-term sustained operation of gaseous detectors for the high rate environment in cms*, Université de Strasbourg (2016).

[92] F. Piuz, R. Roosen and J. Timmermans, *Evaluation of systematic errors in the avalanche localization along the wire with cathode strips read-out mwpc*, *Nuclear Instruments and Methods in Physics Research* **196** (1982) 451.

[93] L. Scharenberg, J. Bortfeldt, F. Brunbauer et al., *X-ray imaging with gaseous detectors using the VMM3a and the SRS*, *Nuclear Instruments and Methods in Physics Research Section A: Accelerators, Spectrometers, Detectors and Associated Equipment* **1011** (2021) 165576.

[94] L. Scharenberg, J. Bortfeldt, F. Brunbauer, K. Desch, K. Flöthner, F. Garcia et al., *Performance of the new RD51 VMM3a/SRS beam telescope — studying mpgds simultaneously in energy, space and time at high rates*, *Journal of Instrumentation* **18** (2023) C05017.

[95] A. Bressan, R.D. Oliveira, A. Gandi et al., *Two-dimensional readout of gem detectors*, *Nuclear Instruments and Methods in Physics Research, Section A: Accelerators, Spectrometers, Detectors and Associated Equipment* **425** (1999) 254.

[96] F. Sauli, *The gas electron multiplier (GEM): Operating principles and applications*, *Nuclear Instruments and Methods in Physics Research Section A: Accelerators, Spectrometers, Detectors and Associated Equipment* **805** (2016) 2.

[97] D. Janssens, *A better understanding of gas gain simulations in GEM detectors*, *CERN summer student program rapport* (2019) .

[98] S. Duarte Pinto, M. Villa, M. Alfonsi, I. Brock, G. Croci, E. David et al., *Progress on large area gems*, *Journal of Instrumentation* **4** (2009) P12009.

[99] G. Baum et al., *The COMPASS RICH project*, *Nuclear Instruments and Methods in Physics Research Section A: Accelerators, Spectrometers, Detectors and Associated Equipment* **433** (1999) 207.

[100] K. Flöthner, D. Janssens, F. Brunbauer, S. Ferry, B. Ketzer, M. Lisowska et al., *The XYU-GEM: Ambiguity-free coordinate readout of the Gas Electron Multiplier*, *Nuclear Instruments and Methods in Physics Research Section A: Accelerators, Spectrometers, Detectors and Associated Equipment* **1052** (2023) 168257.

[101] P. Abbon, C. Adolph, R. Akhunzyanov et al., *The compass setup for physics with hadron beams*, *Nuclear Instruments and Methods in Physics Research, Section A: Accelerators, Spectrometers, Detectors and Associated Equipment* **779** (2015) 69.

[102] S. Bachmann, S. Kappler, B. Ketzer et al., *High rate X-ray imaging using multi-GEM detectors with a novel readout design*, *Nuclear Instruments and Methods in Physics Research, Section A: Accelerators, Spectrometers, Detectors and Associated Equipment* **478** (2002) 104.

[103] F. Sauli, *Novel cherenkov photon detectors*, *Nuclear Instruments and Methods in Physics Research, Section A: Accelerators, Spectrometers, Detectors and Associated Equipment* **553** (2005) 18.

[104] M. Byszewski and J. Wotschack, *Resistive-strips micromegas detectors with two-dimensional readout*, *Journal of Instrumentation* **7** (2012) C02060.

[105] C. Altunbas, M. Capéans, K. Dehmelt et al., *Construction, test and commissioning of the triple-gem tracking detector for compass*, *Nuclear Instruments and Methods in Physics Research, Section A: Accelerators, Spectrometers, Detectors and Associated Equipment* **490** (2002) 177.

[106] ATLAS collaboration, *VMM3a, an ASIC for tracking detectors*, ATL-MUON-PROC-2019-009, CERN, Geneva (2020), DOI.

[107] S. Martoiu, H. Muller, A. Tarazona and J. Toledo, *Development of the scalable readout system for micro-pattern gas detectors and other applications*, *Journal of Instrumentation* **8** (2013) C03015.

[108] The RD51 Collaboration, *Development of micro-pattern gas detectors technologies*, *https://rd51-public.web.cern.ch* (2023) .

[109] D. Verner, D. Yakovlev, I. Band and M. Trzhaskovskaya, *Subshell photoionization cross sections and ionization energies of atoms and ions from he to zn*, *Atomic Data and Nuclear Data Tables* **55** (1993) 233.

[110] M.C.S. Williams, *Particle identification using time of flight*, *Journal of Physics G: Nuclear and Particle Physics* **39** (2012) 123001.

[111] J. Bortfeldt et al., *Picosec: Charged particle timing at sub-25 picosecond precision with a micromegas based detector*, *Nuclear Instruments and Methods in Physics Research Section A: Accelerators, Spectrometers, Detectors and Associated Equipment* **903** (2018) 317.

[112] L. Sohl, *Development of picosec-micromegas for fast timing in high rate environments*, PhD dissertation, Université Paris-Saclay (2022).

[113] I. Giomataris, R. De Oliveira, S. Andriamonje, S. Aune, G. Charpak, P. Colas et al., *Micromegas in a bulk*, *Nuclear Instruments and Methods in Physics Research Section A: Accelerators, Spectrometers, Detectors and Associated Equipment* **560** (2006) 405.

[114] J. Bortfeldt, F. Brunbauer, C. David, D. Desforge, G. Fanourakis, M. Gallinaro et al., *Modeling the timing characteristics of the picosec micromegas detector*, *Nuclear Instruments and Methods in Physics Research Section A: Accelerators, Spectrometers, Detectors and Associated Equipment* **993** (2021) 165049.

[115] Aimè, C., Calzaferri, S., Fiorina, D., Riccardi, C., Salvini, P., Vai, I. et al., *Fast timing detectors for the muon system of a muon collider experiment*, *EPJ Web Conf.* **288** (2023) 10012.

[116] S. Aune, J. Bortfeldt, F. Brunbauer, C. David, D. Desforge, G. Fanourakis et al., *Timing performance of a multi-pad picosec-micromegas detector prototype*, *Nuclear Instruments and Methods in Physics Research Section A: Accelerators, Spectrometers, Detectors and Associated Equipment* **993** (2021) 165076.

[117] A. Utrobicic, *Advancements in a large area 100 channel picosec micromegas detector module*, *RD51 Collaboration meeting* (14-06-2022) .

[118] A. Utrobicic et al., *A large area 100-channel PICOSEC Micromegas detector with time resolution at the 20 ps level*, *Journal of Instrumentation* **18** (2023) C07012 [2304.00056].

[119] R. de Oliveira on behalf of the CERN MPT group, *Private comumication*, *CERN* (2022) .

[120] N. Cartiglia, R. Arcidiacono, A. Bellora, F. Cenna, R. Cirio, S. Durando et al., *The 4D pixel challenge*, *Journal of Instrumentation* **11** (2016) C12016.

[121] W. Legler, *The influence of the relaxation of the electron energy distribution on the statistics of electron avalanches*, *British Journal of Applied Physics* **18** (1967) 1275.

[122] A.C. S.C. Curran and J. Angus, *LXXXVI. Investigation of soft radiation by proportional counters—V. Use as a detector of ultra-violet quanta and analysis of the gas multiplication process*, The London, Edinburgh, and Dublin Philosophical *Magazine and Journal of Science* **40** (1949) 929 [https://doi.org/10.1080/14786444908561424].

[123] J. Byrne, *III.—Statistics of the electron-multiplication process in proportional counters*, *Proceedings of the Royal Society of Edinburgh Section A: Mathematics* **66** (1962) 33–41.

[124] G. Alkhazov, *Statistics of electron avalanches and ultimate resolution of proportional counters*, *Nuclear Instruments and Methods* **89** (1970) 155.

[125] Teledyne LeCroy, *WaveRunner 6 Zi Oscilloscopes 400 MHz-4 GHz*, 2023.

[126] THORLABS, *LED250J - 250 nm LED with Ball Lens, 1 mW (Min), TO-39* , *https://www.thorlabs.com* (2023) .

[127] D.H. von Seggern, *CRC Standard Curves and Surfaces with Mathematica*, FL: CRC Press, 2nd ed. (2016), 10.1201/B16001.

[128] E.A. Manson and E. McDaniel, *Front Matter*, John Wiley Sons, Ltd (1988), 10.1002/3527602852.

[129] Landolt-Börnstein, *Eigenschaften des Plasmas*, vol. IV/3, Springer, 6th ed. (1957).

[130] Hirox, "Hirox rh-2000 digital microscope." Available at `https://hirox-europe.com/products/3d-digital-microscope/rh-2000/`2023.

[131] P.M. Encarnação, A.F. Cortez, M.G. Pinto, P.N. Neves, A.M. Trindade, J. Escada et al., *Experimental ion mobility measurements in ar-co2 mixtures*, *Journal of Instrumentation* **10** (2015) P01010.

[132] A. Deisting, C. Garabatos and A. Szabo, *Ion mobility measurements in Ar-CO2, Ne-CO2, and Ne-CO2-N2 mixtures, and the effect of water contents*, *Nuclear Instruments and Methods in Physics Research Section A: Accelerators, Spectrometers, Detectors and Associated Equipment* **904** (2018) 1.

[133] F.M. Penning, *Über den einfluß sehr geringer beimischungen auf die zündspannung der edelgase*, *Zeitschrift für Physik* **46** (1928) 335.

[134] F.M. Penning, *The starting potential of the glow discharge in neon argon mixtures between large parallel plates: Ii. discussion of the ionisation and excitation by electrons and metastable atoms*, *Physica* **1** (1934) 1028.

[135] M.J. Druyvesteyn and F.M. Penning, *The mechanism of electrical discharges in gases of low pressure*, *Reviews of Modern Physics* **12** (1940) 87.

[136] Ö. Şahin, I. Tapan, N. Özmutlu and R. Veenhof, *Penning transfer in argon-based gas mixtures*, *Journal of Instrumentation* **5** (2010) P05002.

[137] Y. Kalkan, M. Arslandok, A.F. Cortez, Y. Kaya, I. Tapan and R. Veenhof, *Cluster ions in gas-based detectors*, *Journal of Instrumentation* **10** (2015) P07004.

[138] G. Battistoni, P. Campana, V. Chiarella, U. Denni, E. Iarocci and G. Nicoletti, *Resistive cathode transparency*, *Nuclear Instruments and Methods in Physics Research* **202** (1982) 459.

[139] J. Galán, D. Attié, A. Chaus, P. Colas, A. Delbart, E. Ferrer-Ribas et al., *Characterization and simulation of resistive-mpgds with resistive strip and layer topologies*, *Nuclear Instruments and Methods in Physics Research Section A: Accelerators, Spectrometers, Detectors and Associated Equipment* **732** (2013) 229.

[140] G. Bencivenni, R.D. Oliveira, G. Morello and M.P. Lener, *The micro-Resistive WELL detector: a compact spark-protected single amplification-stage MPGD*, *Journal of Instrumentation* **10** (2015) P02008.

[141] Z. Fang, S. He, H. Zhou, Y. Lv, Y. Zhou, J. Liu et al., *Simulation and optimization of fast grounding designs for micro-pattern gas detectors with a resistive layer*, *Nuclear Instruments and Methods in Physics Research Section A: Accelerators, Spectrometers, Detectors and Associated Equipment* **1032** (2022) 166615.

[142] M. Chefdeville, Y. Karyotakis, T. Geralis and M. Titov, *Resistive micromegas for sampling calorimetry, a study of charge-up effects*, *Nuclear Instruments and Methods in Physics Research Section A: Accelerators, Spectrometers, Detectors and Associated Equipment* **824** (2016) 510.

[143] M. Alviggi, M. Biglietti, V. Canale, M.D. Pietra, C.D. Donato, S. Franchino et al., *Small-pads resistive micromegas*, *Journal of Instrumentation* **12** (2017) C03077.

[144] M. Iodice, M. Alviggi, M. Camerlingo, V. Canale, M.D. Pietra, C.D. Donato et al., *Small-pad resistive micromegas: rate capability for different spark protection resistive schemes*, *Journal of Instrumentation* **15** (2020) C09043.

[145] C. Lippmann, W. Riegler and A. Kalweit, *Rate effects in resistive plate chambers*, *Nuclear Physics B - Proceedings Supplements* **158** (2006) 127.

[146] M. Lisowska et al., *Towards robust PICOSEC Micromegas precise timing detectors*, *Journal of Instrumentation* **18** (2023) C07018 [2303.18141].

[147] E. Lopienska, *The CERN accelerator complex*, CERN CDS Service, (2022).

[148] L. Sohl et al., *Spatial time resolution of MCP–PMTs*, *PM2018 - 14th Pisa Meeting on Advanced Detectors* (May 27. - June 2. 2018) .

[149] J. Bortfeldt, F. Brunbauer, C. David, D. Desforge, G. Fanourakis, M. Gallinaro et al., *Timing performance of a micro-channel-plate photomultiplier tube*, *Nuclear Instruments and Methods in Physics Research Section A: Accelerators, Spectrometers, Detectors and Associated Equipment* **960** (2020) 163592.

[150] W. Leo, *Techniques for Nuclear and Particle Physics Experiments: A How-to Approach*, Springer (1994).

[151] S. Kalbitzer and W. Melzer, *On the charge dividing mechanism in position sensitive detectors*, *Nuclear Instruments and Methods* **56** (1967) 301.

[152] E. Mathieson, K.D. Evans, W. Parkes and P.F. Christie, *Signal location by shorted RC line*, *Nuclear Instruments and Methods* **121** (1974) 139.

[153] W. Riegler, *Simulation of detectors with resistive elements, AC-LGADs*, CERN, Presented at: AC LGAD simulations meeting, 30 March 20212021, https://indico.cern.ch/event/1023366/.

[154] K. Shchablo, I. Laktineh, M. Gouzevitch, C. Combaret and L. Mirabito, *Performance of the CMS RPC upgrade using 2D fast timing readout system*, *Nuclear Instruments and Methods in Physics Research Section A: Accelerators, Spectrometers, Detectors and Associated Equipment* **958** (2020) 162139.

[155] E. Mathieson, *A flux problem related to two dimensional image dissection*, *Nuclear Instruments and Methods* **92** (1971) 441.

[156] G. Fraser and E. Mathieson, *Signal location by uniform resistive anodes: (A) Square anodes in the dc limit*, *Nuclear Instruments and Methods* **179** (1981) 591.

[157] G. Fraser, E. Mathieson, M. Lewis and M. Barstow, *Signal location by uniform resistive anodes: (C) Time-dependent performance*, *Nuclear Instruments and Methods in Physics Research* **190** (1981) 53.

[158] H. Anger, *Scintillation camera with multichannel collimators*, *Journal of nuclear medicine* **65** (1964) 515.

[159] C. Gear, *Proceeding skytop conference on computer systems in experimental nuclear physics*, *USAEC Conf-670301* (1969) 552.

[160] M. Lampton and C.W. Carlson, *Low-distortion resistive anodes for two-dimensional position-sensitive MCP systems*, *Review of Scientific Instruments* **50** (2008) 1093.

[161] K. Yang, Y. Bai, W. Cao, Y. Yang, B. Zhu, J. Zheng et al., *Position linearity analysis of circular arc terminated resistive anode using finite element method for photon-counting imaging detectors*, *Review of Scientific Instruments* **94** (2023) 13703.

[162] T. Doke, J. Kikuchi, H. Yamaguchi, S. Yamaguchi and K. Yamamura, *A new two-dimensional position sensitive detector with a good linear response*, *Nuclear Instruments and Methods in Physics Research Section A: Accelerators, Spectrometers, Detectors and Associated Equipment* **261** (1987) 605.

[163] H. Wagner, A. Orthen, H.J. Besch, S. Martoiu, R.H. Menk, A.H. Walenta et al., *On image reconstruction with the two-dimensional interpolating resistive readout structure of the Virtual-Pixel detector*, *undefined* **523** (2004) 287.

[164] N. Hasebe, Y. Ezawa, H. Yoshii and T. Yanagimachi, *Charge waveform of a new two-dimensional position-sensitive silicon detector*, *Japanese Journal of Applied Physics* **27** (1988) 816.

[165] R. Cowin and D. Watson, *Surface charge flow in two-dimensional position sensitive silicon detectors*, *Nuclear Instruments and Methods in Physics Research Section A: Accelerators, Spectrometers, Detectors and Associated Equipment* **399** (1997) 365.

[166] A. Sarvestani, H. Besch, M. Junk, W. Meißner, N. Sauer, R. Stiehler et al., *Study and application of hole structures as gas gain devices for two dimensional high rate x-ray detectors*, *Nuclear Instruments and Methods in Physics Research Section A: Accelerators, Spectrometers, Detectors and Associated Equipment* **410** (1998) 238.

[167] A. Orthen, H. Wagner, H. Besch, R. Menk, A. Walenta and U. Werthenbach, *Investigation of the performance of an optimised microcat, a gem and their combination by simulations and current measurements*, *Nuclear Instruments and Methods in Physics Research Section A: Accelerators, Spectrometers, Detectors and Associated Equipment* **500** (2003) 163.

[168] H.J. Besch, M. Junk, W. Meibner, A. Sarvestani, R. Stiehler and A.H. Walenta, *An interpolating 2D pixel readout structure for synchrotron X-ray diffraction in protein crystallography*, *Physics Research A* **392** (1997) 244.

[169] N. Cartiglia, *Topics in LGAD designs*, *Presented at the 39th RD50 Workshop (Valencia)* (2021) .

[170] L. Menzio, R. Arcidiacono, G. Borghi, M. Boscardin, N. Cartiglia, M. Centis Vignali et al., *Dc-coupled resistive silicon detectors for 4d tracking*, *Nuclear Instruments and Methods in Physics Research Section A: Accelerators, Spectrometers, Detectors and Associated Equipment* **1041** (2022) 167374.

[171] L. Yang, J. Liu, Y. Zhang, W. Wang, D. Yu, X. Li et al., *Note: A two-dimensional position-sensitive micro-channel plate detector with a cross-connected-pixels resistive anode and integrated spectroscopy amplifiers*, *Review of Scientific Instruments* **88** (2017) .

[172] W. Hendrik, *Vielzellenwiderstandsauslese für zweidimensionale Röntgenabbildungen: Optimierung der Abbildungseigenschaften bei Anwendungen mit schneller Bildfolge*, Ph.D. thesis, Universität Siegen (2004)2024.

[173] Q.L. Xiu, M.Y. Dong, R.G. Liu, J. Zhang, Q. Ouyang and Y.B. Chen, *Reconstruction algorithm study of 2D interpolating resistive readout structure*, *Chinese Physics C* **37** (2013) .

[174] A. Sarvestani, H.J. Besch, M. Junk, W. Meißner, N. Sauer, R. Stiehler et al., *Study and application of hole structures as gas gain devices for two dimensional high rate X-ray detectors*, *Nuclear Instruments and Methods in Physics Research, Section A: Accelerators, Spectrometers, Detectors and Associated Equipment* **410** (1998) 238.

[175] X.D. Ju, M.Y. Dong, Y.C. Zhao, C.X. Zhou, J. Dong, Y.B. Zhao et al., *Two-dimensional imaging triple-GEM detector with resistive anode readout*, *Journal of Instrumentation* **12** (2017) P10008.

[176] X.-D. Ju, M.-Y. Dong, Y.-C. Zhao, C.-X. Zhou and Q. Ouyang, *Design and optimization of resistive anode for a two-dimensional imaging triple-GEM detector*, *Chinese Physics C* **40** (2016) [`1602.07438v1`].

[177] K. Perlin, *An image synthesizer*, *SIGGRAPH Comput. Graph.* **19** (1985) 287–296.

[178] R. Arcidiacono, G. Borghi, M. Boscardin, N. Cartiglia, M. Centis Vignali, M. Costa et al., *High-precision 4D tracking with large pixels using thin resistive silicon detectors*, *Nuclear Instruments and Methods in Physics Research Section A: Accelerators, Spectrometers, Detectors and Associated Equipment* **1057** (2023) 168671.

[179] M. Aleksa, J. Blomer, B. Cure, M. Campbell, C. D'Ambrosio, D. Dannheim et al., *Strategic R&D programme on technologies for future experiments*, CERN-OPEN-2018-006, CERN, Geneva (2018).

[180] L. Anderlini, M. Bellini, A. Bizzeti, A. Cardini, R. Ciaranfi, C. Corsi et al., *Fabrication and characterisation of 3d diamond pixel detectors with timing capabilities*, *Frontiers in Physics* **8** (2020) .

[181] C. Bauer, I. Baumann, C. Colledani, J. Conway, P. Delpierre, F. Djama et al., *Radiation hardness studies of cvd diamond detectors*, *Nuclear Instruments and Methods in Physics Research Section A: Accelerators, Spectrometers, Detectors and Associated Equipment* **367** (1995) 207.

[182] L. Bäni, A. Alexopoulos, M. Artuso, F. Bachmair, M. Bartosik, H. Beck et al., *A study of the radiation tolerance of poly-crystalline and single-crystalline CVD diamond to 800 MeV and 24 GeV protons*, *Journal of Physics D: Applied Physics* **52** (2019) 465103.

[183] S. Parker, C. Kenney and J. Segal, *3D — A proposed new architecture for solid-state radiation detectors*, *Nuclear Instruments and Methods in Physics Research Section A: Accelerators, Spectrometers, Detectors and Associated Equipment* **395** (1997) 328.

[184] J. Lange, G. Giannini, S. Grinstein, M. Manna, G. Pellegrini, D. Quirion et al., *Radiation hardness of small-pitch 3d pixel sensors up to a fluence of 3×1016 neq/cm2*, *Journal of Instrumentation* **13** (2018) P09009.

[185] S. Lagomarsino, M. Bellini, C. Corsi, V. Cindro, K. Kanxheri, A. Morozzi et al., *Radiation hardness of three-dimensional polycrystalline diamond detectors*, *Applied Physics Letters* **106** (2015) 193509.

[186] RD42 collaboration, *Development of diamond tracking detectors for high luminosity experiments at the LHC; 1996 ed.*, CERN-LHCC-97-003, CERN, Geneva (1996).

[187] S. Lagomarsino, M. Bellini, C. Corsi, F. Gorelli, G. Parrini, M. Santoro et al., *Three-dimensional diamond detectors: Charge collection efficiency of graphitic electrodes*, *Applied Physics Letters* **103** (2013) 233507.

[188] L. Anderlini, M. Bellini, C. Corsi, S. Lagomarsino, C. Lucarelli, G. Passaleva et al., *Fabrication and first full characterisation of timing properties of 3d diamond detectors*, *Instruments* **5** (2021) .

[189] E. Bossini and N. Minafra, *Diamond detectors for timing measurements in high energy physics*, *Frontiers in Physics* **8** (2020) .

[190] N. Cartiglia, R. Arcidiacono, B. Baldassarri, M. Boscardin, F. Cenna, G. Dellacasa et al., *Tracking in 4 dimensions*, *Nuclear Instruments and Methods in Physics Research Section A: Accelerators, Spectrometers, Detectors and Associated Equipment* **845** (2017) 47.

[191] G. Kramberger, *KDetSim*, *http://kdetsim.org* (2023) .

[192] A. Morozzi, S. Sciortino, L. Anderlini, L. Servoli, K. Kanxheri, S. Lagomarsino et al., *3d diamond tracking detectors: numerical analysis for timing applications with tcad tools*, *Journal of Instrumentation* **15** (2020) C01048.

[193] G. Passaleva and W. Riegler, *Diamond sensors with resistive pillars*, *Private notes* (2021) .

[194] W. Riegler and G.A. Rinella, *Time resolution of silicon pixel sensors*, *Journal of Instrumentation* **12** (2017) P11017.

[195] Z. Li and H. Kraner, *Modeling and simulation of charge collection properties for neutron irradiated silicon detectors*, *Nuclear Physics B - Proceedings Supplements* **32** (1993) 398.

[196] C. Canali, G. Majni, R. Minder and G. Ottaviani, *Electron and hole drift velocity measurements in silicon and their empirical relation to electric field and temperature*, *IEEE Transactions on Electron Devices* **22** (1975) 1045.

[197] R. Wallny et al., *Recent progress in CVD diamond detector R&D*, 2020. 10.22323/1.373.0029.

[198] R. Wallny, *Recent progress in CVD diamond detector R&D*, *Presentation at Vertex* (2019) .

[199] C. Dorfer, D. Hits, L. Kasmi, G. Kramberger, M. Lucchini, M. Mikuž et al., *Three-dimensional charge transport mapping by two-photon absorption edge transient-current technique in synthetic single-crystalline diamond*, *Applied Physics Letters* **114** (2019) .

[200] B. Kraus, P. Steinegger, N.V. Aksenov, R. Dressler, R. Eichler, E. Griesmayer et al., *Charge carrier properties of single-crystal CVD diamond up to 473 K*, *Nuclear Instruments and Methods in Physics Research Section A: Accelerators, Spectrometers, Detectors and Associated Equipment* **989** (2021) 164947.

[201] I. Smirnov, *Modeling of ionization produced by fast charged particles in gases*, *Nuclear Instruments and Methods in Physics Research Section A: Accelerators, Spectrometers, Detectors and Associated Equipment* **554** (2005) 474.

[202] I. Smirnov, *Heed-C++*, *http://ismirnov.web.cern.ch/ismirnov/heed* (2023) .

[203] S. Lagomarsino, M. Bellini, M. Brianzi, R. Carzino, V. Cindro, C. Corsi et al., *Polycrystalline diamond detectors with three-dimensional electrodes*, *Nuclear Instruments and Methods in Physics Research Section A: Accelerators, Spectrometers, Detectors and Associated Equipment* **796** (2015) 42.

[204] L. Anderlini, M. Bellini, C. Corsi, S. Lagomarsino, C. Lucarelli, G. Passaleva et al., *Construction and characterisation of high time resolution 3d diamond pixel detectors*, *Nuclear Instruments and Methods in Physics Research Section A: Accelerators, Spectrometers, Detectors and Associated Equipment* **1046** (2023) 167692.

[205] M. Veltri et al., *A 4D diamond detector for HL-LHC and beyond*, Presented at: The 16th Vienna Conference on Instrumentation, 21–25 February 2022.

[206] J. Galán, *Signal propagation and spark mitigation in resistive strip read-outs*, *Journal of Instrumentation* **7** (2012) C04009.

[207] M. Bianco, H. Danielsson, J. Degrange, A. Düdder, R. De Oliveira, E. Farina et al., *Construction of two large-size four-plane micromegas detectors*, *Nuclear Instruments and Methods in Physics Research Section A: Accelerators, Spectrometers, Detectors and Associated Equipment* **814** (2016) 117.

[208] F. Kuger, *Signal Formation Processes in Micromegas Detectors and Quality Control for large size Detector Construction for the ATLAS New Small Wheel*, Ph.D. thesis, Wurzburg U.2017.

[209] P. Iengo, *Development of a resistive plate device with micro-pattern technique*, *Nuclear Instruments and Methods in Physics Research Section A: Accelerators, Spectrometers, Detectors and Associated Equipment* **958** (2020) 162779.

[210] P. Iengo, *The industrial production of micro pattern gaseous detector: experience from the atlas micromegas*, *Presented at the RD51 Collaboration Meeting* (2023) .

[211] L.L. Jones et al., *The APV25 deep submicron readont chip for CMS detectors*, *Conf. Proc. C 9909201* (1999) 162.

[212] M. Raymond et al., *The APV25 0.25 μm CMOS readout chip for the CMS tracker*, *IEEE Nuclear Science Symposium and Medical Imaging Conference* **2** (2000) .

[213] J. Samarati, P. Iengo, L. Longo, G. Sekhniaidze, O. Sidiropoulou and J. Wotschack, *Characterisation of the charging up effect in resistive micromegas detectors*, *Journal of Physics: Conference Series* **1498** (2020) 012030.

[214] P. Correia, *Charging-up simulations for GEM and Micromegas*, *Presented at the RD51 Collaboration Meeting* (2020) .

[215] S. Gadomski, G. Hall, T. Høgh, P. Jalocha, E. Nygård and P. Weilhammer, *The deconvolution method of fast pulse shaping at hadron colliders*, *Nuclear Instruments and Methods in Physics Research Section A: Accelerators, Spectrometers, Detectors and Associated Equipment* **320** (1992) 217.

[216] L. Jones, *APV25-S1: User guide version 2.2*, RAL Microelectronics Design Group, Chilton (2001).

[217] R. Guida, B. Mandelli and G. Rigoletti, *Studies on alternative eco-friendly gas mixtures and development of gas recuperation plant for rpc detectors*, *Nuclear Instruments and Methods in Physics Research Section A: Accelerators, Spectrometers, Detectors and Associated Equipment* **1039** (2022) 167045.

[218] D. Stocco, *Simulation of RPC detectors with updated R134 cross sections and future prospects*, *Presented at the DRD1 Collaboration Meeting* (2024) .